


1987

Geology, geochemistry, and geochronology of the Lems Ridge olistostrome, Klamath Mountains, California

Matthias Ohr

University at Albany, State University of New York

Follow this and additional works at: [http://scholarsarchive.library.albany.edu/
cas_daes_geology_etd](http://scholarsarchive.library.albany.edu/cas_daes_geology_etd)

 Part of the [Geochemistry Commons](#), [Geology Commons](#), [Geophysics and Seismology Commons](#), [Stratigraphy Commons](#), and the [Tectonics and Structure Commons](#)

Recommended Citation

Ohr, Matthias, "Geology, geochemistry, and geochronology of the Lems Ridge olistostrome, Klamath Mountains, California" (1987). *Geology Theses and Dissertations*. 65.
http://scholarsarchive.library.albany.edu/cas_daes_geology_etd/65

This Thesis is brought to you for free and open access by the Atmospheric and Environmental Sciences at Scholars Archive. It has been accepted for inclusion in Geology Theses and Dissertations by an authorized administrator of Scholars Archive. For more information, please contact scholarsarchive@albany.edu.

Geology, Geochemistry, and Geochronology
of the Lems Ridge olistostrome,
Klamath Mountains, California

A thesis presented to the Faculty
of the State University of New York
at Albany
in partial fulfillment of the requirements
for the degree of
Master of Science

College of Science and Mathematics
Department of Geological Sciences

Matthias Ohr

1987

Geology, Geochemistry, and Geochronology
of the Lems Ridge olistostrome,
Klamath Mountains, California

Abstract of
a thesis presented to the Faculty
of the State University of New York
at Albany
in partial fulfillment of the requirements
for the degree
Master of Science

College of Science and Mathematics
Department of Geological Sciences

Matthias Ohr

1987

Abstract

The Lems Ridge olistostrome (LRO), located within the western Jurassic belt of the Klamath Mountains geologic province, is a melange unit showing a distinct block-in-matrix fabric. The conformable relationship to both an igneous basement and the overlying flysch of the Late Jurassic Galice Formation points to a sedimentary origin. The lack of pervasive deformation and the internal stratification also support a predominantly olistostromal origin of the LRO. The matrix of the LRO consists of pebbly mudstone which interfingers with tuffaceous greenstone and tuff-breccias. Subordinate beds of chert, argillite, and sandstone are also present. The matrix contains abundant ophiolitic clasts, fragments of porphyritic and vesicular volcanics, as well as a variety of sedimentary and metamorphic rocks. A block supported talus deposit is locally dominant and consists of serpentized ultramafics, diabase, and sparse gabbroic rocks.

The LRO has been previously interpreted as a remnant of an ancient fracture zone within the Josephine ophiolite (JO). Basement and clasts were thought as locally derived from the JO which is of Late Jurassic age and has a distinct supra-subduction zone chemistry. Geochemical and geochronological data were obtained to test this hypothesis.

The major and trace element geochemistry of the tuffaceous matrix and the ophiolitic lithologies indicates the presence of several petro-tectonic regimes in the source areas of the LRO: the tuffaceous rocks are transitional between island-arc tholeiitic and calc-alkaline; the basal pillow lavas range from within-plate basalts to enriched MORB compositions; olistoliths of pillow basalt range from depleted to enriched MORB; clasts of sparse mafic scorias are alkaline within-plate basalts. Diabase talus blocks are transitional between N-MORB and island-arc tholeiites, but also include very primitive arc-related rocks.

$^{40}\text{Ar}/^{39}\text{Ar}$ hornblende ages of large gabbro blocks cluster consistently around 190 Ma; a basement gabbro yields the same age within error limits. The metamorphic age of a mica-schist clast is found to be 280 Ma; the total gas age for an andesitic boulder is 173 +/- 6 Ma. Calc-alkaline dikes that cross-cut block-matrix boundaries show ages of 148 Ma and 149 Ma, respectively, and constrain a minimum age for the assembly of the LRO.

It is concluded that the LRO overlies an older basement than previously assumed and contains ophiolitic lithologies, the age and chemistry of which is not compatible with a derivation from the JO. On the other hand, the chemistry of diabase blocks as well as the lithologic assemblage in a talus breccia suggests an

affinity to the JO. The conformable contact to the Galice Formation implies the same genetic link.

A model that integrates this diversity is suggested: the JO formed in a transform dominated marginal basin; its spreading geometry requires the presence of fracture zones parallel to, and projecting into the passive margin of the Hayfork-Rattlesnake Creek remnant arc. The ensuing boundary transform fault is floored by older rocks of the margin, whereas the infill into the transform trough comprises three sources: the passive margin, an active arc that rifted off the older arc, and the incipient JO. The LRO and its basement are thus interpreted as a preserved rift-edge sequence of the Josephine ophiolite.

Acknowledgements

I am deeply indebted to Greg Harper who introduced me to this project and continued his support and interest over the past two years. I feel privileged to thank the members of my committee, John Delano, Greg Harper, and Mark Harrison, from whom I learned about ingenuity and ethics in science, about enthusiasm, obsession, and the limits in scientific research. All members of the Department contributed in numerous ways to the completion of this thesis; each of you helped with companionship and collegiate advice.

My friends in Australia, Spain, Germany, and the United States were truly indispensable.

Love has shown itself in my life. Returning this love to my family and to Shannon makes me a happy and complete person.

This thesis was supported by NSF Grant No. EAR 8518974 to Greg Harper, and by fellowships of the Germanistic Society of America and the Studienstiftung des Deutschen Volkes. A Grant-in-Aid from Sigma Xi is also acknowledged.

Table of Contents

Abstract	i
Acknowledgements	iv
Table of contents	v
List of tables	vii
List of figures	viii
1. <u>Chapter I: Introduction and Regional Setting</u>	1
1.1 Introduction	1
1.2 Regional Geology	2
1.3 Study Area and Previous Work	14
2. <u>Chapter II: Fracture Zones and Melanges: Impli- cations for Ophiolite Geology</u>	18
2.1 Fracture Zones	18
2.2 Melanges and Olistostromes	31
3. <u>Chapter III: Geology and Petrography of the Lems Ridge olistostrome</u>	44
3.1 Introduction	44
3.2 Petrography of the LRO	49
The GO-Road Section	49
The Smith River Section	71
4. <u>Chapter IV: Geochemistry</u>	94
4.1 Analytical Methods	94
4.2 Discriminant Diagrams	96
4.3 N-MORB Normalized Trace Element Plots	124
4.4 The Hf-Th-Ta Diagram	144
4.5 Summary	158
5. <u>Chapter V: Geochronology</u>	164
5.1 Purpose	164
5.2 Methods	167
5.3 $^{40}\text{Ar}/^{39}\text{Ar}$ Results.....	181
5.4 Discussion	203

6. <u>Chapter VI: Discussion and Concluding Remarks</u>	213
<u>References</u>	228
Appendix I - Major and trace element analyses ...	248
Appendix II - REE analyses	259
Outline of INAA	263
Appendix III - Normalized element abundances	267
Appendix IV - $^{40}\text{Ar}/^{39}\text{Ar}$ data.....	270

List of Tables

5.1	Summary of isochron ages, plateau ages, and total gas ages	182
I.1	Major and trace element analyses	249
I.2	250
I.3	251
I.4	252
I.5	253
I.6	254
I.7	255
I.8	XRF analyses of USGS standards	256
II.1	REE analyses	260
II.2	261
II.3	INAA analysis of USGS standard W-1	262
III.1	MORB-normalized element abundances	268
III.2	269
IV.1	Isotopic abundances of K and Ar	271
IV.2	Decay constants for ^{40}K	272
IV.3	Ar/Ar data for LR 10	273
IV.4	LR 171	273
IV.5	LR 871	274
IV.6	LR 1273	274
IV.7	LR 1573	275
IV.8	LR 82	276
IV.9	D-LRO	276
IV.10	LR 15	277
IV.11	Z 53	277
IV.12	U/Pb data for plagiogranite LR 41	278

List of Figures

1.1	Geologic map of the Klamath Mountains	3
1.2	Geologic map of the western Paleozoic and Triassic terrane	6
1.3	Geologic map of the western Jurassic belt	10
1.4	Stratigraphy and age of the western Jurassic belt ..	15
1.5	Location of the study area	16
2.1	The main morphotectonic features of the transform domain in fracture zones	21
3.1	Geologic map of the area of the Lems Ridge olistostrome (LRO)	45
3.2	Observed units within the LRO	51
3.3	GO-road tectono-stratigraphic section	52
3.4	Sheared pebbly mudstone (pm)	62
3.5	Pillow lava from the GO-road	62
3.6	Handsamples of volcanic clasts in sheared matrix ...	63
3.7	Texture of pebbly mudstone	64
3.8	Photomicrographs of recrystallized radiolarians in pebbly mudstone and argillite	65
3.9	Handsample and photomicrograph of pebble conglomerate (Galice Fm.)	66
3.10	Photomicrographs of chert in pebble conglomerate ...	67
3.11	Photomicrograph of quartz arenite pebble in pm	68
3.12	Photomicrograph of quartzite and chert in pm	68
3.13	Photomicrograph of typical pebbly mudstone	69
3.14	Photomicrograph of diabase in breccia	70
3.15	Photomicrograph of serpentinite in breccia	70
3.16	Smith River tectono-stratigraphic section	72
3.17	Photomicrographs of amphibole in gabbro	81
3.18	Contact of mudstone and pillow lava	82
3.19	Photomicrograph of amphibole in andesite block	83
3.20	Photomicrographs of tuffaceous greenstone	84
3.21	Texture of volcanic tuff and breccia	85
3.22	Contact of gabbro block with pebbly mudstone	86
3.23	Handsample of graded volcanic sandstone	87
3.24	Photomicrographs of cataclastic gabbro	88, 89
3.25	Handsamples of cataclastic gabbro	90
3.26	Photomicrographs of graywacke in LRO	91
3.27	Outcrop map along the South Fork of the Smith River	92
4.1	Sample locations	103
4.2	Ti-Zr diagram	117
4.3	Ti/100-Zr-Yx3 diagram	118
4.4	Petrogenetic modelling in the Cr-Y diagram	119
4.5	Cr-Y diagram	120
4.6	Ti/Cr-Ni diagram	121

4.7	Petrogenetic modelling in the Ti-V diagram	122
4.8	Ti-V diagram	123
4.9	MORB-normalized trace element patterns for MORB, IAT, CAB, and WPB	127
4.10	Trace element patterns for tuffaceous greenstone ..	146
4.11	Trace element patterns for scoria clasts	147
4.12	Trace element patterns for basal pillow lava	148
4.13	Trace element patterns for pillow clasts	149
4.14	Trace element patterns for diabase blocks and dikes and lavas from the Josephine ophiolite	150
4.15	Trace element patterns for primitive basalts from the LRO and the JO	151
4.16	Trace element patterns for gabbro blocks and a mafic feeder dike	152
4.17	The Hf/3-Th-Ta diagram	154
4.18	Petrogenetic modelling in the Hf/3-Th-Ta diagram ..	155
4.19	[Ce/Yb]-[Ce] diagram	162
4.20	Summary of results	163
5.1	Decay scheme for ^{40}K	168
5.2	Three age spectra for ideal cases of an undis- turbed sample, Ar-loss, and excess Ar	173
5.3	SUNY Albany Ar-extraction and mass spectrometer assembly	177
5.4	Model isochron plot	179
5.5	Isochron and corrected age spectrum for a hypo- thetical sample containing excess Ar	180
5.6	Age spectrum and isochron for LR 10	190, 191
5.7	Age spectrum and isochron for LR 171	192, 193
5.8	Age spectrum for LR 871	194
5.9	Age spectrum for LR 1573	195
5.10	Age spectrum and isochron for LR 1273	196, 197
5.11	Age spectrum for LR 82	198
5.12	Age spectrum for D-LRO	199
5.13	Age spectrum and isochron for LR 15	200, 201
5.14	Age spectrum for Z 53	202
5.15	207/206 vs. 238/206 diagram for LR 41	206
6.1	Cross-section of the northern part of the LRO	216
6.2	Geology and residual gravity map of the western Klamath Mountains	217
6.3	Reconstruction of the paleo-tectonic setting of the Lems Ridge olistostrome	224
I.1	Graphical correction for Zr data	257
I.2	Correlation of analytical error and concentra- tion for Hf, Th, Ta	258

CHAPTER I

Introduction and Regional Setting

1.1 Introduction

Jurassic ophiolites are a distinctive feature along much of the western Sierra Nevada, the Klamath Mountains, and the Californian Coast Ranges. They appear to record major transform motion and associated oblique spreading parallel to the ancient margin of western North America (Harper and others, 1985). The Late Jurassic Josephine ophiolite (Harper, 1980, 1984; Saleeby and others, 1982) and the conformably overlying flysch of the Galice Formation are the result of Late Jurassic extensional tectonics within a Middle to Late Jurassic arc (Harper and Wright, 1984; Ingersoll and Schweickert, 1986).

One of the strongest lines of evidence for a predominant transform regime within the Josephine back-arc basin is the local occurrence of an unusual sedimentary deposit, the Lems Ridge olistostrome (LRO). Structural, stratigraphic, and geochemical evidence suggested to previous workers that the olistostrome was deposited in a fracture zone valley (Harper and others, 1983; Norman, 1984; Harper and others, 1985). The purpose of this study is to test this hypothesis with geochemical, geochronological, and petrographic data. Since the LRO

promised to be closely related to the Josephine ophiolite, the Galice Formation, and to the volcanic Rogue Formation, it was hoped to further constrain the timing of back-arc extension as well as to clarify the position of the Josephine basin with respect to the inboard continental margin. Instead, the geochemistry and in particular the geochronology on ophiolitic clasts within the olistostrome revealed a similar, but somewhat unexpected tectonic scenario for the Lems Ridge olistostrome.

1.2 Regional Geology

The Klamath Mountains province of northern California and of southwestern Oregon consists of a series of thrust bounded terranes (Fig. 1.1). They range in age from early Paleozoic to Late Jurassic, and are stacked along major thrust faults to form an east-dipping imbricate sequence that, in a general fashion, becomes younger downsection from east to west (Irwin, 1981). All of these terranes have a distinct lithostratigraphic character, but share a history of tectonic accretion that began in the Paleozoic and culminated during the Jurassic. They are exclusively of oceanic origin and include numerous ophiolitic terranes, various island-arc assemblages, and associated sedimentary and metasedimentary rocks.

Irwin (1960) discerned four subprovinces, or belts,

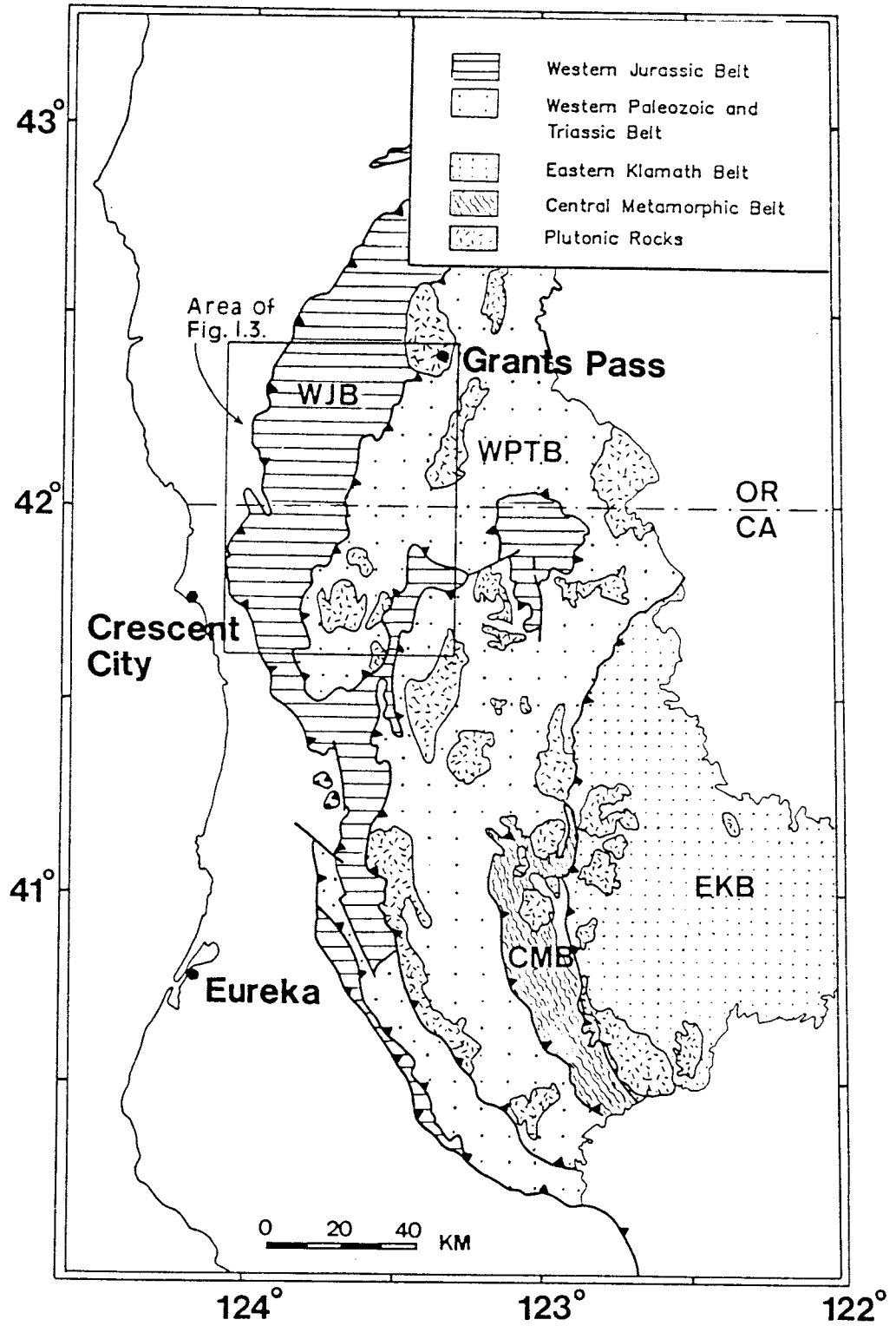


Figure 1.1 Generalized geologic map of the Klamath Mountains geologic province (modified from Jachens and others, 1986).

within the Klamath province (Fig. 1.1); these are from east to west: 1) the eastern Klamath belt, an assemblage of early Paleozoic to Jurassic sedimentary and volcanic rocks built across the Ordovician Trinity ultramafic complex, (Hopson and Mattinson, 1973); 2) the central metamorphic belt that is comprised of metavolcanic and metasedimentary rocks that were subjected to amphibolite-facies conditions during the Devonian (Lanphere and others, 1968); 3) the western Paleozoic and Triassic belt, and 4) the western Jurassic belt. Irwin (1981) reviews the lithologies present in each belt. A summary of the geology of both the western Paleozoic and Triassic belt and the western Jurassic belt is given below.

A minimum age for the juxtaposition of these belts is constrained by the Lower Cretaceous Great Valley sequence that unconformably overlies the southern part of the Klamath province. Furthermore, the three older terranes east of the western Jurassic belt were assembled already by Middle Jurassic times, as Triassic and Jurassic plutons of calc-alkaline affinity intrude into all three belts and their thrust contacts, respectively (Lanphere and others, 1968; Hotz, 1971; Wright, 1981; Saleeby and others, 1982; Irwin, 1985; Wright and Fahan, 1987).

The Klamath province has been described both in terms of a collage of far-travelled exotic terranes (Hamilton, 1969; Irwin, 1973, 1985; Schweickert and others, 1983;

Moores and Day, 1984; Day and others, 1985), and in terms of a relatively simple convergent plate boundary, the tectonic constituents of which are related in a temporal and spatial way and developed parautochthonous to the active margin (Wright, 1982; Harper and Wright, 1984; Gray, 1986). Indeed, it was in the Klamath Mountains that the term "terrane" was first used to imply their exotic or suspect origin (Irwin, 1972). This certainly contributed to the delay in interpreting the terranes of the Klamath province as "native terranes" (Gray, 1986).

The Western Paleozoic and Triassic Belt

Irwin (1972) subdivided this laterally most extensive thrust stack in the Klamath Mountains into three fault-bounded units; comprising from east to west: the North Fork terrane, the Hayfork terrane, and the Rattlesnake Creek terrane. Wright (1982) divided the Hayfork terrane into a structurally lower western Hayfork terrane consisting of coherent Mid-Jurassic volcanoclastic rocks, and the structurally higher eastern Hayfork terrane which is a disorganized melange composed of chert-argillite and sandstone. Fig. 1.2 additionally shows the Stuart Fork terrane (Davis and Lippman, 1962) which is considered correlative with the North Fork terrane by Wright (1982).

The structurally lowermost Rattlesnake Creek terrane

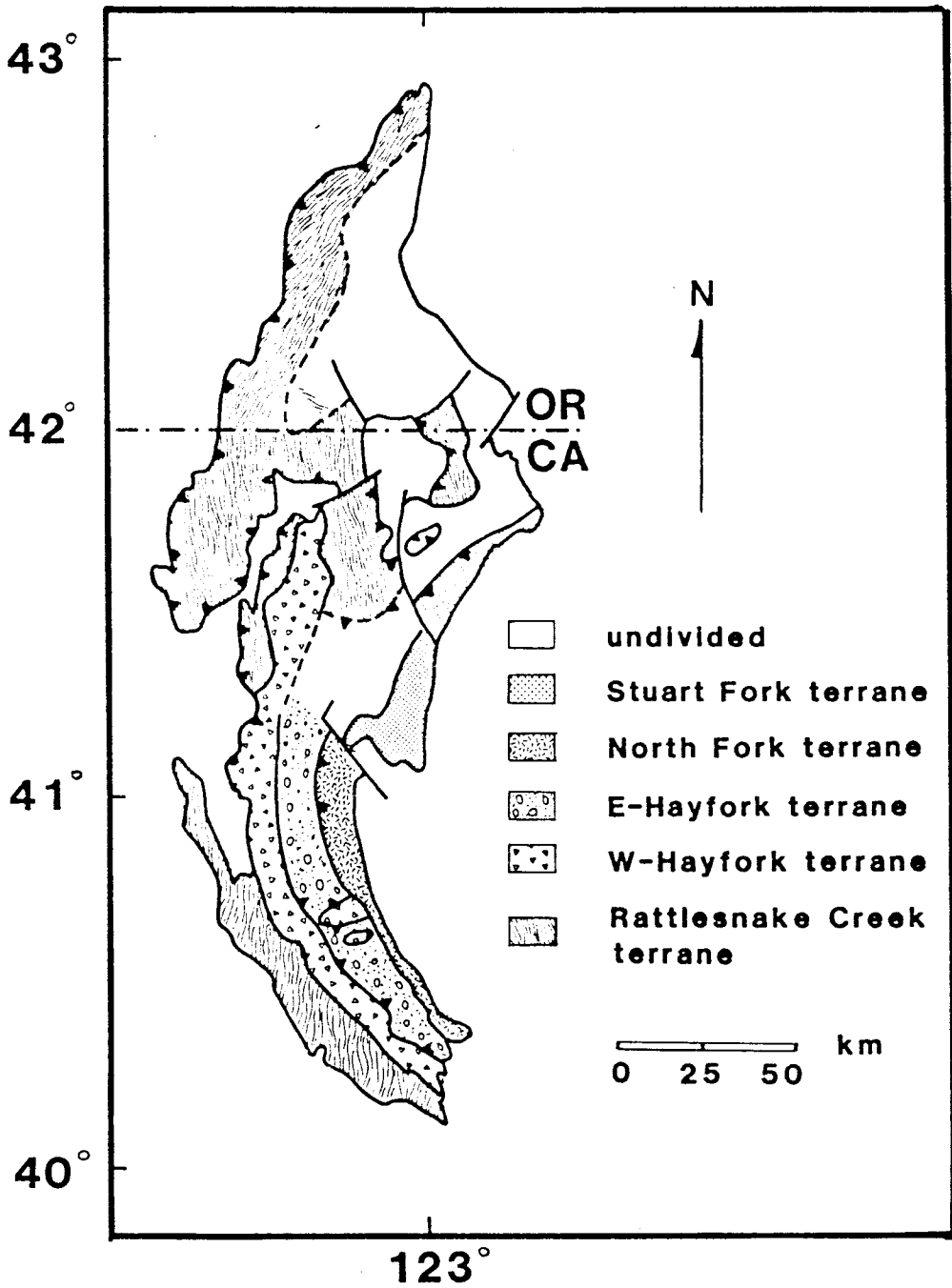


Figure 1.2 Generalized geologic map of the western Paleozoic and Triassic terrane (after Gray, 1986).

(RCT) was first described by Irwin (1972) as a dismembered ophiolite contained within a serpentinite-matrix melange. Blocks include serpentinitized ultramafics, mafic to intermediate plutonic rocks, mafic volcanics and pillow lavas, amphibolite, chert, limestone, and interbedded pebble conglomerate (Gorman, 1985; Wyld, 1985). Fossiliferous chert and limestone blocks range in age from Permian to Early Jurassic, with predominantly Late Triassic ages (Irwin and others, 1977, 1978, 1983).

More recent work has shown that this lower melange unit is overlain by coherent strata of volcanoclastic rocks with minor interbedded flows and hemipelagic sediments (Gray and Peterson, 1982; Gray and Wright, 1984; Gray, 1985). The rocks of this unit appear to be related to the formation of an island-arc, while greenstones and pillow blocks from the underlying melange show an unusual E-MORB geochemistry (Gorman, 1985). Both the lower and the upper unit of the Rattlesnake Creek terrane are cut by gabbros and diorites that yield concordant Pb/U-ages on zircon of 194-208 Ma (Wright, 1981, 1982; Gray and Wright, 1984).

The Stuart Fork, North Fork, and eastern Hayfork terrane all consist of highly disrupted sequences of ophiolitic rocks, Late Triassic pelagic and/or reef sediments and Early Jurassic tuffaceous deposits (Wright, 1982; Ando and others, 1983; Gray, 1985). They are interpreted as an accretionary subduction complex of

Permo-Triassic age that formed outboard from a magmatic arc that is now represented by volcanic and sedimentary rocks in the eastern Klamath belt (Wright, 1982; Gray, 1986).

The terranes briefly described above underwent pervasive deformation in the Late Triassic (prior to the 200 Ma plutons that crosscut the serpentinite-matrix melange of the Rattlesnake Creek terrane), leading to the tectonically disrupted character. Collectively they are thought to build the basement for a Middle Jurassic arc. This arc-complex was constructed west of the existing Permo-Triassic convergent margin (Gray, 1986). The extrusive section of the arc is represented by coherent sequences of interbedded volcanoclastics and argillites of the western Hayfork terrane; K-Ar ages on these rocks range from 168-177 Ma (Fahan and Wright, 1983). In addition, between 174 and 159 Ma a suite of related plutonic rocks was emplaced into the extrusive section and also intruded into the older terranes of the Permo-Triassic subduction complex (Wright, 1981). These plutons thus comprise the plutonic root of a Middle Jurassic arc (Harper and Wright, 1984; Wright and Fahan, 1987), while their presence in the western Paleozoic and Triassic terrane as well as in the central metamorphic belt proves that the amalgamation of these terranes was complete by as early as Middle Jurassic.

The Western Jurassic Belt

The westernmost and youngest terrane of the Klamath province comprises two major thrust sheets (Fig. 1.3): the structurally higher eastern thrust sheet consists of the Josephine ophiolite and overlying "Galice Formation" (Harper, 1980, 1983, 1984) that has been thrust westward over the adjacent and now structurally lower thrust stack (Ramp, 1975), comprised of the Rogue and Galice Formation and the Chetco complex (Garcia, 1979, 1982).

The Rogue Formation consists of calc-alkaline tuffs, breccias, and minor flows that are mafic to silicic in composition (Wells and Walker, 1953; Garcia 1979). Pb-U geochronology on a tuff-breccia from the Rogue Formation has provided a Late Jurassic age of 157 +/- 2 Ma for the Rogue Formation (Saleeby, 1984). Conformably overlying the Rogue Formation is the Galice Formation, a thick sequence of slaty argillite and graywacke turbidites that are locally interlayered with volcanoclastic rocks resembling those of the Rogue (Garcia, 1979, 1982). Whether this intercalating contact of flysch sediments and volcanics is depositional in nature, or came about by structural repetition of the Rogue Formation still remains to be resolved. The occurrence of the Late Jurassic bivalve Buchia concentrica (range from Late Oxfordian to Early Kimmeridgian) within the Galice suggests (within the

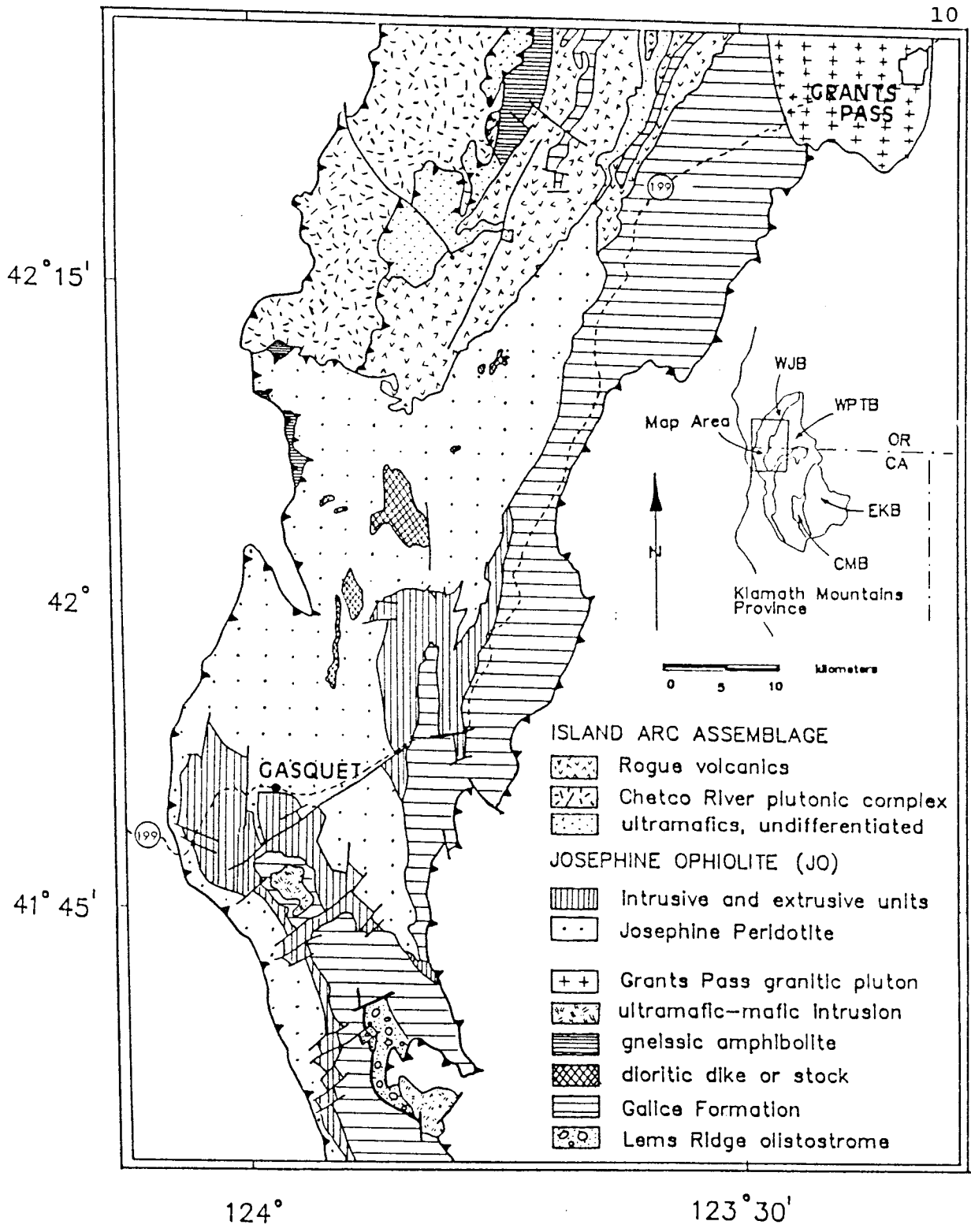


Figure 1.3 Generalized geologic map of the western Jurassic belt (modified from Harding, 1987).

resolution of the time scale) the syndepositional character of the Rogue and Galice Formations.

The Illinois River gabbro and the Rum Creek gabbro (Hotz, 1971; Garcia, 1982) are collectively referred to as the Chetco complex (Hotz, 1971). This predominantly gabbroic plutonic complex ranges from olivine-gabbro to granodiorite, and intrudes the Rogue Formation. Conventional K-Ar ages indicate ages between 152 and 159 Ma (Hotz, 1971; Dick, 1976). Garcia (1979, 1982) concludes on grounds of petrology, stratigraphy, and geochronology that the Rogue Formation represents the extrusive and pyroclastic sequence of a Late Jurassic island arc, while the coeval intrusives of the Chetco complex constitute the plutonic roots of this arc.

The eastern thrust sheet includes the Josephine ophiolite and the "Galice Formation" (Harper, 1984). The Josephine ophiolite is a well preserved and complete ophiolitic sequence consisting of the Josephine Peridotite and an overlying crustal section. The Peridotite is composed of harzburgite tectonite that is cut by numerous serpentinite shear zones. Some of the shear zones contain unusual serpentinites having textures resembling mylonites of quartzofeldspathic mineralogy (Norrell and others, 1987). These mylonites are suggested to represent the downward continuation of crustal oceanic faults into the upper mantle. Overlying the harzburgite is a relatively

thin (less than 4 km) crustal sequence consisting of ultramafic and mafic cumulates, non-cumulate gabbro, a well developed sheeted dike complex, and a carapace of pillow lavas and pillow breccias. Siliceous and argillaceous pelagic rocks overlie the top of the pillow section conformably (Harper, 1983; Pinto-Ausso and Harper, 1985). They grade into volcanic-rich graywackes and slaty argillites which are considered correlative to the Galice Formation which overlies the Rogue Formation (Harper, 1983). Plagiogranites from the Josephine ophiolite yielded Pb-U zircon ages of 157 ± 2 Ma (revised to 160 Ma, Saleeby and others, 1982, and unpublished data), consistent with the occurrence of coeval or somewhat younger flysch on top of the ophiolite.

The western Jurassic belt was subjected to regional prehnite - pumpellyite to lower greenschist facies metamorphism during the late Jurassic Nevadan orogeny. The degree of deformation and metamorphic grade increase from north to south; the Josephine ophiolite is generally less deformed than the overlying Galice Formation (Harper, 1984).

Several lines of evidence constrain the origin of the ophiolite to a Late Jurassic back-arc basin and supra-subduction zone setting (Harper, 1984; Harper and Wright, 1984): 1) the relative position of the ophiolite

inboard from and structurally above the coeval Rogue-Chetco arc-complex complex to the west; 2) the presence of turbidites rich in volcanic detritus above both the Rogue Formation and the ophiolite; 3) the presence of an older (remnant) volcanic arc to the east, whose activity shut down at the time of ophiolite generation; and 4) the geochemical affinities of dikes and lavas from the ophiolite to island-arc tholeiites rather than to mid-ocean ridge basalt. During the Nevadan orogeny the arc, back-arc basin and remnant arc collapsed into a stack of east-dipping thrust sheets (Harper and Wright, 1984). Abundant 148-152 Ma calc-alkaline dikes and sills intrude the entire western Jurassic belt and indicate the eastward migration of arc magmatism and thus the timing of the closure of the Josephine back-arc basin (Saleeby and others, 1982; Harper and Wright, 1984; Harper and others, 1985).

Fig. 1.3 shows the central part of the western Jurassic belt, with the main occurrence of the Josephine ophiolite southwest and northeast of the village of Gasquet, California. Also included is a simplified depiction of the area of the Rogue Formation and Chetco Complex at the top of the map. The study area of this thesis is located at the bottom of the map of Fig. 1.3 and is shown in more detail in Fig. 3.1. The simplified

stratigraphy and geochronology of the main geologic units in the western Jurassic belt is summarized in Fig. 1.4.

1.3 Study Area and Previous Work

The study area is located about 40 km south of the Oregon border and about 20 km inland from the Californian coast, Del Norte county, California. It covers the western parts of the USGS topographic 7.5' quadrangles Ship Mountain and Summit Valley between the latitudes $41^{\circ}35'$ and $41^{\circ}45'$, and the longitudes $123^{\circ}55'$ and $123^{\circ}50'$ (Fig. 1.5).

Access is provided by the Forest Service road 15N01 that traverses the area from northwest to southeast, thereafter referred to as GO-road, since it was intended to connect the villages of Gasquet and Orleans to make the area accessible for logging. However, the road stopped short of its destination, since a court order terminated road construction before the bulldozers could destroy an ancient Indian burial site near Chimney Peak. Logging is now kept out of the wilderness beyond Summit Valley, and the area around the Lems Ridge olistostrome might enjoy what is the most expensive dead-end road in the country.

The LRO is exposed in road cuts along the GO-road and various other unpaved logging roads in the higher elevations. Excellent water-polished and continuous outcrops occur along the South Fork of the Smith River.

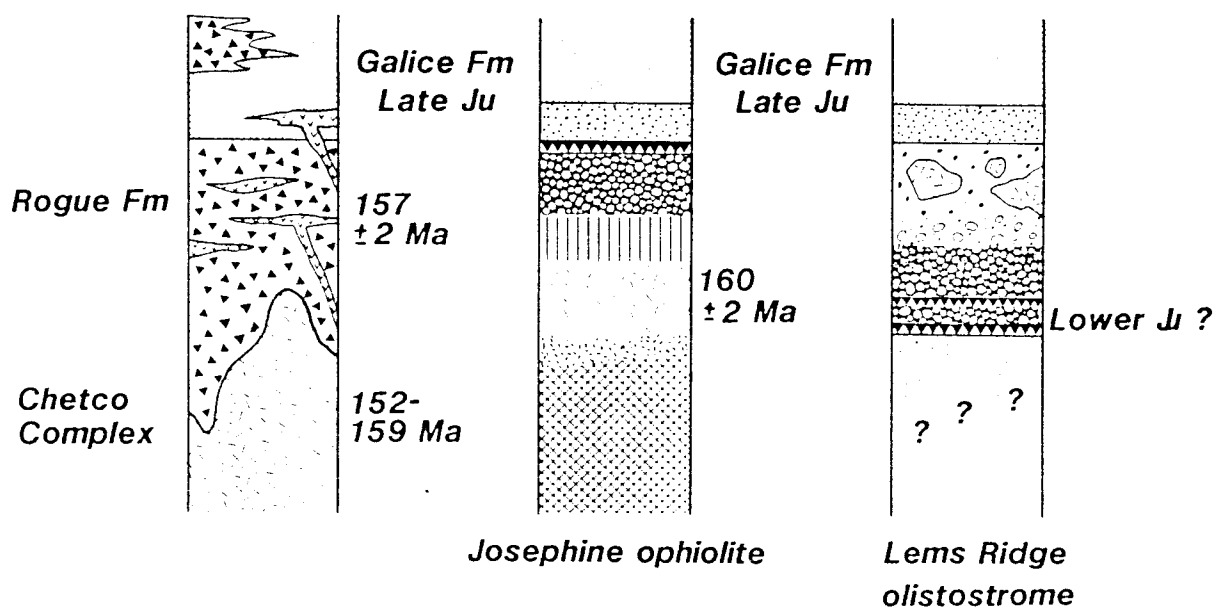


Figure 1.4 Simplified stratigraphy and geochronology of the main units in the western Jurassic belt.

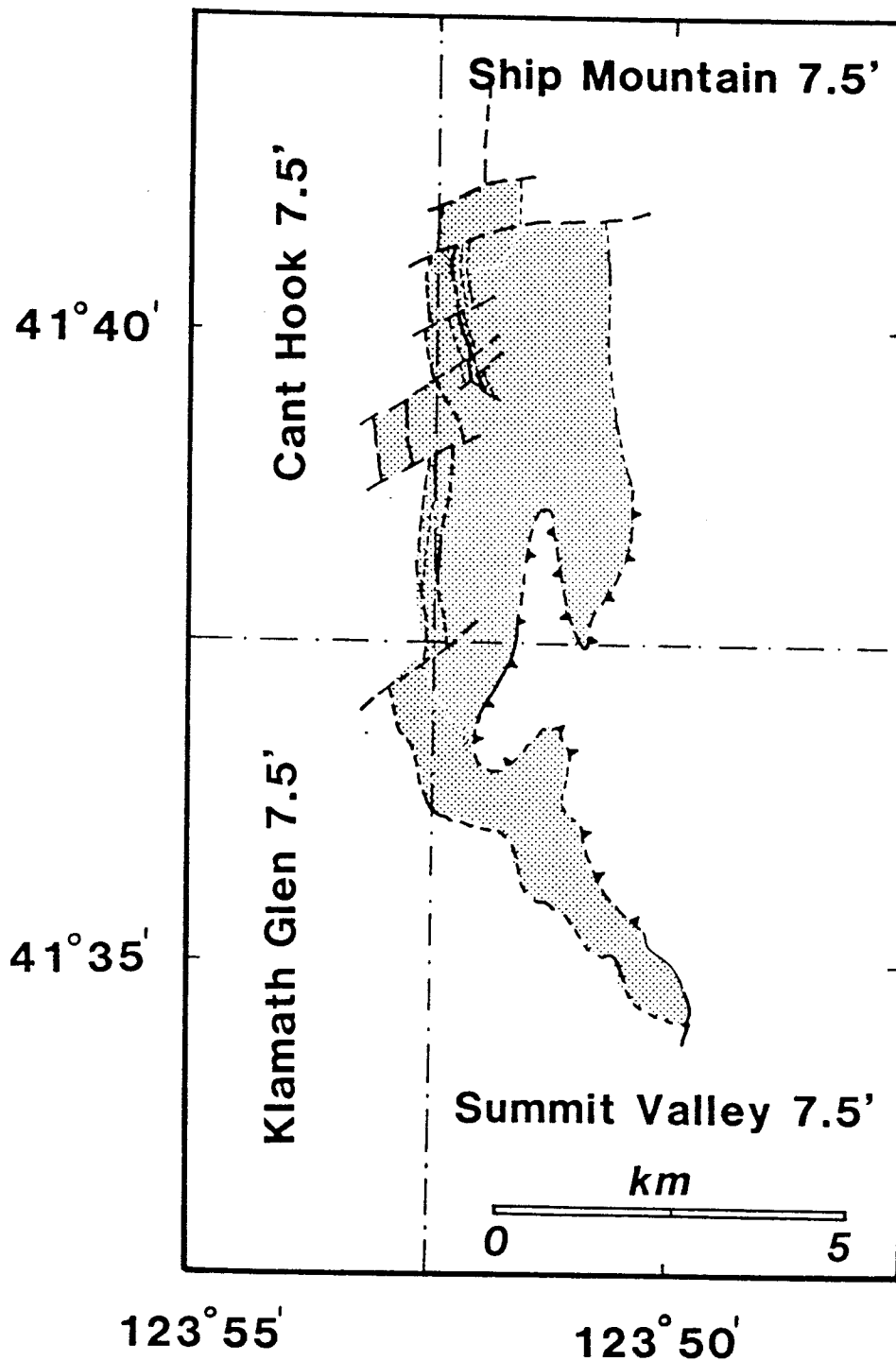


Figure 1.5

The location of the LRO (stippled area) on the 7.5' quadrangles Ship Mountain, Summit Valley, Klamath Glen, and Cant Hook.

Some parts of the river are not accessible, however, unless a raft is used for field work. Outcrops beyond the roads or the river tend to be poor or inaccessible due to the dense vegetation. The topography is rather steep with common landslides and rockfalls. The higher elevations and rugged topography is often held up by the lithologies within the olistostrome, while the slates and graywackes of the Galice Formation favor the development of a gentler and more even topography.

Fieldwork was conducted during 1 1/2 weeks in August of 1985 mainly to collect samples for geochemical analyses and geochronology. A second field session in July of 1986 lasted about 2 1/2 weeks.

Detailed mapping of the area of the Lems Ridge olistostrome, particularly near the thrust contact to the adjacent Rattlesnake Creek terrane was first done by Norman (1984). But even though some of the main features of the olistostrome were already noted (Harper and others, 1983; Norman, 1984; Harper and others, 1985), the assignment of the relative position to the ophiolite as well as the provenance, age, and geochemistry of most lithologies in the LRO were either uncertain or unknown. The present study therefore is considered as complimentary to the excellent reconnaissance work that has been done beforehand, and which has already delineated the extent and character of the olistostrome.

CHAPTER II Fracture Zones and Melanges: Implications for Ophiolite Geology

As pointed out in chapter I, this study builds on the recognition by previous workers that the Lems Ridge olistostrome is 1) indeed of sedimentary origin (and thus satisfies the definition of a sedimentary melange = olistostrome in the sense of Silver and Beutner (1980)), and 2) was already considered a likely candidate to represent the sediment fill of an ancient fracture zone. In this chapter the terminology and geology of both fracture zones and melanges/olistostromes are reviewed, the relationship of the described features with ophiolites are presented, and these findings are compared in subsequent chapters with the actual field and laboratory evidence from the Lems Ridge olistostrome.

2.1 Fracture Zones

Large scale offsets of the mid-ocean ridge system along zones of lateral displacement were recognized as early as 1959 (Vacquier, 1959), but it was not until 1965 that geologists predicted the true nature of these faults (Wilson, 1965). They were called transform faults to indicate that any relative movement within the complex network of divergent and convergent margins is accommodated

(i.e. transformed) along this type of strike-slip boundary.

Transform faults are defined as shear boundaries parallel to the movement vector between two plates, and they lie along small circles normal to their particular pole of rotation. Lithosphere is generally neither created nor destroyed along transforms. The tectonically active part of the fault is governed by a strike-slip regime and is characterized by shallow-focus earthquakes along subvertical planes.

Karson and Dewey (1978) call the entire linear topographic feature "fracture zone", and they distinguish 1) the transform segment of predominantly strike-slip deformation, and 2) the non-transform segment, where older oceanic lithosphere is juxtaposed against younger lithosphere.

Across the transform segment of a fracture zone, three morphotectonic provinces have been defined (Karson and Dick, 1983):

- (1) the transform valley: this topographic surface expression of a fracture zone is typically several to a few tens of kilometers wide and displays considerable relief;
- (2) the transform domain: this is the region affected by continued strike-slip deformation;
- (3) the principal transform displacement zone (PTDZ): this

is an interval of some finite width, usually less than 1 km wide, along which active strike-slip faulting may be concentrated at some given time.

It appears that variations in the structural and petrological features of fracture zones are mainly related to different spreading rates. That is, the overall thermal regime is apparently the most significant factor in the development of ridge-transform systems. Spacing of fracture zones is a particularly obvious example, where narrow and wide spacing correlates well with slow and fast spreading rates, respectively (Fox and Gallo, 1984). Fig. 2.1 summarizes the main morphotectonic features of the transform domain.

Differences between slow, moderate, and fast spreading systems are a function of the age (and thus the thermal character) of the lithosphere that is juxtaposed against the truncated edge of the ridge axis. One can expect that thick and cold lithosphere induces a lateral conductive flow of heat across the fracture zone. As a result, the extent of partial melting would decrease, and the ability of the segregated melts to reach the surface would be restricted. Thus the total magma supply to shallow-level magma chambers decreases as the ridge-transform intersection is approached and the crust thins correspondingly. The magnitude of this "cold edge effect"

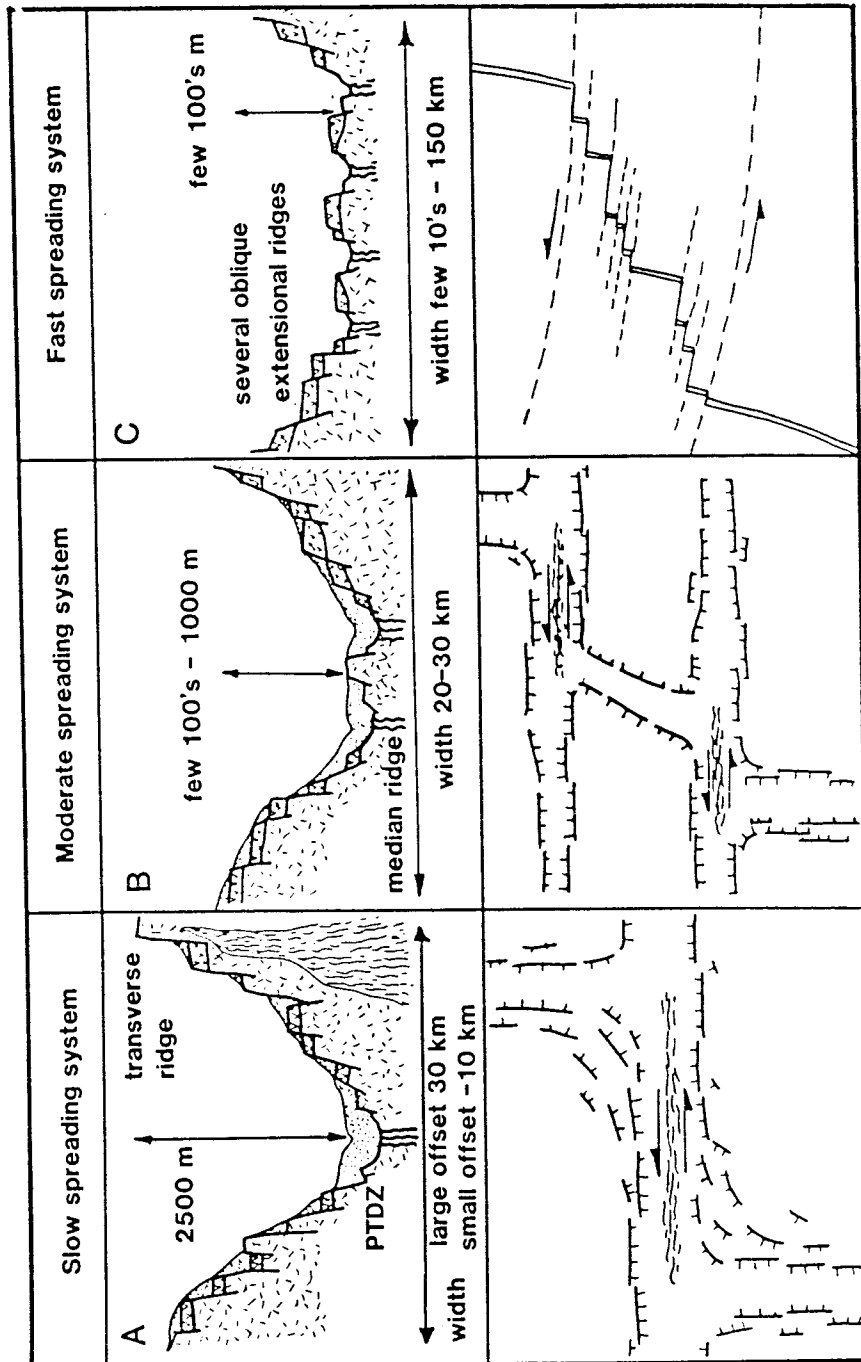


Figure 2.1

The main morphotectonic features of the transform domain in fracture zones. Top: cross section; bottom: map view (modified from Fox and Gallo, 1984)

(Fox and Gallo, 1984) should therefore be greatest at large offset and slowly slipping fracture zones, whereas at small offset and fast slipping systems the effect is expected to be less profound with less crustal thinning.

Seismic investigation by Sinha and Louden (1983) and Cormier and Detrick (1984) provide quantitative evidence for the existence of anomalous thin crust beneath the Oceanographer and the Kane fracture zones, respectively. Crustal thicknesses of 4-5 km and as little as 2 km beneath the nodal basins are reported (see review by Detrick and White, 1986). As an alternative to restricted magma supply as the controlling factor, crustal thinning in a pull-apart environment has been suggested (Dick, pers.comm., 1985). The latter is consistent with the lack of an extrusive carapace and the predominant exposure of peridotite in some nodal basins (Fisher and others, 1986). Furthermore, the great depth of the nodal basins and the relief to the adjacent transverse ridges could be explained as an isostatic response to dramatically varying crustal thickness across short distances.

An alternative mechanism of slackened crustal production is suggested by Whitehead and others (1984). Their key idea is that in reality there is nothing like an infinite, linear magma chamber along mid-ocean ridges. Rather, pockets of melt rise diapirically from deeper levels of the asthenosphere to form isolated magma

chambers. From these spots of maximum crustal production, melt is assumed to flow laterally: that is, parallel to the ridge itself. At increasing distance away from these spots of upwelling, the crust would gradually become thinner. The point of minimal thickness would be a discontinuity in lateral melt flow and would be the most likely place for a fracture zone to occur.

The proposed lack of linear steady magma chambers is consistent with the observation of deep microearthquakes at Mid-Atlantic Ridge fracture zones, extending to depths greater than 8 km (Francis and others, 1977) even locally beneath the median valley itself (Toomey and others, 1985; Solano and Bibee, 1985).

Faulting and Structure of Fracture Zones

Prior to deep-tow and submersible investigations, the recovery of fracture zone rocks was only possible by dredging from the bounding walls of the fracture zone. In particular, the frequent recovery of gabbroic and ultramafic rocks led early workers to the suggestion that fracture zone escarpments represent single, large faults and that fracture zones thus provide tectonically controlled exposures of the deeper parts of oceanic crust (Bonatti and Honnorez, 1976; Prinz and others, 1976). With higher resolution investigations, however, it became clear

that the flanking walls display a stair-step pattern of predominantly inward facing, small-throw normal faults which are linked by terraces and talus ramps (see Fig. 2.1; Choukroune and others, 1978).

Faulting and structural trends at ridge-transform intersections are discussed in detail by Karson and Dick (1983) and OTTER (1984). As the intersection is approached, the fault trends along the ridge become oblique to both the fracture zone and ridge orientations (see Fig. 2.1). Most authors agree that the reorientation of the fault scarps is due to a rotation of the principal stress directions as the fracture zone is approached. Therefore it is reasonable to assume that normal faulting, possibly with an oblique-slip component, prevails along these faults as the valley of the transform segment is approached. The same authors suggest that this structural pattern is related to the extent of coupling between lithospheric slabs of different age, and therefore develops differently at slowly slipping and moderately slipping systems (Searle, 1986).

Strike-slip faulting is confined to narrow zones of lateral displacement. Slowly slipping systems display mostly a single, well defined PTDZ, whereas faster slipping fracture zones are characterized by many subparallel transform segments which are linked together by a relay of oblique, extensional ridges (Fig. 2.1; Searle, 1983; Fox and Gallo, 1984). The intensive fracturing associated with

strike-slip faulting may provide access for seawater to penetrate into deeper crustal levels. The hydration of mafic and ultramafic rocks and the subsequent vertical tectonism induced by rising serpentinite diapirs appear to be important features of many fracture zones (Honnorez and Bonatti, 1976; Francis, 1981).

Fault rocks dredged from the Vema fracture zone (Honnorez and others, 1984) include gneissic and mylonitic amphibolites as well as associated gabbros and metagabbros. These rocks display a complete progression of recrystallization with deformation to a point where the foliated rocks do not contain any relict igneous minerals or textures. Honnorez and others (1984) suggest that metamorphism and deformation within a ductile shear environment took place simultaneously. For a heat source they propose a combination of magmatically driven hydrothermal heat along with transform related, shear-induced heat. Higher level fault rocks in fracture zones include cataclasites and non-coherent fault gouges. Fault scarps itself are characterized by accumulations of mass wasted talus and debris, as well as brecciated igneous rocks.

Petrology of Fracture Zones

Among the three types of plate boundaries, transform

faults are probably the least researched concerning their petrological and geochemical features. Studies of volcanic rocks from the vicinity of fracture zones were first performed by Thompson and Melson (1972). They noticed a more common occurrence of alkali basalts, but recent evidence is meager. Hekinian and Thompson (1976) noted that basaltic rocks are more fractionated towards fracture zones; they interpreted higher contents in FeO and Ti and the lower abundances in Cr and Ni as suggestive of a higher degree of fractionation. Similar results for abyssal tholeiites from the Oceanographer fracture zone were reported by Shibata and others (1979).

Bender and others (1983), and Langmuir and Bender (1984) summarized two features of basalt geochemistry near fracture zones. They found that those basalts have the following characteristics:

- (1) For a given MgO content they often have higher abundances of incompatible elements and Ti.

Characteristic rare-earth element ratios such as La/Sm and La/Yb are also higher than in typical N-type MORB.

- (2) They show a chemical discontinuity across transform faults, both in major and trace elements, as well as in isotopic ratios. Such slight discontinuities have been known since the work of Schilling and others (1983).

In general, it emerges that fracture zone basalts have distinctly higher concentrations of incompatible elements than basalts from ridge segments remote from fracture zones. Langmuir and Bender (1984) attribute this to a decreased extent of partial melting in the vicinity of a ridge-transform intersection, probably due to a depressed thermal regime near fracture zones where cold oceanic crust is butting up against the spreading ridge (the cold edge effect of Fox and Gallo (1984)). LeRoex and others (1983) also found enriched and more alkalic basalts close to a fracture zone, but instead suggest that a higher degree of fractionation causes the enrichment in Fe and Ti. In a reappraisal of Langmuir and Bender's data (1984), Karson and Elthon (1987) suggest that variable eruption rates can cause geochemical trends that were previously thought to be controlled by variable degrees of partial melting.

Cooling rate, magma supply, and eruption cyclicality are generally thought to control fractionation at ridge-transform intersections (Sinton and others, 1983). Along mid-ocean ridges with an approximately uniform N-type MORB composition, a steady-state magma chamber with balanced supply and eruptions provides magmas that are well mixed and have experienced only a low degree of fractionation. Highly fractionated lavas are often associated with propagating rifts and fracture zones: here moderate cooling rates, small magma bodies and a limited

replenishment allow enhanced degrees of fractionation.

Short ridge segments that intervene between two major fracture zones should also show more evolved lavas due to the superposition of two cold edge effects. Thompson and others (1980), and Stroup and Fox (1981) report enriched basalt compositions from the Cayman ridge that have higher Ti, Zr, and Y than normal MORB.

Fracture Zones and Ophiolites

The relatively close spacing of fracture zones along ocean-ridges as well as the presence of fracture zones in transform dominated marginal basins implies that ophiolites should commonly contain parts of oceanic lithosphere that was generated at or near fracture zones. Thus linear features that resemble former fracture zones should be present in ophiolites; likewise structures and rock-types associated with fracture zones are expected to be preserved.

Evidence for the proximity of an ophiolite to a fracture zone may include the following:

- (1) A thinner ophiolite crustal section as compared to normal oceanic crust. Since ophiolites usually do not expose crustal sections greater than 3-4 km thick, they can be correlated with the anomalously thin crust observed at fracture zones.

- (2) The strike of sheeted dikes at a high angle to the inferred trend of an ancient fracture zone in the ophiolite.
- (3) The occurrence of amphibolite facies mylonites (or other deformed rocks that show high-T mineral assemblages) which trend subparallel to the inferred spreading direction of the ophiolite.
- (4) The observation of progressive deformation from brittle failure to ductile flow with stratigraphic depth.
- (5) Cross-cutting relationships of strongly deformed mafic and/or ultramafic rocks with less deformed younger mafic dikes or trondhjemites (Karson and Dewey, 1978). Such dikes may have been injected as older crust with a transform history was carried past the termination of the adjacent active spreading segment.
- (6) The juxtaposition of strongly deformed ophiolitic rocks (generated at a ridge-transform corner) with less deformed younger ophiolitic assemblages (generated at a nontransform-ridge corner) along a sharply defined linear belt (Karson and Dewey, 1978).
- (7) Indications of a rugged paleotopography such as redepositioned pillow breccias and abundant rock debris.
- (8) Fracture zones are ideal places for the accumulation of talus and debris flows; olistostromes and talus

breccias striking at a high angle to dike orientation may be common.

- (9) The alignment of arc volcanism in a back-arc basin approximately perpendicular to the sheeted dike orientation. Such arc volcanism localized along fracture zones has been described from the Marianas trough (Hussong and Fryer, 1983).
- (10) The occurrence of enriched lavas as noted near modern fracture zones. In addition, distinct differences in magmatic affinities across fracture zones might be detectable; e.g. older island-arc tholeiitic lavas might be juxtaposed to younger MORB-tholeiitic lavas, considering the fact that many ophiolites appear to have formed in back-arc settings.

Fracture zone assemblages have been recognized in several ophiolites; e.g. the Kings-Kaweah ophiolite (Saleeby, 1979), the Arakapas fault of the Troodos complex (Simonian and Gass, 1978), the Semail ophiolite of Oman (Smewing, 1980), the Coastal Complex of Newfoundland (Karson and Dewey, 1978), the Miocene East Taiwan ophiolite (Suppe and others, 1981), and the Sore Lyklingsholmen Formation of Norway (Amalixsen and Sturt, 1986).

While the former examples represent well preserved and coherent ophiolitic sections, the Taiwan and Norway complexes only exist as fragments and dismembered

assemblages. Nevertheless, plutonic breccias and talus deposits intercalated with pelagic sediments and/or extrusive sequences, olistostromal material with clasts of ophiolitic lithologies, distinct enriched geochemistry, and abundant mass wasting can prove to be indicators for the close relationship between ophiolite generation and the presence of fracture zones.

2.2 Melanges and olistostromes

Chaotic rock bodies were already described from the the central Himalayas by the late 1800's (Griesbach, 1891). However, it was not until the work of Greenly (1919) on the geology of Angelsey that the term "melange" was coined. Greenly (1919) describes the local Gwna melange as a

"tectonically derived chaotic rock body of immense scale and related to thrusting".

By qualifying the Gwna melange as an "autoclastic melange" he implied a predominantly tectonic origin of this unit. As an essential character of an autoclastic melange he considers:

"the general destruction of the original junctions,.., especially bedding, and a shearing down of the more tractable material until it functions as a matrix in which fragments of the more obdurate rocks float as isolated lenticles of phacoids."

As opposed to the older term "melange", the term

"olistostrome" has been in use for only thirty years. It was originally introduced by Flores (1955), derived from the Greek words "olistomai" (to slide) and "stroma" (accumulation):

"By olistostrome, we define those sedimentary deposits occurring within normal geological sequences that are sufficiently continuous to be mappable, and that are characterized by lithologically or petrographically heterogeneous material that was accumulated as a semifluid body ...; in any olistostrome we distinguish a "binder" or "matrix" represented by prevalently pelitic material containing dispersed bodies of harder rock that may range in size from pebble to boulder and up to several cubic kilometers."

Accumulation is generally thought to be governed by flow processes, including turbidity currents as well as chaotic debris flows (Flores, 1955). The fragments included within the matrix are called olistoliths, although terms such as "block" or "clast" are still widely used.

Abbate and others (1970) criticized Flores' approach on several points. They excluded turbidites from the definition and discounted the assumption that olistostromes necessarily have to occur conformably within normal marine sequences. They also considered monolithological deposits with or without matrix as olistostromes. Concerning size limits, Abbate and others (1970) preferred to see olistostromes as chaotic units of limited size, say 100 to 200 meters thick, but also stress the importance of the internal structure of such a deposit. In general, they favor a tectonic interpretation for very large or

relatively undisturbed masses.

Ever since the original definitions of "melange" and "olistostrome" came about, the terms have been reinterpreted and used simultaneously to an extent, where they were applied interchangeably. One dispute centered on the issue whether to use "melange" as a descriptive term only, or if a genetic implication should be made, such as tectonic versus sedimentary mixing (Hsu, 1968, 1974; Berkland and others, 1972; Cowan, 1974, 1978; Cloos, 1982).

In order to appreciate the fundamental conceptual differences over melanges and olistostromes, a brief excursion to Hsu (1968, 1974) and the rebuttal by Berkland and others (1972) is in order. Hsu (1968) considers melanges as bodies of deformed rocks that are characterized by the inclusion of entirely tectonically mixed fragments into a pervasively sheared matrix, where the fragments are of both native and exotic nature. Similar units of sheared and fragmented strata without any exotic components were called broken formations. To form a melange includes two processes (Hsu, 1968): 1) fragmentation and 2) subsequent mixing of these broken fragments into a matrix that deformed plastically.

In contrast to this definition of melanges as produced by tectonic processes only, Hsu (1968, 1974) defines olistostromes as purely sedimentary features, as put

forward by Flores (1955). Such chaotic masses move along topographic gradients and their emplacement as a finite sedimentary unit is controlled by the applicable flow regime.

By separating melanges and olistostromes as genetically different rock bodies, melanges have to be considered as tectonic units bounded by shear surfaces, while olistostromes are usually separated from overlying and underlying units by depositional contacts, and therefore have to be regarded as stratigraphic units.

Yet, such a strict distinction between melanges and olistostromes poses severe problems in cases where the olistostrome has undergone tectonic deformation subsequent to its sedimentary emplacement, or where it is incorporated in a larger melange complex. Then olistostromes attain the pervasively sheared and deformed character which is so essential to this melange definition. That is, they become all but indistinguishable from melanges. To escape this dilemma, Hsu (1974) proposed a variety of criteria to facilitate a distinction, including shape and nature of clasts as well as fabric and nature of the matrix.

Facing this unhandy alliance of terminology with inferred geologic history, Berkland and others (1972) suggested a redefinition of the term melange:

"A melange is a mappable body of rock characterized by the inclusion of fragments and blocks of all sizes, both exotic and native,

embedded in a fragmented and generally sheared matrix of more tractable material."

Thus having reduced "melange" to a descriptive field-term, subsequent study then qualifies melanges as either the result of tectonic processes (tectonic melange) or as the result of sedimentary processes (sedimentary melange). Along with this redefinition of melanges, Berkland and others (1972) reject Hsu's notion of exotic blocks as inherently being tectonically emplaced, and define them as follows:

"They are variably sized masses of rock occurring in a lithological association foreign to that in which the mass formed."

Silver and Beutner (1980) restate the results of Berkland and others (1972) and arrive at the conclusion that melanges are mappable bodies of fragmented and mixed blocks in a matrix. Appropriate modifiers to constrain the genetic implication for such a rock body are recommended: Sedimentary melanges (= olistostromes) are chaotic rock bodies that result from sedimentary mixture of blocks and are produced by down-slope gliding or flow processes. Tectonic melanges are chaotic rock bodies which result from a tectonic mixing process such as stratal disruption, boudinage, and shearing along thrust faults (e.g. in accretionary prisms).

In addition to the two models discussed above, at least two other, alternative mechanics for melange formation are mentioned in the literature: 1) diapiric flow

in overpressured, water-saturated sediment (e.g. in accretionary wedges) gives rise to mud diapirs and mud volcanoes which produce fabrics resembling the typical chaotic block-in-matrix fabric of melanges (Williams and others, 1984); mud diapirs further attain their similarity to tectonic melanges in accretionary terrains as a result of subsequent deformation associated with plate convergence; and 2) tectonically driven flow within the accreted sediment pile (Cloos, 1982). This reverse flow model accounts for the uplift of rocks from mantle depths, for the fragmentation and dispersal of rocks in a pelitic matrix, and thus for the chaotically mixed character of a melange.

Only a few melanges are unequivocally considered as of sedimentary origin: such olistostromes occur in the northern Apennines of Italy and are interpreted to have formed either related to nappe emplacement (Abbate and others, 1970), or are related to the presence of a block-faulted passive continental margin (Naylor, 1981). Another melange of undoubtedly olistostromal origin is the Lichi melange of Taiwan (Page and Suppe, 1981). Page (1978) compares the Franciscan melanges with these olistostromes of Italy and Taiwan and stresses the fact that both tectonic and sedimentary mixing processes were operating to form the Franciscan. Such multistage mechanics of melange

formation in the Franciscan Complex are also suggested by Cowan (1978) and Aalto (1981). All authors consider the relationship of melanges to adjacent sedimentary units as the most important feature that distinguishes olistostromes and tectonic melanges (e.g. Page, 1978). The internal structure of melanges also is a distinctive feature, but is often obliterated by secondary deformation that may not be related to melange formation itself.

Other than "melange" there are several less commonly used terms for coarse grained, fragmental rocks which include "wildflysch" (Kauffman, 1884), "chaos" (Noble, 1941), "breccia" along with appropriate qualifiers, and "diamictite" (Flint and others, 1960). The most recent attempt to weed the jungle of terminology was made by Sundell and Fisher (1985). They emphasize particle size as the prime distinction, since the size of fragments often spans a range of many orders of magnitude. Sundell and Fisher (1985) consider constraints on matrix, presence or absence of exotic blocks, as well as the shape and size distribution of fragments to be of second order importance. They suggest a non-genetic size classification for very coarse-grained fragmental rocks from diamictite, to megamictite and teramictite, to oromictite (with increasing particle size). They propose to combine these rocknames with modifiers that indicate the process and/or

the environment of mixing.

Cowan (1985a) describes four different structural styles or types of melanges that are most common in western North America. Each type still fits the general notion of a melange as having a chaotic fabric typified either by stratal disruption or by blocks of various sizes and origin within a fine-grained pelitic matrix. Types I and II of Cowan (1985a) are analogous in that fragmentation and stratal disruption of both types occurred mainly owing to layer-parallel extension of only partly consolidated sediments during imbricate faulting and/or gravitationally driven deformation. As opposed to the sandstone-mudstone sequences of type I, type II melanges include lithologically different sediments such as layered green tuff and chert, along with fine-grained sandstone and mudstone. Connelly (1978) interprets such sequences in the Uyak Complex of Alaska as deposited on the abyssal ocean floor in a successive manner, and subsequently scraped off and dismembered within a subduction complex. However, interlayering of extrusive pillow lavas, tuff, and pelitic sediments is atypical for oceanic settings. Cowan (1985b) therefore favors an origin of type II melanges as sediment accumulations in structurally controlled basins near a continental margin landward from a subduction zone.

Type III melanges, in contrast, differ from type I and

type II melanges in that their block-in-matrix fabric does not resemble previously stratiform layers. Rather the rock fragments are chaotically dispersed in a pelitic matrix to form a polymict mudstone. Clearly disruption did not take place in situ, nor does the bulk deformation of the inclusions show a homogeneous character as would be expected by tectonic deformation at the place of deposition. Therefore most fragments must be derived from somewhere other than their immediate surrounding. By means of petrographical, paleontological, geochemical, and geochronological evidence, an attempt can be made to reconstruct their provenance. Emplacement as mud-rich, submarine debris flows or olistostromes seems to be most compatible with the "ready-made" character of type III melanges.

A fourth type of melange probably develops in brittle fault zones, evidenced by the presence of a semipenetrative foliation of anastomosing subparallel shear-fractures that wrap around lenticular tectonic inclusions. This deformation style is called structural slicing (Bosworth, 1984) and differs from necking and boudinage that occur due to the ductility contrast of the affected lithologies.

Sedimentary gravity flows

The chaotic block-in-matrix fabric of sedimentary

melanges is usually attributed to processes of gravity induced sliding, slumping, and flow. Middleton and Hampton (1976) coined such flow processes "sediment gravity flow", indicating that the sediment is moved under the influence of gravity; that is, the interstitial fluid does not cause the grain motion, but is being moved itself by the grain motion. Most classifications for mass movements are genetic; that is, they are based on transport processes and coarse particle support mechanisms (Nardin and others, 1979). Middleton and Hampton (1976) distinguish four types of sediment gravity flow according to the main particle support mechanism:

- Turbidity current: fluid turbulence
- Fluidized sediment flow: upward intergranular flow, escaping pore fluid.
- Grain flow: grain interaction, grain dispersive pressure
- Debris flow: matrix strength

Pebbly mudstone, matrix-supported conglomerates, and breccias are all typical olistostromal deposits and commonly interpreted to be the result of debris flows (Page, 1978; Lowe, 1979). Debris flows are mixtures of variably sized boulders, clay minerals and water, which are put into movement by gravitational force. The coarser particles are supported by the cohesive strength of the

water-clay matrix. Lowe (1979) emphasizes the simultaneous presence and interaction of buoyancy, grain interaction, and cohesive matrix strength to account for the uniform suspension of larger particles in pebbly mudstone deposits. Debris flows probably show a continuum of support and lift mechanisms as a function of particle size, and thus include both traction loads (larger clasts) and suspended loads (smaller clasts) (Lowe, 1979).

Since "debris flow" is a genetic (and not a descriptive) term for matrix supported sediment gravity flows, the characteristics of a resulting sedimentary deposit can only be inferred: such a deposit would be expected to be matrix supported, to have little preferred fabric of the clast component, to have poorly developed grading, and to exhibit essentially unstratified and massive beds.

Melanges and ophiolites

Melanges often develop in close association with ophiolites in zones of ancient or recent plate convergence. Ophiolitic melanges occur within suture zones, comprising ophiolitic rocks mixed with sedimentary and metamorphic rocks (Coleman and Irwin, 1974). These disrupted ophiolitic sequences are commonly set in sheared serpentinite matrixes. Coleman (1977) includes both types

of melanges, those of sedimentary (olistostromal) and those of tectonic origin, in the term ophiolitic melange. This is not surprising, since a whole continuum of melanges is usually found at or close to convergent plate margins (Cowan, 1985a). A definition of ophiolitic melanges by Gansser (1974) seems to be too restricted, however, in that it relates them predominantly to obduction processes and requires that they result from sedimentary with only subsequent tectonic mixture. A diametrically opposite view is expressed by Hsu (1974) who considers ophiolitic melanges as invariably subduction related and of exclusively tectonic origin.

Ophiolitic melanges are no longer considered to be solely trench deposits; they form where instabilities of both tectonic and gravitational nature occur, and usually include very diversified rock-assemblages of either native or local sources: in the rarest cases it is possible to assign unequivocally the location and the mechanism of melange formation (McCall, 1983; Cowan, 1985). In concurrence with the abundant presence of alpine ophiolite breccias ("ophicalcites", Cornelius, 1935), Saleeby (1979) suggested that serpentinite melanges from the Sierra Nevada foothills developed as ocean-floor melanges along fracture zones by the effect of protrusive activity and wrench faulting. Weissert and Bernoulli (1985) also suggest fracture zones as likely places for the fragmentation and

redemption of ophiolitic breccias in a tectono-sedimentary fashion. Brecciated chaotic deposits containing abundant ophiolitic material are also reported from passive continental margins where rifting is marked by synsedimentary horst-and-graben structures and especially tilted blocks (Tricart and Lemoine, 1986; ODP Leg 107 Scientific Party, 1986; Lister and others, 1986). Such rift-edge deposits appear to be a good analog for melange-type deposits that are evidently not related to subduction, and clearly formed owing to sedimentary flow processes.

CHAPTER III: Geology and Petrography of the Lems Ridge Olistostrome

3.1 Introduction

Rocks mapped as the Lems Ridge olistostrome occur in an elongate, north-south trending belt between the southern extension of the Josephine ophiolite to the west, and the Rattlesnake Creek terrane to the east (see Fig. 3.1 for a summary of the geology of the LRO area). The adjacent section of the Josephine ophiolite represents an attenuated crustal sequence that is tipped up along the east-dipping limb of a major, south-southeast plunging syncline. The Galice Formation overlies the Josephine ophiolite conformably and is locally strongly deformed; strongly foliated graywackes and slates of the Galice contain lower greenschist facies assemblages. The distinctly less deformed and lower grade rocks (prehnite-pumpellyite facies) of the LRO are in fault contact with the higher grade Galice along the Buck Mountain fault. The fault continues northward where pebbly conglomerate and graywacke-shale sequences to the east are also less foliated and of lower metamorphic grade than the Galice Formation to the west. The Buck Mountain fault is therefore 1) either an east-dipping normal fault juxtaposing less deformed rocks from a higher level with

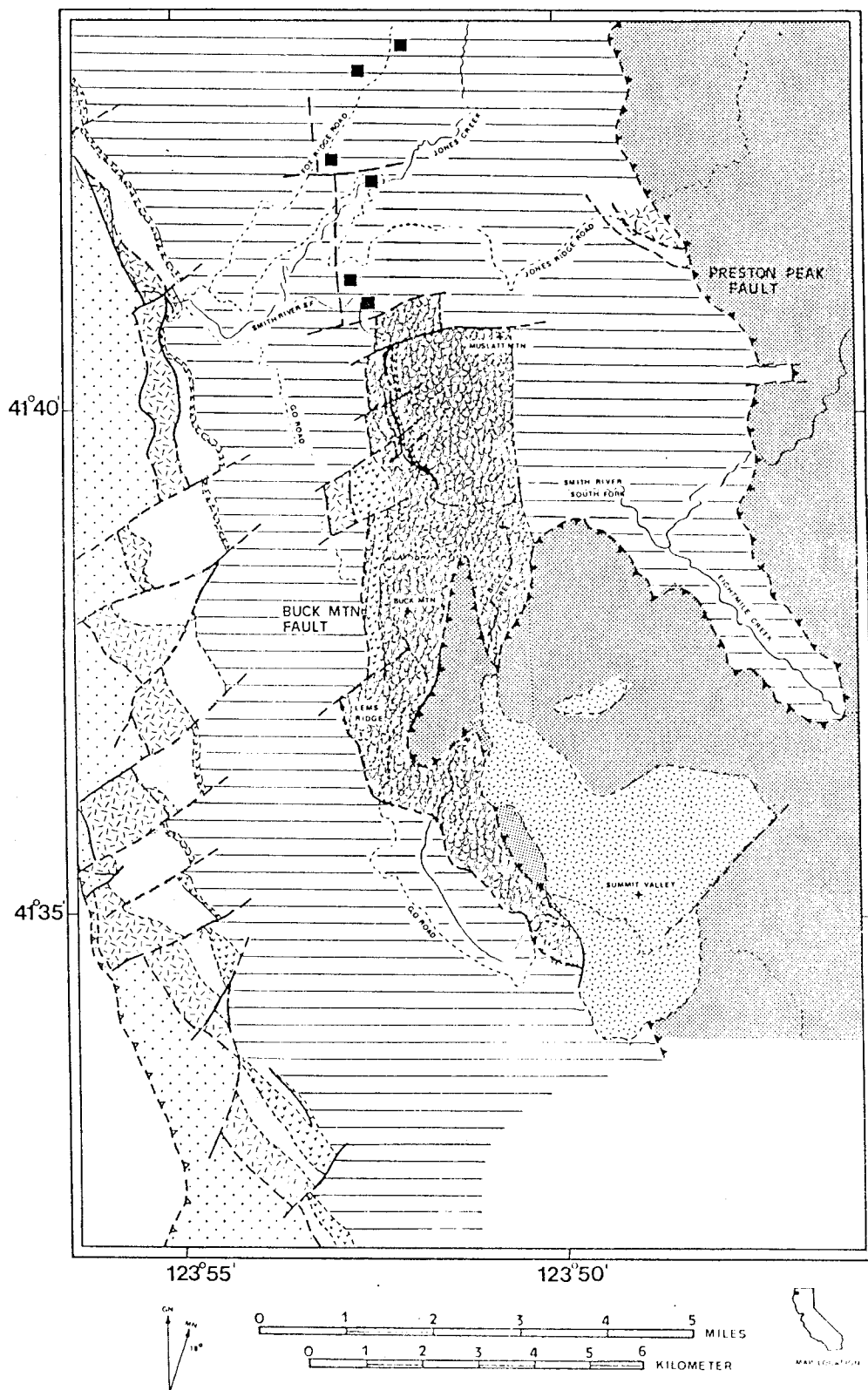
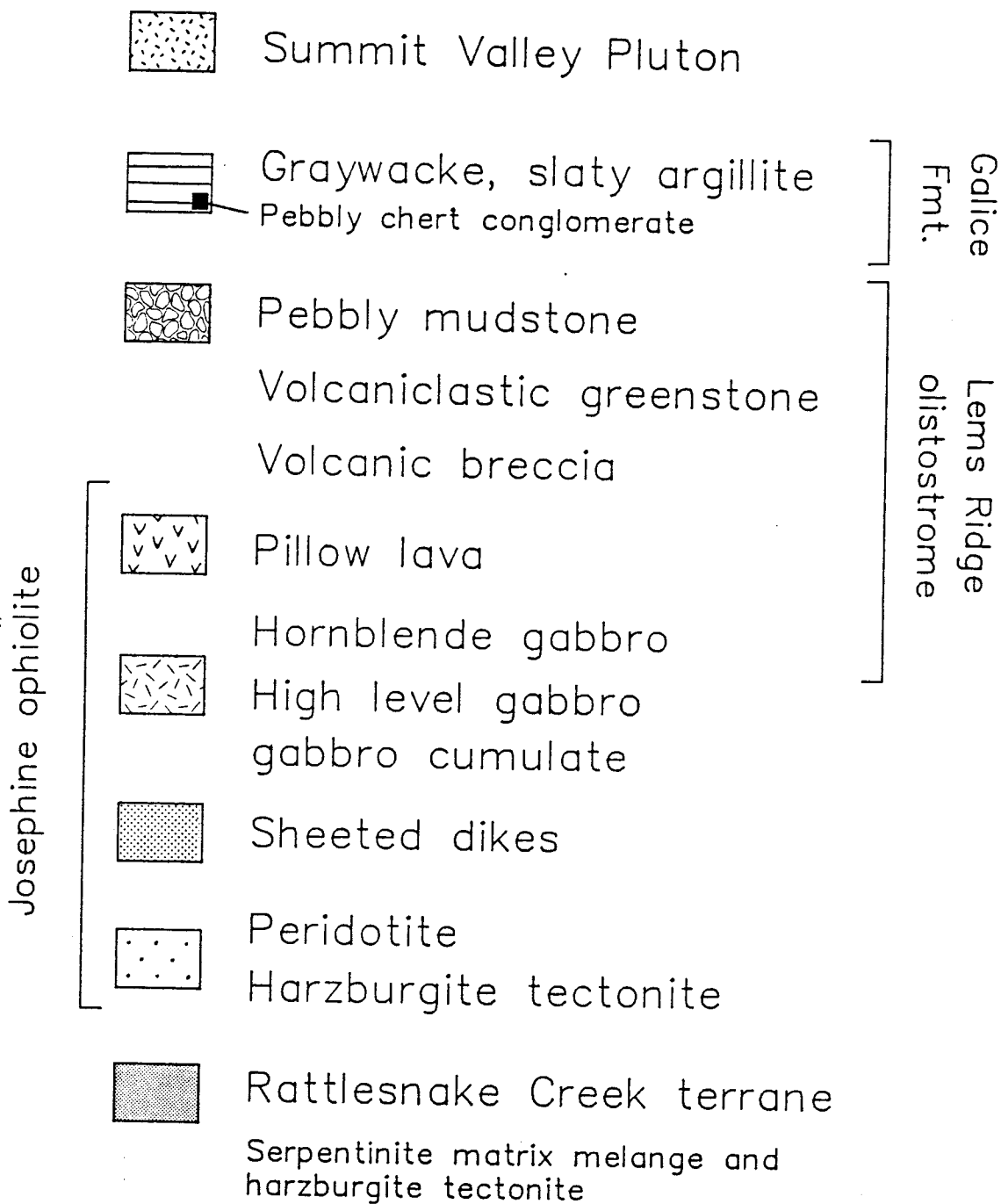


Figure 3.1 Geologic map of the area of the LRO (modified from Norman, 1984; Harper, unpublished data). For key, see next page



Key and explanation for fig. 3.1

strongly deformed and higher grade rocks from lower levels; or, 2) represents an upper level thrust fault related to the basal thrust beneath the Josephine ophiolite to the west.

Along its northern extension the LRO is apparently conformably overlain by the Galice Formation. Further to the south the LRO is in thrust contact with ultramafic rocks of the RCT along the Preston Peak fault (Norman, 1984; Harper and others, 1985). The Preston Peak fault is a thrust that emplaces the RCT over the western Jurassic belt, but is complicated by later faults and folds (Snoke, 1977).

The Preston Peak fault is cut by the Summit Valley pluton, an intrusive complex of dominantly olivine pyroxenite and hornblende gabbro that has been dated at 150 Ma (U/Pb zircon age) (Harper and others, 1986). Based on the cross-cutting relationships, the pluton postdates the Nevadan-age juxtaposition of the LRO and the RCT. The LRO is intruded by the Summit Valley pluton and is widely contact metamorphosed.

The LRO is comprised of two distinct clastic units, both of which contain clasts that span a wide range of size and composition: (1) a pebbly mudstone unit of predominantly continental affinity that alternates and is interlayered with, (2) massive volcanoclastic greenstones

and breccias. Mudstone and the massive greenstone constitute the main body of the LRO. A third, matrix-free talus deposit occurs locally and consists of diabase and ultramafic blocks.

A foliation within the mudstone and the tuffaceous volcanoclastic rocks is only weakly developed and is generally bedding parallel. It strikes consistently northeast and dips moderately southeast. Usually only the matrix is foliated, wrapping around the virtually unflattened clasts.

The apparent thickness of the LRO is about 1300 m, inferred from two stratigraphic sections that were taken along the GO-road and the South Fork of the Smith River. However, some structural thickening is very likely to have occurred, so that the real thickness may be less (keeping in mind that there was also a certain degree of tectonic thinning due to flattening).

Unlike tectonic melanges, the LRO displays an at least semi-coherent stratigraphy that to a certain extent appears also to be laterally continuous. Sedimentary contacts are commonly preserved. The abundant clasts in the LRO do not exhibit a homogeneous bulk deformation, but range from completely undeformed to highly strained and recrystallized, recording only the deformation prior to deposition. The emplacement of the grand variety of exotic clasts in both the volcanic and terrigenous matrix is

therefore entirely due to sedimentary processes.







3.2 Petrography of the LRO

In the following section the rock units of the LRO and their clast component will be described in stratigraphic order. As mentioned above, the internal stratigraphy is inferred from two tectono-stratigraphic sections. They represent continuous outcrops along the GO-road below Buck Mountain (Fig. 3.3) and along the South Fork of the Smith River between Horse Creek and Quartz Creek (Fig. 3.16), respectively. The location of these sections are indicated in Fig. 3.2. The map of Fig. 3.2 shows also the observed extent of the gross units within the LRO.

The GO-Road Section: Chert, Pillow Lavas and
Pillow Breccias, Pebbly Mudstone, and Talus Breccia

The GO-road tectono-stratigraphic section (Fig. 3.3) includes rocks from the base of the LRO at the Buck Mountain fault up to a block-on-block breccia exposed on Buck Mountain. Stratigraphic thicknesses are calculated using the orientation of a thin chert bed (N45E, 53SE) at the base of the section. The total thickness up to the base of the breccia of Buck Mountain is inferred to be 900 m.

Key and explanation to fig. 3.2

-  Talus block breccia
-  Pebbly mudstone
-  Tuffaceous greenstone
-  Pillow lava
-  Hornblende gabbro
-  Pebbly conglomerate in Galice Fm.

3.3
 ┌───┐ GO-road tect.— strat. section

3.16
 ┌───┐ Smith River tect.— strat. section

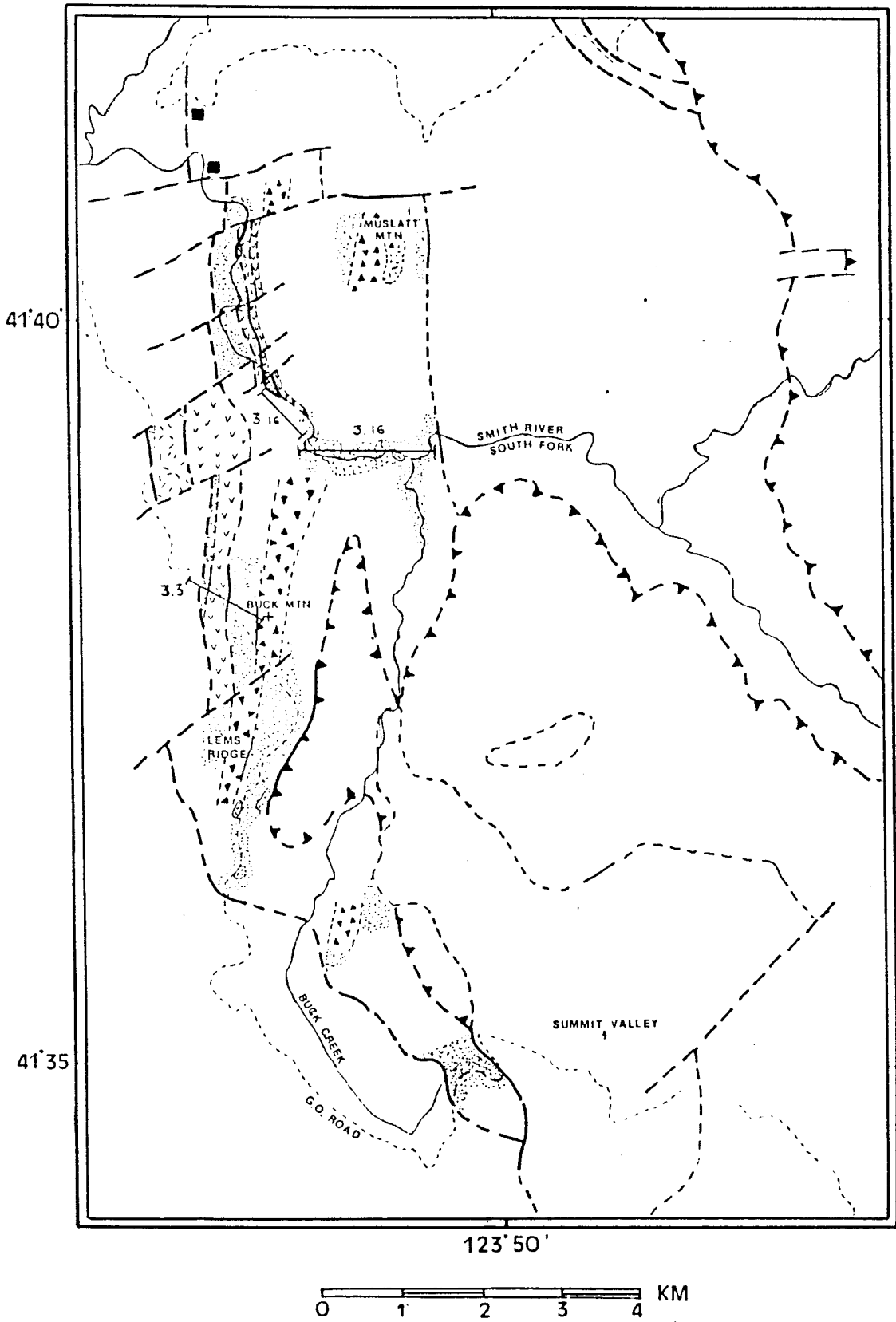


Figure 3.2 Observed units in the LRO

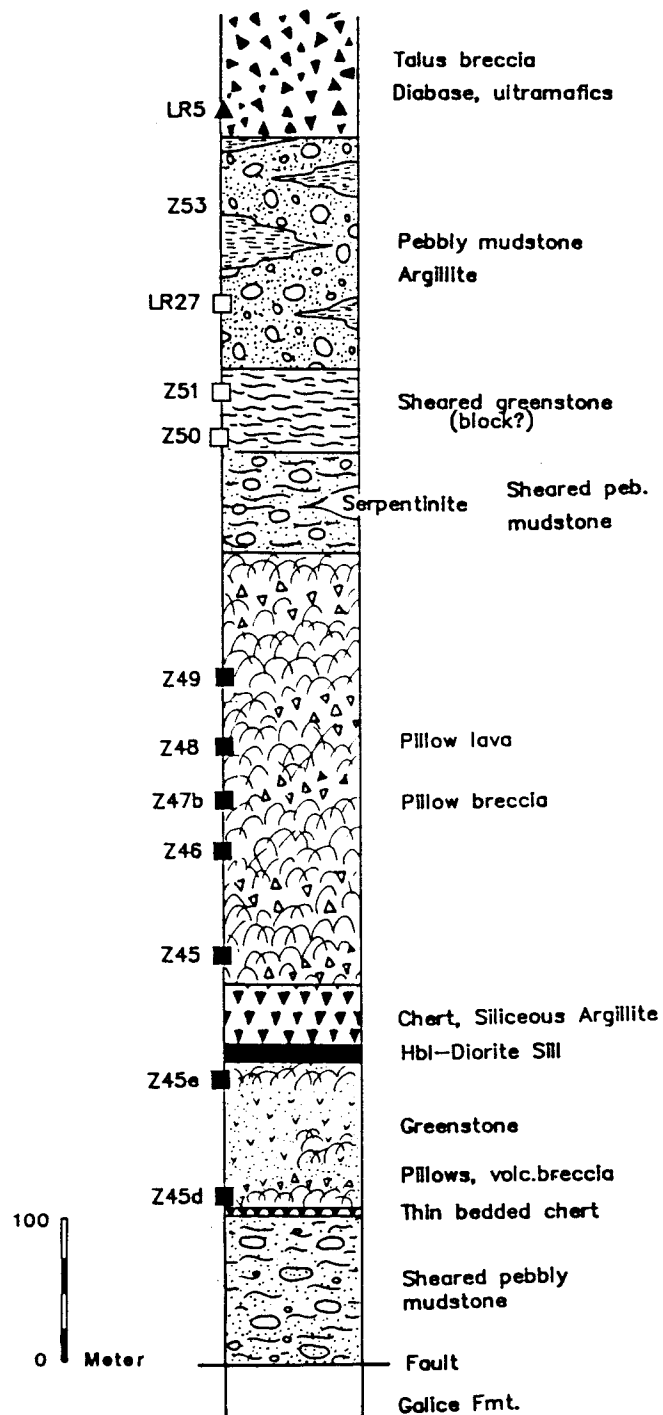


Figure 3.3 GO-road tectonostratigraphic section of the lower LRO.
 Filled squares = pillow lavas; open squares = pillow clasts;
 filled triangle = diabase block

A sequence of intensely sheared black slaty argillite marks the basal fault contact to the underlying Galice Formation. It is correlated with pebbly mudstone that occurs higher in the section, since limestone boulders occur occasionally in the strongly foliated slaty matrix (Fig. 3.4).

The sheared mudstone is overlain by a dark gray, thin-bedded chert that weathers pale gray to white. The chert appears to be laterally extensive. Radiolarians separated from the chert are poorly preserved: they are, however, definitely younger than Triassic and older than Late Jurassic in age (C. Bloome, pers.comm., 1987).

Overlying the chert is a 100 m thick sequence of mafic greenstone. Pillow lavas and pillow breccias occur at the base; toward the top, well preserved pillows are present. Only few dikes are present in this lower part of the section. A thick hornblende phyric dike, however, occurs between the upper well preserved pillow lavas and a 50 m thick sequence of dark gray chert and argillite.

Pillow lavas and minor isolated and broken-pillow breccias constitute the overlying, 320 m-thick volcanic unit (Fig. 3.5). This unit is later referred to as the "GO-road pillow lavas"; these lavas were continuously sampled upsection and their geochemistry will be discussed in chapter 4. Lavas at the base of this unit show a characteristic reddish-purple color due to the presence of

hematite which was probably imparted by hydrothermal alteration. Pillows have long dimensions that range from 20 cm up to 1 m and do not appear to be flattened. The concave downward pillow shapes indicate that the section is not overturned. Some pillows also show radial fractures which formed by contraction during initial cooling. Many pillows have chilled margins; margins of some pillows have spalled off and now constitute the interstitial material between pillows. Isolated-pillow breccias contain droplets of lava that are not greater than a few centimeters, but have complete rims of chilled margins.

The pillow lavas are generally aphyric, but some contain microphenocrysts of plagioclase and cpx. The lowermost lavas, such as Z 45 and Z 46, are extremely vesicular; vesicles are filled by a variety of secondary minerals, including calcite, chlorite, epidote, and quartz. The igneous texture of the groundmass is well preserved, showing spherulitic to lathwork textures. The metamorphic mineral assemblage consists of albite + chlorite + epidote +/- calcite +/- quartz +/- pumpellyite. Plagioclase is albitized and shows partial replacement by chlorite and sericite.

The GO-road pillow sequence is probably in fault contact with the overlying pebbly mudstone. About 70 m of sheared pebbly mudstone occurs above the contact and contains ultramafic and volcanic clasts, the latter

possibly reworked from the underlying pillow lavas. The matrix is pervasively sheared while the volcanic clasts appear to be only slightly flattened (Fig. 3.6a and 3.6b).

A section of dense, coherent cataclastic greenstone occurs on top of the sheared mudstone. Pillow shapes are not discernible, but stretched chilled margins indicate the former presence of pillow lavas. Variolites are flattened and the secondary minerals show grain-shape preferred orientation. Along discrete zones of intense shearing a dense, brown matrix contains sparse rounded crystal fragments (porphyroclasts). The greenstones apparently have been subjected to intense cataclasis; fracturing and comminution have continued to reduce the overall grain size, until some larger brittle grains are "floating" in a more ductile matrix. Such greenstone can be classified as ultracataclasite in the sense of Sibson (1977). Since the greenstone unit is isolated from the main, essentially undeformed pillow lava sequence below and is also not continuous along strike, it is considered to be a block within pebbly mudstone.

Pebbly mudstone occurs in a 170 m thick unit overlying the sheared greenstone, but is generally widespread throughout the LRO. It crops out along much of the GO-road where the lower stratigraphic level of the LRO is predominantly exposed. When fresh, the pebbly mudstone has a black, organic-rich matrix that is comprised of very

fine-grained mica, quartz, and feldspar. It weathers greenish-gray to yellow and tends to become friable. Dominantly pebble-size clasts impart a typical clastic texture to the unit (Fig. 3.7). The clasts are matrix supported and generally angular to subrounded, but matrix-poor varieties exist as well and commonly contain larger clasts. A weak foliation is developed in the pebbly mudstone matrix, but it is non-penetrative and wraps around the pebbles.

Sedimentary lithologies constitute the dominant clast types: chert, siliceous argillite, shale, siltstone, crenulated slate, graywacke, quartzite, and, to a lesser extent, quartz arenite are all common. Even reworked clasts of pebbly mudstone occur, producing something like a breccia-in-breccia texture.

Siliceous argillite pebbles sometimes contain recrystallized radiolarian "ghosts" (Fig. 3.8a); similar radiolarian ghosts also occur in semi-continuous argillite beds that are interlayered with tuffaceous rocks closer to the top of the LRO (Fig. 3.8b).

Chert is probably the most abundant clast-type; it is invariably rounded to subrounded, and often contains rhomb shaped dolomite crystals that are commonly altered to an opaque mineral. These chert pebbles resemble chert that occurs abundantly in a coarse pebble conglomerate within the Galice Formation.

This pebble conglomerate consists of flattened pebbles of siliceous argillite, chert, quartzite, and sparse volcanics (Fig. 3.9a). The spaced cleavage planes are defined by minute mica concentrated within the stretched tails of shale clasts that underwent the most flattening. Extension veins filled with quartz and calcite are perpendicular to the foliation and are offset along the cleavage planes (Fig. 3.9b). Chert and siliceous argillite in the conglomerate contain dolomite (or dolomite replaced by magnetite) rhombs, much like chert clasts in the pebbly mudstone (Fig. 3.10a and 3.10b).

The Galice pebble conglomerate occurs just east of the inferred northern continuation of the Buck Mountain fault (Fig. 3.1). The pebbles are identical in kind and abundance to clasts within the pebbly mudstone of the LRO. It is suggested that the belt of pebble conglomerate outcrops traces the extension of the Buck Mountain fault into the Galice Formation; in addition, the intensity of foliation in the Galice Formation is much lower east of the inferred fault trace. This counters arguments that the Buck Mountain fault represents the main thrust between the RCT and the western Jurassic belt (Cashman, pers.comm. to Harper, 1985) and precludes any interpretation of the LRO as a tectonic klippe of the RCT.

Clasts of quartz arenite are less abundant in the

pebbly mudstone. They show commonly deformation features such as undulatory extinction, deformation lamellae, and subgrain development (Fig. 3.11).

Completely recrystallized quartzites with typical triple-junction grain boundaries usually account for the largest clasts and range in size up to over several centimeters. They are angular to subrounded and occur in matrix-poor varieties of pebbly mudstone (Fig. 3.12).

The mixed character of pebbly mudstone is exemplified in Fig. 3.13, showing three different clast types in a matrix-supported variety of pebbly mudstone.

Other distinct sedimentary clasts include limestone cobbles, one of which has a faunal assemblage with affinities to the middle parts of the early Permian McCloud limestone of the eastern Klamath terrane (C. Stevens, written comm., 1985; P. Goldstrand, written comm., 1986). It implies that the eastern Klamath terrane was nearby at the time of deposition of the LRO.

Metamorphic clasts include micaschists, foliated quartzites with mica aligned in the foliation plane, and very rarely garnet-bearing schists. The presence of these rocks requires a deeply eroded continental source area adjacent to the LRO. These metamorphic clasts are associated in outcrop with the early Permian McCloud limestone cobbles, also suggesting the proximity of a continental margin.

The pebbly mudstone also contains vesicular volcanic clasts (scorias). Their geochemistry is discussed in chapter 4. Greenstone and plutonic fragments, as well as ultramafic rocks are rare in the pebbly mudstone, but where present, they occur in distinctly coarser boulder to block sizes.

A coarse block breccia consisting of diabase and serpentized ultramafic rock boulders overlies pebbly mudstone. Block sizes range up to several meters and there is no matrix component visible. The breccia occurs along Buck Mountain, but similar units consisting of diabase, gabbro, and ultramafic rocks occur throughout the olistostrome. Diabase blocks are phaneritic to aphanitic with plagioclase phenocrysts sometimes visible. Textures vary from spherulitic to lathwork; microphenocrysts of cpx are common (Fig. 3.14). Abundant interstitial chlorite is also present. The mineral assemblage consists of albite + chlorite + actinolite + epidote (or alternatively clinozoisite), indicating prehnite-pumpellyite or lower greenschist facies conditions during regional metamorphism. Occasional "one-way chilling" of dike margins indicates mutual intrusive relationships similar to those in sheeted dike complexes in ophiolites. The ultramafic blocks weather orange-red to yellow and include lined mantle rocks as well as ultramafic cumulates.

The scale bar in all photomicrographs is 1 mm.

- Figure 3.4 Sheared pebbly mudstone: limestone block in strongly foliated argillaceous matrix.
- Figure 3.5 Pillow lava from the GO-road.
- Figure 3.6a,b Volcanic clasts enveloped by sheared tuffaceous and argillaceous matrix containing smaller chert and volcanic fragments.
- Figure 3.7 Typical pebbly mudstone with pebble- to clast-size rock fragments in a dark muddy matrix.
- Figure 3.8a Pebble of siliceous argillite containing recrystallized radiolarians in pebbly mudstone.
- Figure 3.8b recrystallized radiolarians in siliceous argillite overlying tuffaceous greenstone.
- Figure 3.9a Handsample of pebble conglomerate (Galice Fm.) from Jones Creek.
- Figure 3.9b Photomicrograph of pebble conglomerate; calcite vein is offset along spaced cleavage traces.
- Figure 3.10 Photomicrographs of chert pebbles in pebble conglomerate (a. with dolomite; b. with an opaque mineral replacing dolomite).
- Figure 3.11 Photomicrograph of quartz arenite pebble in pebbly mudstone; note the deformation features.

- Figure 3.12 Photomicrograph of quartzite and chert pebbles in matrix poor variety of pebbly mudstone.
- Figure 3.13 Photomicrograph of crenulated slate, graywacke, and foliated quartzite pebble in pebbly mudstone.
- Figure 3.14 Photomicrograph of a diabase block, showing lathwork texture in the groundmass and phenocrysts of plagioclase and cpx.
- Figure 3.15 Photomicrograph of a serpentized ultramafic cumulate, showing bladed antigorite, magnesite, and Cr-spinel.



Figure 3.4



Figure 3.5

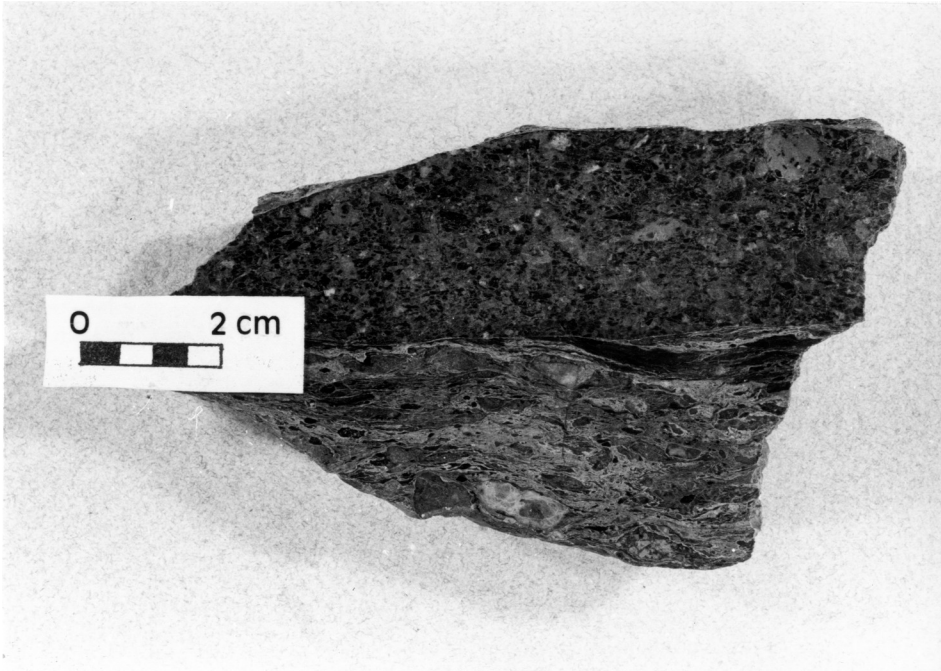


Figure 3.6a

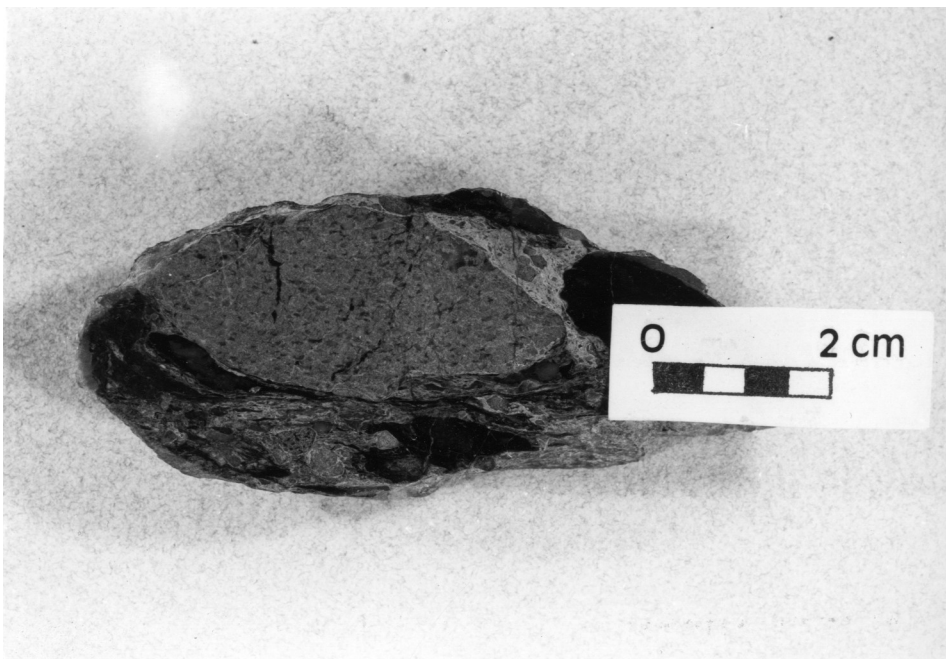


Figure 3.6b



Figure 3.7

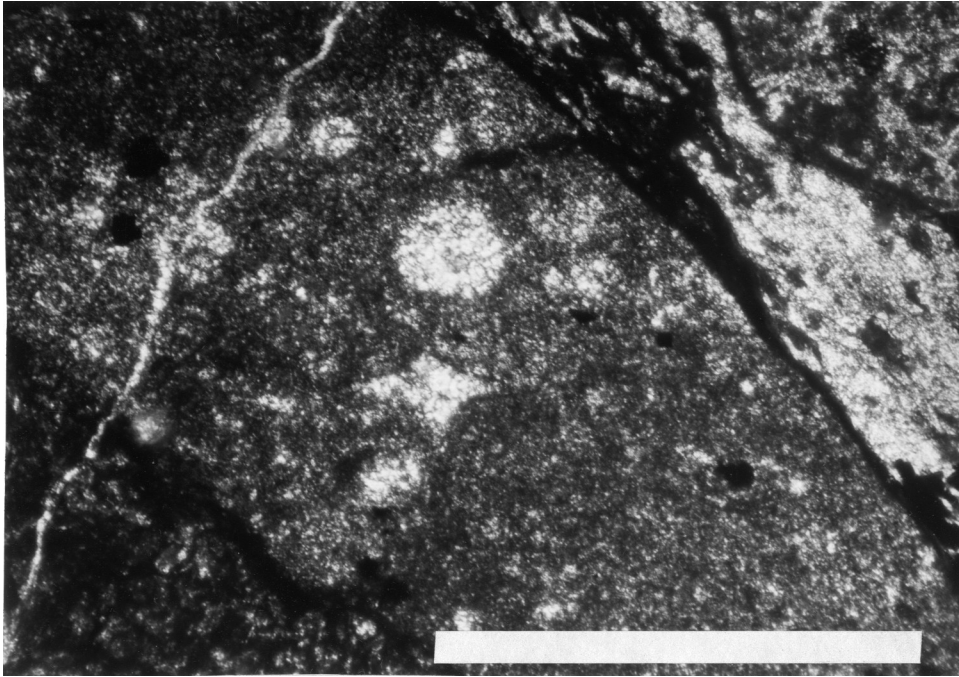


Figure 3.8a

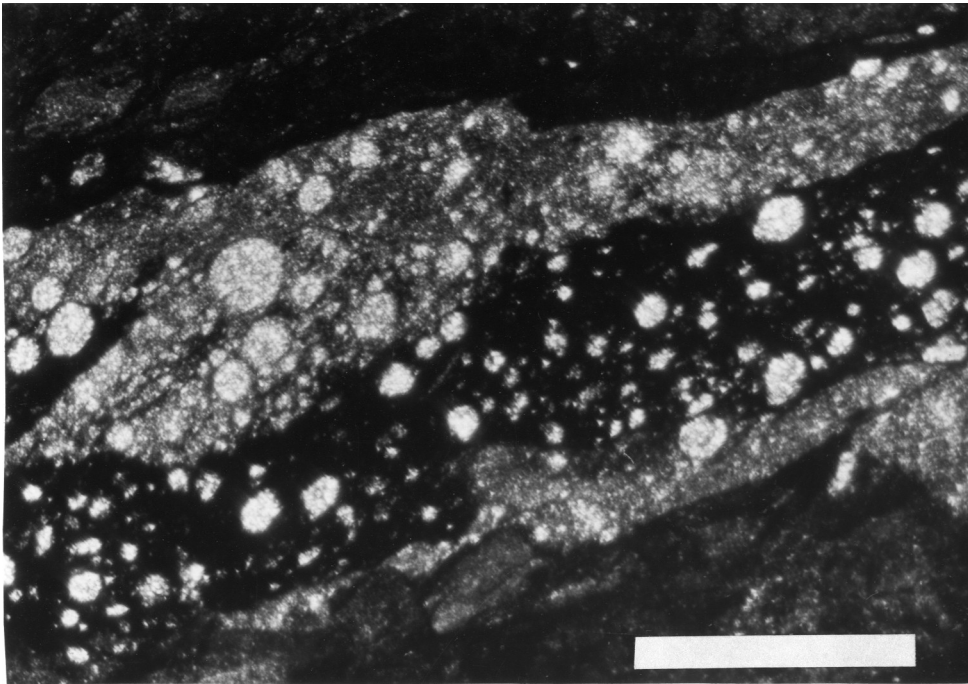


Figure 3.8b

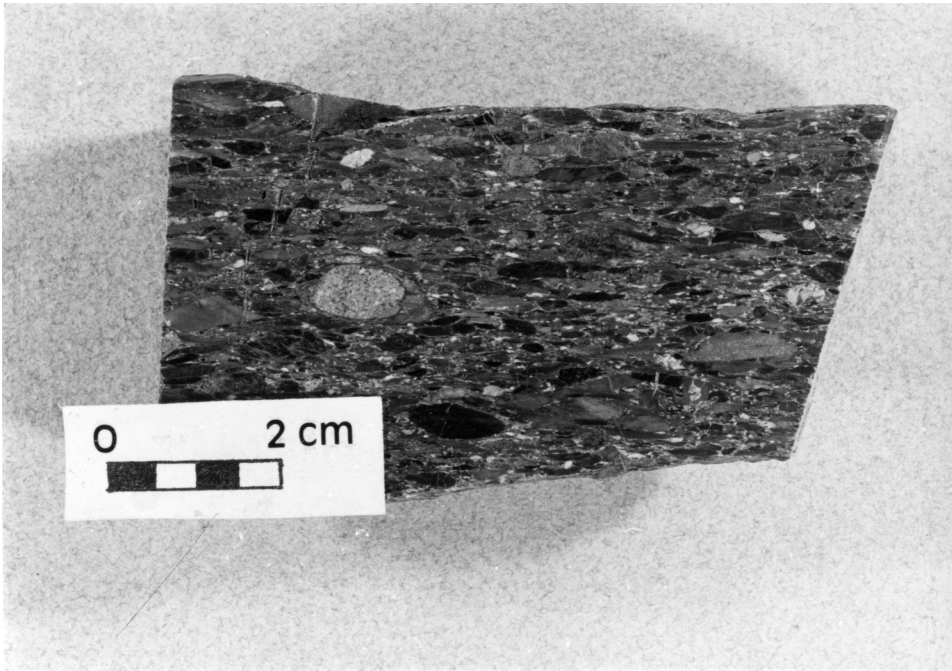


Figure 3.9a

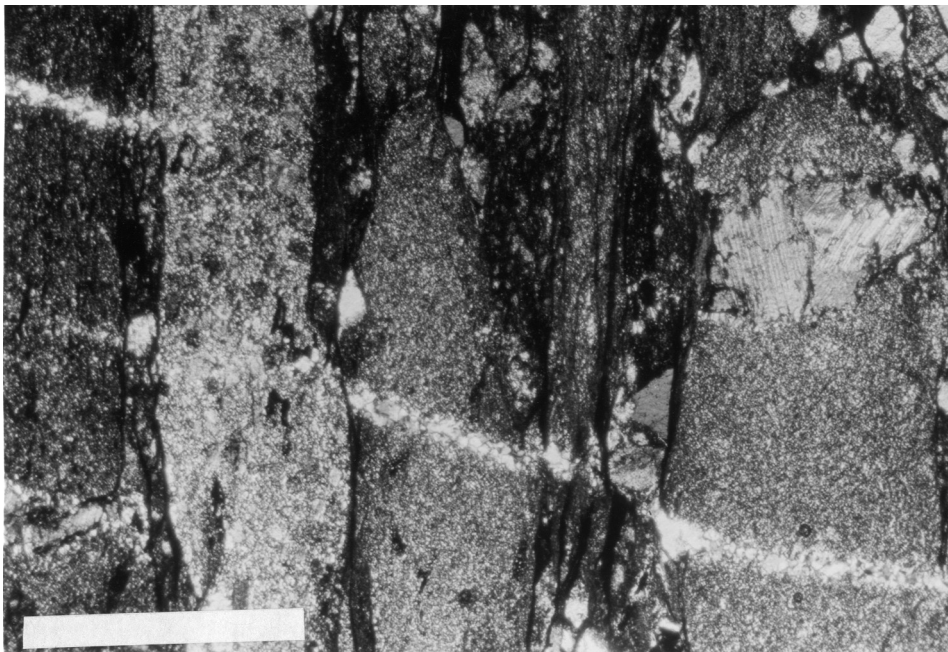


Figure 3.9b

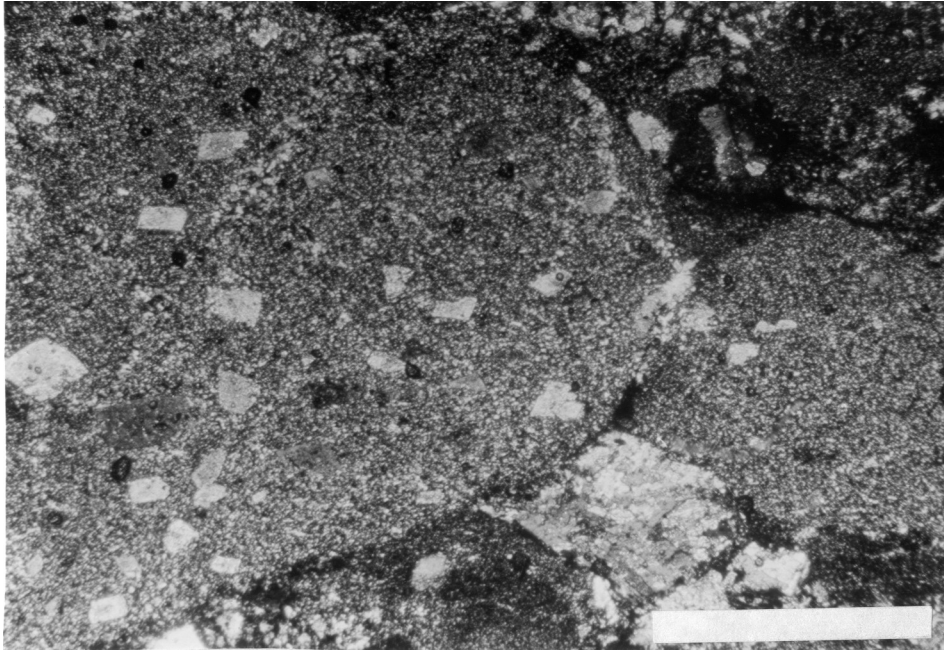


Figure 3.10a

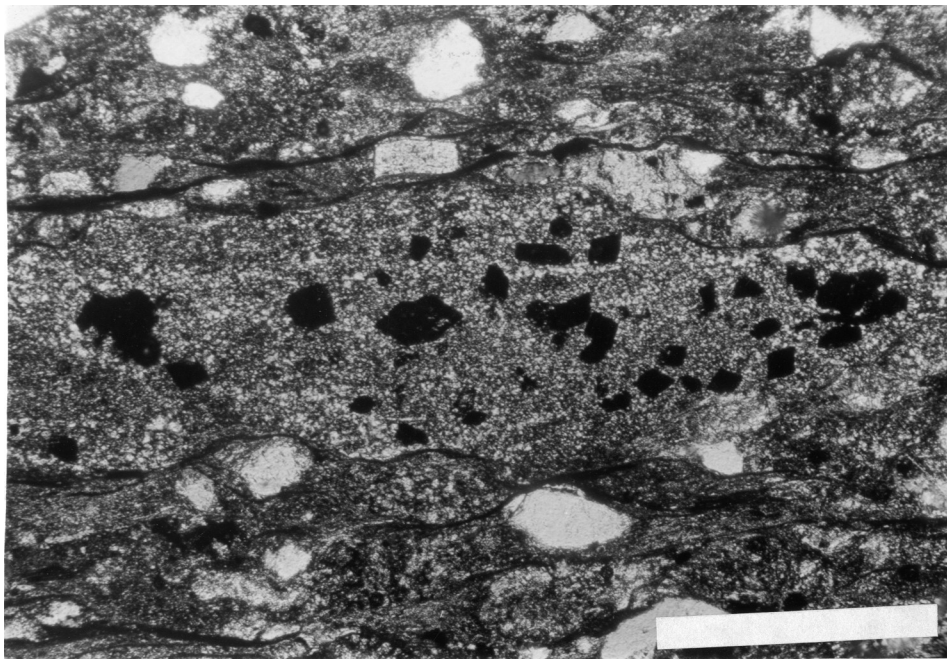


Figure 3.10b

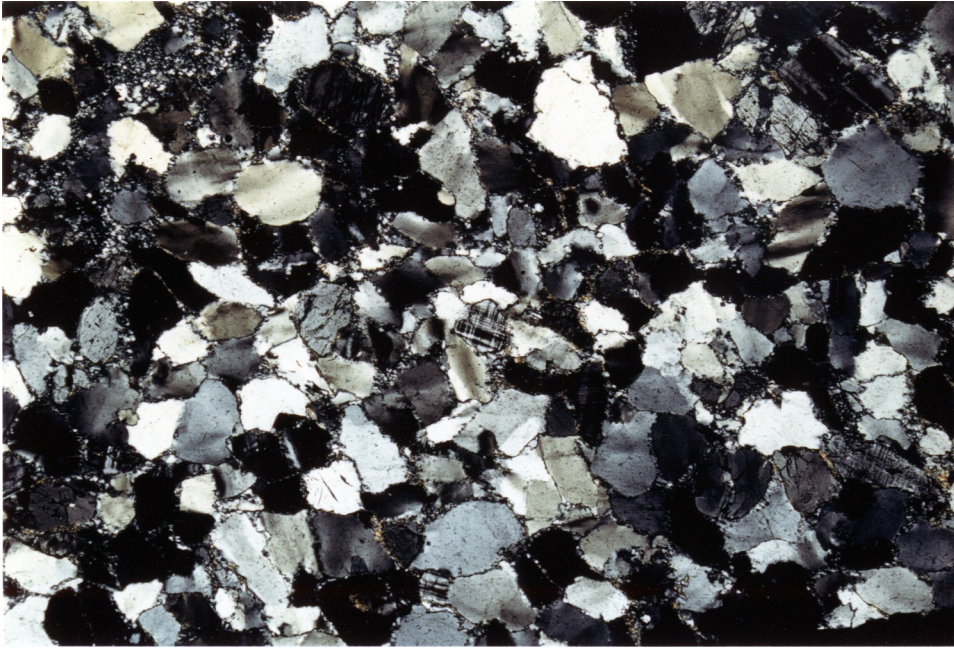


Figure 3.11

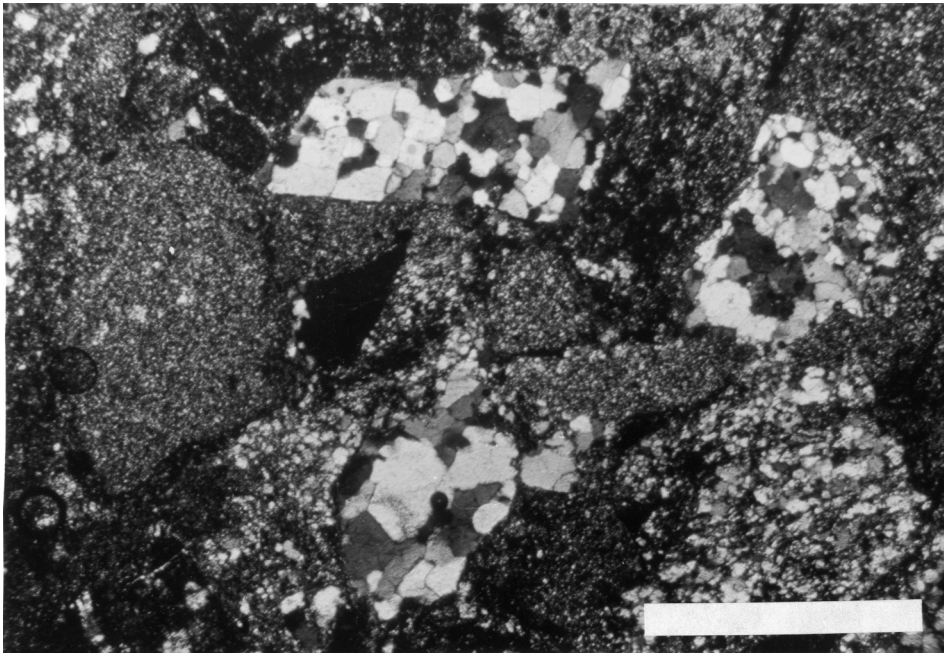


Figure 3.12

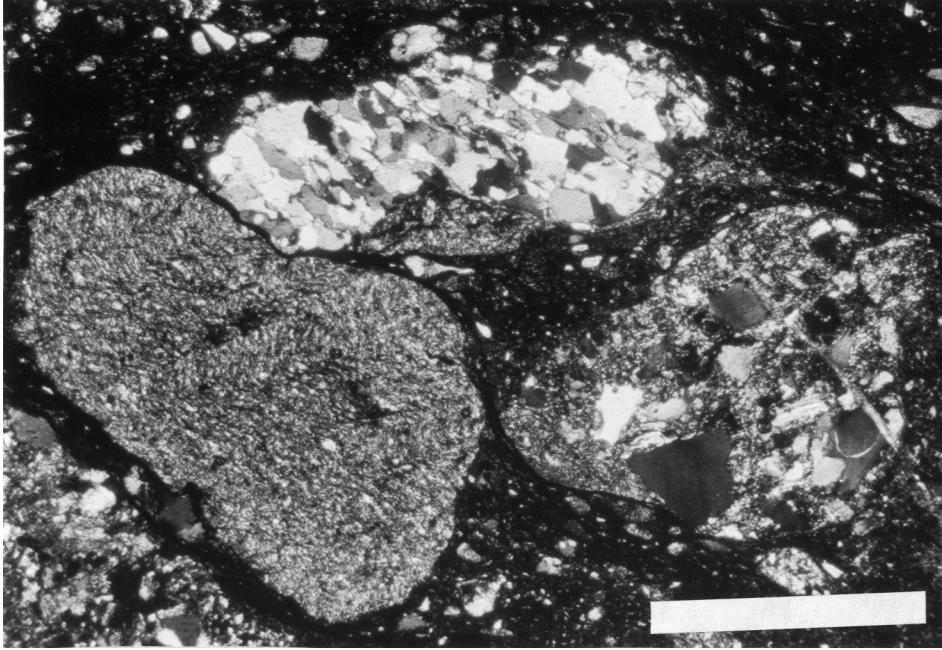


Figure 3.13

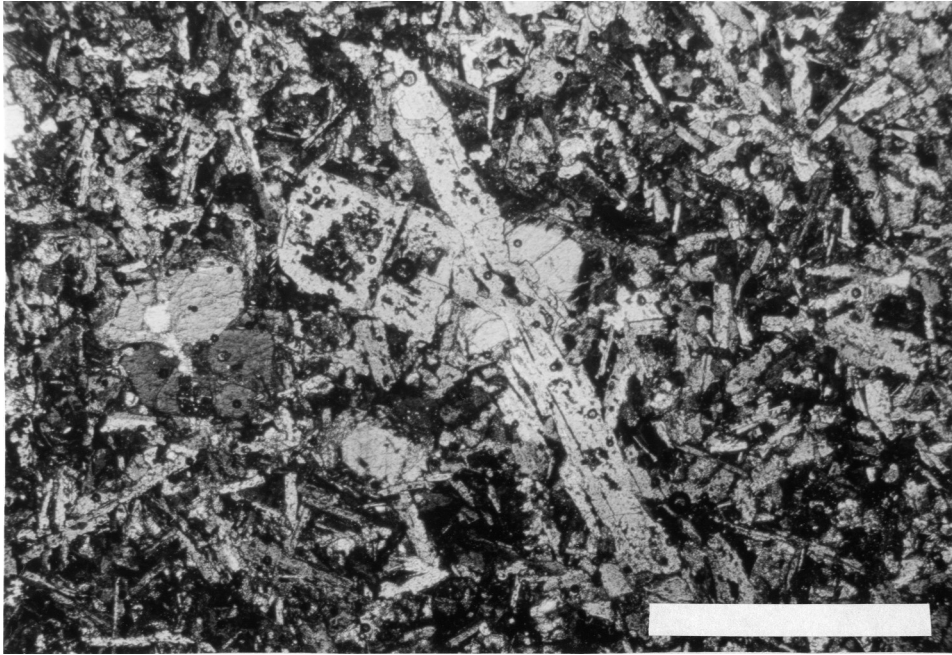


Figure 3.14

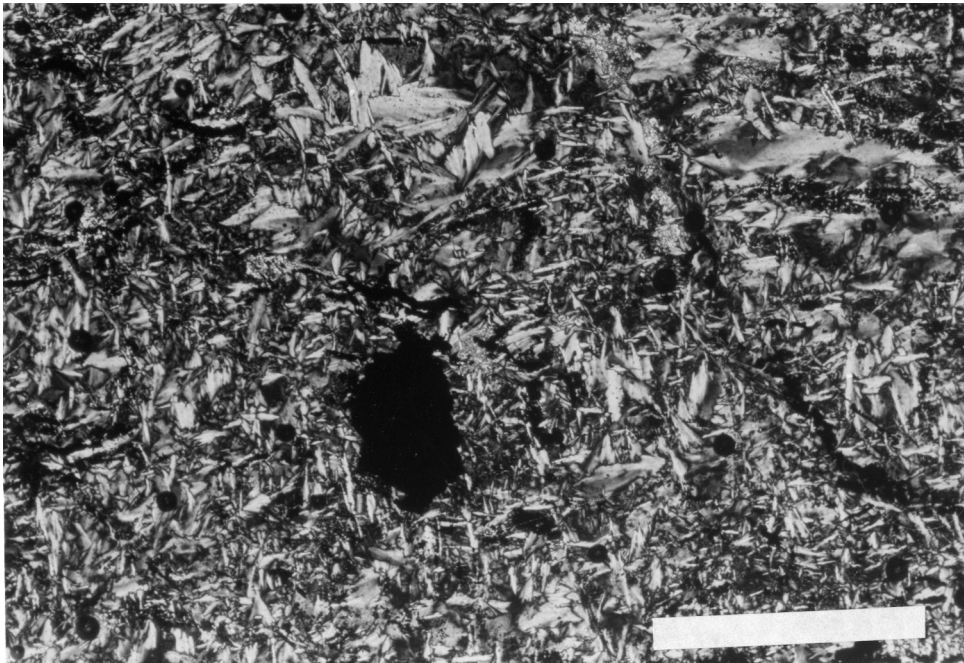


Figure 3.15

They are extensively serpentized; most blocks contain lizardite as the serpentine mineral; antigorite is usually not abundant, but one sample consists almost completely of bladed antigorite + magnesite + octahedral Cr-spinel (Fig. 3.15). Euhedral Cr-spinel is indicative for ultramafic cumulates, whereas anhedral Cr-spinel and a lineation defined by elongated opx (or talc replacing opx) indicate the presence of altered refractory, harzburgitic mantle rocks. Pyroxenite cumulates that do not show extensive alteration are less abundant.

The Smith River Section: Gabbro, Pillow Lavas, Volcaniclastic Rocks, Gabbro Blocks, Graywackes, and Dikes

A second tectono-stratigraphic section was compiled along the South Fork of the Smith River (Fig. 3.16). Continuous water polished outcrops expose a complete sequence of the LRO perpendicular to strike. Stratigraphic thicknesses are calculated using the orientation of a graded tuffaceous sandstone bed (N45E, 55 SE). The section shown in Fig. 3.16 is truncated at the bottom and does not include pebbly mudstone and chert that occurs between the river and the Buck Mountain fault to the west (Fig. 3.2).

The lower 240 meters exhibit fine to medium grained hornblende gabbro with a granular, subhedral texture. It consists of green hornblende, strongly zoned and altered

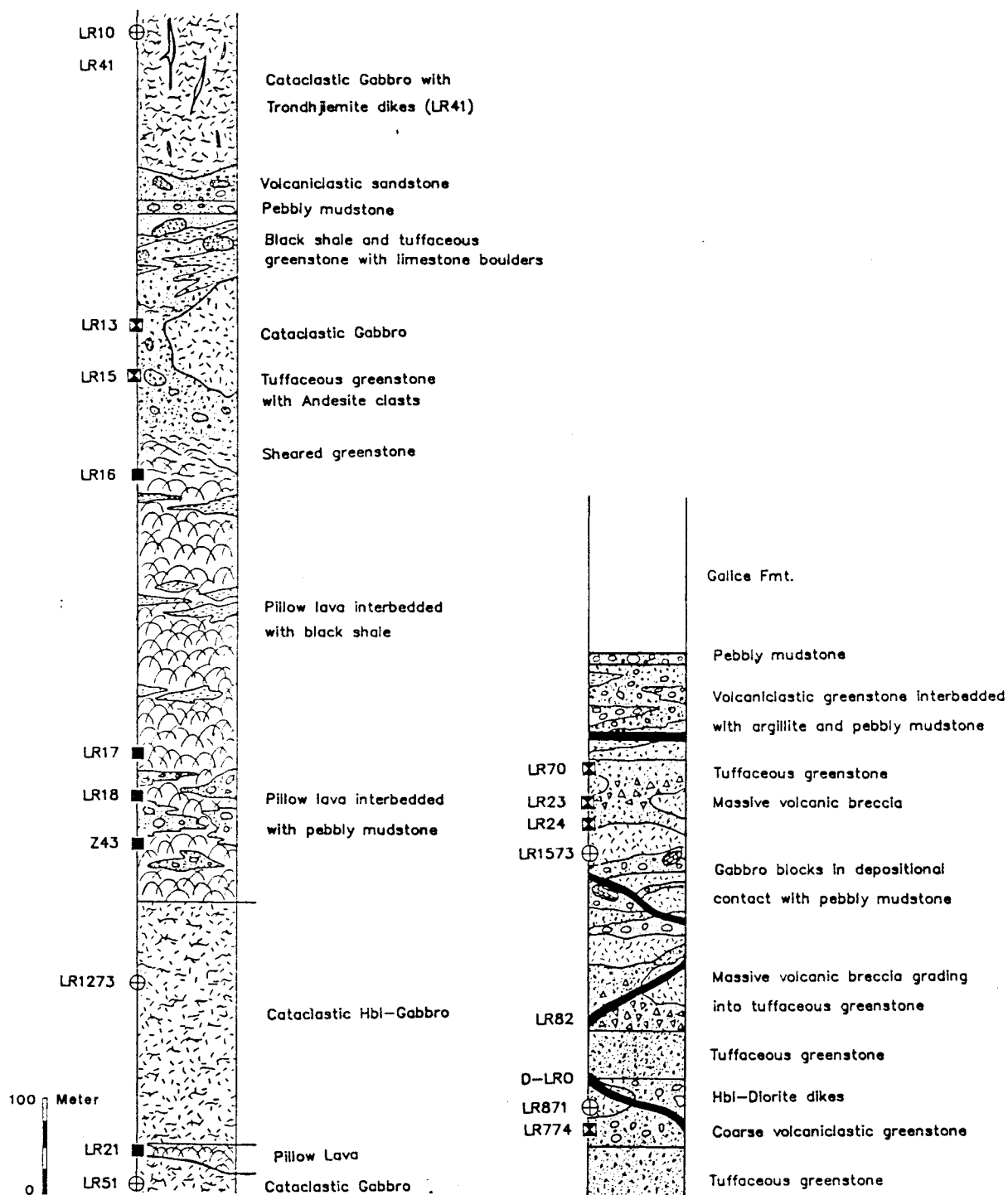


Figure 3.16

Tectono-stratigraphic section of the LRO along the South Fork of the Smith River (for location, see fig. 3.2).

plagioclase, and minor Fe-Ti oxide. The green hornblende occurs as both blocky crystals and smaller poikilitically enclosed crystals in plagioclase. The poikilitic crystals appear to be homogeneous and unaltered. The larger crystals (1-4 mm in size) show a strong zonation and have overgrown cores (Fig. 3.17a). Extinction and pleochroism is continuous from the rim into the core, precluding an interpretation that the hornblende is replacing cpx. It seems certain, however, that two distinct amphibole phases are present in the crystals: this has to be kept in mind, since hornblende of these gabbros was used for $^{40}\text{Ar}/^{39}\text{Ar}$ geochronology (chapter 5). Chemical inhomogenities other than the observed zonation (e.g. exsolution) are not easily detectable using standard petrographic microscopes. Figs. 3.17a and 3.17b show such amphibole crystals from LR 1273, which are representative for other gabbros as well.

A 400-meter-thick pillow lava sequence is in fault contact with the underlying gabbro section; texturally and mineralogically they resemble the GO-road pillow sequence: some samples lack pumpellyite, perhaps suggesting a somewhat higher metamorphic grade. The Smith River lavas are distinct from the GO-road lavas, however, in that they exhibit interfingering contacts with argillite and pebbly mudstone (Fig. 3.18). Depositional contacts of this kind are observed throughout the pillow lava section, suggesting a conformable relationship between the extrusive and the

clastic units of the LRO. A non-descript dense, sheared greenstone unit overlies the pillow lavas; possibly the expression of a fault contact with the overlying volcanoclastic and tuffaceous section of the LRO.

The next unit upsection is a coarse-grained tuff containing rare boulders of porphyritic andesite. In those andesitic boulders phenocrysts of plagioclase, khaki-brown hornblende and minor cpx, are surrounded by a very fine grained groundmass of plagioclase, magnetite, and possibly some altered glass (Fig. 3.19). Hornblende is usually euhedral but contains composites of magnetite and plagioclase: nevertheless hornblende from LR 15 was dated by the $^{40}\text{Ar}/^{39}\text{Ar}$ technique (chapter 5).

Volcanoclastic and tuffaceous greenstone is the typical rock unit along the South Fork of the Smith River. It is commonly interlayered with black argillite, siltstone, and pebbly mudstone. Sedimentary contacts are often irregular to disrupted, indicating soft-sediment deformation (Norman, 1984). These greenstones occur in three varieties: (1) a homogeneous greenstone with only faintly preserved clastic textures, which is recrystallized to a fine aggregate of various alteration minerals; (2) a fine to medium grained tuffaceous variety with preserved clastic textures, containing fragments of porphyritic volcanics and mafic minerals, as well as sparse clasts of chert, shale, and siltstone (Figs. 3.20a and 3.20b); and

(3) a coarse tuff or volcanic breccia consisting of pebble- to boulder-size volcanic and subordinate plutonic fragments (Figs. 3.21 a and 3.21b).

The most spectacular clasts within this thick volcanoclastic unit are gabbro blocks that are up to 200 meters in diameter. All of them display sharp depositional contacts to the surrounding matrix (Fig. 3.22). Argillite and pebbly mudstone surrounding these blocks exhibit a more strongly developed anastomosing cleavage than is usually the case. The strongest evidence that these gabbros are huge olistoliths emplaced by sedimentary processes is derived from the preservation of intricate sedimentary structures as little as 20 cm away from the contact with these huge blocks. Fig. 3.23 shows a graded tuffaceous sandstone bed that occurs directly at the contact with a 200-m-gabbro block (LR 10). Grading in this sample also indicates that the bed is not overturned.

The gabbros are mineralogically identical to LR 1273 at the base of the section. Contrary to this basal gabbro, however, all other gabbros show preserved depositional relationships to the surrounding matrix, and are therefore considered to be isolated blocks. LR 1273, in turn, is associated with pillow lavas that appear to represent the basal unit of the LRO; therefore these linear outcrops (Figs. 3.2 and 3.27) are tentatively considered as a (structural) basement on top of which the pillow lavas and

clastic units of the LRO were deposited in a quasi-stratigraphic manner. This will be the working hypothesis for the geochronological study on these gabbroic rocks (chapter 5).

The gabbro blocks show various stages of brittle deformation: hypidiomorphic textures with only incipient cracking perpendicular to the cleavage in the grains are succeeded by fractures that exhibit small shear displacements, as indicated by offset cleavage traces in hornblende and feldspar (Fig. 3.24a), or simply by lateral offset of an entire grain (Fig. 3.24b). Fragmentation proceeds with the production of wear fragments as a result of frictional sliding on fractures (Fig. 3.24c). This results in grain-size reduction and development of a fine grained, narrow zone of comminuted material. These narrow zones may coalesce (Fig. 3.24d) to form wider bands of extremely fine grained fragments. Grain-size reduction sometimes results in fragments close to optical resolution; grain-size reduction usually also results in strain hardening so that the fine grained matrix behaves in a more ductile manner (Mitra, 1984). Coarser grains may continue to fracture, but develop only stable fractures due to the ductility contrast across the grain-matrix boundary. The gabbro blocks are cataclastic fault rocks recording major brittle deformation and were incorporated as such into the argillaceous or tuffaceous matrix of the LRO. Handsamples

of intensively sheared and of less deformed gabbro are shown in Fig. 3.25.

The entire upper 800 meters of the Smith River section is comprised of a succession of tuffaceous rocks that are interlayered with pebbly mudstone and contain these huge gabbro blocks. Toward the top of the section individual beds of radiolarian bearing siliceous argillite, as well as of siltstone and lithic graywacke occur (Figs. 3.26a and 3.26b). Those graywackes are reported to be similar to volcanic to volcanic-rich graywacke of the lower Galice Formation (Norman, 1984). They contain, however, also abundant non-volcanic lithic fragments, and some quartzofeldspathic wackes do not contain volcanic fragments at all. Slates and graywackes of the Galice Formation overlie the uppermost pebbly mudstone bed without any apparent structural break. This and the increasing occurrence of siltstone and graywacke beds interlayered with tuff and pebbly mudstone indicate a gradual transition to a depositional environment represented by the Galice Formation; thus an apparently conformable relationship between the LRO and the Galice Formation is suggested.

Hornblende-phyric dikes occur throughout the entire thickness of the tuffaceous unit and are associated with the intrusion of the Summit Valley pluton. They cut the contacts between the volcanic and argillaceous matrix and

isolated gabbro blocks (e.g. LR 82 and D-LRO). Hornblende ages on these dikes indicate a minimum age for the assemblage of the LRO (chapter 5). Toward the top of the section the dikes become parallel to bedding and attain the character of sills.

From this stratigraphic section and from outcrop mapping, a river map has been compiled, showing the geology between the mouth of Horse Creek and the upper contact to the Galice Formation (Fig. 3.27).

The scale bar in all photomicrographs is 1 mm.

- Figure 3.17a,b Photomicrographs of amphibole crystals in gabbro LR 1273.
- Figure 3.18 Mudstone interfingering with pillow lavas on the South Fork of the Smith River, 200 m upstream from the mouth of Horse Creek.
- Figure 3.19 Photomicrograph of porphyritic andesite from a tuffaceous breccia, overlying the Smith River pillow lavas.
- Figure 3.20a,b Photomicrographs of porphyritic volcanic fragments in tuffaceous greenstone; note the fractured sedimentary clast in 3.20b.
- Figure 3.21a Handsample of brecciated volcanic tuff.
- Figure 3.21b Waterpolished exposure of massive volcanic breccia on the South Fork of the Smith River; note the irregularly oriented, narrow zones of intense shearing.
- Figure 3.22 Sharp contact of strongly cleaved pebbly mudstone with a gabbro block (between Yellowjacket Creek and Buck Creek).
- Figure 3.23 Coarse-grained tuffaceous sandstone grading into laminated silt- and mudstone. This graded bed occurs directly underlying gabbro block LR 10, about 300 m west of Yellowjacket Creek.
- Figure 3.24 Various stages of brittle deformation of amphibole and plagioclase indicated by shear offset along cracks normal to cleavage (a and b). Frictional sliding and kinking

along these cracks leads to grain-size reduction by friction and wear (c and d).

- Figure 3.25 Handsamples of cataclastic gabbro, showing (a) well preserved gabbroic texture with little apparent deformation, and (b) a pervasively sheared sample with only faintly preserved relict texture.
- Figure 3.26 Photomicrographs of volcanic-rich graywacke near the contact to the Galice Formation, (a) in PPL, (b) under crossed Nicols.
- Fig. 3.27 Geologic outcrop map along the South Fork of the Smith River, between the mouth of Horse Creek and the contact with the Galice Formation.

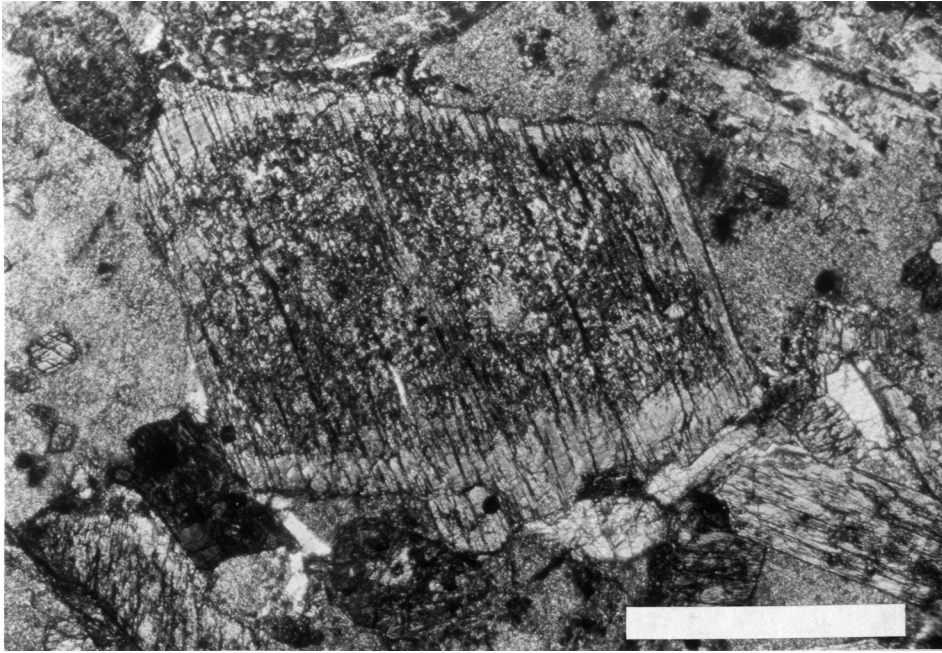


Figure 3.17a

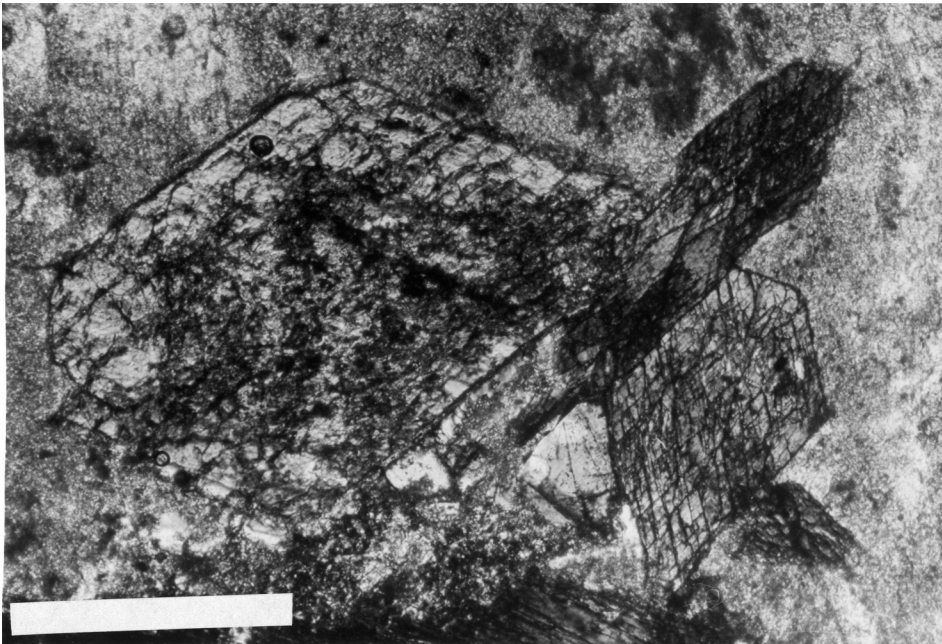


Figure 3.17b



Figure 3.18

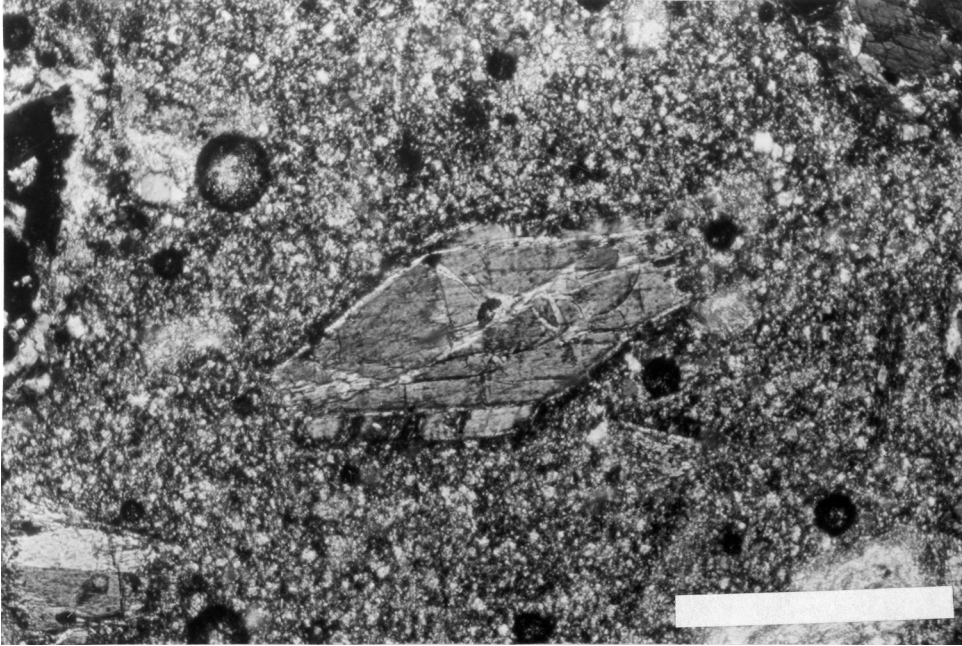


Figure 3.19

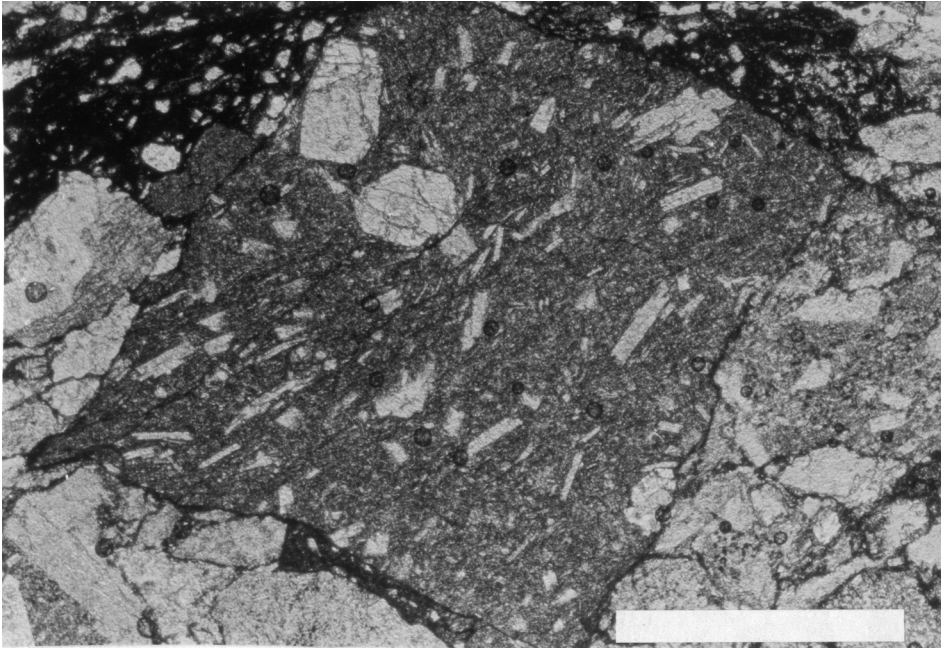


Figure 3.20a

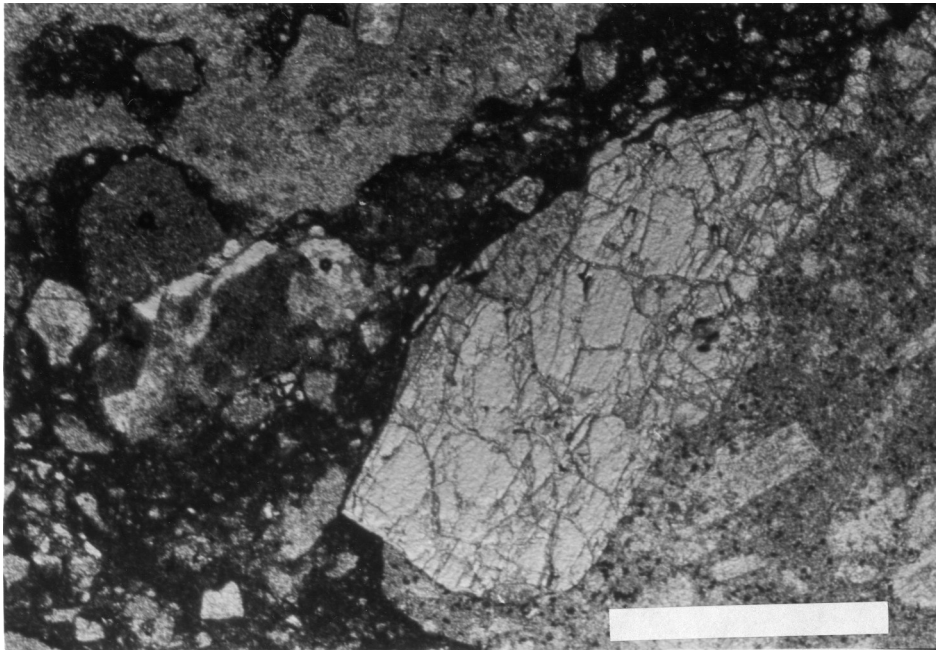


Figure 3.20b

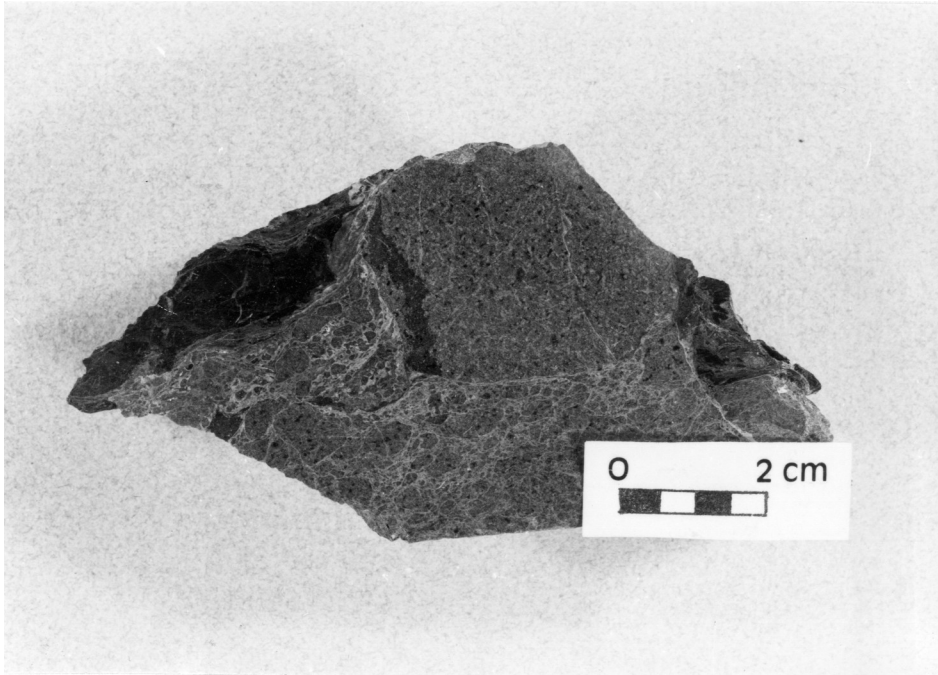


Figure 3.21a



Figure 3.21b



Figure 3.22

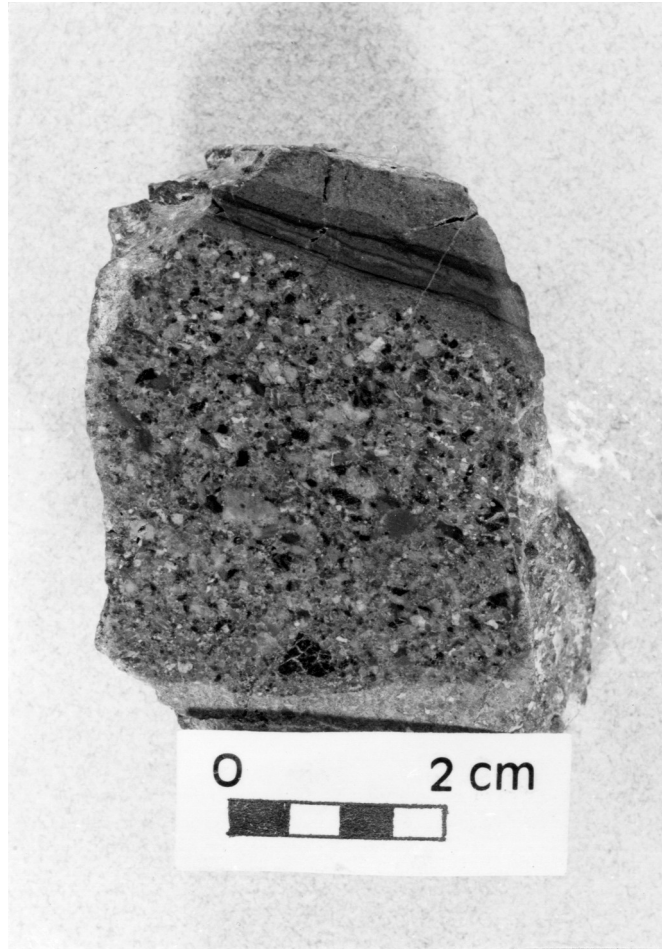


Figure 3.23

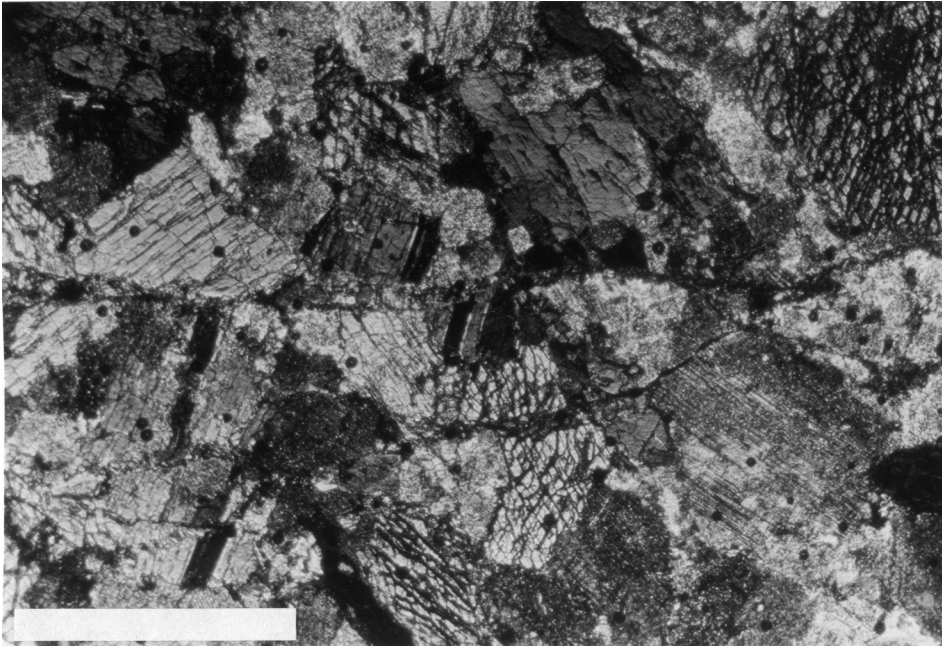


Figure 3.24a

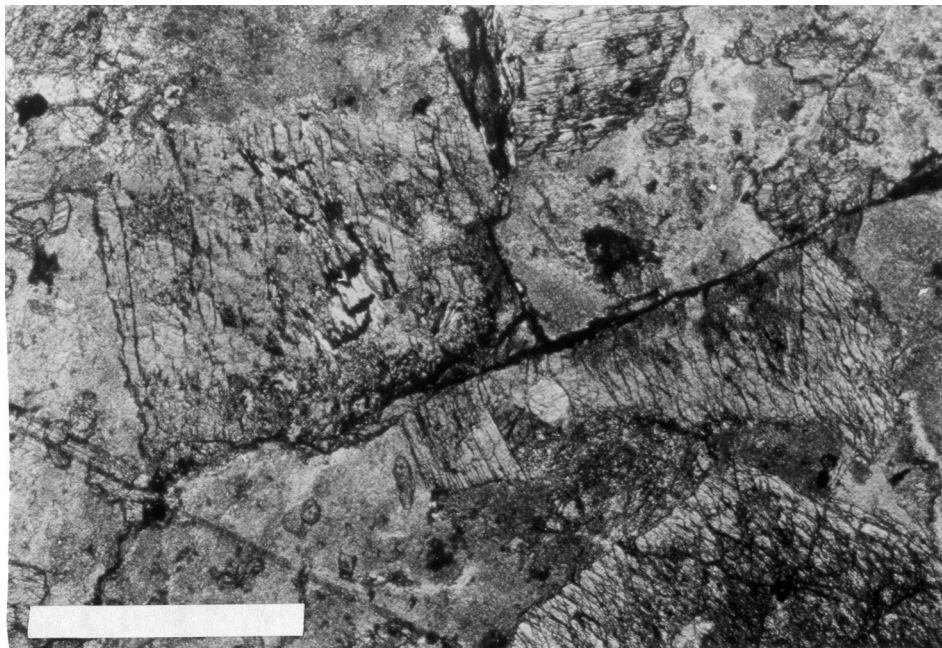


Figure 3.24b

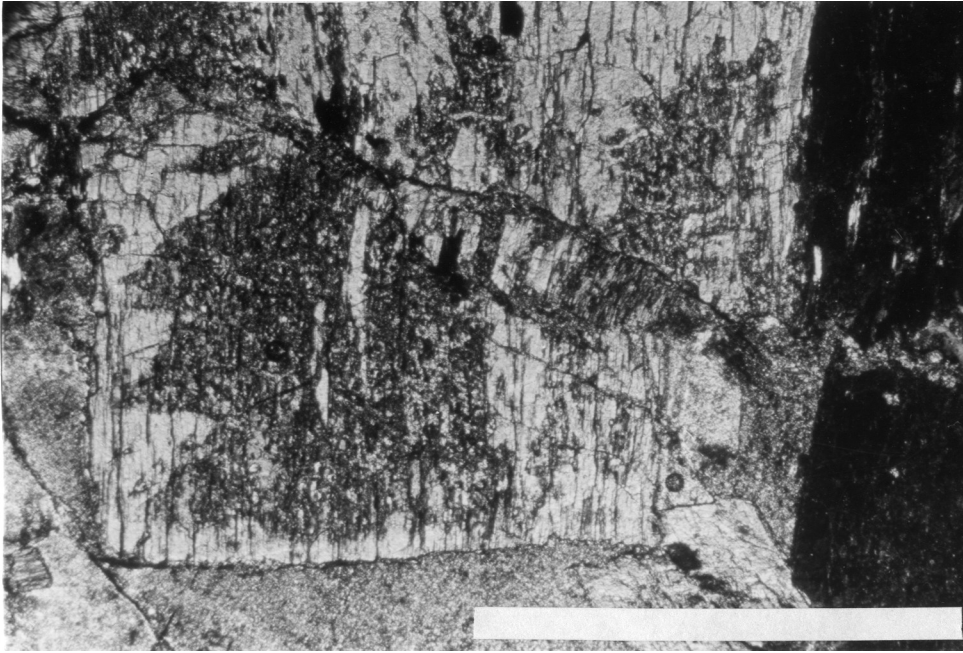


Figure 3.24c

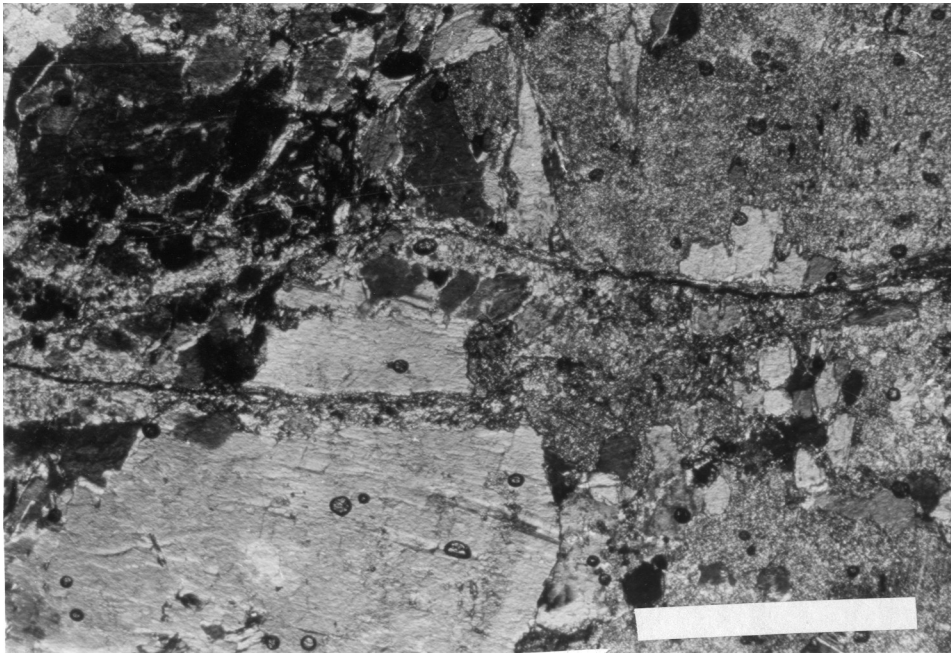


Figure 3.24d



Figure 3.25a



Figure 3.25b

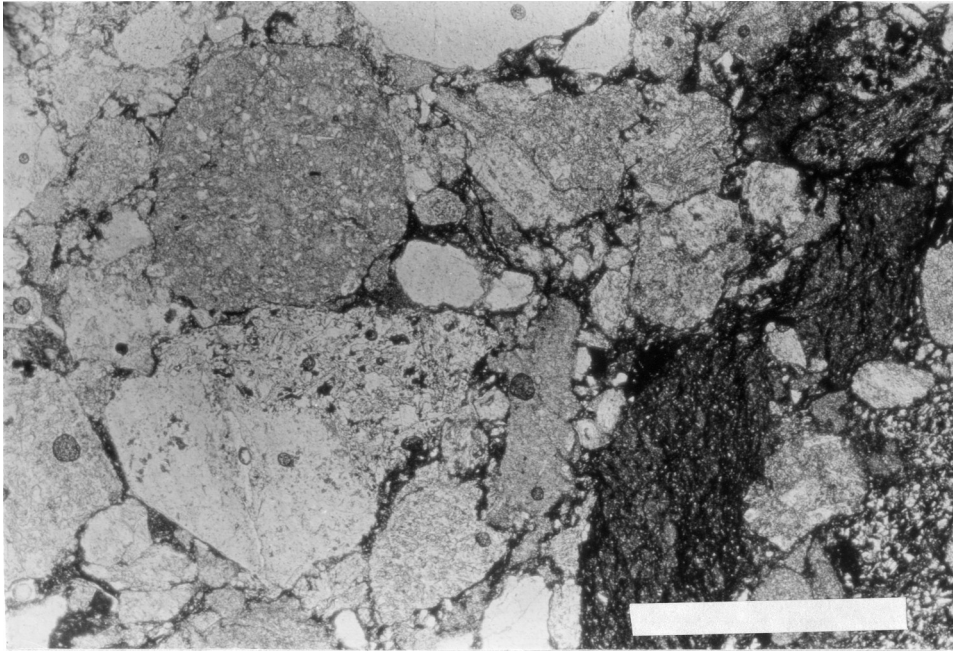


Figure 3.26a

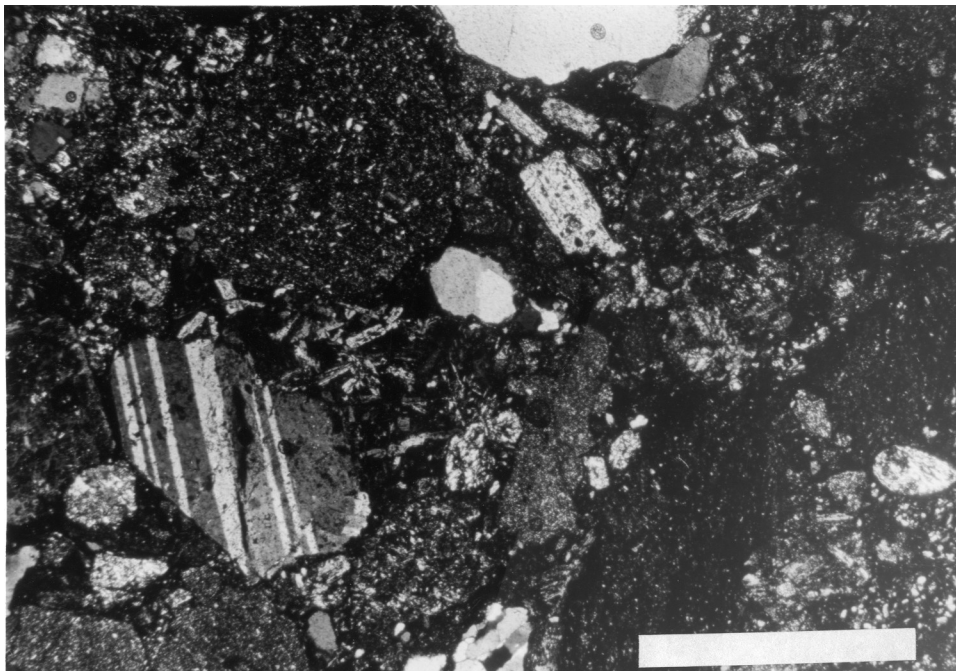
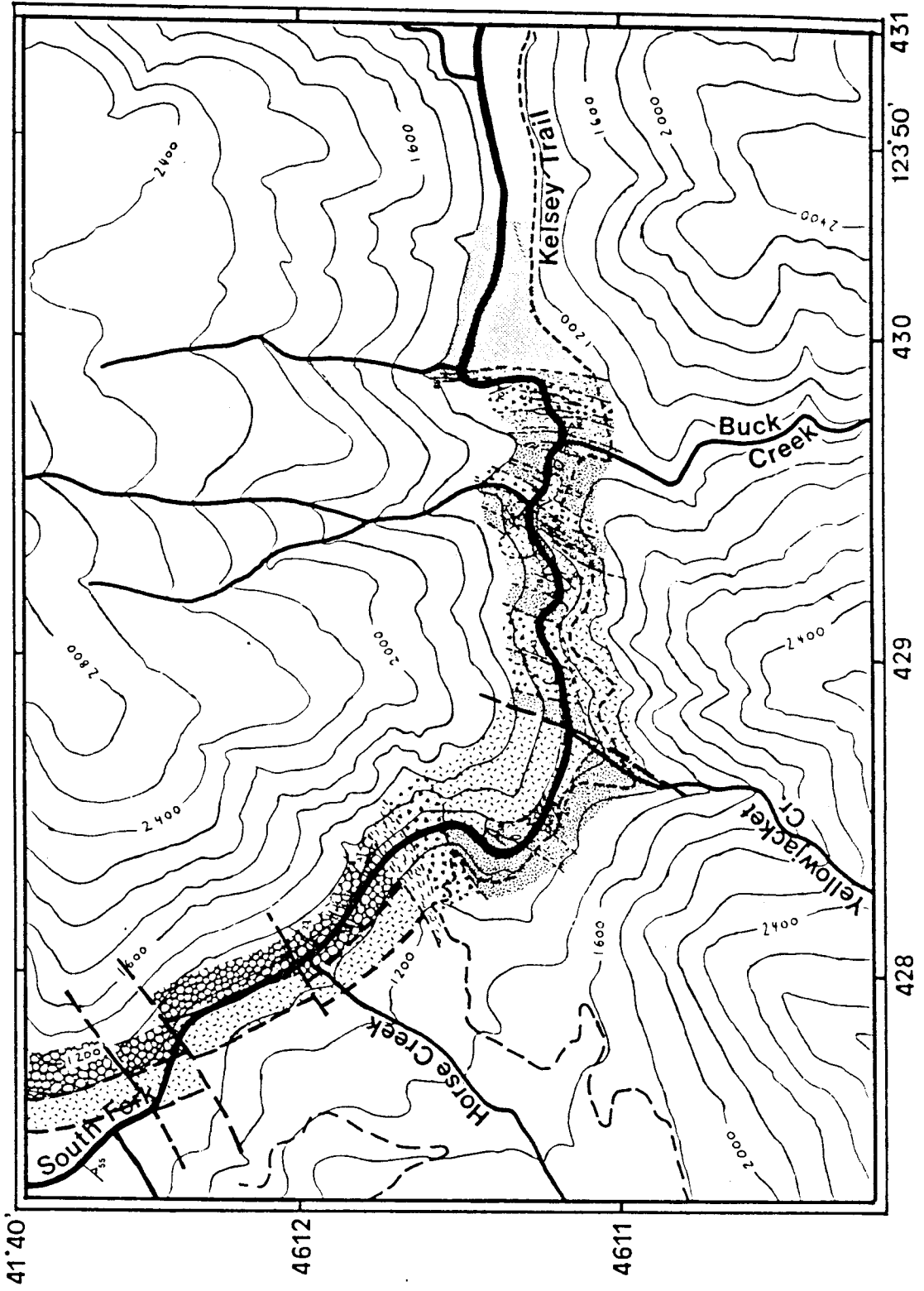
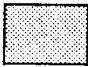








Figure 3.26b



- | | |
|---|--|
|  | Galice Formation |
|  | Pebbly mudstone, Argillite
Limestone boulders |
|  | Homogeneous volcanoclastic
greenstone |
|  | Volcanic breccia, coarse tuff |
|  | Sheared greenstone |
|  | Pillow lava |
|  | Hornblende gabbro |

Lems Ridge olistostrome

Key and explanation to fig. 3.27.

CHAPTER IV: Geochemistry

4.1 Analytical Methods

Major and trace element abundances of 30 rocks from the Lems Ridge olistostrome were determined by X-ray fluorescence at the Geochemical Laboratories of McGill University, Montreal (S.T. Ahmadeli, analyst). Two analyzed standards (SCo-1, SGR-1) were run as unknowns to assess the accuracy of the analyses (J.W. Delano, pers.comm., 1987). Two problems were observed:

- Nb was generally much too high compared to published values for SCo-1 and SGR-1, and is therefore omitted from the data tables in Appendices I and III.
- Zr was generally high, especially for unusual primitive basalts. Several of these rocks were analyzed by XRF at the University of Massachusetts, Amherst (J. Spark, analyst), for cross-reference. Using these data all the remaining samples were corrected graphically for Zr (see Fig. 1 in Appendix I). The uncertainty for Zr is therefore considerable.

A suite of pillow basalts from the base of the olistostrome was analyzed at the University of Utah, (G. Harper, analyst), and is used to complement basalt analyses which were done for this study. Comparison of analyses from the University of Utah and Amherst give nearly

identical results.

Fifteen of the LRO-rocks were additionally analyzed for rare earth elements and other trace elements by instrumental neutron activation (INAA), using the facilities at Cornell University, Ithaca (M. Ohr and G. Harper, analysts). A representative suite of dikes and lavas from the Josephine ophiolite was analyzed at the same facility and is used for comparison with LRO-samples. Analytical uncertainties for the rare earth elements are generally lower than 8%, except for highly depleted rocks. The elements Tb and Yb are usually determined with a precision of 8-15%. Again, an analyzed standard (W-1) was run as an unknown to control the accuracy of the measurements. The elements Ta, Th, and Hf have in general very low abundances and show often substantial analytical errors as high as 60%, depending on concentration and on the counting time during INAA (see Fig. 2 in Appendix I). Extremely long counting times result in nearly identical Th/Ta ratios, but with smaller analytical uncertainties. A detailed outline of the principles of neutron activation analyses is provided in Appendix II.

All available major and trace element data are listed in Appendices I through III. Appendix I shows all element abundances except the rare earth elements. It also lists the published values of SCo-1 and SGR-1 compared to the values obtained from McGill University. Appendix II lists

the rare earth data, including an analysis for W-1 in comparison with the USGS values. Finally Appendix III provides for N-MORB normalized trace element abundances (Pearce, 1983).

4.2 Discriminant diagrams

In modelling the ancient setting of the Lems Ridge olistostrome, it is crucial to infer as much information as possible about the provenance of the abundant ophiolitic lithologies within the olistostrome. While a qualitative petrographic approach might be useful to correlate the sedimentary and metamorphic components to probable source areas, the provenance of the ubiquitous ophiolitic rocks in the LRO has to be assessed by geochemical and geochronological (see chapter V) methods.

Igneous rocks of different tectonic settings show sufficiently distinct geochemical characteristics to effectively recognize their tectonic significance (e.g. Pearce, 1984). The inferred position of the LRO adjacent to a long-lived continental margin which underwent significant extension and compression during Late Jurassic time (Harper, 1984; Harper and Wright, 1984) implies the simultaneous presence of tectonomagmatic regimes of very different character. The prevailing presence of these

tectonic regimes adjacent to the olistostrome should be reflected in the presence of rocks with distinct geochemical signatures.

In the past decade general agreement has been reached that ophiolites represent pieces of ancient oceanic crust that formed in a diversity of environments (Dalziel and others, 1974; Upadhyay and Neale, 1979; Moores, 1982; Coleman, 1984). Together with stratigraphic and structural information it has become apparent that many geochemical features of ophiolitic rocks were not reconcilable with the traditional view that ophiolites have always formed in mature ocean basins. With the accumulation of good chemical data from recent tectonic settings, it became possible to empirically discriminate those settings according to their geochemistry (e.g. Pearce and Cann, 1973; Wood and others, 1979). A series of discriminant diagrams became available that, withstanding widespread alteration by hydrothermal fluids and regional metamorphism, effectively distinguish volcanic rocks of different rock series as well as tectonic setting.

The next step was to apply this framework to ancient oceanic rocks and to infer their petrotectonic setting. However, often enough the results stirred considerable discussion because the geologic evidence apparently contradicted the tectonic setting determined by geochemical

discriminant diagrams. With the advent of firmer petrogenetic models and additional high resolution data (Pearce and Norry, 1979; Saunders and others, 1979; Pearce and others, 1984) many of these disputes were reconciled, and it became evident that most ophiolites formed in fore-arc, back-arc, island-arc, or small ocean basin settings.

The first part of this section is therefore concerned with the application of simple binary and ternary discriminant diagrams in order to recognize the "inventory" of igneous rocks in the Lems Ridge olistostrome. The Ti-Zr diagram of Pearce and Cann (1973) serves to separate tholeiitic rocks from calc-alkaline rocks by means of their Ti content with increasing fractionation. The Ti/100-Zr-Yx3 diagram of Pearce and Cann (1973) builds on the same principle, but most rocks plot in an overlap field and are therefore not discernible; only within-plate basalts can be discriminated effectively. The Cr-Y diagram of Pearce (1980), and the Ti/Cr-Ni plot of Beccaluva and others (1979) are effective in discriminating tholeiitic island-arc basalts (IAT) from tholeiitic mid-ocean ridge basalts (MORB) by virtue of their lower Y and Ni abundances when plotted against a fractionation index. In addition the Ti-V plot of Shervais (1982) discriminates basalts of within-plate settings from tholeiitic rocks of convergent,

as well as divergent settings.

As a second way of presenting geochemical data, I chose to use N-MORB normalized trace-element patterns, similar to those used by Pearce (1983) and Saunders and Tarney (1984). These multi-element diagrams provide a convenient means of comparing samples on the basis of their complete trace-element composition; they are increasingly used to highlight geochemical variations between igneous rocks from different tectonic settings.

Rare earth element diagrams as a third way of visualizing geochemical trends are considered of lesser importance, since MORB-normalized trace-element plots already contain the most critical rare earth element information. Nevertheless, complete chondrite normalized rare earth diagrams are presented together with trace-element plots in order to emphasize the observed trends and to make the data comparable with other studies.

All the available information on the petrotectonic setting of the rocks contained in the Lems Ridge olistostrome can be summarized in a ternary Hf/3-Th-Ta plot of Wood and others (1979). This diagram not only discriminates between lavas erupted at convergent and divergent plate margins, but is also capable of highlighting various mantle enrichment trends.

Discrimination diagrams and element mobility

For elements to be useful in characterizing different magma types, they should ideally (Pearce and Cann, 1973):

- 1) display greater variation in abundances between samples of different magma types than they do between samples of the same magma type,
- 2) be reproducible by standard methods of geochemical analyses, even for low concentrations, and
- 3) not be affected by post-crystallization alteration such as weathering or metamorphism, that is, they must be immobile during secondary processes.

Mobility of elements can be best assessed by comparing their ionic potential. The ionic potential is defined as the ratio of ionic charge over the ionic radius (Z/r) of a particular element. Elements with low (<3) and very high (>12) ionic potentials are usually mobile in aqueous fluids, while those with intermediate ionic potentials are considered to generally be immobile (Hart and others, 1974; Pearce, 1983). Accordingly, the latter are termed high field-strength elements (HFS) and include Ta, Nb, Zr, Hf, Ti, and Y, whereas the mobile low field-strength elements (LFS) include Cs, Rb, K, Ba, Sr, and Th. The LFS elements are equivalent to the large-ion-lithophiles (LIL) of Schilling (1973). Of these, only Th appears to generally be immobile during low-T alteration (Saunders and Tarney, 1984); however some authors suggest that it may be mobile

in extreme cases of alteration (Wood and others, 1976; 1979). The rare earth elements have ionic potentials between LFS and HFS elements; in particular the light rare earth elements (LREE) are suspected to sometimes be mobile during hydrothermal alteration (Hellman and Henderson, 1977; Ludden and Thompson, 1979). As seawater is characterized by a negative Ce anomaly, rocks that underwent extensive interaction with seawater are likely to show related Ce anomalies on chondrite normalized REE plots. The heavy rare earth elements (HREE) are almost certainly immobile and thus behave like typical HFS elements (Ludden and Thompson, 1979).

All discrimination diagrams, trace-element patterns, and rare earth element plots use, as far as possible, consistent symbols for rocks that are discussed in this section. A key for the symbols used in Figs. 4.1 through 4.20 is provided below. Some diagrams use slightly different symbols, which are then keyed at the appropriate place. Sampling locations for the rocks analyzed for this study are shown in Fig. 4.1.

The Ti-Zr Diagram

The Ti-Zr diagram (Fig. 4.2) is suitable to display the distinct fractionation trends of rocks of the tholeiitic and calc-alkaline series, respectively. The

Symbols for Figs. 4.1 through 4.20

☒	Tuffaceous breccia and tuffaceous greenstone]	Tuffaceous matrix] Lems Ridge olistostrome	
⊖	Hornblende Gabbro				
⊕	Mafic dike in gabbro]	Clasts in the LRO		
★	Vesicular volcanics				
▲	Diabase dike				
□	Pillow lava]	basal lavas of LRO		
▣	G.O. Road] Pillow lava
▤	Smith River				
●	Typical dikes and lavas]	Josephine ophiolite		
◻	Dikes and lavas W'of LRO				
⊙	Primitive dikes and lavas				

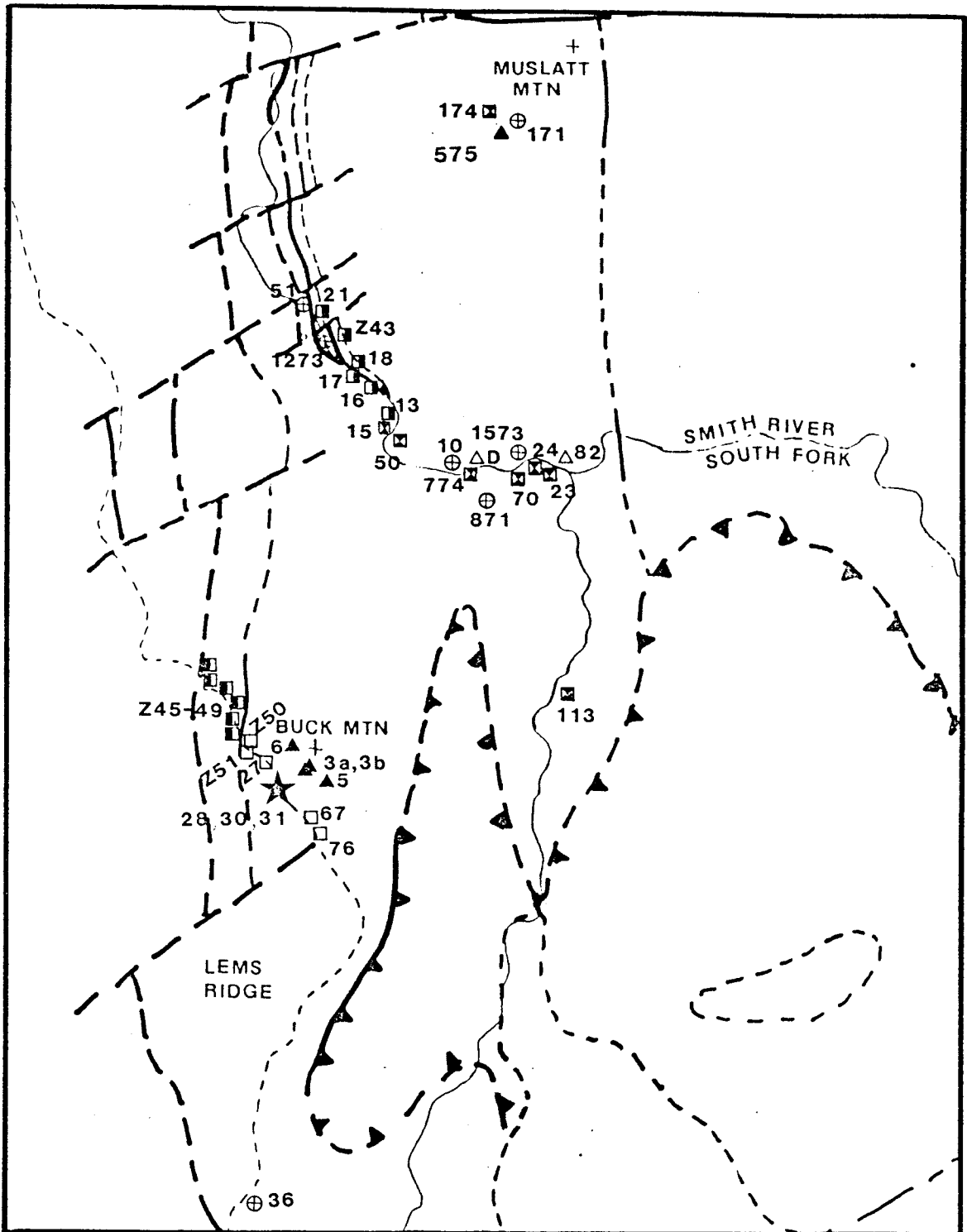


Figure 4.1

Sample locations for analyzed rocks from the Lems Ridge olistostrome. For explanation of symbols, see previous page.

tholeiitic trend is characterized by significant Fe- and Ti-enrichment due to olivine, pyroxene, and plagioclase fractionation. Rocks derived from a calc-alkaline parent magma do not exhibit this enrichment trend with progressing fractionation, probably owing to the early fractionation of Fe-Ti phases. Therefore tholeiitic rocks define a straight line with a positive slope of Ti/Zr of about 100 (Sun and Nisbett, 1978), while calc-alkaline trends are flat or display a negative slope and generally have lower Ti abundances.

The analyzed greenstones of the tuffaceous matrix of the LRO show distinctly low Ti abundances for given Zr concentrations. Two tuff samples, however, have rather high Ti; both are tuffaceous breccias and carry predominantly diabase clasts of probable tholeiitic chemistry. The remaining tuff samples are predominantly matrix supported and show the typical calc-alkaline Ti-depletion.

All pillow basalts plot along a positive linear trend, indicating a tholeiitic fractionation path. Pillows collected from the GO-road outcrops generally appear to be more evolved than lavas that outcrop along the South Fork of the Smith River. Pillow lava olistoliths and clasts are similar to pillows from the river, but one clast is clearly derived from a highly enriched source.

Diabase blocks in the olistostrome show a bimodal

distribution; two samples show very low Ti abundances, but contrary to the calc-alkaline tuffaceous samples, they also have extremely low Zr concentrations. The three other diabase blocks, all from Buck Mountain, lie along a typical tholeiitic trend (Fig. 4.2) and are, at least in this diagram, indistinguishable from the analyzed pillow basalts.

Pearce and Cann (1973) suggest the use of the Ti-Zr diagram as a discriminant plot for ocean-floor basalts, low-potassium tholeiites (IAT) and calc-alkaline basalts. However, there are overlaps for rocks low in Ti and Zr that often make it impossible to discriminate tectonic settings.

The Ti-Zr-Y Diagram

The ternary Ti/100-Zr-Yx3 diagram (Fig. 4.3) suffers from the same drawback of overlapping fields, but separates within-plate basalts quite successfully, owing to their generally higher Zr/Y ratios. Again, all but two tuffaceous samples cluster in the field for calc-alkaline basalts, while most of the pillow basalts and diabase dikes plot in field B and therefore give no additional information. Two pillow lavas from the lower GO-road sequence and one pillow clast in the LRO have high Zr/Y ratios and fall into the within-plate basalt field. In

addition three mafic vesicular, volcanic clasts (scorias) are plotted. They can be classified as alkaline by virtue of their high Nb/Y ratios of 1.92, 1.07, and 1.03, respectively (where Nb is estimated as $Nb = Ta \times 19$; Wood and others, 1979). Ratios of Nb/Y >1 characterize alkaline magmas; ratios of Nb/Y <1 are typical for tholeiitic and calc-alkaline magmas (Pearce and Cann, 1973). These scorias are therefore certainly not calc-alkaline as suggested by the Ti/100-Zr-Yx3 plot. This inconsistency is probably caused by the considerable uncertainty for high Zr abundances (see above, and Fig. I.1).

The Cr-Y Diagram

The Cr-Y plot (Figs. 4.4 and 4.5) utilizes Y instead of Ti as an incompatible element. Tholeiitic island-arc lavas (IAT) are commonly displaced toward lower Y-values at a given Cr concentration (Pearce, 1980; Pearce, 1982). This plot is particularly useful in relating variations between tholeiitic basalts to differences in their partial melting and fractional crystallization history, since Y and Cr do not partake in processes causing mantle heterogeneity (Pearce, 1982).

For a original mantle composition of Cr = 2,500 ppm, and of Y = 5 ppm (Wood, 1979), Pearce (1982) summarizes four models (Fig. 4.4) that can account for the observed

differences between IAT and MORB: 1) the degree of partial melting, 2) the presence of residual minor phases, 3) remelting and mixing of the residual mantle source, and 4) mixing with a component derived from subducted oceanic crust.

Model 1 (Pearce and Norry, 1979) explains the lower abundance of Y in IAT in terms of an increased extent of partial melting compared to MORB, say 20-40%. In contrast, the backward extrapolation of typical MORB along the indicated fractionation path requires lower degrees of partial melting (ca. 15%) of a undepleted mantle source. Model 2 (Saunders and others, 1979) assumes the presence of minor Y-bearing phases such as apatite or zircon in the residuum. If true, this would displace the compositions of partial basaltic melts to lower Y-values, especially for lower degrees of melting. Backwards extrapolation of the fractional crystallization vector for IAT will therefore intersect at about 15% partial melting. However, Watson (1980) showed that the high solubility of apatite in basic magmas at upper mantle temperatures and pressure results in the consumption of all stable apatite already at very small degrees of partial melting, and thus virtually precludes the occurrence of residual apatite in mantle source regions. Even under hydrous, low-T melting conditions residual apatite occurs in amounts too small to have

significant effects on the Y and REE concentration of the ensuing liquids (Watson, 1980). Model 3 (Green, 1973) involves remelting of the residuum from a previous 15% melting episode and mixes this melt with original tholeiitic melts. Model 4 (Pearce, 1982) investigates the contamination of the original upper mantle peridotite with a Cr- and Y-poor melt or aqueous component driven off the subducting slab. Intersection of the fractionation path with the displaced melting trend yields again about 15% partial melt. The various authors consider models 2 through 4 as possible explanations to account for the Y-depletion of IAT without requiring unrealistically high degrees of partial melting. Watson (1980) also clearly showed the limited usefulness of petrogenetic models involving minor residual phases in explaining the observed Y and REE patterns in basaltic rocks.

An alternative model is put forward by Pearce and others (1984) to account for very low-Y island-arc rocks (boninites): they model residual oceanic lithosphere that already experienced a previous melt extraction as a transient source for early stage island-arc basalts. Such a source would have lost its basaltic component and is therefore depleted in Y, while Cr remained buffered in the residuum during this first melt extraction. The ensuing melting trend is similar to the one in model 4, but the source does not show a depletion in Cr with respect to the

original mantle composition.

The depletion of island-arc lavas in HFS elements such as Y and Yb is a general feature and is prominent with respect to MORB for given Cr values, but, as we shall see later, is also apparent with respect to LFS and the more incompatible HFS elements such as Th, Ce, Zr, Hf, and Sm.

Since Cr is strongly partitioned in early fractionating mafic phases, the initial fractionation trends are modelled subparallel to the Cr axis (Pearce, 1982), with Cr-spinel as the singlemost important precipitating phase (Fig. 4.4). However, Barnes (1985) points out that the high solubility of Cr in basalts precludes the precipitation of Cr-spinel at Cr concentrations lower than about 500 ppm. Since Cr solubility is both a function of temperature and oxygen fugacities, cooler and highly oxidized systems (e.g. hydrous island arc melts) would be buffered at significantly lower Cr concentrations. In either case, Cr-spinel fractionation does not appear to be responsible for very low-Cr rocks. The late stage kink of the depicted fractionation trend is attributed to the onset of plagioclase fractionation (Pearce, 1982).

Pillow lavas from the base of the Lems Ridge olistostrome plot in the MORB field (Fig. 4.5) but somewhat displaced to lower Y-values. As already noted in the Ti-Zr

diagram, the GO-road lavas seem to be more evolved than pillows from the river. Pillow lavas from the lower part of the GO-road sequence plot outside of the MORB field and are, as already noted in the Ti-Zr-Y diagram, probably within-plate lavas. Pillow clasts appear to be similar to the less evolved Smith River pillows.

Diabase blocks show again a bimodal distribution with three samples being somewhat transitional to lower Y contents, while two blocks show very low Y and high Cr abundances typical for primitive arc-tholeiitic lavas.

For reference, dikes and lavas from the Josephine ophiolite are also plotted (REE data and HF, Th, and Ta are available for most of the samples). The Josephine ophiolite displays a well-known transitional geochemistry between MORB and IAT (Harper, 1984). Using Cr and Y, these representative rocks span a wider range of Cr contents at somewhat lower Y than is typical for MORB. However, a group of samples show a distinct Y-depletion and Cr-enrichment, similar to the primitive arc-tholeiites of the LRO. It is apparent that the five diabase blocks sampled from within a block-supported breccia in the LRO show the same bimodality as the lavas and dikes of the Josephine ophiolite (Ohr and others, 1986).

The Ti/Cr-Ni Diagram

The Ti/Cr-Ni diagram (Fig. 4.6) builds on the same principles applied to both the Ti-Zr and Cr-Y plots. Here a ratio of an incompatible over a compatible element is chosen as a fractionation index. This enhances the tholeiitic fractionation trend in a subparallel fashion to the Ti/Cr axis, showing a sharp increase in Ti/Cr with decreasing Ni. Along an empirical boundary IAT are clearly separated from MORB, the Ti/Cr lower in IAT at a given Ni content (Beccaluva and others, 1979).

The LRO pillow lavas define a suite of ocean floor basalts that becomes generally more evolved toward higher Ti/Cr. Diabase breccia blocks plot in the MORB field, but two samples are again displaced toward very primitive island-arc tholeiitic compositions that resemble boninitic chemistry.

Josephine samples do not reveal their strong arc-component in this diagram, although the more evolved samples show Ni values low enough to suggest a transitional character between IAT and MORB. As in the Cr-Y plot, very primitive arc volcanics suggest either the presence of two distinct magma types within the Josephine suite or derivation of the more evolved rocks from a primitive parental magma (as will be discussed below).

The Ti/V Diagram

The Ti-V diagram (Figs. 4.7 and 4.8) utilizes the variable geochemical behaviour of the transition metal vanadium in its three possible valence states. V^{3+} is predominant under conditions of low oxygen fugacity and has ionic characteristics similar to the other compatible transition metals, such as Cr, Ni, and Sc. Intermediate oxygen fugacities favor varying proportions of V^{3+} , V^{4+} , and V^{5+} , while at high partial oxygen pressure V^{5+} is the dominant valence state. This means the ionic potential of V is a strong function of the prevailing oxygen fugacity in a particular magmatic environment. The Z/r ratios for V^{3+} , V^{4+} , and V^{5+} are 8.1, 6.0, and 4.1, respectively: the oxidized phase behaves therefore like a HFS element, and the reduced V^{3+} is transitional to LFS elements.

More important, however, is the strong dependence of the crystal/liquid fractionation coefficient on the prevalent oxygen pressure. Shervais (1982) gives bulk partition coefficients for vanadium, \bar{D}_V , that vary from 0.15 ($f_{O_2} = 10^{-7}$) to about 1.15 ($f_{O_2} = 10^{-12}$), calculated for assumed refractory spinel lherzolite to harzburgite mineralogies. Thus \bar{D}_V is >1 in reducing magmatic environments and becomes $\ll 1$ for increasingly oxidizing magmatic settings. This renders oxidized V^{5+} as a incompatible element and reduced V^{3+} as a compatible

element. Since in tholeiitic rocks the partition coefficient for Ti is always $\ll 1$, the depletion of V relative to Ti can be used to assess variations in magma sources, degree of partial melting, and subsequent fractional crystallization of tholeiitic rocks from different tectonic settings (Shervais, 1982).

Upper mantle MORB sources experience partial melting under relatively reducing conditions, while more oxidizing conditions are found in many convergent margin settings (Gill, 1976; 1981). Accordingly the Ti/V ratios of primary melts increase with increasing \bar{D}_V ; Ti/V ratios also increase with decreasing fractions of melt produced (Fig. 4.7). Partial melts of a MORB source show initial Ti/V ratios of about 20-50. Similar melts produced under more oxidizing conditions have lower initial Ti/V ratios of 10-20, typical for IAT (Shervais, 1982). Subsequent olivine and plagioclase fractionation proceeds parallel to initial Ti/V trends. For clinopyroxene or spinel fractionation, Ti/V ratios increase somewhat; that is, the fractionation path crosses constant Ti/V ratio lines at low angles. Under no circumstances will silicate fractionation evolve magmas that have Ti/V ratios lower than the primary melt (Shervais, 1982).

Pillow basalts from the LRO define two distinct trends of Ti/V ratios: 1) Smith River pillows with Ti/V = 22-30,

and 2) GO-road pillows with $Ti/V = 40-50$ (Fig. 4.8).

According to Fig. 4.7 there are three possible explanations to account for this observed difference:

- The higher Ti/V ratios of the GO-road pillows are due to a smaller degree of partial melting of the same source under reducing conditions (melting trend 2, with 20% and 10% melting of a MORB source, respectively).
- The lower Ti/V ratios of the Smith River pillows could be alternatively explained by partial melting of a somewhat more oxidized source than typical for MORB (melting trend 3, 10% melting in an IAT setting).
- The higher Ti/V ratios are due to the onset of cpx fractionation that will displace initial Ti/V toward higher values.

This means pillow lavas within the LRO have either the same source, but melting conditions are variable, or have different sources. The similar stratigraphic position of both pillow sections with respect to the overlying mudstone or tuff sequence favors the former hypothesis, possibly an effect of decreased melting in the vicinity of a fracture zone (Bender and others, 1984; Fox and Gallo, 1984; see section 2.1).

Three of the diabase blocks plot along the same trend as the pillow basalts from Smith River having Ti/V ratios

of 24-28 (Fig. 4.8). However, two other diabase clasts show very low Ti/V ratios, coinciding with primitive island-arc rocks from the Josephine ophiolite that have equally low Ti/V ratios of 10-16. The high Ti/V diabase clasts may or may not be related to the pillow basalts: Fig. 4.7 offers again speculative explanations of either different source areas (melting trends 2 and 3), or increased melting of a reducing MORB source. The primitive low-Ti rocks with near chondritic Ti/V ratios can be modeled in either of two ways: 1) extensive melting followed by olivine and plagioclase fractionation of a source represented by melting trend 3, or 2) less extensive melting and negligible subsequent fractionation of the initial melt (melting trend 4). However, the JO samples with very low V concentration still would require unrealistically extensive melting of more than 50% of an undepleted mantle source. Again it seems most likely that these rocks were derived from an already depleted source with correspondingly lower Ti and somewhat lower V concentrations.

The remaining samples from the Josephine ophiolite have Ti/V ratios of 18-24 and are transitional between MORB and IAT. They must have been derived from sources indicated by melting trends 2 or 3, or have evolved from primitive lavas by extensive clinopyroxene fractionation (Fig. 4.7).

- Figure 4.2 The Ti-Zr diagram after Pearce and Cann (1973).
- Figure 4.3 The Ti/100-Zr-Yx3 diagram after Pearce and Cann (1973).
- Figure 4.4 Petrogenetic modelling in the Cr-Y diagram (modified from Pearce, 1982).
- Figure 4.5 The Cr-Y diagram after Pearce (1980).
- Figure 4.6 The Ti/Cr-Ni diagram after Beccaluva and others (1979).
- Figure 4.7 Petrogenetic modelling in the Ti-V diagram (modified from Shervais, 1982).
- Figure 4.8 The Ti-V diagram after Shervais (1982).

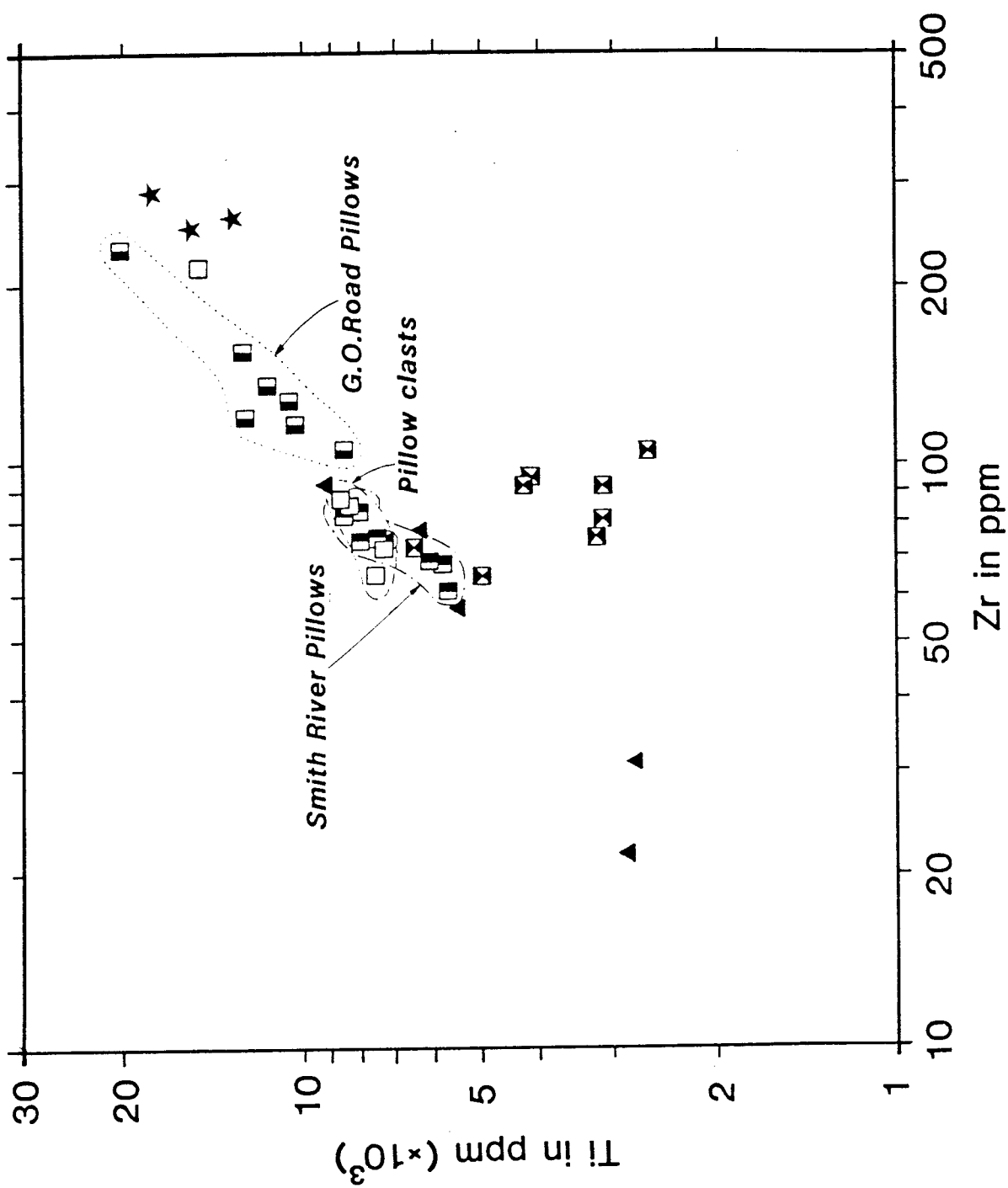


Figure 4.2

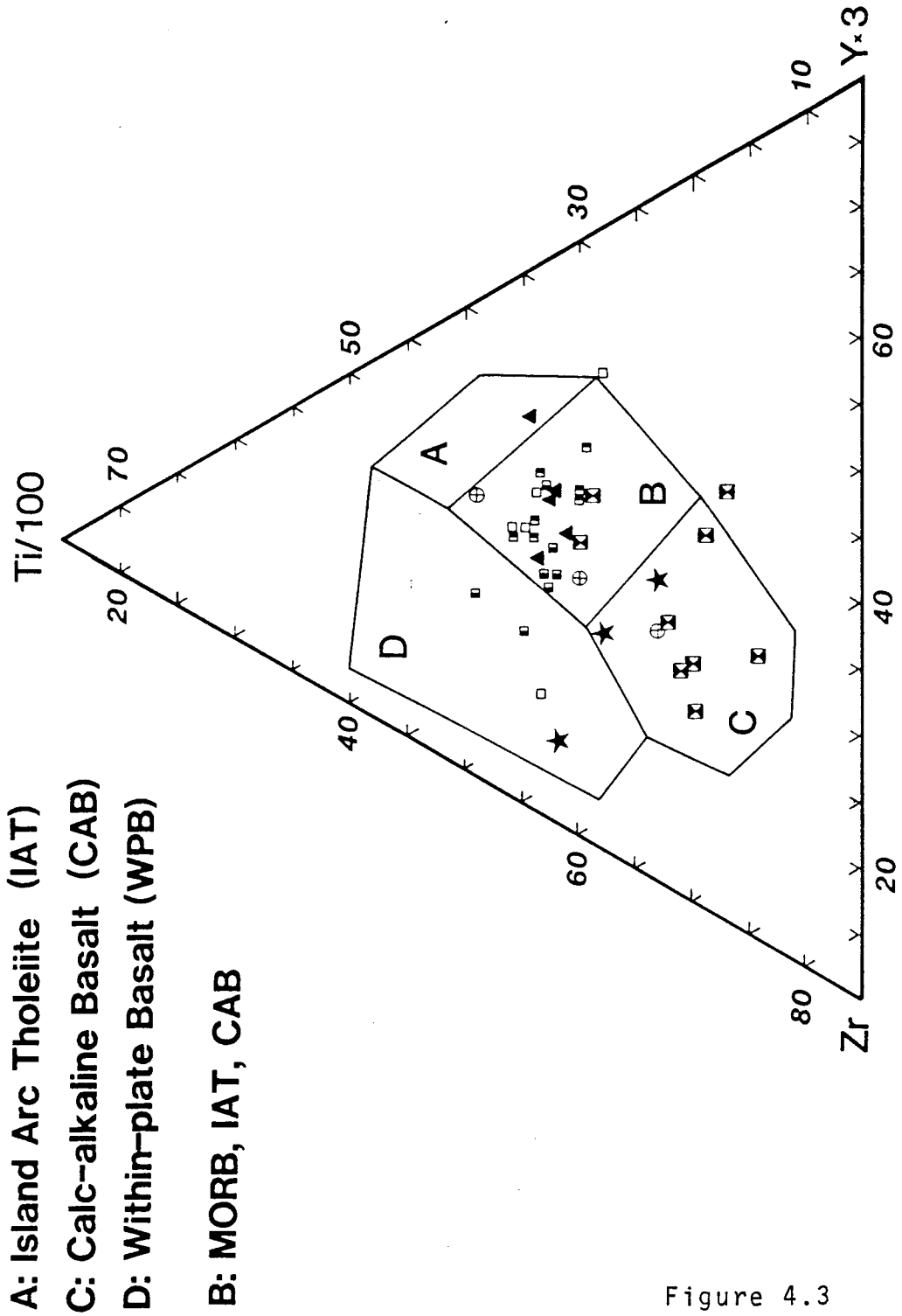


Figure 4.3

- 1) higher degree of partial melting
 - - - 2) residual minor phases
 - - - 3) repeated melting
 - - - 4) mixing with subduction zone component

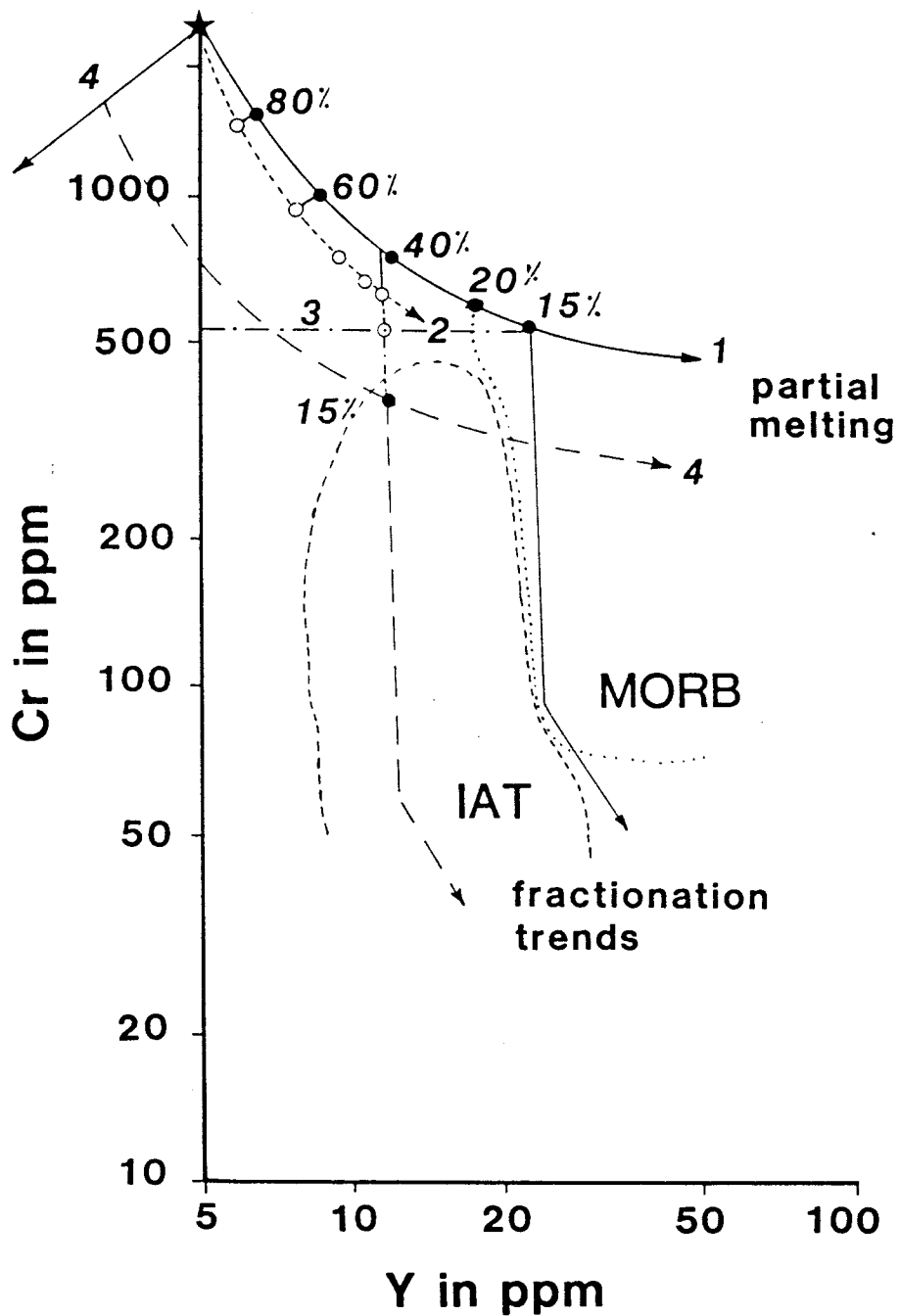
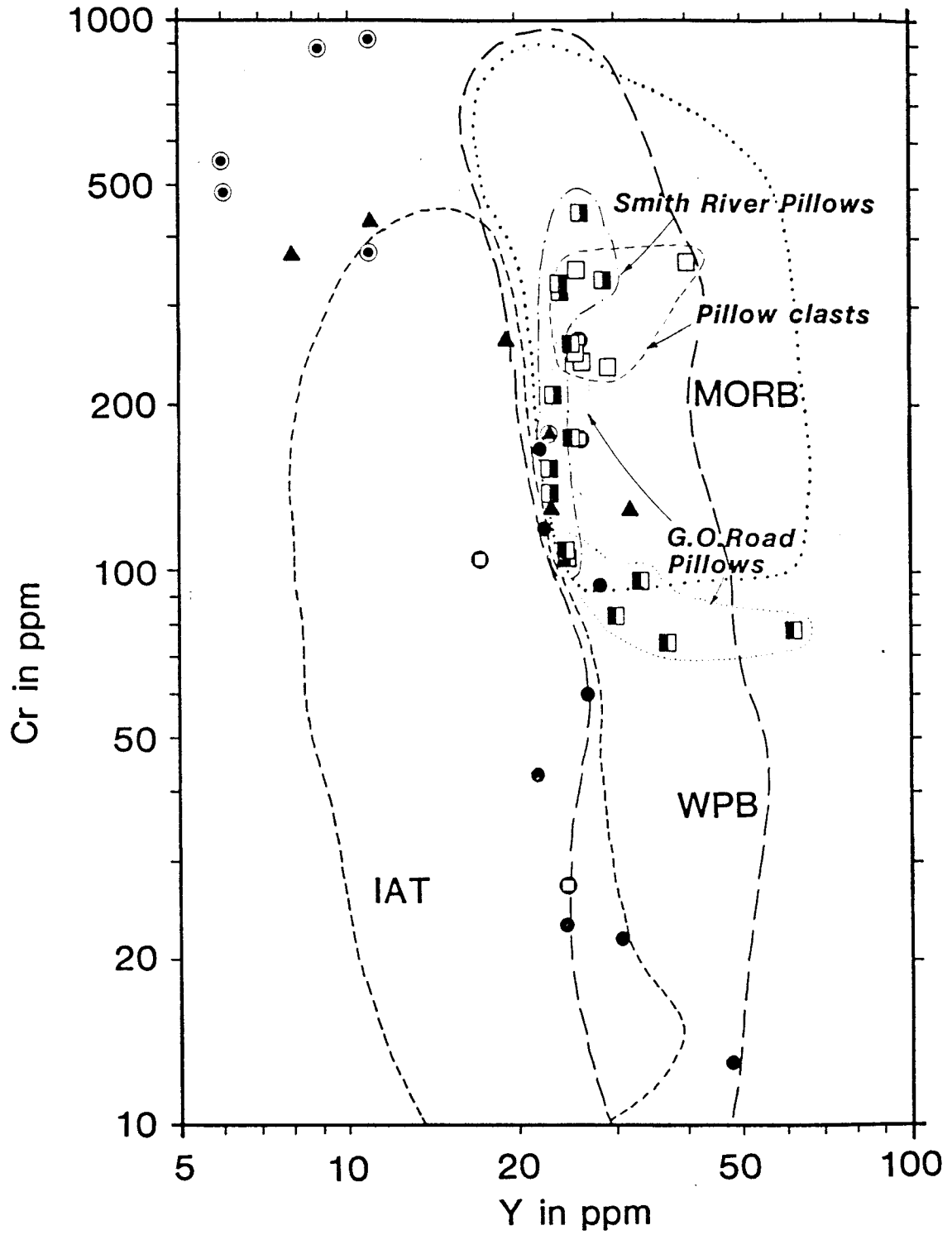


Figure 4.4



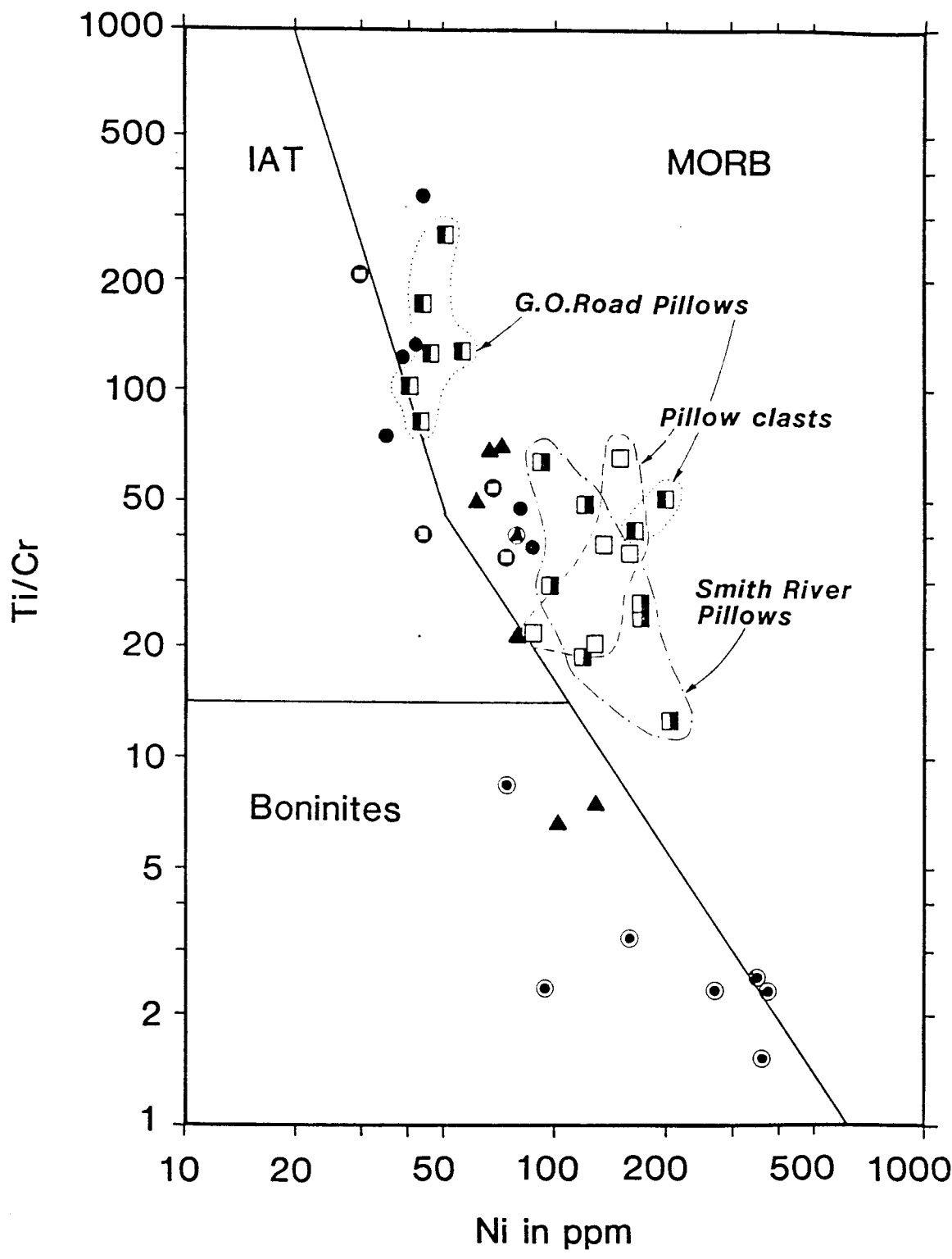


Figure 4.6

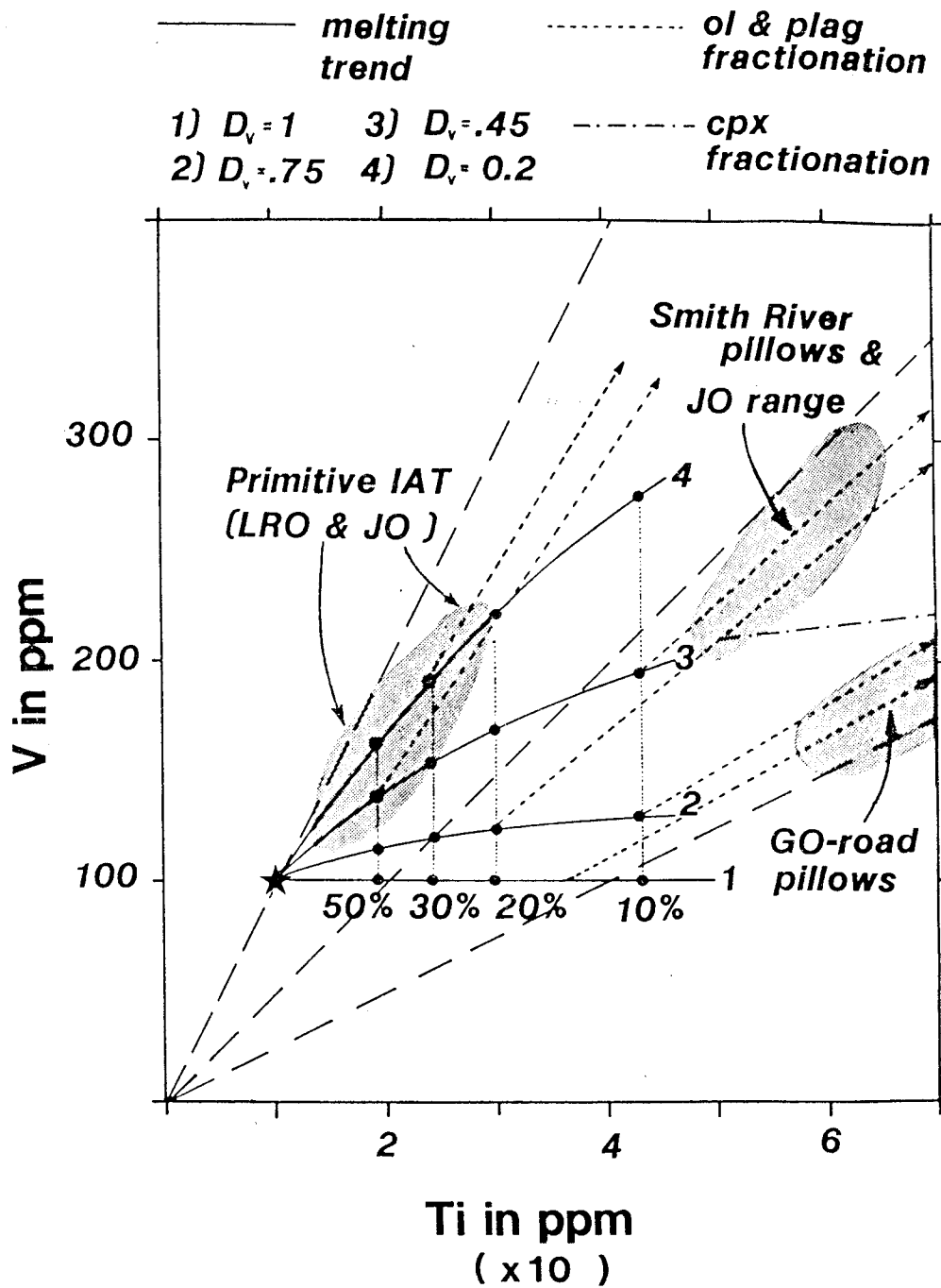


Figure 4.7

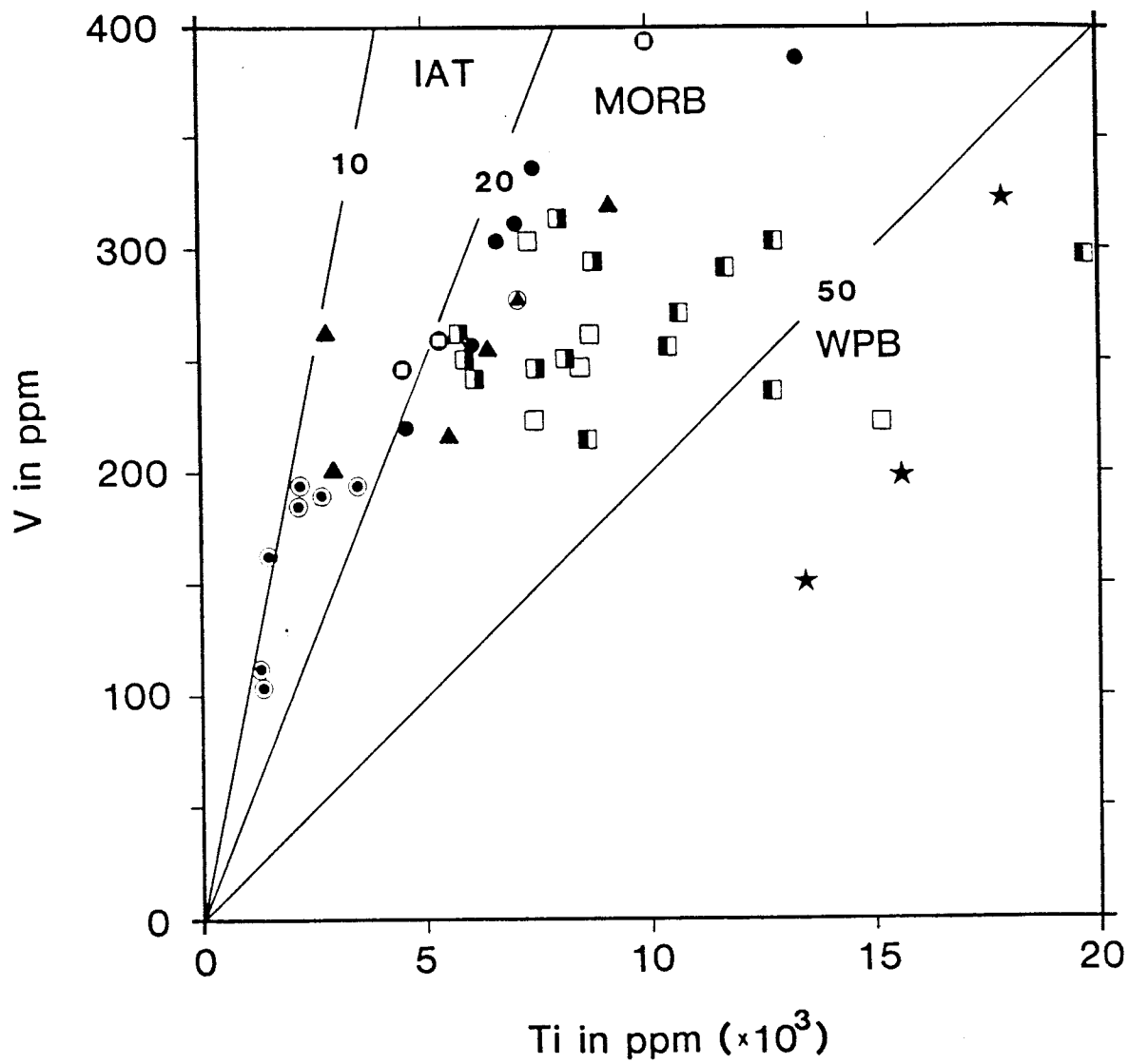


Figure 4.8

4.3. N-MORB normalized trace element patterns

The need for a more powerful means to distinguish between rocks of MORB and IAT parentage is obvious. Even a discussion that went beyond an empirical discrimination of ophiolitic rocks in the preceding diagrams left several questions unresolved:

- Are pillow lavas from the Lems Ridge olistostrome chemically related to dikes and lavas from the Josephine ophiolite?
- Are the differences between LRO pillow suites due to differences in source composition, or rather related to effects of melting and fractionation?
- Are dike blocks from the Buck Mountain breccia similar to the LRO pillows, to the Josephine suite, or to both?
- Are the less evolved dikes and lavas from the Josephine ophiolite and from the LRO parental to the main suites, or do they represent a discrete magma type?
- And finally, there is a question not yet touched upon: what is the chemical signature of the huge gabbro blocks and of the sparse mafic dikes that intrude these blocks? How are they chemically related to the ophiolitic lithologies of both the LRO and the Josephine ophiolite?

All of the preceding diagrams utilize the enrichment or depletion of HFS elements with respect to some fractionation index to discriminate between MORB and IAT magmas. This is indeed one distinguishing feature of island-arc lavas. However, much more prominent is the enrichment in elements with low ionic potential, that is the LFS elements, relative to HFS elements. In fact, the first studies that delineated different rock series in island-arcs (Gill, 1970; Jakes and White, 1971) showed the enrichment in LFS elements as the prime feature of tholeiitic island-arc rocks relative to MORB. This enrichment can be readily recognized in fresh or unaltered rocks. Ophiolitic rocks, however, have generally undergone extensive hydrothermal alteration that primarily affects the more mobile LFS elements, thus obliterating whatever primary LFS signature there was. Th seems to be the only immobile LFS element; therefore ratios of Th over incompatible HFS elements are valuable indicators for enrichment trends operating at convergent plate boundaries. In addition, in island-arc rocks Ta is generally depleted with respect to Th and the LREE (Kay, 1980; Saunders and others, 1980; Thompson and others, 1984), while tholeiitic ocean floor basalts do not show a decoupling of Ta from Th and the LREE. Unfortunately these critical elements have very low abundances which cannot be detected with standard XRF methods: only the recent

widespread use of neutron activation analyses has provided the needed precision to determine these element abundances and to put them into a petrogenetic context.

MORB-normalized trace element plots usually contain a complete suite of incompatible LFS and HFS elements. For this study the following elements were used, with decreasing incompatibility: Ba, and Th (as LFS), Ta, Ce, Zr, Hf, Sm, Ti, Y, Yb (all HFS elements; Ce-Sm-Yb indicating REE fractionation trends), Cr, and Ni (as fractionation indices). The rationale behind using these incompatible elements is that major changes in the shapes of patterns result from enrichment or contamination processes affecting the sources of the basalts in question, whereas melting and fractionation only affect the level of a pattern but have little effect on its shape (Pearce, 1983).

N-MORB normalized trace-element patterns have the potential to display characteristic patterns for 1) normal and enriched ocean floor basalt (E-type MORB), 2) island-arc tholeiites, 3) rocks belonging to the calc-alkaline series, and 4) alkaline and tholeiitic within-plate basalts. The distinguishing features between these rock types are summarized below. In Fig. 4.9 the resulting geochemical patterns are shown. The subsequent presentation of rock suites from the LRO and the Josephine

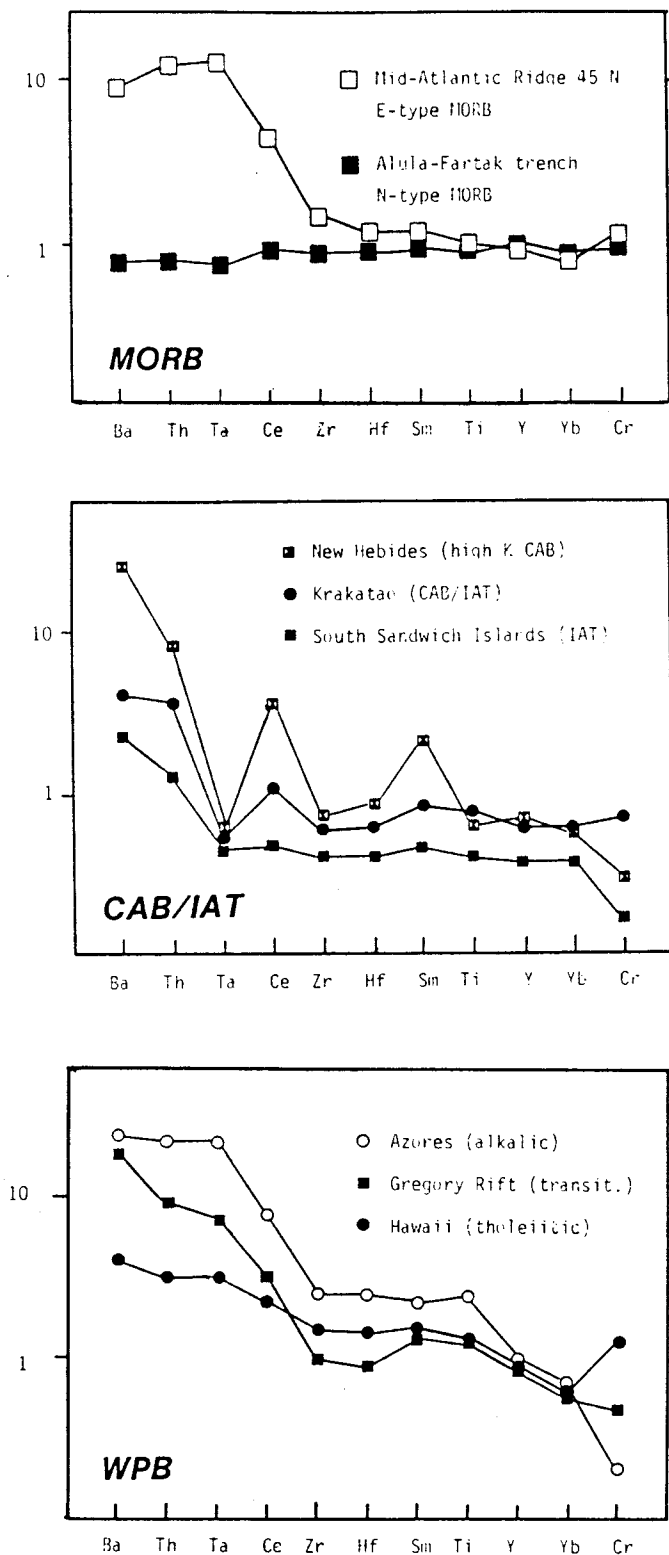


Figure 4.9

MORB normalized trace element patterns for (a) MORB, (b) island-arc tholeiites and calc-alkaline basalts, (c) within-plate basalts (modified after Pearce, 1982).

ophiolite (Figs. 4.10-4.20) will then serve to classify them further with respect to their tectonomagmatic setting, and will discuss the mutual relationships of these rocks in their tectonic context.

N-type MORB (Sun and others, 1979) shows low abundances of the highly incompatible elements Rb, K, Ba, Th, Ta, La, Ce (the more "hygromagmatophile" (HYG) elements of Wood and others (1979)). These low abundances with respect to the less incompatible (or less HYG elements) elements Hf, Zr, Ti, Y, HREE actually require melt extraction from a previously depleted source (Gast 1968, O'Nions and others, 1977). REE patterns therefore are LREE depleted and have La/Sm_N and La/Yb_N ratios lower than chondritic. N-MORB normalized trace-element plots show of course flat patterns close to unity.

T- and E-type MORB (also termed P-MORB (Schilling, 1975)) have higher abundances of the LFS and the more HYG elements with respect to the less HYG elements. REE patterns display flat (T-type) to concave upward (E-type) patterns. Trace element patterns show enrichment in LFS elements and more HYG elements such as Ta and the LREE; that is, Th and Ta are not decoupled from each other and occur in about the same proportions. The remaining less HYG elements define a flat trend parallel to the normalizing line. A combination of mantle depletion and

repeated re-enrichment by the addition of a volatile incompatible-rich component has been proposed to account for this selective enrichment in E-type MORB (Sun and others, 1979). Alternatively, a combination of source heterogeneity and decreased extents of partial melting of a depleted MORB source have been suggested (Bender and others, 1984). In either case, a significant fractionation of LREE and HREE during melting occurs only under special circumstances, such as equilibrium batch melting (Shaw, 1970), or the presence of phases such as garnet that retain the HREE in the residuum together with very small degrees of partial melting.

Island-arc tholeiites are characterized by low abundances of the elements Ta through Yb, while the LFS and Th are selectively enriched. It is generally agreed that this selective enrichment is caused by metasomatism of the mantle source by fluid phases rich in LFS elements (the "subduction component" of Pearce 1983). Those aqueous fluids are thought to be derived from dehydrating subducted oceanic crust and sediments (Best, 1975; Hawkesworth, 1977; Saunders and Tarney, 1979; and Kay, 1980). The selective depletion of Ta and Ti, as well as the relative depletion of all HFS elements with respect to the LFS elements, however, is somewhat more controversial. It is proposed that the retention of small and high-charged elements in the dehydrated oceanic crust alone could produce the high

LFS/HFS ratios observed in arc-basalts (Anderson and others, 1979). The prevailing low HFS abundances can also be explained by repeated melt extractions from a mantle source that is only buffered by continuous LFS-element transfer from the subducting slab, thus leading to a net decrease of HFS in the source (Saunders and Tarney, 1984). Characteristic negative Ta and Ti anomalies could be due to the stability of titaniferous minor phases under higher oxygen and volatile pressures (Saunders and others, 1980), or might be related to the high La/Ta ratios in subducted oceanic sediment (Kay, 1980). This model suggests that subducted sediment is a significant contributor of LFS elements and LREE that are added to the source of island-arc lavas. In such a way enriched upper mantle therefore inherits high LREE/Ta and Th/Ta ratios from subducted oceanic sediments. A source area that is most compatible with the outlined enrichment and depletion features would be a refractory upper mantle peridotite which experienced a previous melt extraction and is modified by LFS-rich hydrous fluids or melts derived from the subducted oceanic slab. REE patterns of IAT are usually flat with chondritic La/Sm_N and La/Yb_N ratios which is, considering the continuum of depleted to enriched MORB patterns, of minor discriminant significance. MORB normalized plots, however, show enrichment in Ba, Th, and sometimes Ce, while the HFS form a flat trend parallel to,

but at a lower level than the MORB line. Slight negative anomalies in Ta and Ti are typical. It thus appears that the most effective distinction between IAT and MORB can be made using ratios like Th/Ta and La/Ta (Joron and Treuil, 1977) or Th/Yb and Ta/Yb (Pearce, 1982).

Calcalkaline patterns are, like IAT patterns, selectively enriched in LFS elements, but the magnitude of this enrichment is much greater (Pearce, 1983). In addition to the water-soluble LFS elements, the LREE are also enriched, suggesting that melt components participate in the enrichment processes (Crawford and others, 1986). The HREE and Y no longer behave as incompatible elements and are readily accommodated in crystallizing phases during the fractionation to intermediate and acidic calc-alkaline rocks (Baker, 1982). Pronounced negative Ta and Ti spikes are probably due to the early onset of magnetite fractionation, where Ta is incorporated in titaniferous stable phases. An alternative model is put forward by Kay (1980), relating calc-alkaline arc magmatism to extensive melting of subducted sediment. The high La/Ta ratios of pelagic sediments would be inherited by the resulting calc-alkaline magmas, explaining Ta depletion which at times occurs not correlated to a similar Ti depletion (Kay, 1984; Thompson, 1984). In contrast to the generally flat REE patterns of IAT, calc-alkaline rocks show strong fractionation of rare earth elements, expressed in very

high LREE/HREE ratios.

Within-plate basalts show dramatic enrichment for all elements except the least incompatible HREE and Y. Therefore REE patterns have a concave upward shape with very high La/Sm_N and La/Yb_N ratios. Trace element plots show the strongest enrichment for the most incompatible elements. For some continental rift basalts there are negative Hf and Zr spikes reported (Baker and others, 1977), but usually the enrichment pattern is not very sensitive to discern between continental and oceanic within-plate basalts (Pearce, 1982).

It should be possible to assess the questions raised at the beginning of this section by comparing the shape of the patterns for rocks that were analyzed for their complete trace-element spectrum by XRF and INAA. Element patterns for calc-alkaline tuffaceous rocks, alkaline within-plate basalts, tholeiitic pillow lavas and dikes, and tentatively for gabbro blocks in the LRO are discussed below.

Tuffaceous Greenstones

The geochemical patterns of two tuffaceous greenstones, LR 70 and LR 113, from the pyroclastic matrix of the LRO are shown in Figs. 4.10a and 4.10b. Both samples are fine grained, and original components are largely

replaced by quartz, calcite, epidote, and chlorite. From other chemical evidence (e.g. Fig. 4.4, and Fig. 4.5) it is inferred that these and similar greenstones are calc-alkaline. Despite extensive recrystallization, both samples show similar REE- and trace-element patterns. The LREE enrichment is 24 to 28 times chondrite and the LREE are preferentially enriched relative to the HREE. The corresponding La/Yb_N ratios are 4.0 and 4.3, respectively, which is typical for calc-alkaline basalts (Gill, 1981). Both samples also define a typical calc-alkaline trace-element pattern (compare Figs. 4.9 and 4.10b) with selective enrichment of Ba, Th, and the LREE relative to the less incompatible HFS elements. The depletion of Ta and Ti seems to be correlated. Cr and Ni contents are low to intermediate, consistent with an enhanced calc-alkaline fractionation. Thus it appears that 1) the regional low grade metamorphism, and the widespread alteration did not affect the pattern of the immobile elements used (Ba may be an exemption), and that therefore 2) the diagrams can be used to provide useful information on altered magmatic rocks. The calc-alkaline tuffaceous component of the LRO clearly reflects the presence of an active mature volcanic arc in close proximity to the depositional basin of the olistostrome.

Volcanic Clasts

Volcanic clasts that are extremely vesicular and resemble mafic scorias were already classified as alkaline to transitional basalts by virtue of their high Nb/Y ratios. They also show Zr/Y and Ti/V ratios that are typical for alkaline within-plate lavas. Their REE patterns (Fig. 4.11a) display a broad, but regular range of slightly upward concave shape which is characterized by a very strong enrichment in LREE relative to HREE. La/Sm_N and La/Yb_N ratios are 2.5-3.8, and 10.8-12.6 respectively. The very high abundances of LREE in alkaline rocks are thought to be the consequence of derivation from undepleted source regions through relatively small degrees of melting at depth. Recycled crustal material rich in incompatible elements may also contribute to this enrichment (Thompson and others, 1984). In a MORB-normalized diagram (Fig. 4.11b), the clasts define a range that is characterized by a strong enrichment of most incompatible elements. Only Y and Yb show more variation, but are generally depleted with respect to the other elements. A negative anomaly for Hf and Zr is apparent for two samples. Both patterns substantiate the previous finding that the volcanic clasts in the pebbly mudstone section indicate the presence of alkaline volcanism in the vicinity of the LRO-basin and, because of their fragile nature, are inferred to have

erupted contemporaneously with deposition of the olistostrome. Alkaline magmas are rare, but do occur in mature oceanic and continental arcs; on the other hand they could be related to the initial rifting of the mid-Jurassic arc to the east, prior to the opening of the Josephine back-arc basin (Harper and Wright, 1984). Allan (1986) describes the occurrence of associated alkaline and calc-alkaline lavas during the initiation of arc-rifting in the Mexican volcanic belt, southwest Mexico. However, other authors designate primitive island-arc tholeiites and boninites as the initial products of back-arc extension (Crawford and others, 1986; Cameron and others, 1979).

Pillow lavas from the base of the LRO

The elemental abundances of pillow lavas from the basal portion of the LRO (Z 47b, Z 49, and LR 17), are shown in Fig. 4.12. Samples Z 47b and Z 49 show a LREE enriched pattern (Fig. 4.12a) that is typical for E-type MORB. La/Yb_N ratios are 2.2 and 2.1, respectively. They show Th/Ta ratios of about 1, and low ratios of HFS elements over both Th and Ta (Fig. 4.12b). E-type MORB is known to show LREE- and LFS enrichment without decoupling of Th and Ta (Fig. 4.9). Sample LR 17 displays an unfractionated REE patterns with a La/Yb_N ratio of 1.0, similar to T-type MORB and tholeiitic island-arc lavas.

Since Ta is not depleted with respect to the LFS elements, and since the LFS elements are enriched compared to the less incompatible HFS elements, a T- or E-type MORB origin can be inferred for LR 17 as well.

Returning to Fig. 4.8 it is now possible to decide on the cause for the distinctness between GO-road pillow lavas (Z 47b, Z 49) and Smith River pillow lavas (LR 17). Both suites were apparently extracted from the same E-MORB source (trend 2 in Fig. 4.8), but the pillow sequence along the GO-road experienced an unusual low degree of melting. The higher contents in incompatible elements such as Ti and Zr for the GO-road pillows are therefore not necessarily due to enhanced fractionation, but might as well be explained by this lower extent of melt extraction. The same holds for the lower Cr and Ni contents. One ocean-floor setting where enriched basaltic lavas are produced occurs in the vicinity of fracture zones. There depressed thermal gradients do not allow large degrees of melting (see chapter 2.1, and references therein).

Pillow clasts in the LRO

Two pillow clasts (LR 67, Z 51) show very distinct REE patterns (Fig. 4.13a). LR 67 is similar to the enriched lavas along the GO-road and shows a strong LREE enrichment, with a La/Sm_N ratio of 2.6, and a La/Yb_N ratio of 4.0. The

highly concave upward shape of the pattern might be due to selective enrichment of La during hydrothermal alteration and palagonitization, since no known enrichment, melting, or fractionation process can explain for a 50% enrichment of La over Ce. Ce reflects probably the original LREE enrichment, even though it appears that Ce is too high with respect to the other HFS elements. Comparison with fig. 4.9, however, shows that high Ce contents are not atypical for E-type MORB. Z 51, a large olistolith immediately overlying the continuous GO-road pillow-sequence, is markedly LREE depleted ($La/Yb_N = 0.59$) and appears to be similar to N-type MORB. The complete trace-element spectrum (Fig. 4.13b) is somewhat inconclusive, in that the crucial elements Th and Ta are either below detection limit (Th), or are estimated ($Ta = [Nb] \times 19$). Nevertheless, the flat, unenriched pattern favors an interpretation consistent with a normal ocean floor basalt. Pillow clasts resemble, 1) the enriched character of the basal pillows and pillow-breccias, and 2) show also N-type MORB varieties. Higher Cr and Ni contents are consistent with a more primitive chemistry.

In summary, all pillow basalts from the LRO are mid-ocean ridge basalts displaying various degrees of enrichment, and as a group are very different from lavas and dikes from the Josephine ophiolite, which carry a

distinct arc component (see below).

Diabase Blocks in the LRO: A Comparison to Dikes and Lavas from the Josephine Ophiolite

Diabase blocks from the LRO show a bimodal distribution in the discriminant diagrams that were employed in Figs. 4.2 through 4.8, much like the selected Josephine dikes and lavas. Since the majority of the JO rocks shows a strong arc component (Harper, 1984, and unpublished data), it is worthwhile to speculate about an arc-related origin of these dikes contained in the talus breccia from Buck Mountain. Information derived from the previous diagrams, however, is somewhat inconclusive, because the diabase blocks plotted almost indistinguishably from the LRO-pillows, which are recognized as E-type MORB.

In Figs. 4.14 and 4.15 three LRO-diabase samples are compared to a suite of dikes and lavas from the Josephine ophiolite by means of their geochemical patterns. The JO suite displays a broad but regular REE pattern (Fig. 4.14a) that is slightly convex upward. The LREE and HREE ends are both tilted somewhat downward to indicate slight depletions. La/Sm_N ratios are 0.8-0.9, La/Yb_N are 1.0-1.2, and ratios of Sm/Yb_N are therefore 1.2-1.3. Crawford and others (1986), and Weaver and others (1979) describe the petrology of basalts erupting in the earliest stages of

back-arc spreading in the Marianas arc and Brainsfield Strait and report similarly bent REE patterns. They give ratios of $\text{La}/\text{Sm}_N = 0.8$, $\text{La}/\text{Yb}_N = 1.1$, and $\text{Sm}/\text{Yb}_N = 1.4$ (Crawford and others, 1986), much like the samples from the Josephine ophiolite. This is perhaps not too surprising, since Harper (1984) and Harper and Wright (1984) already inferred a back-arc basin origin for the Josephine ophiolite based on regional geology, geochronology, sedimentary petrography and geochemistry of dikes and lavas. The enrichment of early back-arc basin basalts in LREE and LFS elements relative to N-type MORB, however, is not persistent throughout the spreading life of a back-arc basin (Crawford and others, 1981), and mature marginal basins generally erupt more LREE depleted lavas very similar to N-type MORB (Gill, 1976; Hawkins, 1979, Weaver and others, 1979). The Josephine basin was probably too short lived to develop typical N-type MORB magmas. This interpretation is supported by the trace element pattern shown in Fig. 4.14b. Enrichment in Ba, Th, and Ce contrast with depletions in Ta and Ti along with a somewhat depleted but flat trend of the other incompatible elements. This is very similar to IAT patterns in fig. 4.9 and consistent with a derivation of these rocks from a previously depleted mantle source that underwent subsequent enrichment related to the subduction process. The chemical evidence presented in Figs. 4.14a and 4.14b nicely supports the interpretation

that the JO represents a well preserved supra-subduction zone ophiolite (Harper and Wright, 1984) in the sense of Pearce and others (1984).

Two of the LRO diabases, LR 3a and LR 5, define a REE range identical to the JO samples, and show the same enrichment and depletion trends with La/Sm_N , La/Yb_N , and Sm/Yb_N ratios of 0.8, 1.0, and 1.2, respectively. LR 3a and LR 5 also show a very similar trace-element pattern to the JO samples, except that Th/Ta ratios are smaller, but nevertheless significant for an island-arc related origin. Based on their trace-element geochemistry, those diabases from the LRO having higher Ti and Zr can be correlated with the basaltic rocks typical of the Josephine ophiolite.

A third diabase sample, LR 575, is chemically different and shows a distinctly LREE depleted REE pattern without depletion on the HREE end. It is identical to rocks dredged from the intersection of the Yap and Marianas trenches (Crawford and others, 1986), in that it shows a very low La/Yb_N ratio of 0.4, and a Sm/Yb_N ratio of 1.1. Crawford and others (1986) interpret these rocks as very primitive island-arc tholeiites that -- since there are no LREE involved in the metasomatism -- reflect the unmodified, depleted source peridotite. Enrichment is restricted to water-soluble elements such as Ba and Sr, but at lower levels than for typical IAT. Other arc-related volcanics (calc-alkaline basalts, island-arc tholeiites,

and boninites) all show LREE enrichment with respect to their depleted upper mantle sources, suggesting that both slab-derived hydrous fluids and silicate melts participate in the metasomatism process. For the most primitive IAT it appears therefore likely that dehydration of the subducting slab took place at shallow levels of less than 50 km (Crawford and others, 1986), and therefore did not involve partial melting of subducted crust and sediment needed to transport LREE into the overlying mantle. These primitive IAT would therefore erupt near the trench at the initiation of subduction or during major reorganization of a convergent boundary setting.

As noted above, the Josephine also contains very primitive basalts (A 20, R 20, Y 5), which were not included in Figs. 4.14a and 4.14b. Their REE patterns are shown in Fig. 4.15a: while A 20 has a pattern much like LR 575 with a slight LREE depletion, R 20 and Y 5 resemble more the broad U-shape of boninites (Sun and Nisbett, 1978; Cameron and others, 1979; Hickey and Frey, 1982). This U-pattern reflects the mixture of two distinct components: a LREE and incompatible element rich hydrous component is added to a extremely depleted harzburgite component (Sun and Nisbett, 1978; Pearce and others, 1984). An alternative model relates the formation of boninitic rocks to low pressure interaction of N-type MORB and harzburgite in a

subcrustal magma chamber (Johnson and others, 1986; Fisk and Abott, 1986). The trace element pattern of boninites shows an accentuated IAT pattern, with a very strong depletion in HFS elements, creating a bowl-shaped pattern. Boninites have Ti and HREE contents lower than of fertile peridotite (Hickey and Frey, 1982): this implies either depletion or retention of these elements in the mantle source. Unusually low Ti/Zr ratios for boninites of 40-70 support the latter, inferring that the crystal/liquid distribution coefficient for Ti is greater than for Zr due to the presence of retentive phases in the residuum.

Boninites are thought to be associated with tholeiitic basalts of MORB affinities, both produced during the inception of back-arc basin development (Crawford and others, 1981). It is therefore plausible that these primitive JO basalts are not parental to the more evolved JO dikes and lavas, but represent one end member of a mixing between the two distinct magma batches of boninitic (?) and N-MORB affinity. This possibility will be further explored in the Hf/3-Th-Ta diagram (Fig. 4.17 and 4.18) of Wood and others (1979).

In the MORB-normalized diagram of Fig. 4.15b it can be seen that LR 575 is distinct from A 20, Y 5, and R 20, in that it is not depleted in Ta and Ti with respect to the other HFS elements. In addition, LR 575 differs from R 20 and Y 5 in that it is low in Th. LR 575 could therefore

represent a very primitive IAT which has not experienced the addition of melt components from the subducting slab, as suggested above. Y 5 and R 20 both show Ta and Ti depletion, as well as Th enrichment and are more typical for arc rocks. A 20 appears to be transitional between LR 575 on the one hand, and Y 5 and R 20 on the other hand. A progressively maturing subduction process could perhaps cause a sequential eruption of very primitive IAT (LR 575) to more enriched rocks of boninitic affinities (Y 5, R 20).

Gabbro Blocks

Figs. 4.16a and 4.16b give some information on the geochemistry of the huge gabbro olistoliths that are so abundantly dispersed in the LRO. Both LR 10 and LR 36 show LREE enriched REE patterns ($La/Sm_N = 0.8$ and 1.0 , $La/Yb = 2.2$ and 1.8). The low La/Sm ratios with respect to the high Sm/Yb ratios suggest that La and/or Ce was mobile during the intensive secondary alteration of these rocks. Along with the trace-element evidence from Fig. 4.16b the gabbros can be interpreted as arc-related plutonic rocks, showing the usual high Th/Ta and LFS/HFS ratios. In particular Ti, Y, and Yb seem to be depleted, suggesting that the gabbros represent late stage fractionation products whose HREE were preferentially partitioned into early cumulus phases. Whether the hornblende gabbros are related to arc magmatism

active during the deposition of the LRO (represented by the tuffaceous matrix) is uncertain, but this will be illuminated by assigning $^{40}\text{Ar}/^{39}\text{Ar}$ ages to these gabbro blocks in chapter V.

The main point to make in this context concerns the relationship between a mafic dike and its host rock LR 10. The dike LR 11a shows an enriched pattern for Ba, Th, and Ta, with a somewhat depleted but flat trend for the remaining HFS elements, very different from LR 10 and LR 36. Rather, LR 11a is geochemically identical to pillows that outcrop just a few hundred meters downstream along the Smith River, and which were recognized as E-type MORB (see Fig. 4.16b and compare to Fig. 4.12b). It is tempting to correlate these dikes with the extrusive pillow sequence downstream. The dikes could represent sparse feeder dikes to the pillow lavas, a speculation that will be dealt with in more detail in chapter VI.

4.4 The Hf-Th-Ta Diagram

All geochemical information can be conveniently summarized in a ternary Hf/3-Th-Ta diagram (Fig. 4.17), first proposed by Wood and others (1979). While Th/Ta ratios discriminate divergent and intraplate settings from destructive margin settings, the Hf/Ta ratio places

(a) Chondrite normalized REE plots, and (b) N-MORB normalized trace element plots for:

- Figure 4.10 Tuffaceous greenstones in the LRO.
- Figure 4.11 Scoria clasts from pebbly mudstone within the LRO.
- Figure 4.12 Basal pillow lavas from the LRO (both Smith River and GO-road).
- Figure 4.13 Pillow clasts from pebbly mudstone within the LRO.
- Figure 4.14 Diabase blocks from LRO compared to typical mafic dikes and lavas from the Josephine ophiolite.
- Figure 4.15 Primitive dikes and lavas from the Josephine ophiolite compared to a primitive diabase block from the LRO.
- Figure 4.16 Gabbro blocks from LRO and a diabase dike intruding in such a block.

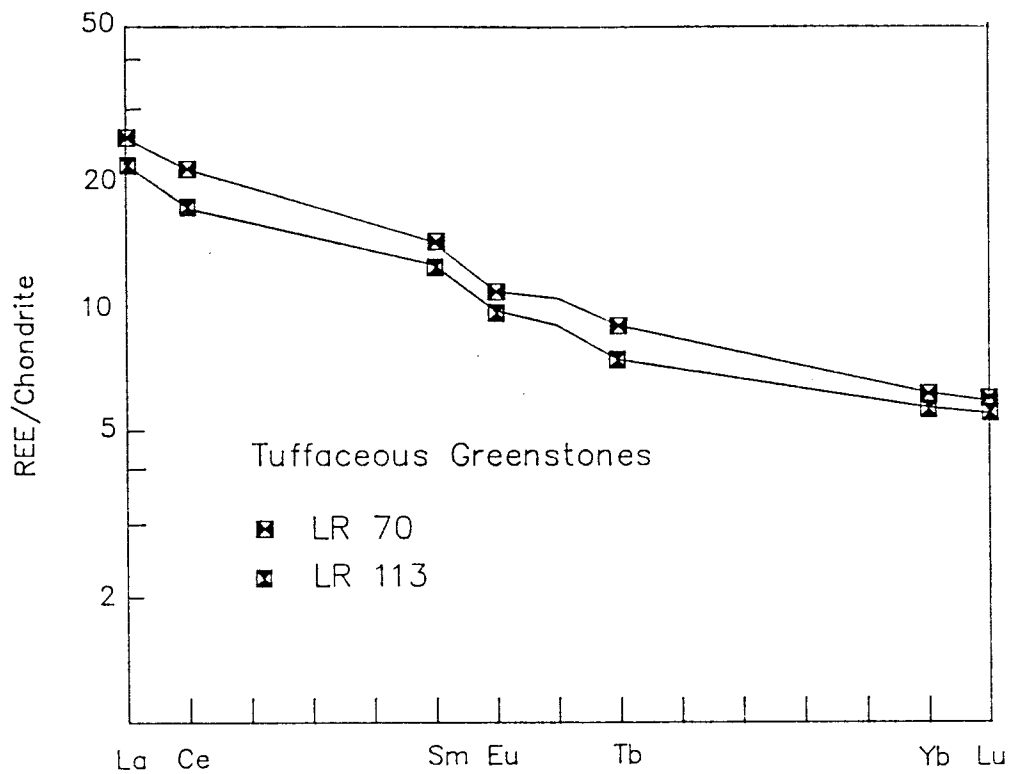


Figure 4.10 a

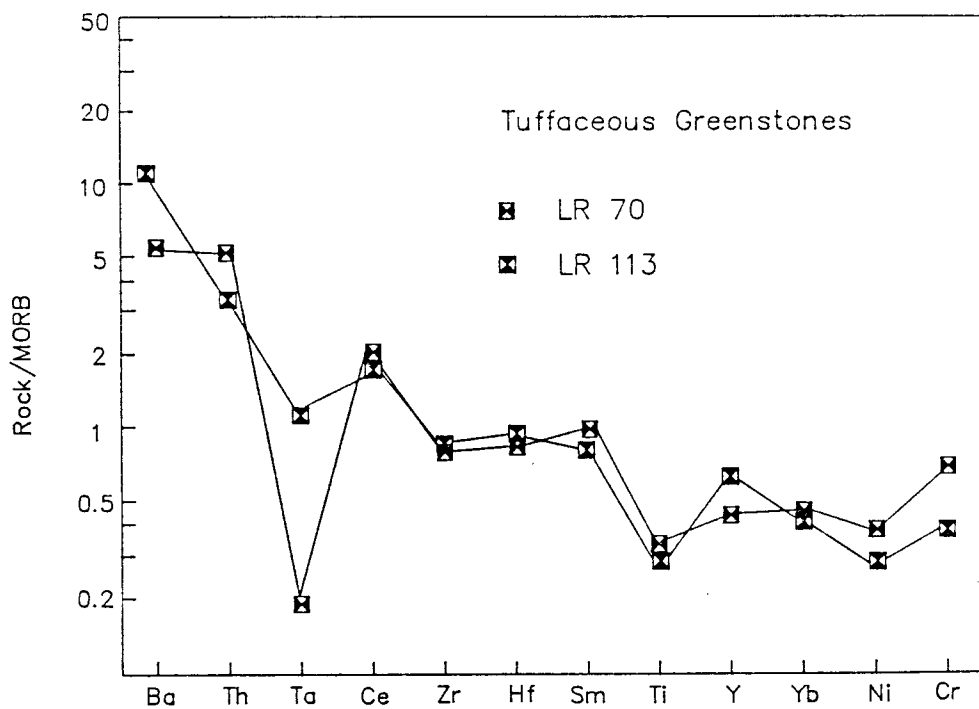


Figure 4.10 b

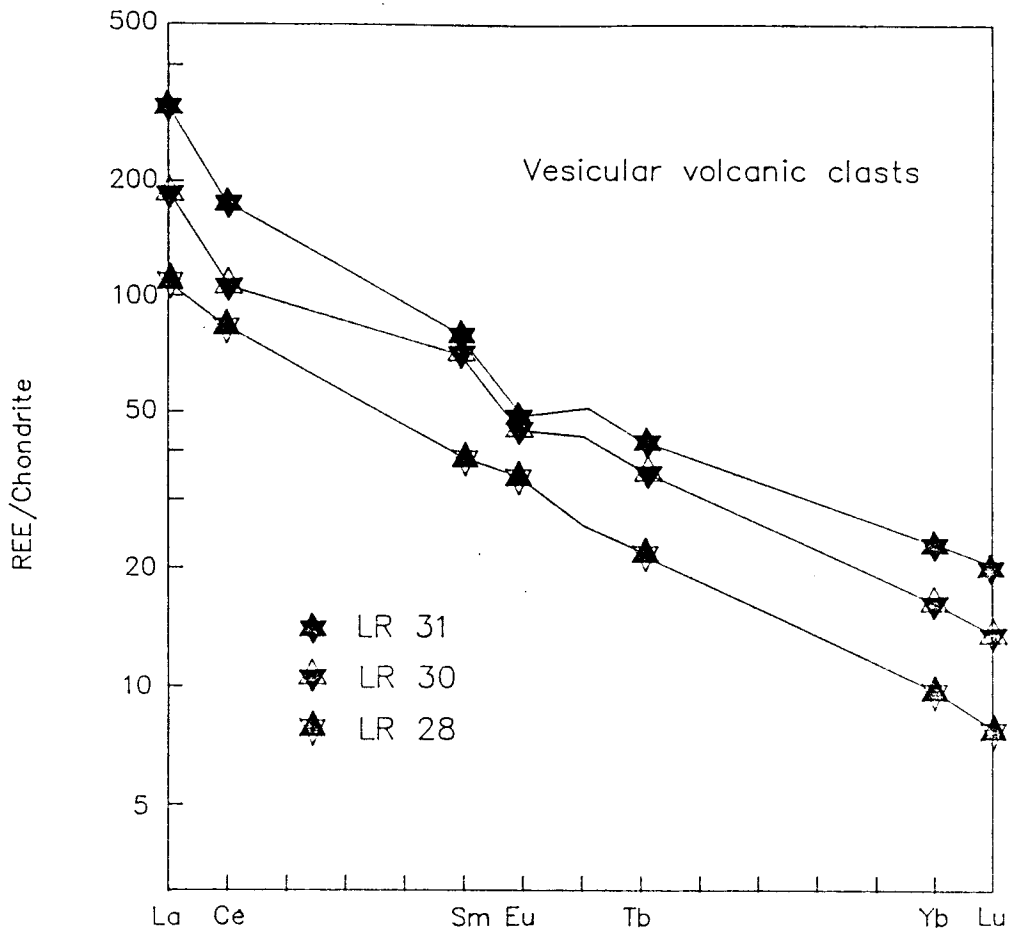


Figure 4.11a

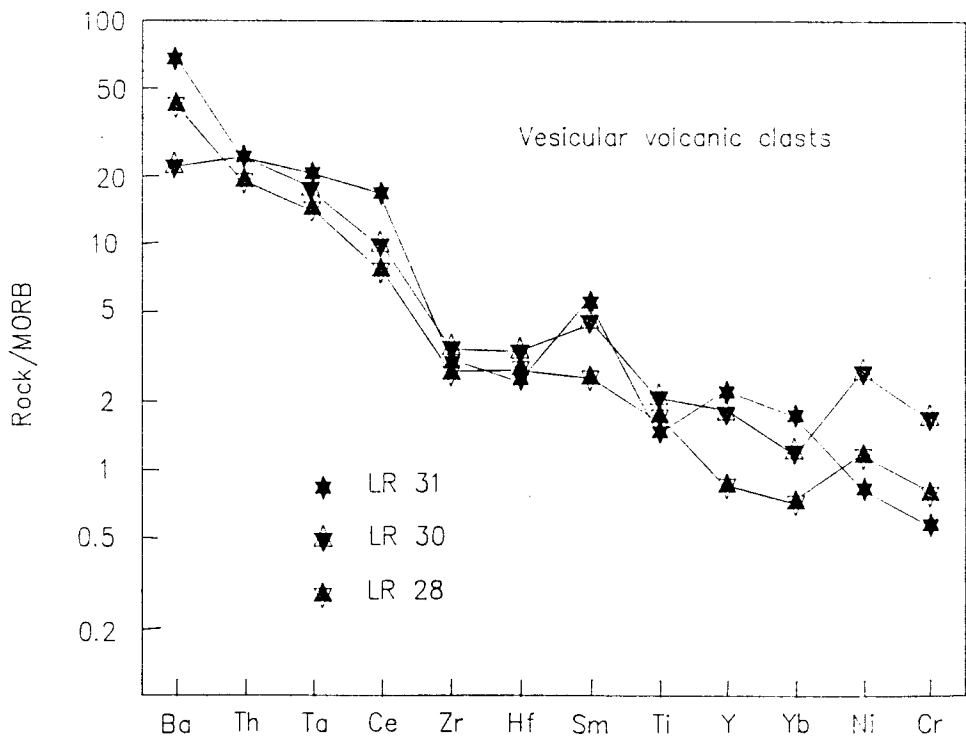


Figure 4.11b

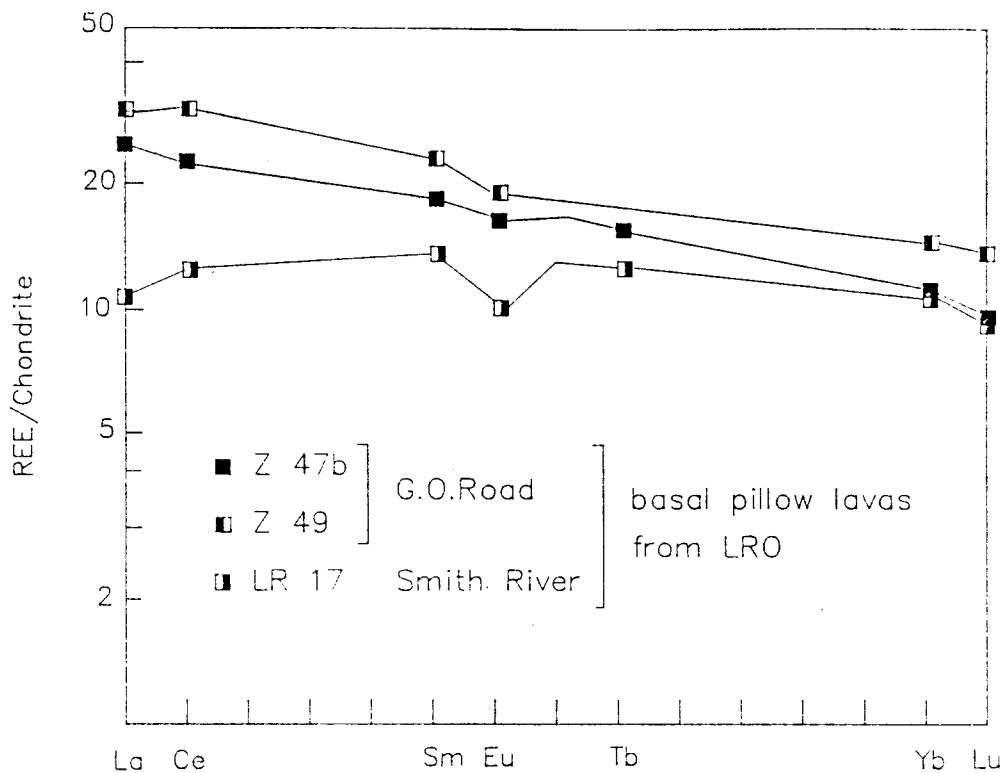


Figure 4.12a

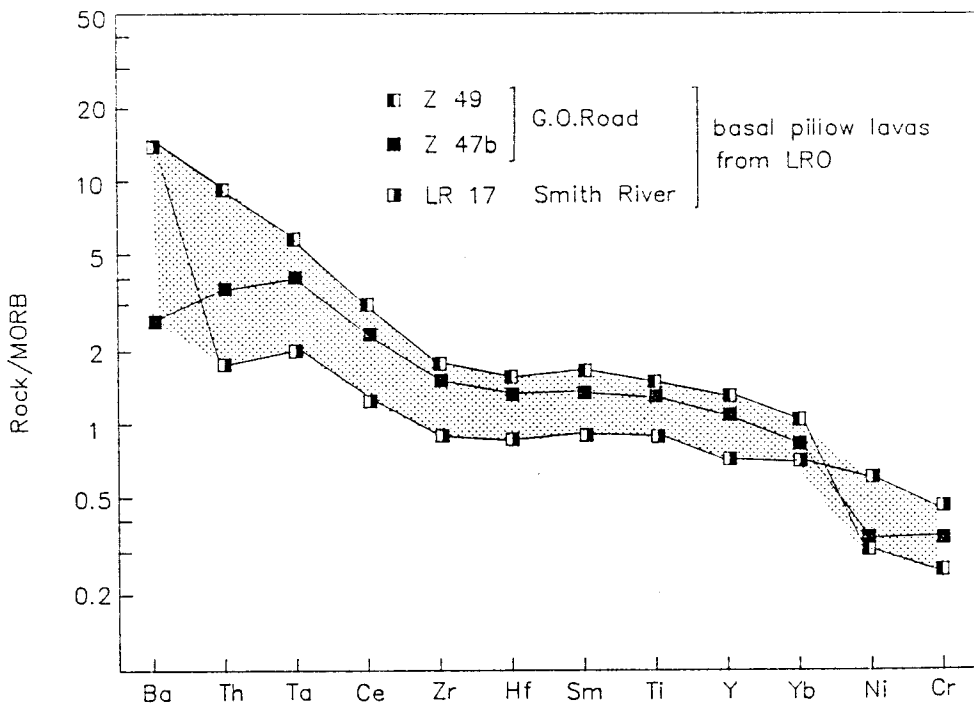


Figure 4.12b

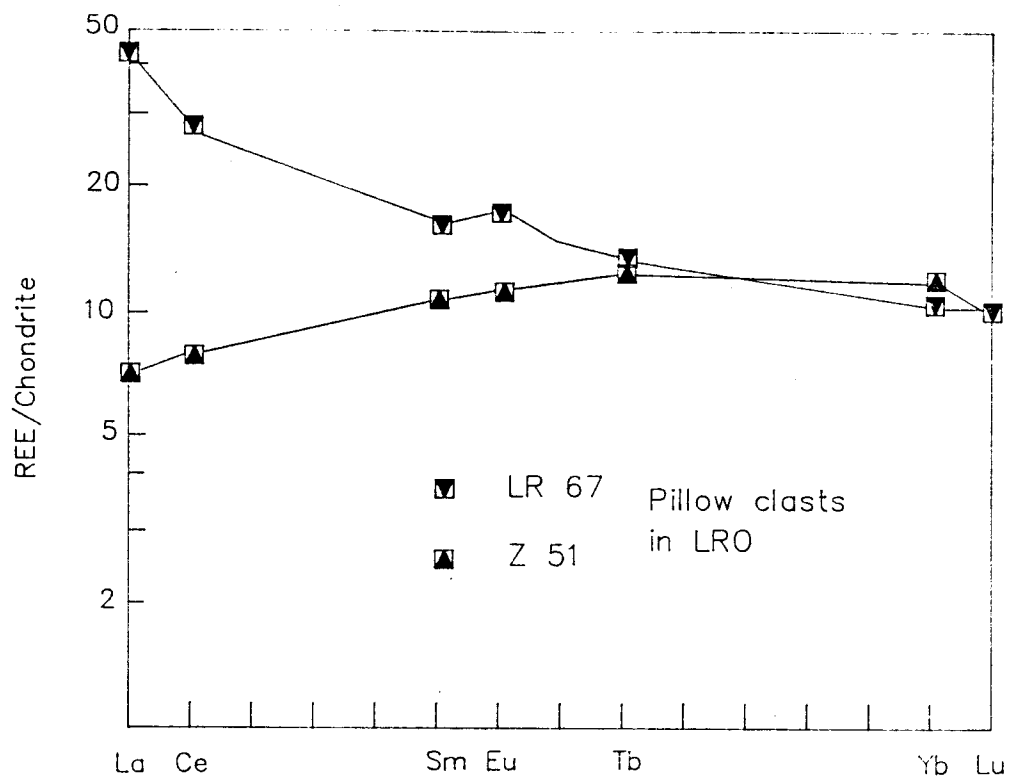


Figure 4.13a

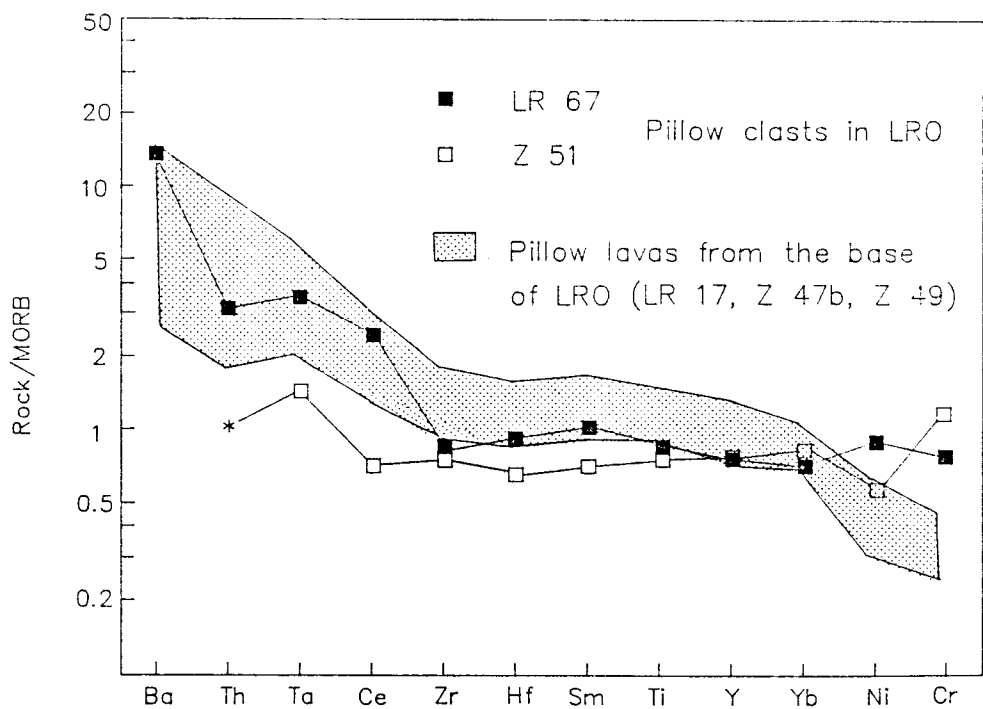


Figure 4.13b

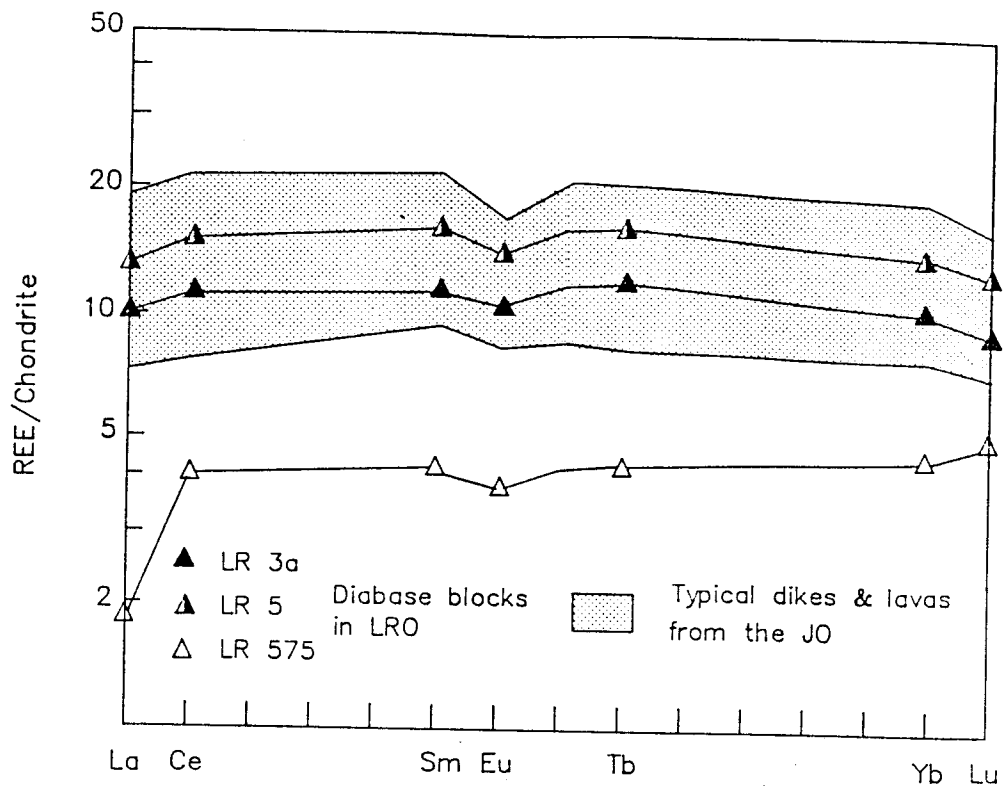


Figure 4.14a

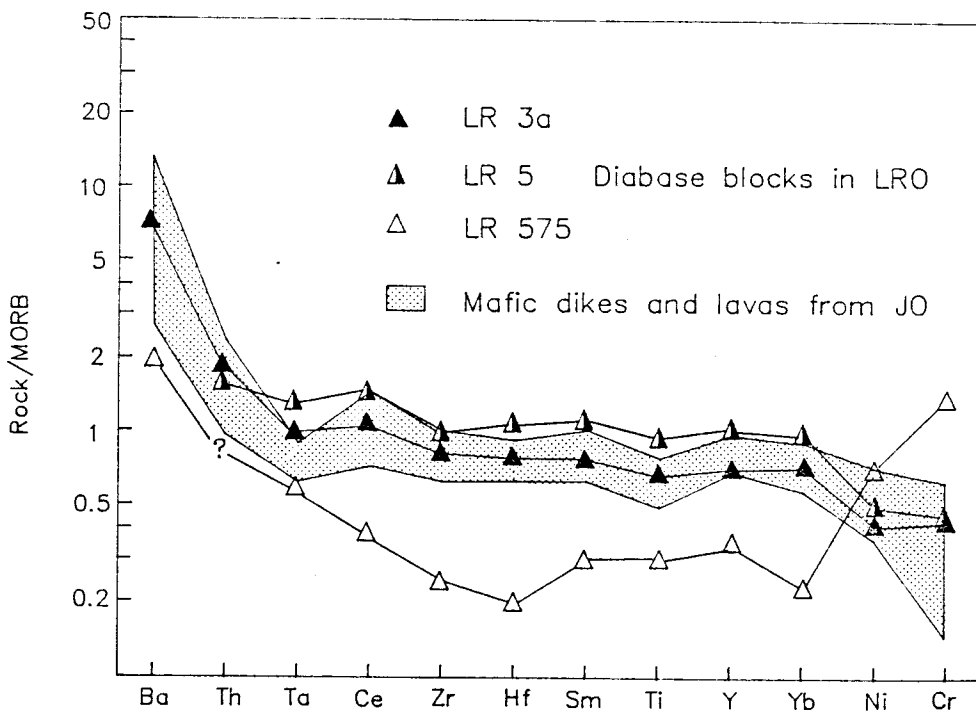


Figure 4.14b

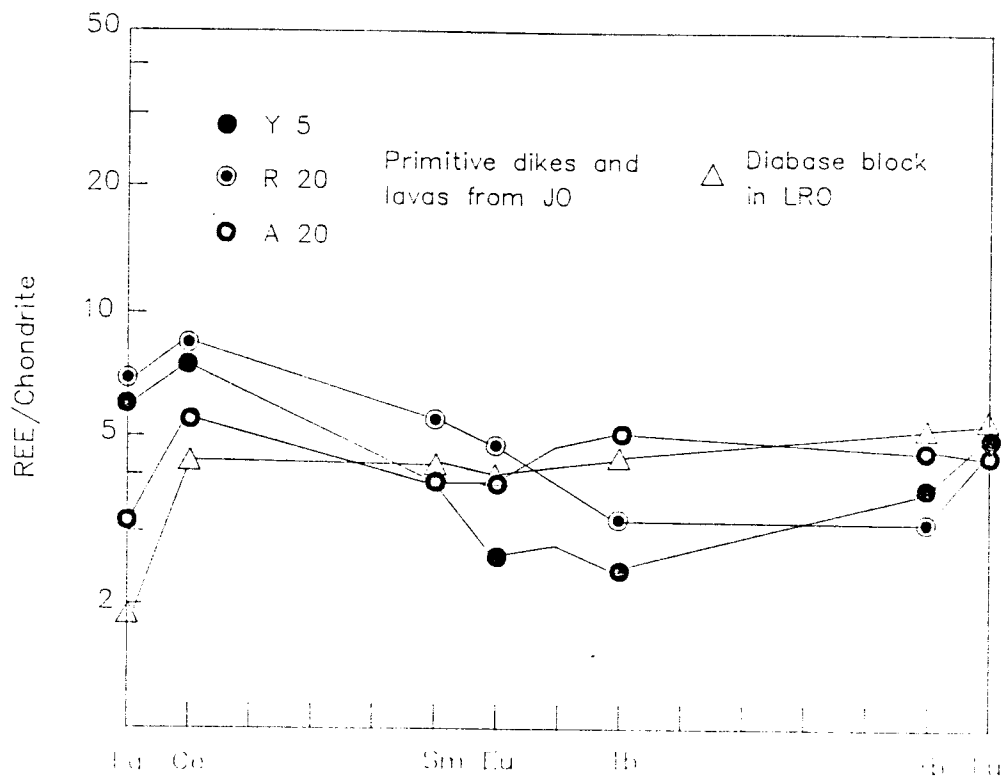


Figure 4.15a

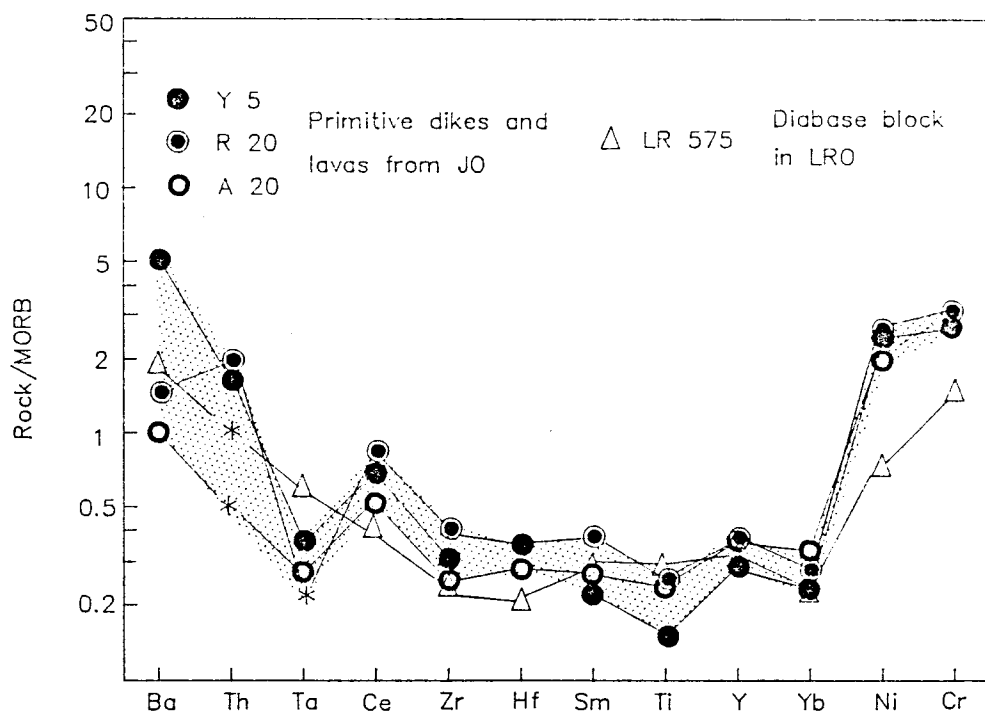


Figure 4.15b

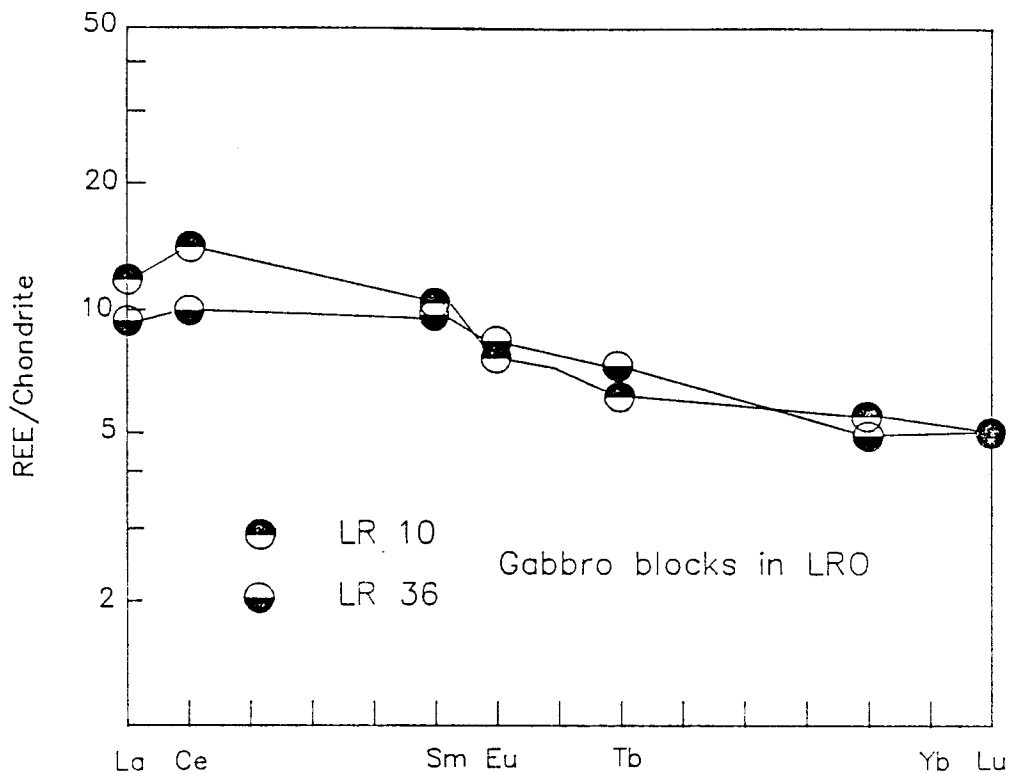


Figure 4.16a

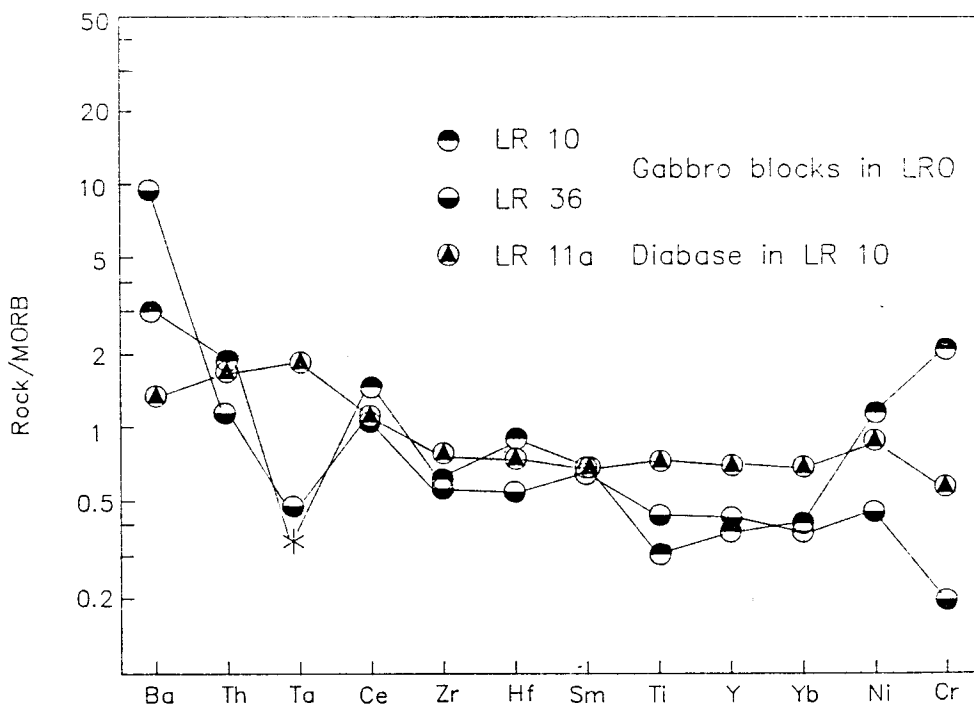
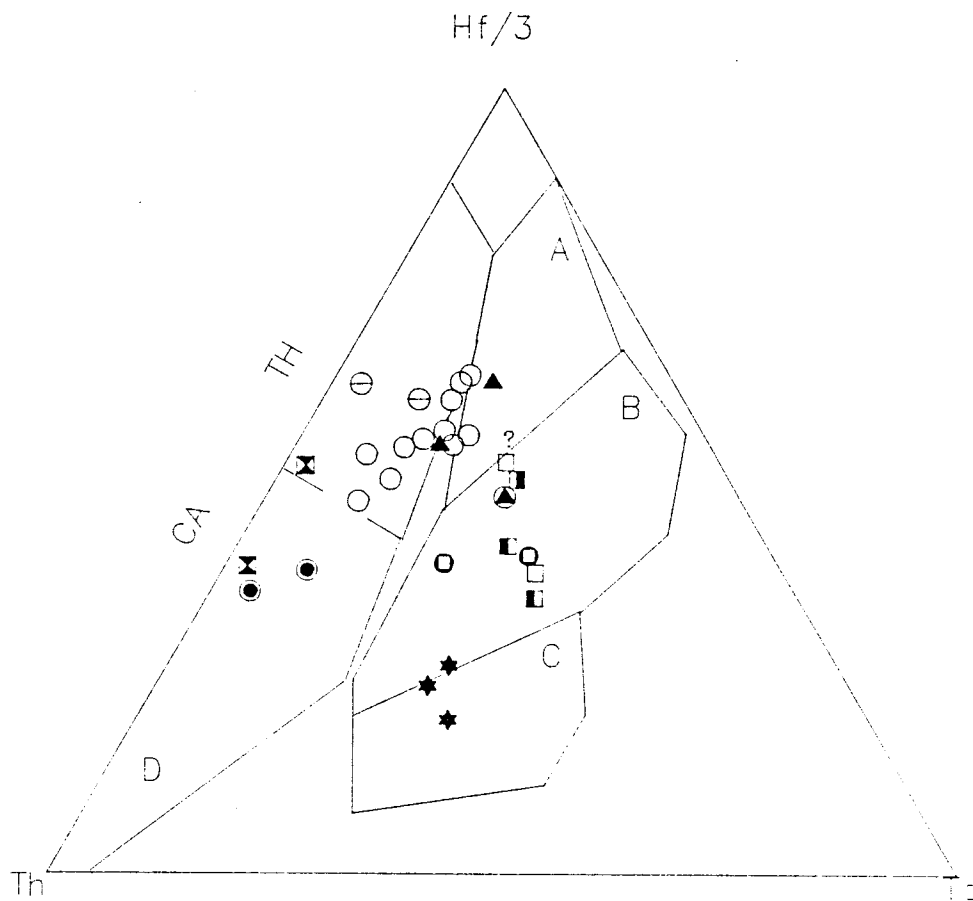


Figure 4.16b

constraints on the character of mid-ocean ridge basalts. N-type MORB is characterized by $Hf/Ta > 7$, while enriched MORB has Hf/Ta ratios between 2 and 7 (Wood and others, 1979). The diagram is not sensitive to crystal fractionation, so that intermediate and silicic lavas plot close to their basic parents; this is, the resulting increase in Th/Hf and Th/Ta in the residual liquid is not large enough to shift the original melt composition significantly (Hf and Ta partition preferentially into Fe-Ti oxides and other minor phases).

The diagram is particularly useful to highlight the effect of enrichment and depletion of the bulk upper mantle in incompatible elements (Fig. 4.18). Enrichment trends will move the mantle composition toward increased Th and Ta contents, that is away from the Hf apex (trend 1). Depletion events such as repeated melting will extract the more incompatible elements Th and Ta , and the mantle composition will move toward the Hf apex into the MORB field (trend 2). Primary melts generated over a subduction zone are preferentially enriched in Th and other LFS elements, and will follow a path parallel to the Hf - Th axis (trend 3). It is apparent that mantle regions yielding partial melts that are extremely depleted in Ta have to undergo an additional depletion before the Th -rich subduction component is added (Pearce and others, 1984). The same holds for primitive rocks such as LR 575, which



- A: N-Type MORB
 B: E-Type MORB and tholeiitic within-plate lavas
 C: Alkaline within-plate lavas
 D: Destructive Margin lavas

Symbols are the same as used before, except for the typical JO suite.

here: ○ = typical lavas and dikes from the JO.

Figure 4.17 The Hf-Th-Ta diagram after Wood and others (1979).

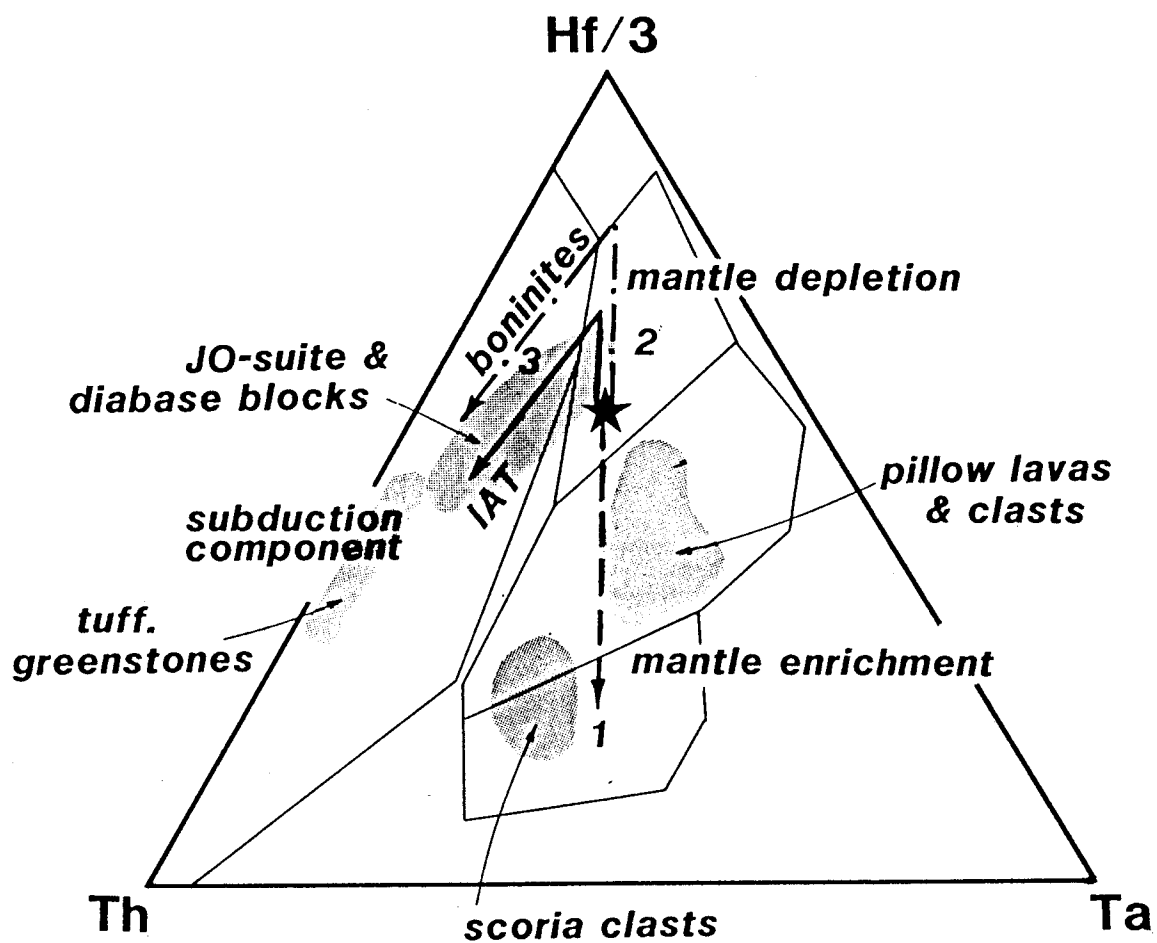


Figure 4.18 Petrogenetic modelling in the Hf-Th-Ta diagram (after Pearce and others, 1984).

are low in both Th and Ta.

The lithologies present in the LRO define four distinct areas in the Hf-Th-Ta plot (Figs. 4.17 and 4.18) which are correlated to the main geochemical information that was derived in sections 4.2 and 4.3. The basal pillow lavas are E-type MORB. Diabase blocks are transitional between N-MORB and IAT, while one diabase is a primitive IAT. Vesicular volcanic clasts in the LRO are alkaline within-plate basalts. The tuffaceous matrix of the LRO is calc-alkaline to transitional to IAT.

The dikes and lavas from the Josephine ophiolite span a wide range of compositions: E-type MORB's are extremely uncommon in the JO and occur only immediately west of the LRO. Their occurrence so close to the LRO, however, might be more than coincidental, and encourages speculations about a genetic relation of the basal LRO pillow lavas to the Josephine ophiolite (see chapter VI). Sparse primitive basalts (Ti = 0.4-0.6%; Zr = 30-50 ppm; Harper, 1984 and unpubl.data) contrast with the main suite of seemingly evolved basalts which are transitional between N-MORB and IAT (Ti = 0.9-1.3%; Zr = 70-90 ppm; Ti/V = 18-25; Harper 1984; unpublished data, and this study); the latter constitute the vast majority of dikes and lavas in the JO. A quick and simplified calculation for the degree of crystal fractionation required to produce these typical

Josephine basalts shows that the primitive basalts are unlikely to be parental to the more evolved species:

$$\frac{C(L)}{C(0)} = F^{D-1}$$

or for $D \ll 1$:

$$\frac{C(L)}{C(0)} = \frac{1}{F}$$

(Cox and others, 1979)

where $C(0)$ is the initial concentration in the unfractionated parental melt, $C(L)$ is the concentration in the liquid remaining, F is the proportion of liquid remaining after fractionation, and D is the crystal/liquid distribution coefficient for a particular element. This model requires that the liquid is a uniform reservoir and the solid crystals are removed as fast as they are formed.

Pillow R 20:	Ti = 0.36%	Pillow D 74:	Ti = 1.18%
	Zr = 29 ppm		Zr = 71 ppm

$$D(\text{Ti}) = 0.15$$

$$D(\text{Zr}) = 0.15$$

therefore

$$F(\text{Ti}) = 0.24$$

$$F(\text{Zr}) = 0.34$$

or for the most highly evolved pillow lavas (G 54: Ti = 2.21%; Zr = 175 ppm):

$$F(\text{Ti}) = 0.12$$

$$F(\text{Zr}) = 0.12$$

Thus a magma of the composition R 20 would have to be

88% crystallized to produce G 54. The observed trend might be much better explained as a mixing line between very primitive IAT and mature back-arc basin basalt.

4.5 Summary

The principal results of this geochemical study can be summarized as follows (see also Figs. 4.19 and 4.20):

- The pyroclastic tuffaceous matrix of the LRO is calc-alkaline to transitional to island-arc tholeiitic, suggesting an active, mature volcanic arc adjacent to the LRO.
- Vesicular volcanic clasts (scoria) in the pebbly mudstone section are alkaline basalts and have the character of within-plate lavas.
- The pillow lava sequences along the GO-road and the Smith River are enriched E-type MORB; some of the lower GO-road lavas are high-Ti within-plate basalts. The two pillow suites differ from each other, in that their parental magmas are the result of varying degrees of partial melting of an enriched MORB source. The pillow lavas are distinctly different from the main Josephine suite, which is transitional between IAT and N-type MORB. It is striking, however, that the only E-type MORB's in the Josephine ophiolite

occur directly west of the LRO. Conclusions regarding the tectonic setting of the LRO in chapter VI will take this fact into consideration. Pillow clasts in the LRO are similar to the pillow lavas at the base of the olistostrome: they show E-type MORB chemistry and occasionally also include lavas that have a distinct within-plate basalt character.

- Diabase blocks from a talus breccia in the LRO are distinct from the LRO pillow lavas and resemble transitional lavas and dikes of the Josephine ophiolite. Some diabase blocks are primitive IAT and appear to be similar, though less enriched in Th and LREE, to primitive basalts from the Josephine ophiolite.
- Very primitive basalts of the JO are not parental to the main ophiolitic suite but rather represent one end member of a mixing event between initial island-arc lavas and mature back-arc basin MORB.
- Mafic dikes in gabbro blocks are E-type MORB and might represent feeder dikes to the LRO pillows.

Three main processes acting upon magmatic systems and thereby causing compositional changes were recognized in this chapter: 1) the effect of fractional crystallization, 2) varying degrees of partial melting, and 3) enrichment of sources by melt and/or fluid metasomatism. All three

processes can be visualized in a Ce/Yb_N vs. Ce_N diagram. Crystallization does not fractionate Ce from Yb, and both elemental abundances increase at the same rate in evolving systems (Cox and others, 1979) This is expressed in a horizontal trend in Fig. 4.19. Decreased extent of melting in a upper mantle source can separate the LREE from HREE, which may be retained in residual phases such as garnet or pyroxene with liquid/crystal distribution coefficients D_{Yb} much greater than D_{Ce} . Therefore a ratio of LREE/HREE, such as Ce/Yb, increases with Ce which partitions preferentially into the liquid phase. The resulting trend in Fig. 4.19 will show a slight positive slope. Metasomatism and enrichment processes that enhance almost exclusively LFS and LREE abundances separate Ce and Yb most effectively and cause a trend with a positive slope close to 1. All three processes were discussed in the preceding sections and the affected rocks from the LRO and the Josephine ophiolite define the respective trends mentioned above (Fig. 4.19). In particular, it appears obvious that the primitive IAT rocks are not parental to the transitional JO and diabase block suite. It is also suggested that pillow lavas from the LRO differ owing to varying degrees of melting of a common source (Fig. 4.19, and above).

The simultaneous presence of rocks from the various mentioned tectonomagmatic regimes within the relatively

coherent stratigraphic section of the Lems Ridge olistostrome is summarized in the simplified stratigraphic column of Fig. 4.20, implying a complex tectonic setting. Both geochemical information obtained in this chapter and geochronological data to be presented in chapter V will be used for a concluding assessment of the ancient tectonic setting of the Lems Ridge olistostrome in chapter VI.

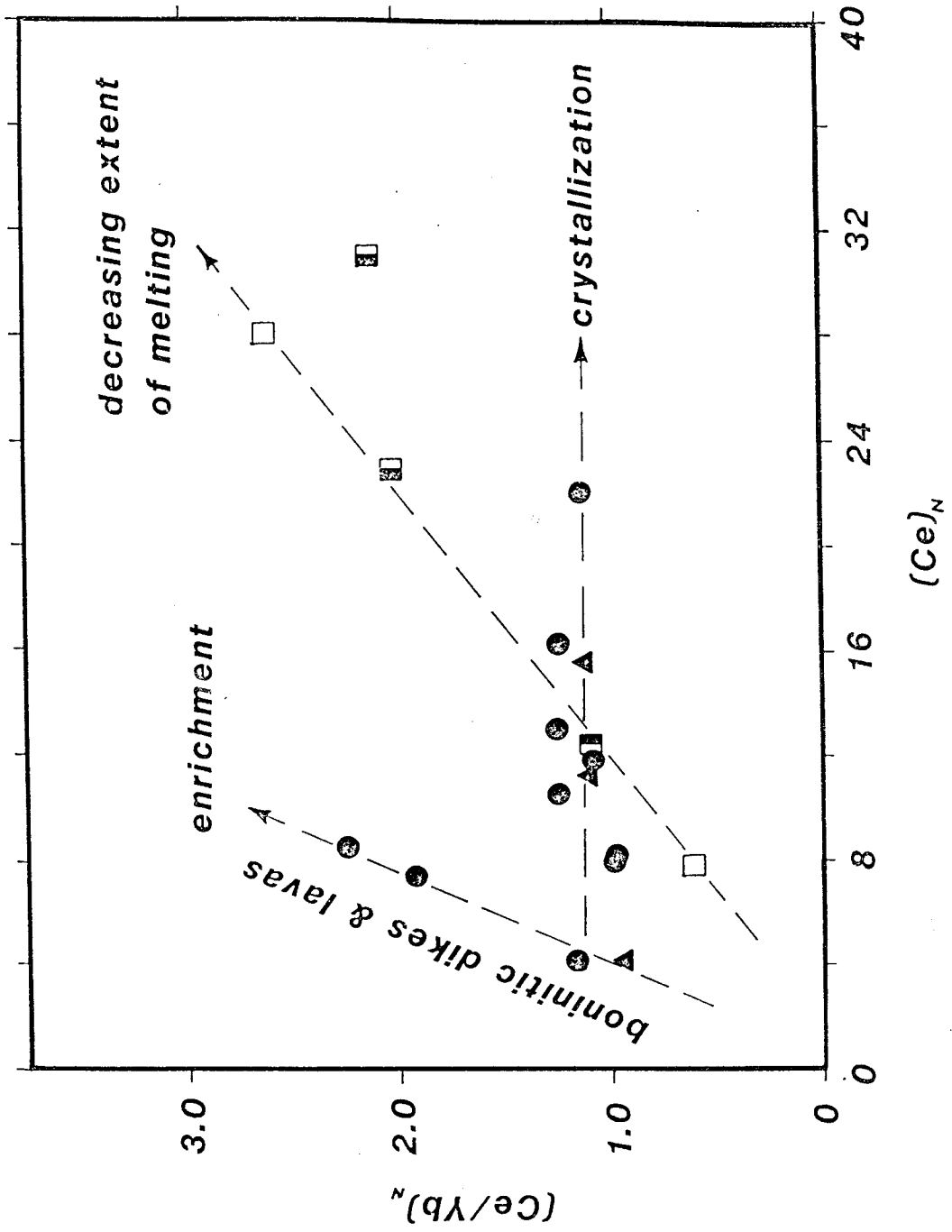


Figure 4.19 The $(Ce/Yb)_N$ - $(Ce)_N$ diagram.

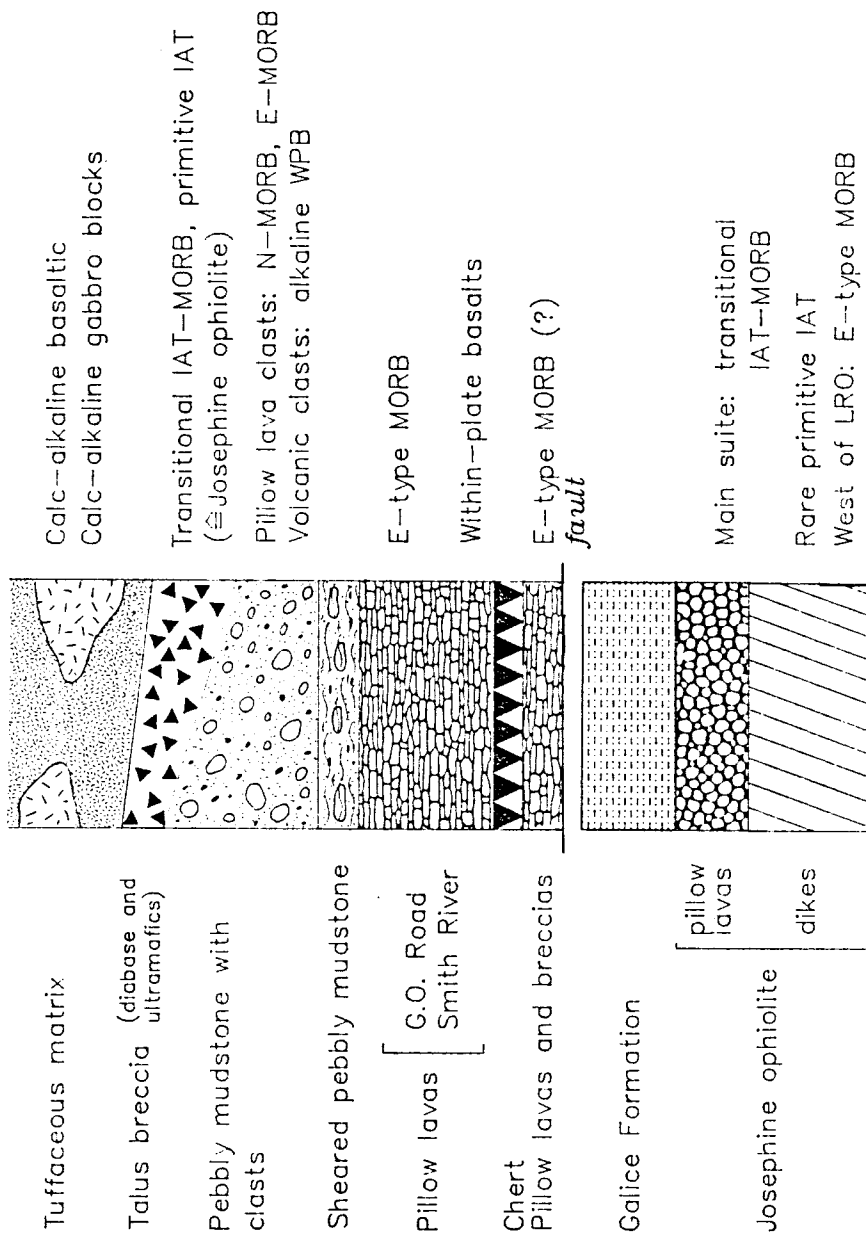


Figure 4.20

Summary of the geochemistry of the Lems Ridge olistostrome and the Josephine ophiolite in a simplified tectono-stratigraphic column.

CHAPTER V: Geochronology

5.1. Purpose

One of the prime objectives of this study is to place constraints on the age of the Lems Ridge olistostrome (LRO). The only available age information prior to this has been obtained from radiolarians that were separated from chert boulders within the olistostrome. They were reported to be of the same Late Jurassic age as chert that overlies the Josephine ophiolite to the north (D.L. Jones, pers.comm. to Harper and others, 1983). The interpretation of previous workers that the Lems Ridge olistostrome is closely associated with the Josephine ophiolite was derived from the apparent resemblance of these radiolarian faunas. The same samples as well as radiolarians separated from a thin chert bed at the base of the LRO were re-examined and showed such insufficiently preserved rads that an unequivocal faunal age could not be assigned (C. Bloome, pers.comm., 1987). However, the faunal assemblage is apparently younger than Late Triassic and older than Late Jurassic (C. Bloome, pers.comm., 1987).

It is therefore desirable to place quantitative constraints on the age of the olistostrome. Several lithologies have K-bearing minerals and thus potential for $^{40}\text{Ar}/^{39}\text{Ar}$ dating:

Hornblende gabbros constitute the most prominent blocks within the olistostrome. They give a maximum age of the LRO and can also be used to test the hypothesis that the abundant ophiolitic boulders were indeed locally derived from the Josephine ophiolite (Harper and others, 1985).

The tuffaceous matrix is distinctly calc-alkaline and carries both hornblende-phyric volcanic fragments and isolated, single hornblende crystals. Hornblende ages on these volcanoclastic rocks would indicate the depositional age of the olistostrome. They were thought to aid in correlation with the Rogue Formation to the north. However, this approach fell somewhat short of its goal, for reasons pointed out in section 5.4.

Andesite clasts with hornblende phenocrysts represent either concomitant active arc volcanism, or are reworked from older sources. Their ages also help to assess the presence and timing of arc-volcanism adjacent to the LRO.

Mica-schist clasts occur within the pebbly mudstone portion of the olistostrome which is predominantly derived from continental and terrigenous sources. Metamorphic ages of these non-volcanic clasts could indicate a specific source area within the older Klamath terranes and thus pinpoint the native character of the entire western Jurassic belt with respect to North America.

Calc-alkaline dikes and sills intrude the LRO, showing

crosscutting relationships with both matrix and olistostromal blocks. Thus they place a minimum age on the assembly of the olistostrome. Abundant dikes also occur within the entire Josephine ophiolite and overlying Galice Formation, and are interpreted to mark the eastward migration of arc-magmatism during the Nevadan orogeny (Harper and Wright, 1984). Since they are pre- or syn-Nevadan they also place a tight upper bracket on the Nevadan orogeny.

Geochronologic results are hoped to address the validity of models that depict the LRO as overlying the Josephine ophiolite and containing lithologies of this Late Jurassic ophiolite. If so, the obtained ages, in particular for the gabbro blocks, should cluster around Late Jurassic ages. Distinctly younger or older ages will require a revision of the existing model (Harper and others, 1983; Harper and others, 1985).

$^{40}\text{Ar}/^{39}\text{Ar}$ analyses were performed using the departmental facilities at SUNYA. The principles of the $^{40}\text{Ar}/^{39}\text{Ar}$ dating and analytical techniques are outlined in section 5.2. Results are presented and discussed in sections 5.3 and 5.4, and the data tables are listed in Appendix IV.

In addition, a Pb-U zircon age was obtained from a plagiogranite that forms irregular pods in one of the dated

gabbro blocks. The analysis has been carried out by J. Wright and is briefly referred to in section 5.4.

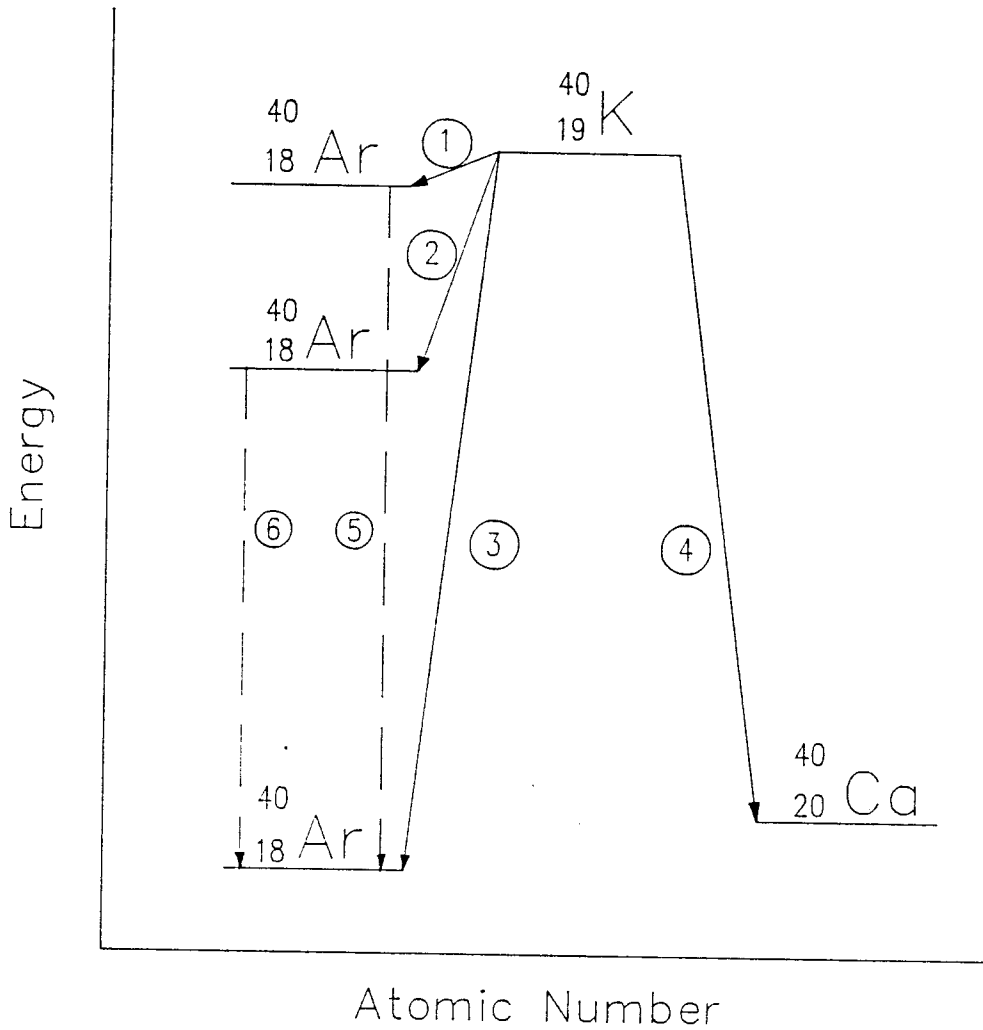
5.2 Methods

The $^{40}\text{Ar}/^{39}\text{Ar}$ method of dating as described by Merrihue and Turner (1966) has the potential to overcome certain limitations which are inherent to the conventional K/Ar method. Either method is based on the decay of ^{40}K to ^{40}Ar . About 11 % of the ^{40}K present in a sample decays to an excited stage of ^{40}Ar which then converts to the groundstate of ^{40}Ar , while a small portion of ^{40}Ar decays directly to the groundstate of ^{40}Ar . The remaining 88.8 % of ^{40}K converts by beta-decay to ^{40}Ca . This decay scheme is shown in Fig. 5.1.; the tables in Appendix IV give the isotopic abundances of the naturally occurring isotopes of potassium and atmospheric argon, as well as the decay constants for ^{40}K .

Since the decay constants for ^{40}K are satisfactorily well known, an age of a sample can be determined by its K content and the ^{40}Ar component derived from the decay of ^{40}K . The fraction of ^{40}K atoms that decay to ^{40}Ar is given by (λ_e/λ) , and the growth of ^{40}Ar can be written as:

$$^{40}\text{Ar} = \lambda_e/\lambda \cdot ^{40}\text{K} (e^{\lambda t} - 1)$$

$$t = 1/\lambda \cdot \ln(^{40}\text{Ar}/^{40}\text{K} (\lambda/\lambda_e) + 1)$$



1 = electron capture, 11.0 %, 0.05 MeV

2 = β^+ - decay, 0.001 %, 0.49 MeV

3 = electron capture, 0.16 %, 1.51 MeV

4 = β^- - decay, 88.8 %, 1.32 MeV

5 = γ , 1.46 MeV

6 = 2γ , 1.02 MeV

Figure 5.1

Decay scheme for the branched decay of ^{40}K to ^{40}Ar and ^{40}Ca (modified from Faure, 1977).

Among the limitations of this conventional method are that 1) no excess ^{40}Ar became incorporated into the sample, and 2) all of the radiogenic ^{40}Ar ($= ^{40}\text{Ar}^*$) produced must be retained in the sample.

Excess ^{40}Ar is common in geological samples (e.g. Lanphere and Dalrymple, 1976; Harrison and McDougall, 1981) and results in anomalously old conventional K/Ar ages. On the other hand, ^{40}Ar may be lost by diffusion resulting in meaningless young K/Ar ages. The conventional method also requires the measurement of absolute concentrations of K and Ar on two separate portions of the same sample, thus potentially giving rise to problems of sample inhomogeneity and sample size.

The $^{40}\text{Ar}/^{39}\text{Ar}$ method avoids the described problems of sample preparation and analysis, and can also critically assess the effects of excess ^{40}Ar as well as the diffusion history of $^{40}\text{Ar}^*$ in the sample.

The method is based on the formation of ^{39}Ar by irradiation of K-bearing samples, thus converting a fraction of ^{39}K to ^{39}Ar by neutron capture.

The resulting concentration of ^{39}Ar is proportional to that of ^{39}K , and the concentration ^{39}K is in turn proportional to the amount of ^{40}K present in the sample. Thus a ratio of $^{40}\text{Ar}/^{39}\text{Ar}$ is also proportional to a ratio of $^{40}\text{Ar}/^{40}\text{K}$ of the conventional method. Provided that the

^{39}Ar created by neutron bombardment is distributed identically to ^{39}K , a spectrometrically measured $^{40}\text{Ar}/^{39}\text{Ar}$ ratio therefore corresponds to an apparent age. It is critical to know what fraction of ^{39}K is converted to ^{39}Ar . This fraction is dependant on various irradiation parameters. However, these parameters -- such as neutron flux, cross-section of ^{39}K for capture of neutrons, and the ratio of fast to thermal neutrons -- are difficult to determine. Therefore standards of known age, so called flux-monitors, are irradiated and analyzed along with the unknown samples. The standard are used to determine the parameter J ("J-factor") which is a function of the age of the flux-monitor and those irradiation parameters:

$$J = \frac{e^{\lambda t} - 1}{(^{40}\text{Ar}^*/^{39}\text{Ar})_{\text{FM}}}$$

- λ = decay constant for ^{40}K
 t = age of the flux monitor
 $^{40}\text{Ar}^*/^{39}\text{Ar}_{\text{FM}}$ = ratio of the flux monitor

Since there is a regular gradient of J within a irradiation tube, the unknowns are placed between the flux monitors, so that an interpolation can be made and every unknown has a characteristic J that describes its irradiation conditions. This leaves the age of the unknown as the only not yet determined variable:

$$t = 1/\lambda \cdot \ln ({}^{40}\text{Ar}^*/{}^{39}\text{Ar}_K \cdot J + 1)$$

This is however an idealized case, because along with the production of ${}^{39}\text{Ar}$ from ${}^{39}\text{K}$, several interfering reactions occur that generate a variety of Ar-isotopes (Dalrymple and others, 1981). Therefore a series of correction factors must be applied to the measured ${}^{40}\text{Ar}/{}^{39}\text{Ar}$ ratio of the sample. Most of these interfering reactions involve isotopes of K and Ca. The three principal interferences are 1) ${}^{40}\text{Ar}$ derived from ${}^{40}\text{K}$, 2) ${}^{39}\text{Ar}$ derived from ${}^{42}\text{Ca}$, and 3) ${}^{36}\text{Ar}$ derived from ${}^{40}\text{Ca}$. Fortunately, ${}^{37}\text{Ar}$ is produced nearly entirely from ${}^{40}\text{Ca}$: thus its abundance allows an assessment of the Ca-interference.

Dalrymple and Lanphere (1971) developed a general expression for $F = {}^{40}\text{Ar}^*/{}^{39}\text{Ar}_K$ that accounts for the corrections made for the interferences listed above, and for atmospheric Ar:

$$F = \frac{A - (C_1 B) + (C_1 C_2 D) - C_3}{1 - (C_4 D)}$$

- A = measured ${}^{40}\text{Ar}/{}^{39}\text{Ar}$
 B = measured ${}^{36}\text{Ar}/{}^{39}\text{Ar}$
 D = measured ${}^{37}\text{Ar}/{}^{39}\text{Ar}$ after correction for the decay of ${}^{37}\text{Ar}$
 C_1 = atmospheric ${}^{40}\text{Ar}/{}^{36}\text{Ar}$ (= 295.5)
 C_2 = correction factor $({}^{36}\text{Ar}/{}^{37}\text{Ar})_{\text{Ca}}$
 C_3 = correction factor $({}^{40}\text{Ar}/{}^{39}\text{Ar})_{\text{K}}$

C_4 = correction factor $(^{39}\text{Ar}/^{37}\text{Ar})_{\text{Ca}}$

Thus the age expression becomes:

$$t = 1/\lambda \cdot \ln (F \cdot J + 1)$$

The $^{40}\text{Ar}/^{39}\text{Ar}$ technique allows an age determination for each gas fraction produced during incremental heating of the sample to successively higher temperatures. The theoretical background for this stepwise degassing technique is provided by a model (Turner, 1968) suggesting that the first heating increments release gas from the periphery of a mineral grain, while subsequent steps at higher temperatures release Ar from locations that lie progressively inward toward the center of a grain. Depending upon the thermal history of the sample, the internal distribution of ^{40}Ar may or may not be uniform, while the distribution of ^{39}Ar should be uniform in either case (or at least reflect the initial distribution of K).

The result of an incremental heating experiment can be presented as an age spectrum, the apparent ages on the y-axis plotted against the cumulative percent of ^{39}Ar released on the x-axis. This format of presentation is referred to as an age spectrum. Apparent ages derived from the $^{40}\text{Ar}^*/^{39}\text{Ar}_K$ ratios may define a plateau that represents the time at which a mineral closed to ^{40}Ar diffusion. Depending on the geologic and thermal history of the sample

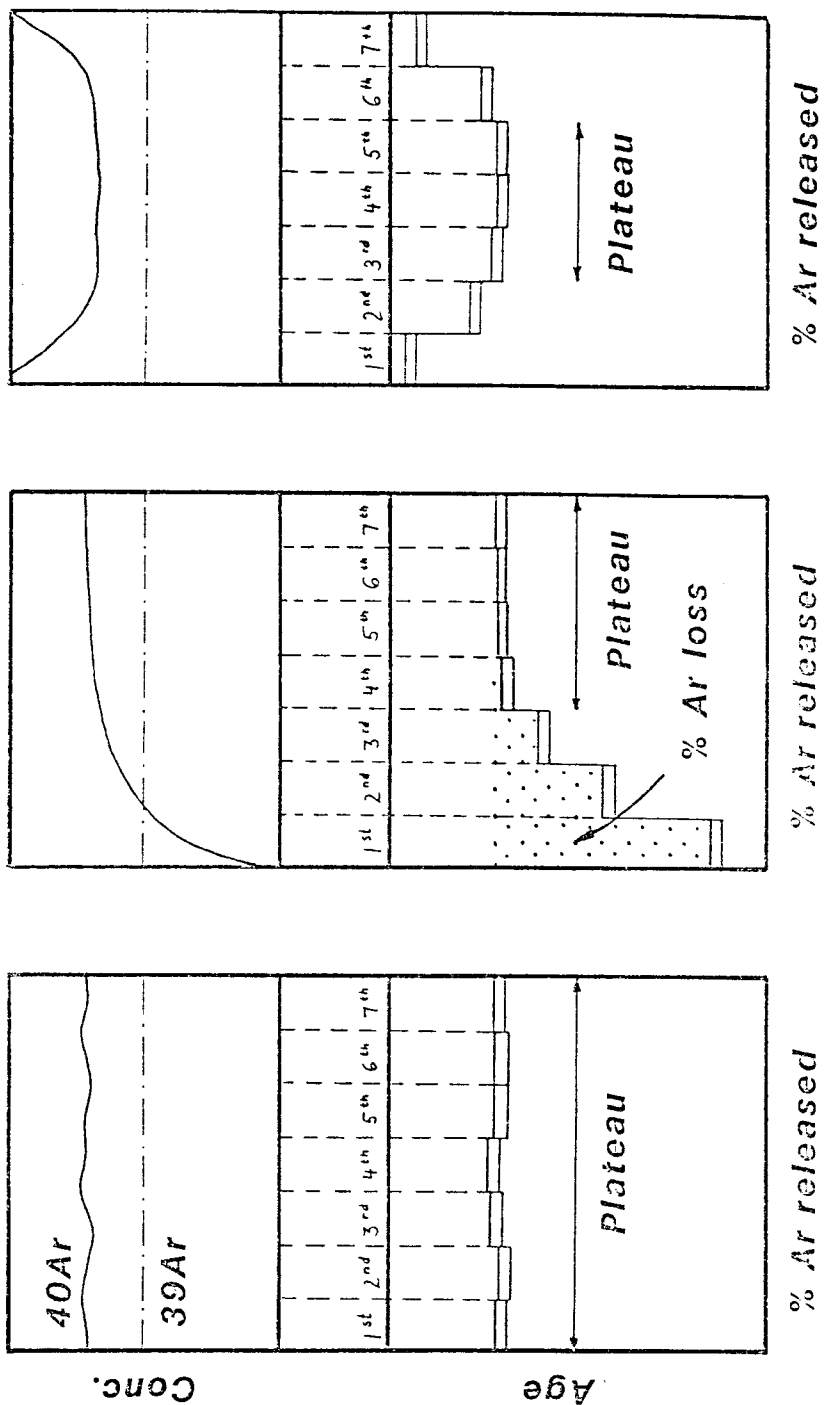


Figure 5.2 Distribution of ^{40}Ar and ^{39}Ar from the rim of a grain toward the center, and the corresponding age spectra for three idealized cases: (a) a undisturbed sample, (b) a sample that experienced episodic loss of ^{40}Ar , and (c) a sample with excess ^{40}Ar .

area, and on the diffusion parameters of a mineral with respect to Ar, other patterns may develop: ideal cases of an undisturbed sample, a sample that experienced episodic loss of ^{40}Ar , and a sample with excess ^{40}Ar incorporated into the crystals are shown in Fig. 5.2.

The complexity of a spectrum is often due to several interfering processes that all affect the distribution and release of Ar-isotopes in geological samples. Harrison (1983) reviews eight factors that have an impact on the interpretation on less than ideal age-spectra.

- (1) Multiple episodic loss
- (2) Slow cooling
- (3) Presence of mixed phases
- (4) Resolution of the age-spectrum
- (5) Excess ^{40}Ar
- (6) Recoil artifacts of ^{39}Ar during irradiation
- (7) Grain size and grain distribution
- (8) Phase changes during Ar-extraction.

In addition, Harrison and Heizler (1987) discuss the complicating effect of multiple trapped Ar-components on an age-spectrum.

In summary, the $^{40}\text{Ar}/^{39}\text{Ar}$ dating technique has the distinct advantage that isotopic ratios can be measured mass-spectrometrically from the same sample, and also

provide information on the spatial distribution of Ar-isotopes within a mineral sample. Not only can isotope ratios be measured more precisely than absolute amounts of K and Ar, the method furthermore allows measurements of very small samples.

Sample preparation

Each sample was crushed to a maximum grain diameter of about 600 μm and sieved to yield two splits of 600-180 μm and 180-125 μm . In general the coarsest possible fraction containing relatively few composite hornblende-plagioclase grains was used for mineral separation. Standard heavy liquids and magnetic separation techniques were used to obtain mineral separates. The resulting separates were cleaned ultrasonically and then re-examined for purity. For most samples handpicking was done at this point to insure near 100% purity. The samples were irradiated for 80 hours in the Ford reactor at the University of Michigan.

Analytical Procedures and Data Reduction

Isotopic ratios were measured using a Nuclide rare-gas spectrometer at SUNY Albany. The extraction system allows a routine analysis of up to 3 steps per hour. The system consists of a double vacuum Ta furnace with accurate temperature control during sample-heating, and a gettering

section to purify the extracted gas fraction. Purification followed standard procedures using both turbo and ion pumps to pump away hydrogen and water, and Ti-Zr getters to scrub off the remaining reactive gases. Data acquisition and reduction is fully automated. Initial intensities of ^{40}Ar , ^{39}Ar , ^{37}Ar , and ^{36}Ar are calculated by time-regressing over five data points (10 points for ^{36}Ar). The regressed values are subsequently corrected and an apparent age for a fraction is calculated from the corrected ratios. A schematic illustration of the entire assembly at SUNYA is shown in Fig. 5.3.

Samples were incrementally heated between 10 and 20 steps, depending on their K content. It is desirable to do many incremental heating steps to insure adequate age spectrum resolution. For low-K samples (like the amphiboles in this study) too many steps result in small gas fractions with high analytical uncertainty and may preclude unambiguous age determinations. The age spectra for some samples (e.g. LR 10 and LR 15) probably owe their irregularities partly to this "over-resolution".

Presentation of data

Hornblende ages reported in section 5.3 refer to plateau ages, isochron ages, and total gas ages respectively. Total gas ages are calculated by weighting

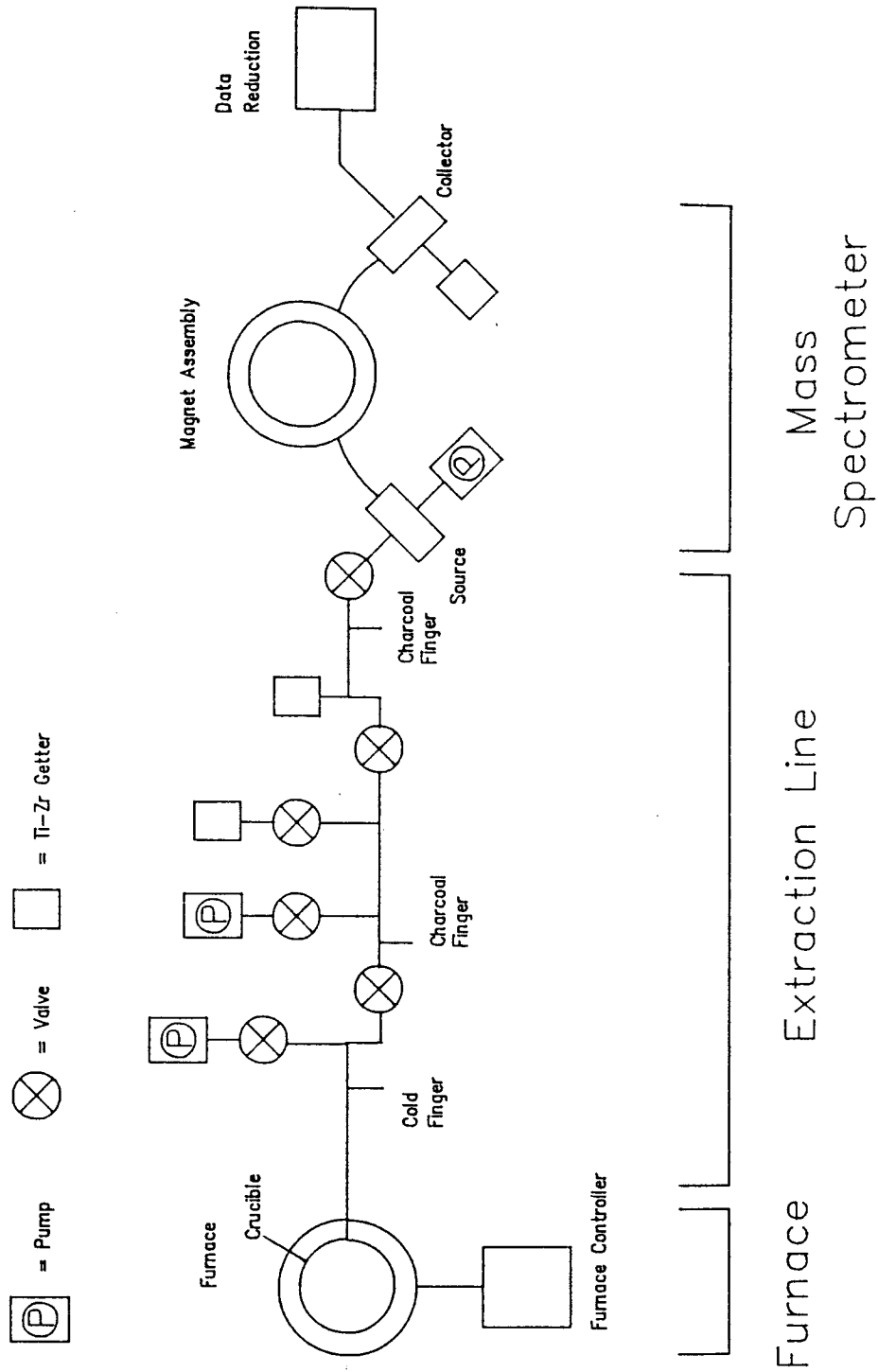


Figure 5.3

Schematic illustration of the Ar-extraction and mass spectrometer assembly at SUNYA.

an apparent age to its corresponding fraction size. Errors are assigned in the same way. A total gas age is equivalent to a K/Ar age. If a release spectrum does not indicate characteristic Ar-uptake or Ar-loss profiles, this integrated gas age can be a reasonable estimate for argon closure in the sample.

Many age spectra do not define a plateau but show complex patterns; nevertheless it is often possible to assess the existence of excess ^{40}Ar , slow cooling, or apparently simple episodic Ar-loss. In order to determine the composition of the trapped Ar component it is useful to generate an isotope correlation diagram, namely a plot of $^{36}\text{Ar}/^{40}\text{Ar}$ vs. $^{39}\text{Ar}/^{40}\text{Ar}$. The data are regressed using the method of York (1969). One of the advantages of this isochron plot is that analytical errors in ^{40}Ar and ^{39}Ar are small with respect to errors in ^{36}Ar . Therefore the errors in X and Y are relatively uncorrelated. It is also possible to readily determine the composition of a trapped $^{40}\text{Ar}/^{36}\text{Ar}$ component from the y-intercept, representing 0% radiogenic ^{40}Ar . The age is calculated from the intercept of the isochron with the x-axis, representing 100% radiogenic ^{40}Ar . Such an ideal isochron is shown in Fig. 5.4.

It is apparent from Fig. 5.5 that steps in an age spectrum do not necessarily have to define a plateau in order to constrain an isochron. For this hypothetical

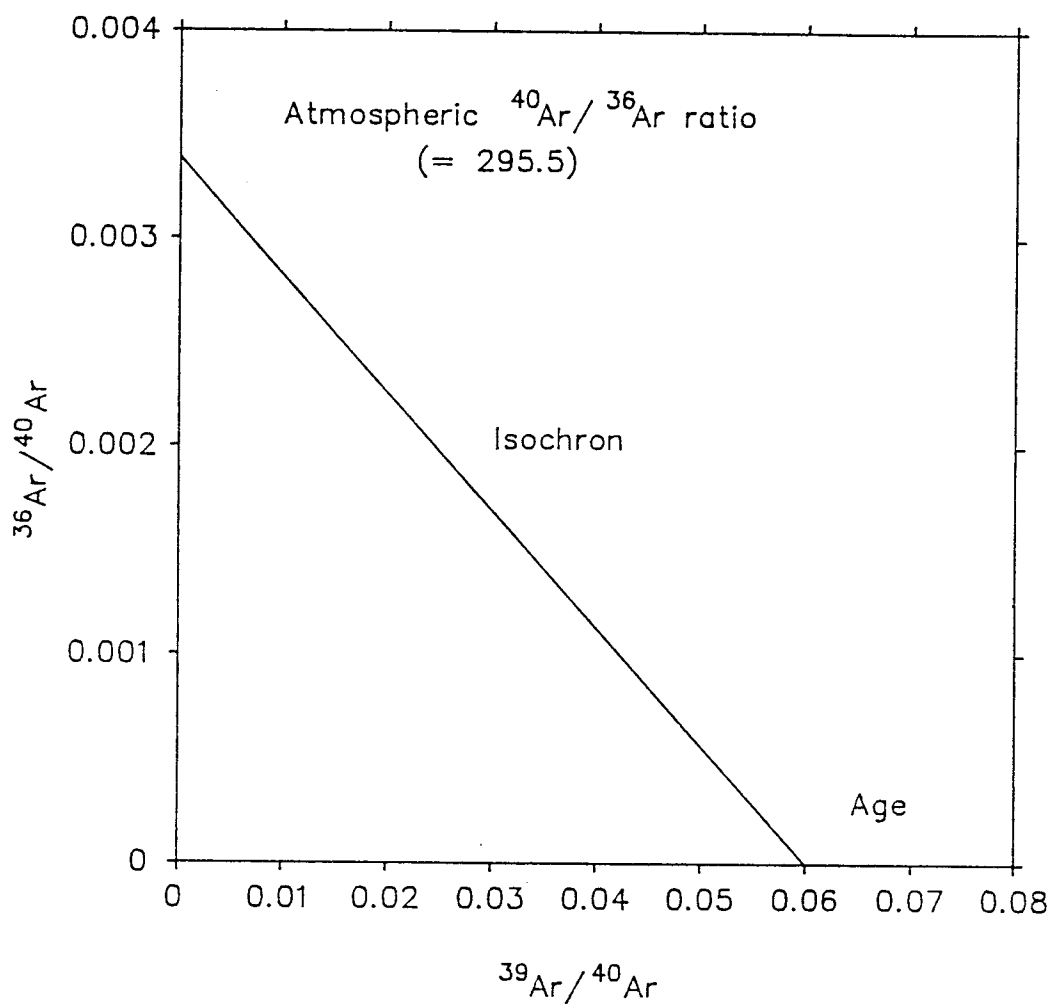


Figure 5.4 The $^{36}\text{Ar}/^{40}\text{Ar}$ vs. $^{39}\text{Ar}/^{40}\text{Ar}$ isotope correlation diagram.

Figure 5.5 Example of a hypothetical sample that contains excess ^{40}Ar for which an isochron diagram reveals the real age (next page).

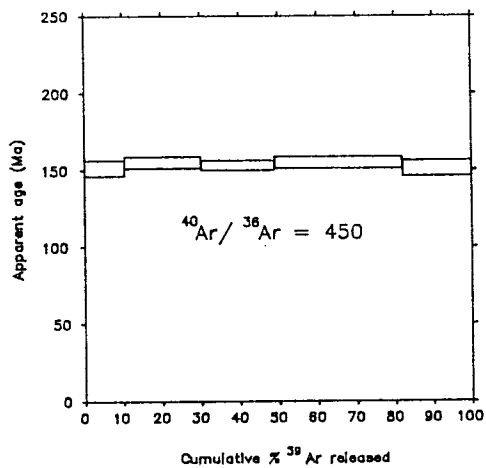
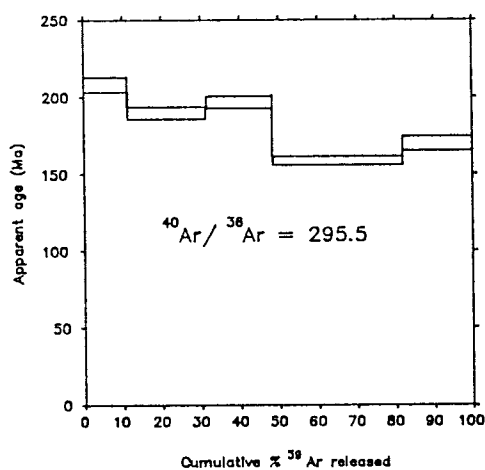
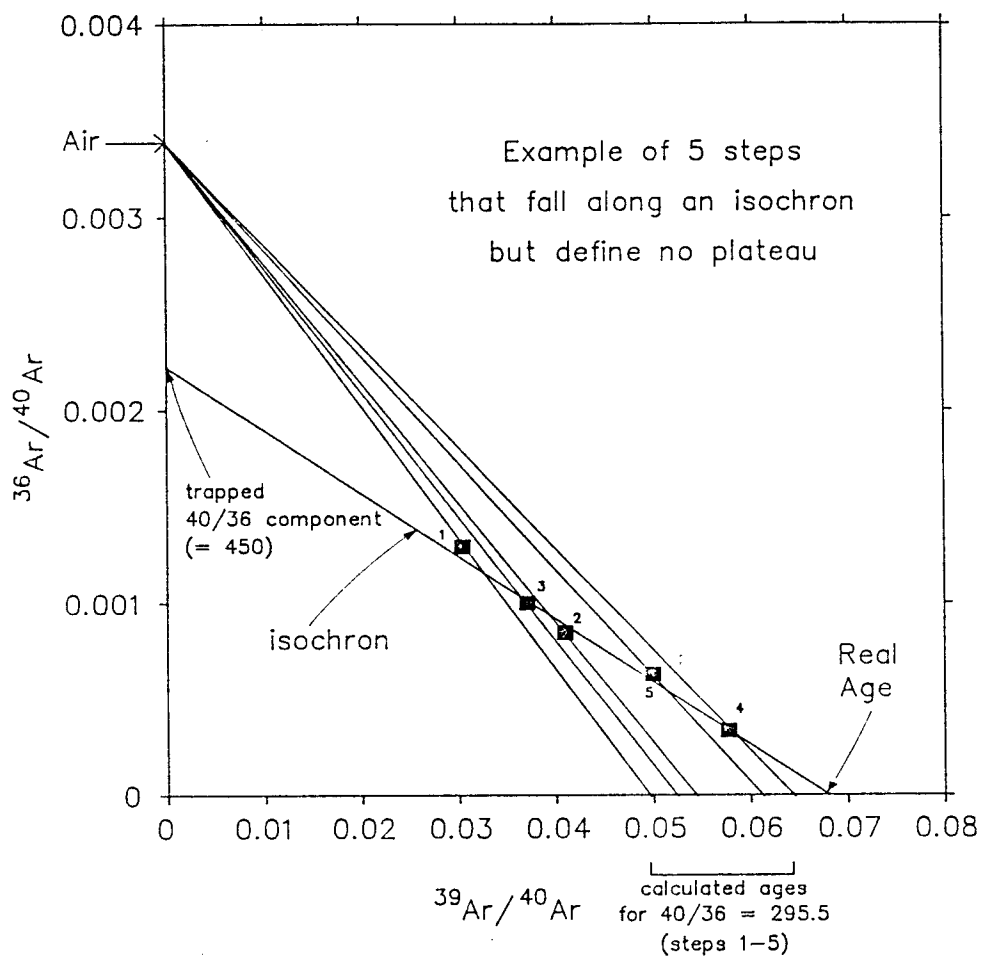


Figure 5.5

sample containing excess ^{40}Ar recalculating individual steps of a previously irregular spectrum by using the inferred $^{40}\text{Ar}/^{36}\text{Ar}$ composition yields a plateau with an age equal to the obtained isochron age (in Fig. 5.5: $^{40}\text{Ar}/^{36}\text{Ar} = 450$, and $J = 0.006$). It is therefore always worthwhile to plot the isotopic ratios on an isochron diagram: a complex age spectrum might contain a well defined isochron and thus give information which could not have been derived from inspection of the age spectrum alone.

Unfortunately many isochron diagrams also yield apparently unsystematic data that cannot be regressed in a simple way. This might be due to the presence of more than one trapped Ar composition (Harrison and Heizler, 1987). If these trapped components do not form thermally distinct reservoirs, but rather outgas simultaneously, a complex age spectrum as well as scattered isochron data will be the result.

5.3 $^{40}\text{Ar}/^{39}\text{Ar}$ Results

Eight hornblende and one muscovite sample were dated using the $^{40}\text{Ar}/^{39}\text{Ar}$ technique. The inferred ages for all nine samples are summarized in table 5.1. This section presents these results in the same order as listed in table 5.1. The age spectra and corresponding isotope correlation

Table 5.1

Sample	Isochron age	MSWD	Plateau age	Total gas age
LR 10	192 +/- 9 Ma	1.98	190 +/- 9 Ma	176 +/- 7 Ma
LR 171	190 +/- 9 Ma	11.4	191 +/- 2 Ma	190 +/- 2 Ma
LR 871	—	—	191 +/- 4 Ma	192 +/- 6 Ma
LR 1273	185 +/- 9 Ma	1.38	196 +/- 3 Ma	199 +/- 5 Ma
LR 1573	—	—	199 +/- 4 Ma	200 +/- 6 Ma
LR 82	—	—	—	149 +/- 4 Ma
D-LRO	—	—	148 +/- 1 Ma	148 +/- 2 Ma
LR 15	191 +/- 5 Ma	6.29	—	173 +/- 8 Ma
Z 53	—	—	280 +/- 0.5 Ma	258 +/- 1 Ma

diagrams for all samples are shown in Figs. 5.6 through 5.14

Hornblende gabbros

A total of five gabbro samples were dated; four of them (LR 10, LR 171, LR 871, LR 1573) are gabbro blocks that occur in the tuffaceous or argillaceous matrix of the LRO. Sedimentary contacts between blocks and matrix are usually well preserved. One sample (LR 1273) was collected from a continuous outcrop of gabbro along the South Fork of the Smith River that is in fault contact with the overlying pillow sequence as well as with the underlying pebbly mudstone.

Sample LR 10 is collected from a huge gabbro block occurring west of the mouth of Yellowjacket Creek along the South Fork of the Smith River. Its "thickness" is inferred to be approximately 180 meters (see chapter 3.3). The first 50% of ^{39}Ar released define apparent ages that young progressively, starting at 185 Ma decreasing to 140 Ma. The remaining 50% of argon release shows a poorly constrained plateau with apparent ages scattering between 187 and 207 Ma. These steps yield a plateau age of 190 ± 9 Ma (Fig. 5.6a). The two domains seem to be correlated with highly variable K/Ca ratios. The first five steps show K/Ca ratios between 0.05 and 1, while the remaining steps have

fairly constant K/Ca averaging 0.025. An isochron defined by the plateau steps indicates an age of 192 +/- 9 Ma, and an initial trapped $^{40}\text{Ar}/^{36}\text{Ar}$ component of 304 +/- 39 (Fig. 5.6b). An isochron for the first five steps projects to a similar $^{40}\text{Ar}/^{36}\text{Ar}$ composition, but indicates a markedly younger age of 149 +/- 6 Ma.

Sample LR 171 is part of a small (diameter less than 1m) gabbro block collected close to Muslatt Mountain (Fig. 4.1). It shows the least cataclastic deformation of all examined gabbros. The age spectrum (Fig. 5.7a) in a general way resembles that of LR 10, in that relatively young ages are defined by the first few heating steps and are correlated with higher K/Ca ratios. However, only the first 17% of the ^{39}Ar released show these higher K/Ca ratios which are correlated with lower ages. This early release is followed by 10 steps, the apparent ages of which scatter between 184 Ma and 208 Ma. Although somewhat disturbed these steps reveal an integrated age of 191 +/- 2 Ma. A poorly defined isochron (MSWD = 11.4) indicates an atmospheric $^{40}\text{Ar}/^{36}\text{Ar}$ value of 283 +/- 93 and an age of 190 +/- 9 Ma (Fig. 5.7b). The total gas age for LR 171 is 190 +/- 2 Ma.

Sample LR 871 was collected on the South Kelsey Trail between Yellowjacket Creek and Buck Creek (Fig. 4.1), and is inferred to belong to the same gabbro olistolith as LR 10 (see fig. 3.25). The age spectrum of LR 871 (Fig. 5.8)

is characterized by early apparent ages of greater than 200 Ma, followed by two steps with lower ages of 155 Ma. Again, high K/Ca ratios are associated with this initial release. This is followed by a 6 step plateau that is comprised of 67% of the total ^{39}Ar released and yields a plateau age of 191 ± 4 Ma.

Sample LR 1573 is a block of about 100 m diameter from the South Fork of the Smith River (Fig. 4.1), set in a pebbly mudstone matrix and displaying excellent sedimentary contacts with the overlying and underlying pebbly mudstone units. The age spectrum (Fig. 5.9) is complex with apparent ages that show an antithetic correlation with the calculated K/Ca ratios, with the higher ratios associated with the lowest apparent ages. This shows quite well for steps 5 through 9, and steps 12 through 14. The differences in K/Ca, however, are rather subtle. Steps 4 through 9 comprise 46% of the total ^{39}Ar released and define a hump-shaped plateau with an age of 199 ± 4 Ma. The isotopic ratios of the individual steps do not constrain a meaningful isochron. An integrated gas age over all steps yields 200 ± 6 Ma.

A fifth gabbro sample, LR 1273, was collected from a continuous gabbro outcrop on the mouth of Horse Creek (Fig. 4.1); here gabbro is in fault contact with an overlying sequence of pillow lavas, but does not show preserved stratigraphic contacts with the matrix of the LRO. The age

spectrum for LR 1273 (Fig. 5.10a) shows high apparent ages of 210-250 Ma for the initial 7% ^{39}Ar released. Two minor steps with ages of 183 and 189 Ma, respectively, are followed by a well defined plateau that is comprised of 8 steps and represents 85% of the total gas released. The apparent ages range between 192 and 201 Ma, and constrain a plateau age of 196 ± 3 Ma. On a $^{36}\text{Ar}/^{40}\text{Ar}$ vs. $^{39}\text{Ar}/^{40}\text{Ar}$ plot (Fig. 5.10b) the plateau steps define an isochron, although the data cluster close to the abscissa introducing a large uncertainty for the y-intercept. The inferred $^{40}\text{Ar}/^{36}\text{Ar}$ component has a non-atmospheric composition of 377 ± 64 . The x-intercept yields a younger isochron age of 185 ± 9 Ma compared to the 196 ± 3 Ma plateau age. The K/Ca ratios for all plateau steps average 0.03, indicating the degassing of a homogeneous amphibole phase.

Calc-alkaline Dikes

Calc-alkaline dikes intruding the LRO show cross-cutting relationships with both the gabbro blocks and tuffaceous matrix; they also cut the undisturbed contacts between these plutonic blocks and the matrix of the LRO. Hornblendes from two such dikes (LR 82, D-LRO; for the sampling location see Fig. 4.1) were dated.

The age spectrum of LR 82 (Fig. 5.11) is disturbed with apparent ages ranging from 136 Ma to 176 Ma; no

plateau is developed and there is also no obvious relation between K/Ca and the age of the individual steps. The initial release of gas fractions from sites with relatively high K/Ca ratios is not reflected in the age spectrum. K/Ca ratios drop from initial values of 1.5 to 0.04 and exhibit a slight rise to about 0.09 for the remaining 45% of the total ^{39}Ar released. In the absence of a well defined isochron, the only age estimate is therefore obtained from the integration of all steps to a total gas age of 149 ± 4 Ma.

A second dike, D-LRO, produced a similar, but somewhat less irregular age spectrum (Fig. 5.12). An initial step with an anomalously old age of 180 Ma is followed by steps ranging from 138 to 158 Ma. The spectrum appears to be highly unsystematic in its mid-section, but shows more constant apparent ages between 145 and 153 Ma for the remaining 44% of argon release with nearly constant K/Ca. The last six steps constrain a plateau age of 148 ± 1 Ma. The total gas age of 148 ± 2 Ma is calculated omitting the first step and thus perhaps excluding an excess argon component.

Andesite clasts

Sizable porphyritic volcanic clasts are rare in both the pebbly mudstone and the volcanoclastic section of the

LRO. Sample LR 15 is an andesitic volcanic clast from a volcanoclastic breccia overlying pillow lavas and sheared greenstone on the South Fork of the Smith River. The age spectrum (Fig. 5.13a) is complex: relatively young ages for the first few steps are followed by a hump-shaped release pattern showing older apparent ages up to 210 Ma. Between 52 and 80% cumulative release there are five successive steps with overlapping ages ranging between 192 and 210 Ma. After the early release of a high-K phase, the K/Ca ratios average 0.032 for the remaining 65% of the spectrum. No unequivocal age can be assigned: a $^{40}\text{Ar}/^{39}\text{Ar}$ isochron age of 191 +/- 5 Ma is somewhat misleading, since most steps scatter close to the abscissa and do not define a straight line (Fig. 5.13b). The slope is determined by the low radiogenic fusion step and a cluster of points representing the "plateau" between 52 and 80%, forcing a seemingly well constrained age of 191 Ma. An integrated total gas age yields a significantly younger age of 173 +/- 8 Ma.

Metamorphic Clasts

The micaschist clast Z 53 was collected from undeformed pebbly mudstone that overlies pillow lavas and sheared pebbly mudstone along the GO-road. The age spectrum for a muscovite (Fig. 5.14) resembles a pattern typical for argon loss, but suffers from the unsystematic behaviour of

- Figure 5.6 (a) Age spectrum and (b) isochron diagram for LR 10.
- Figure 5.7 (a) Age spectrum and (b) isochron diagram for LR 171.
- Figure 5.8 Age spectrum for LR 871.
- Figure 5.9 Age spectrum for LR 1573.
- Figure 5.10 (a) Age spectrum and (b) isochron diagram for LR 1273.
- Figure 5.11 Age spectrum for LR 82.
- Figure 5.12 Age spectrum for D-LRO.
- Figure 5.13 (a) Age spectrum and (b) isochron diagram for LR 15.
- Figure 5.14 Age spectrum for Z 53.

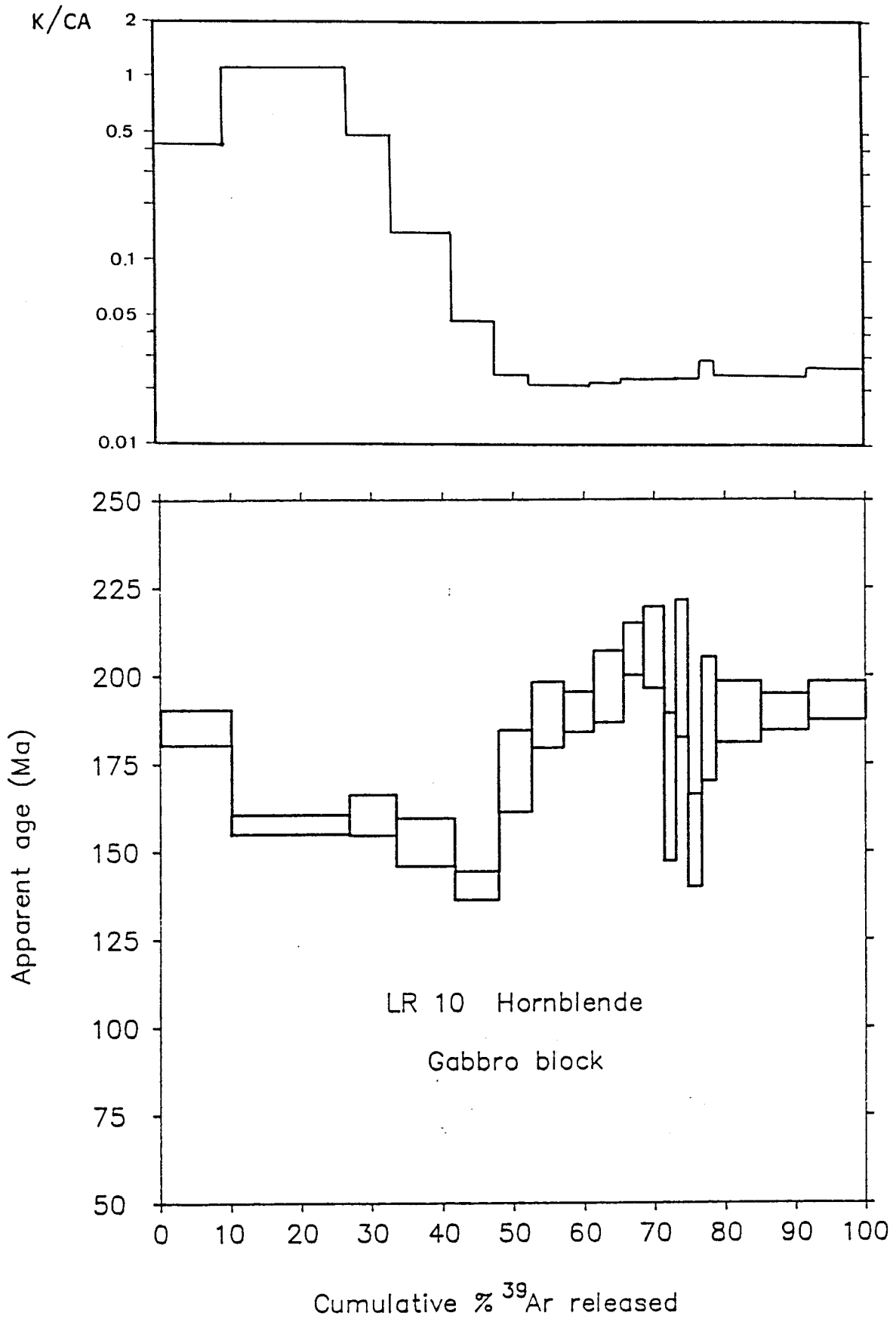


Figure 5.6a

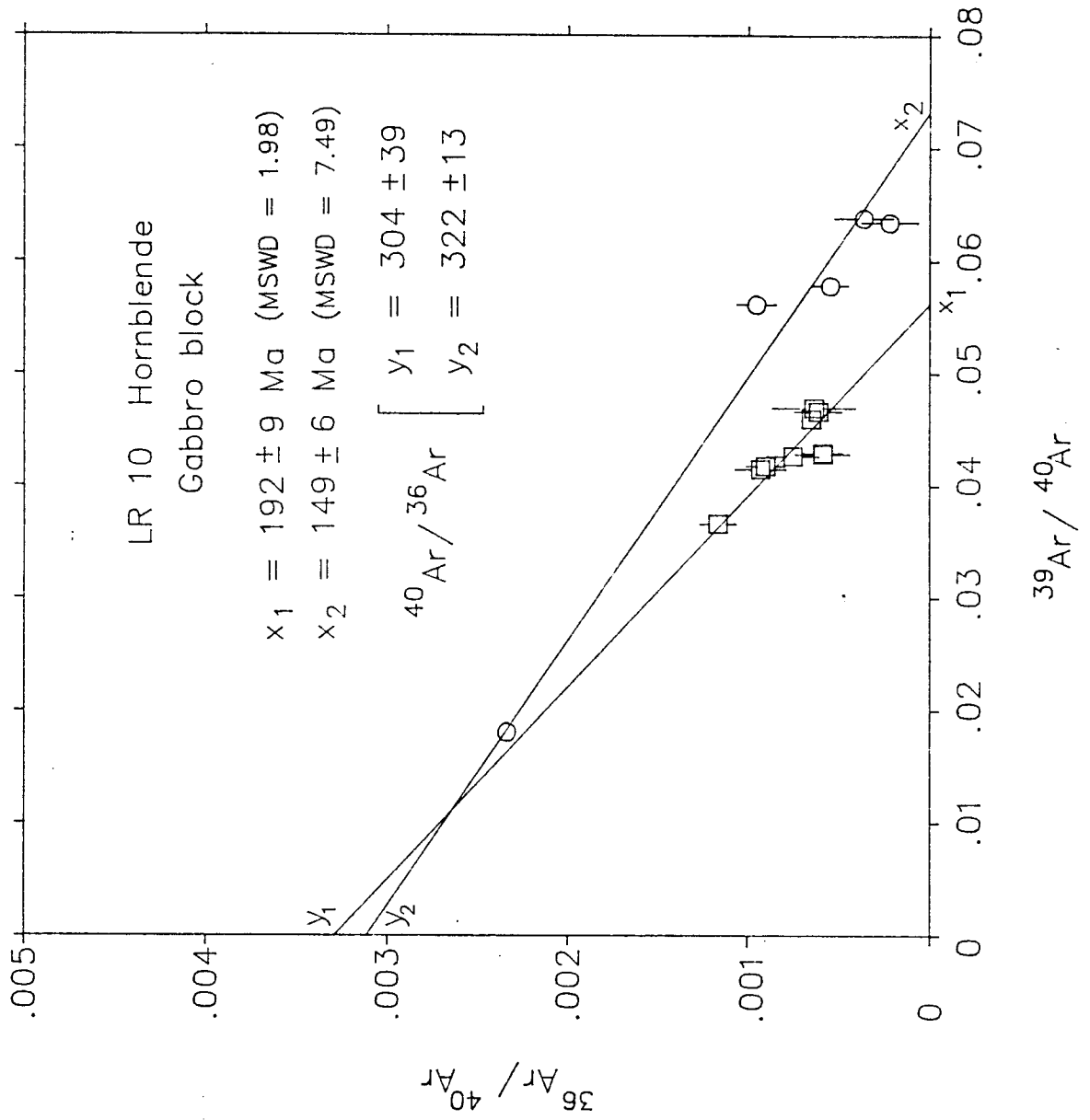


Figure 5.6b

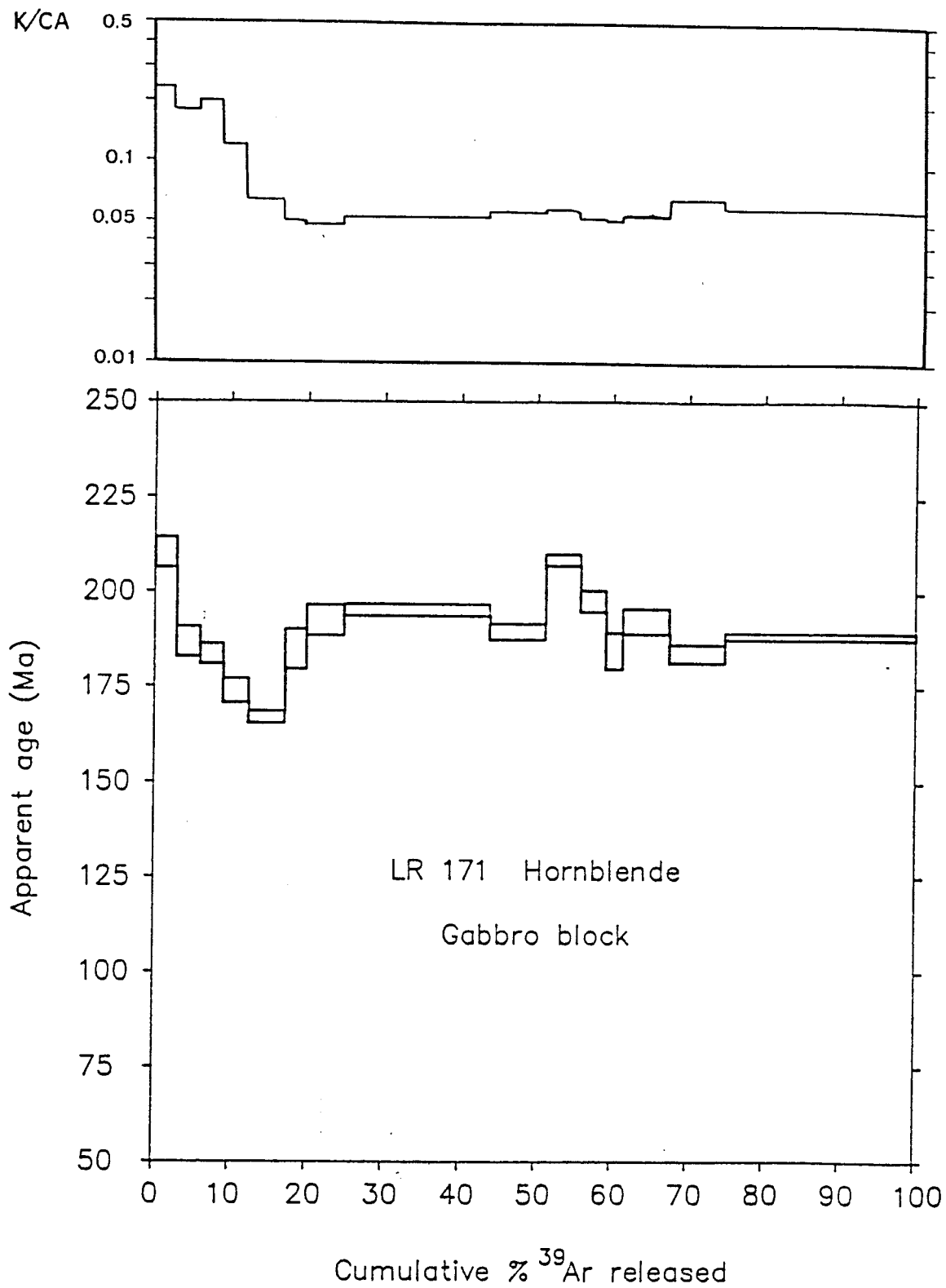


Figure 5.7a

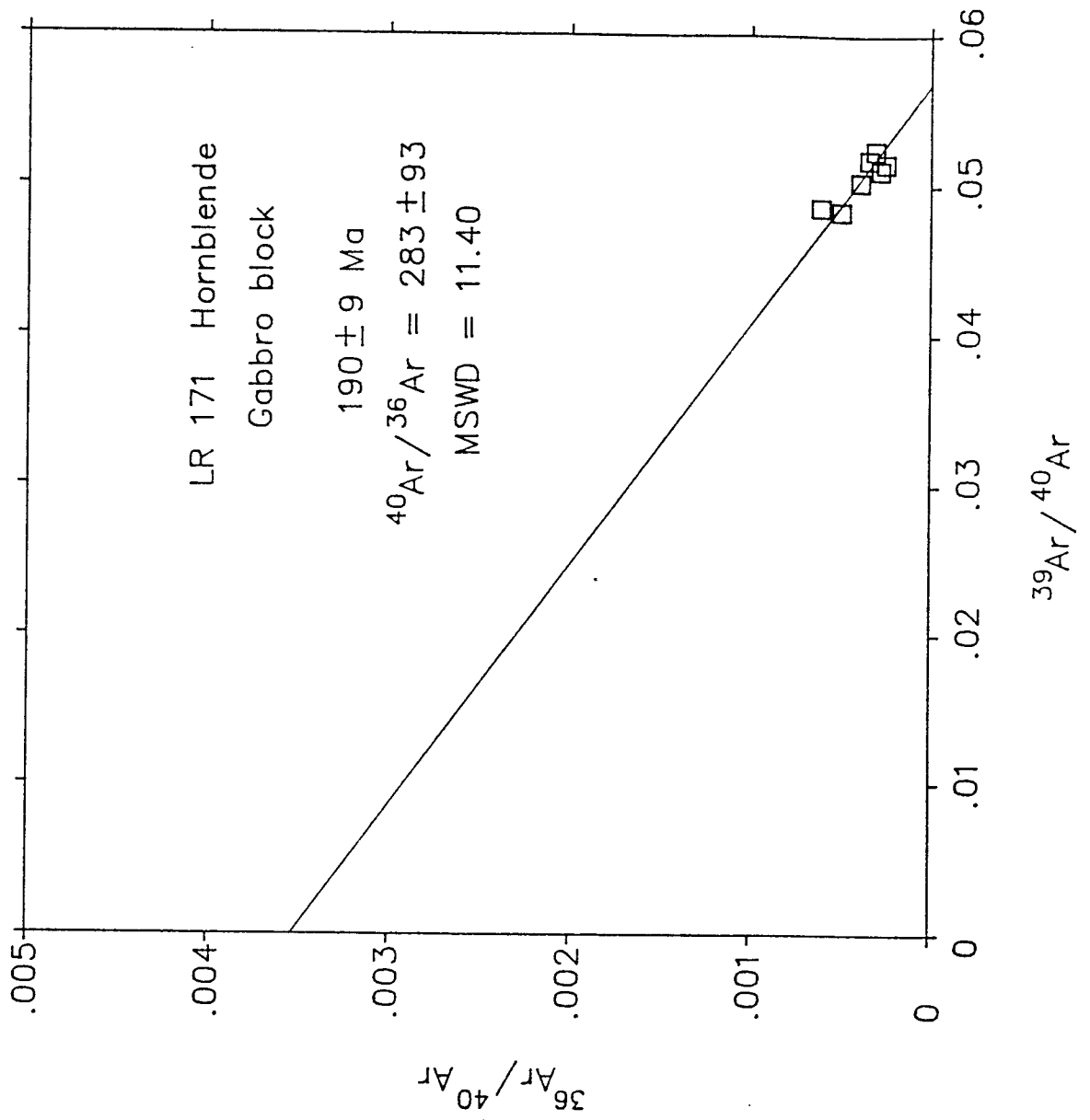


Figure 5.7b

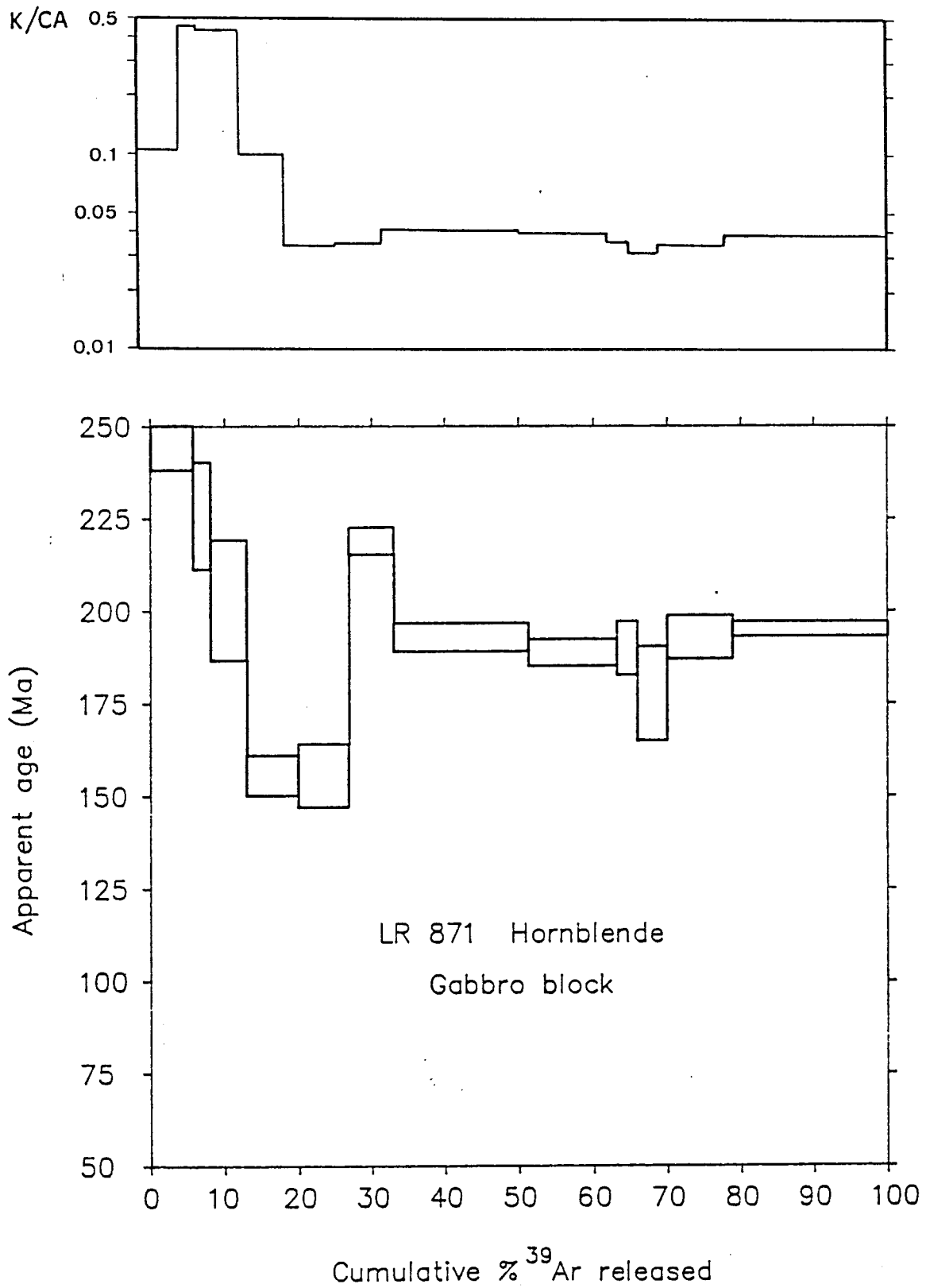


Figure 5.8

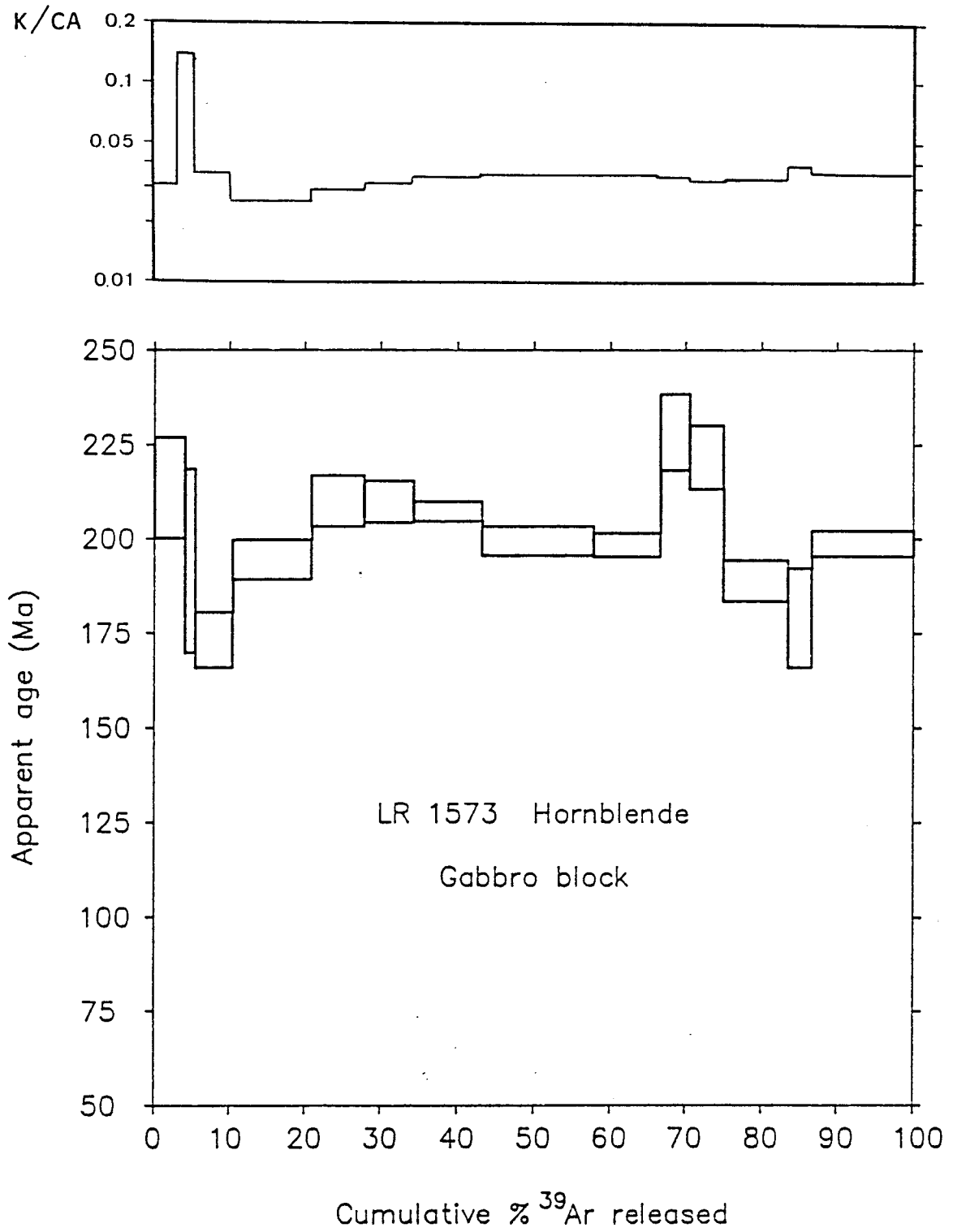


Figure 5.9

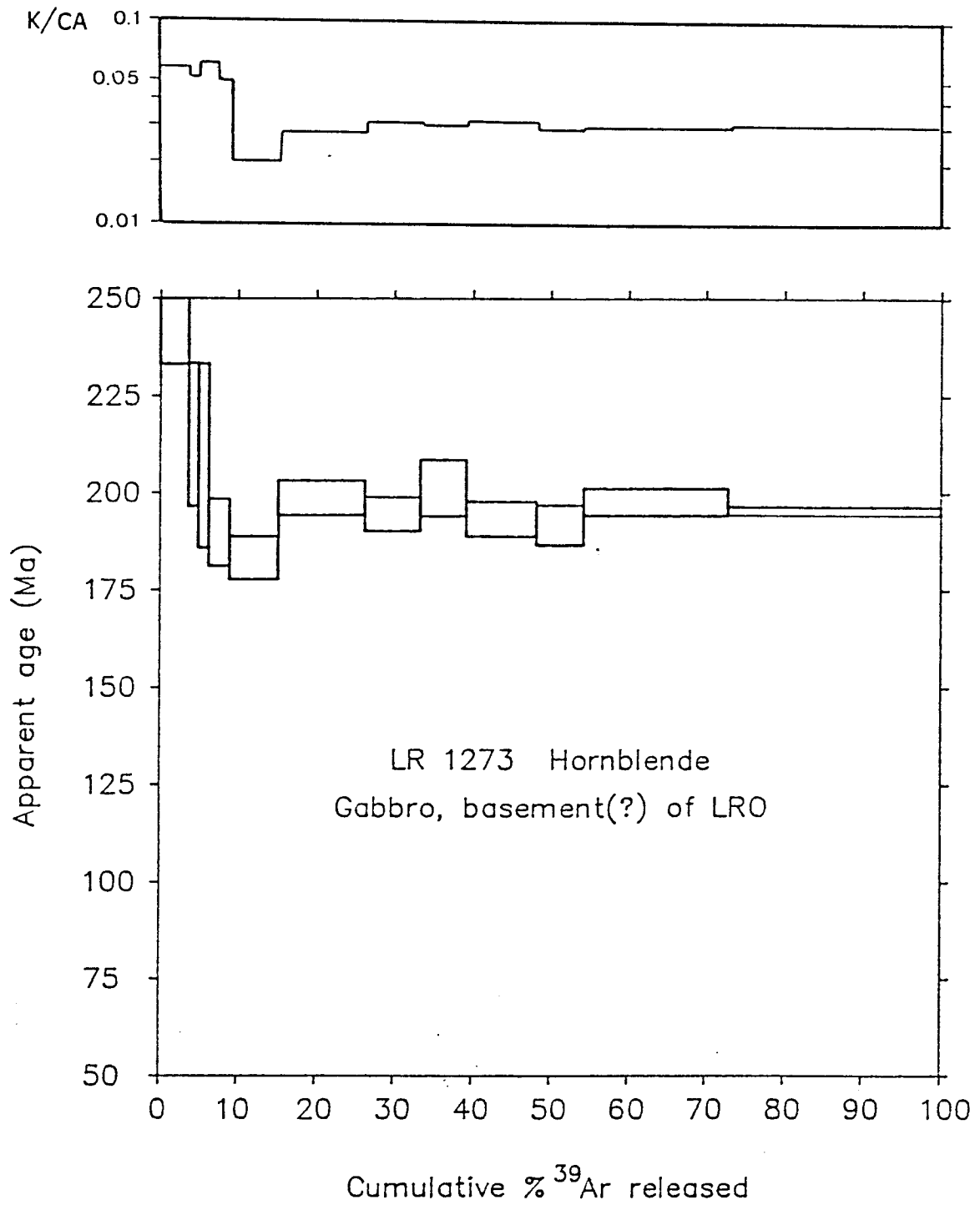


Figure 5.10a

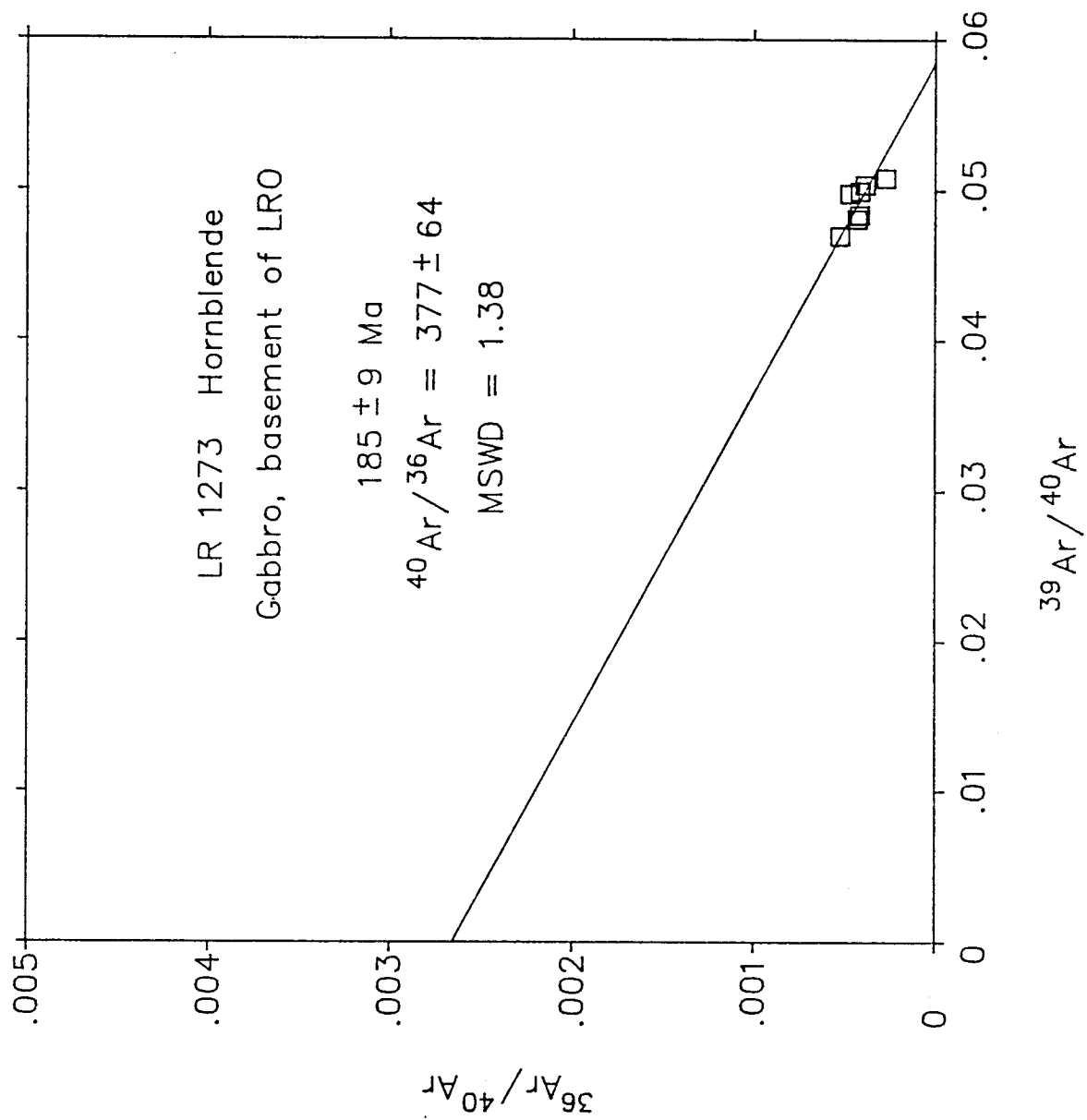


Figure 5.10b

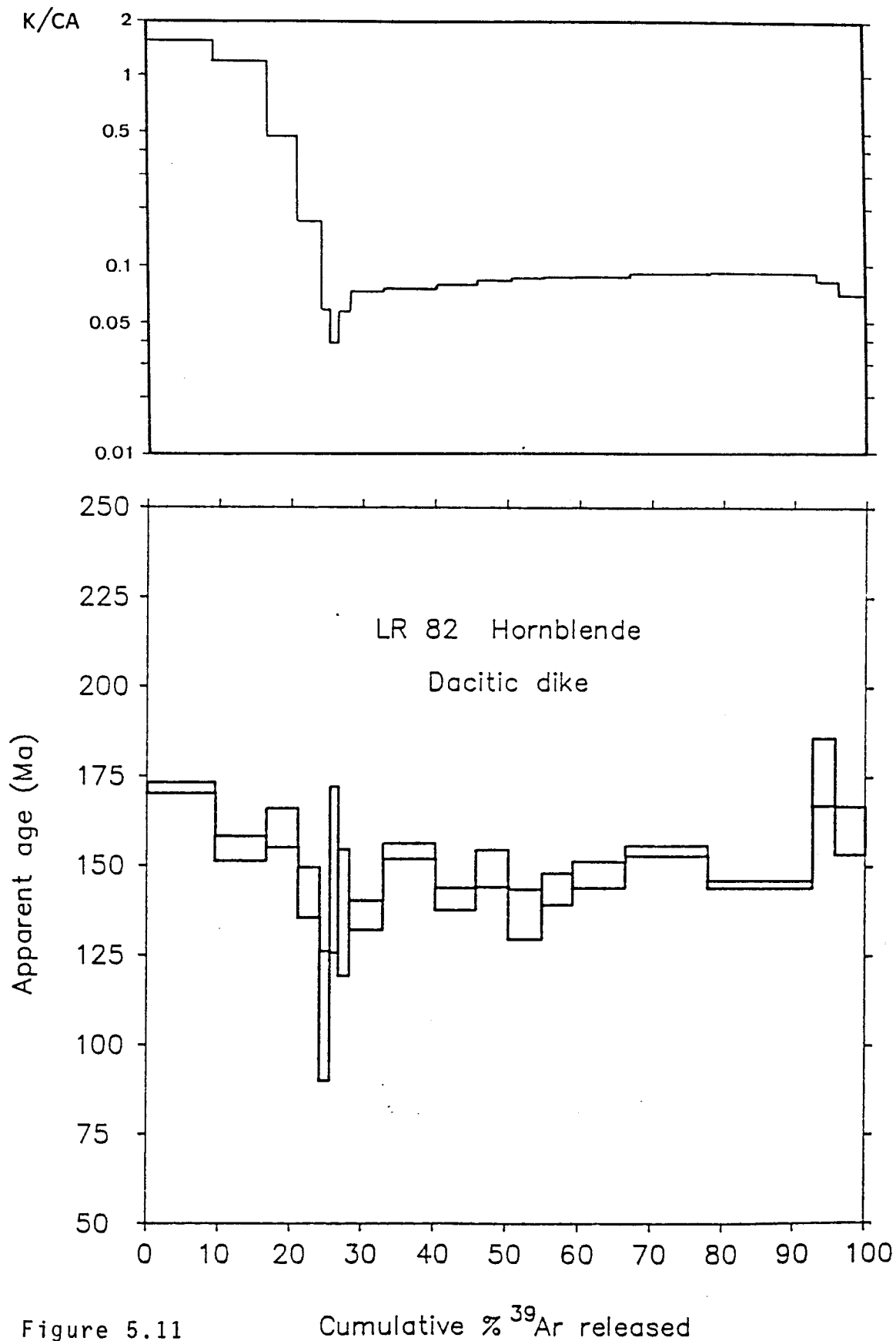


Figure 5.11 Cumulative % ^{39}Ar released

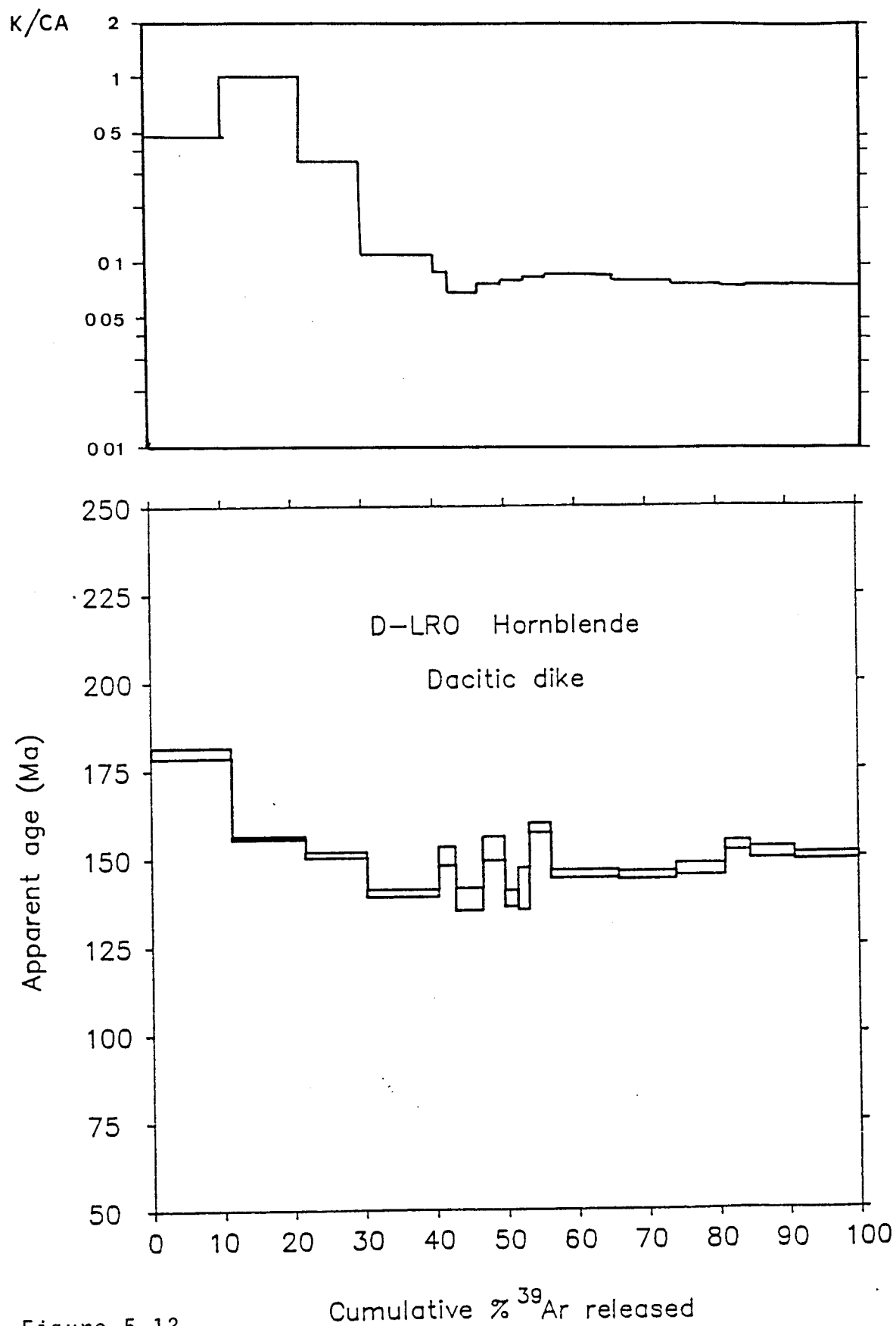


Figure 5.12

Cumulative % ^{39}Ar released

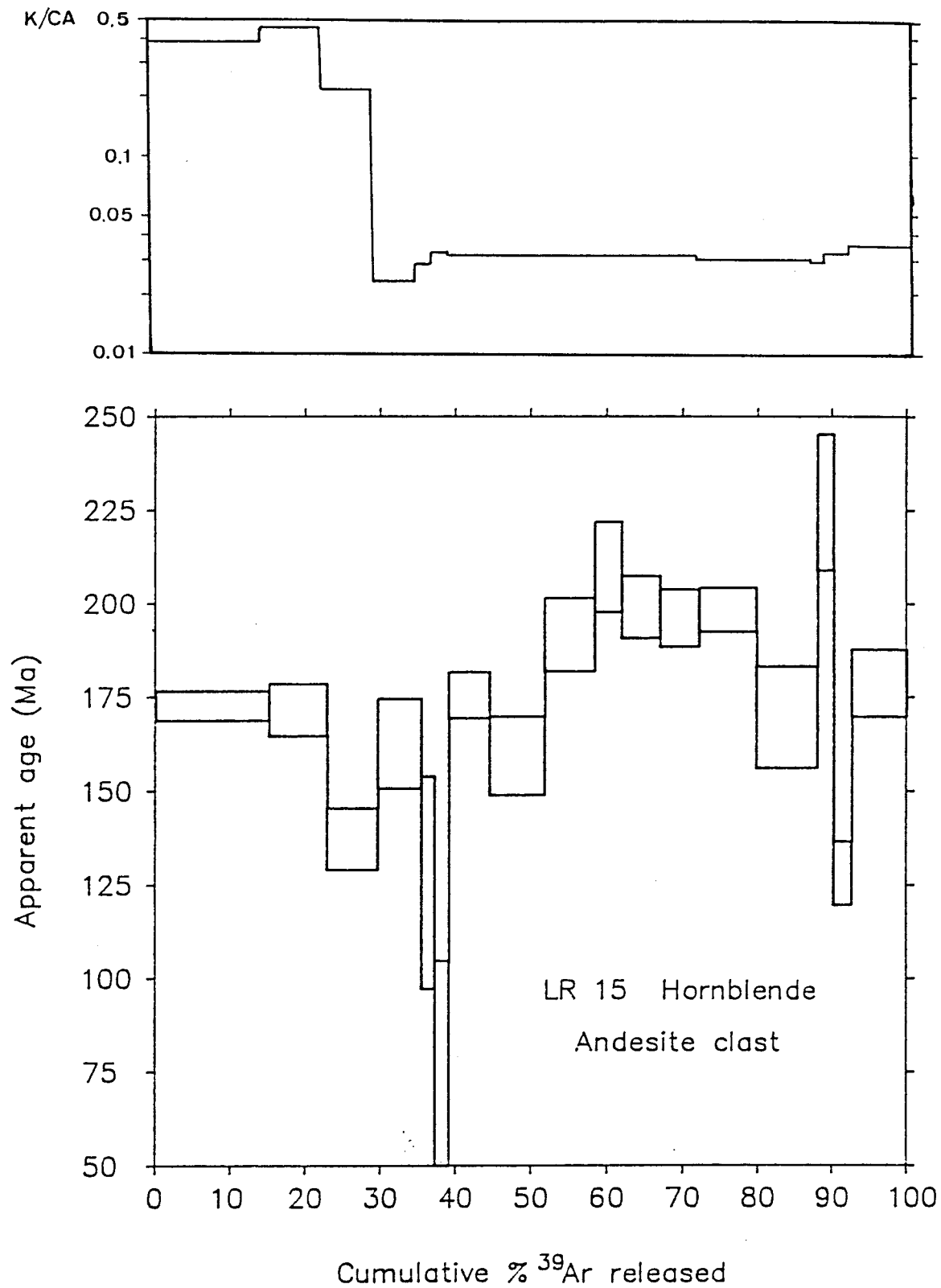


Figure 5.13a

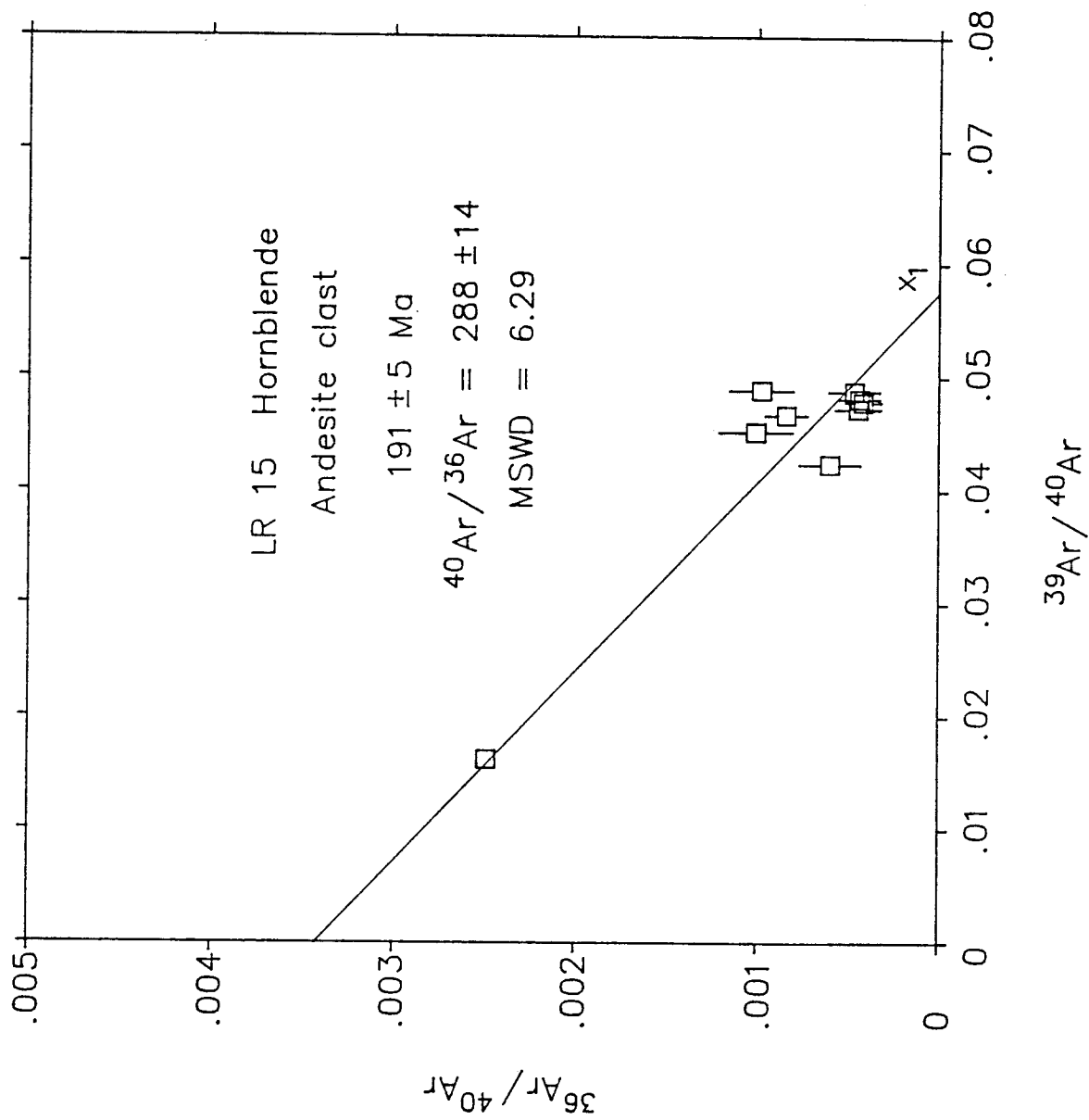


Figure 5.13b

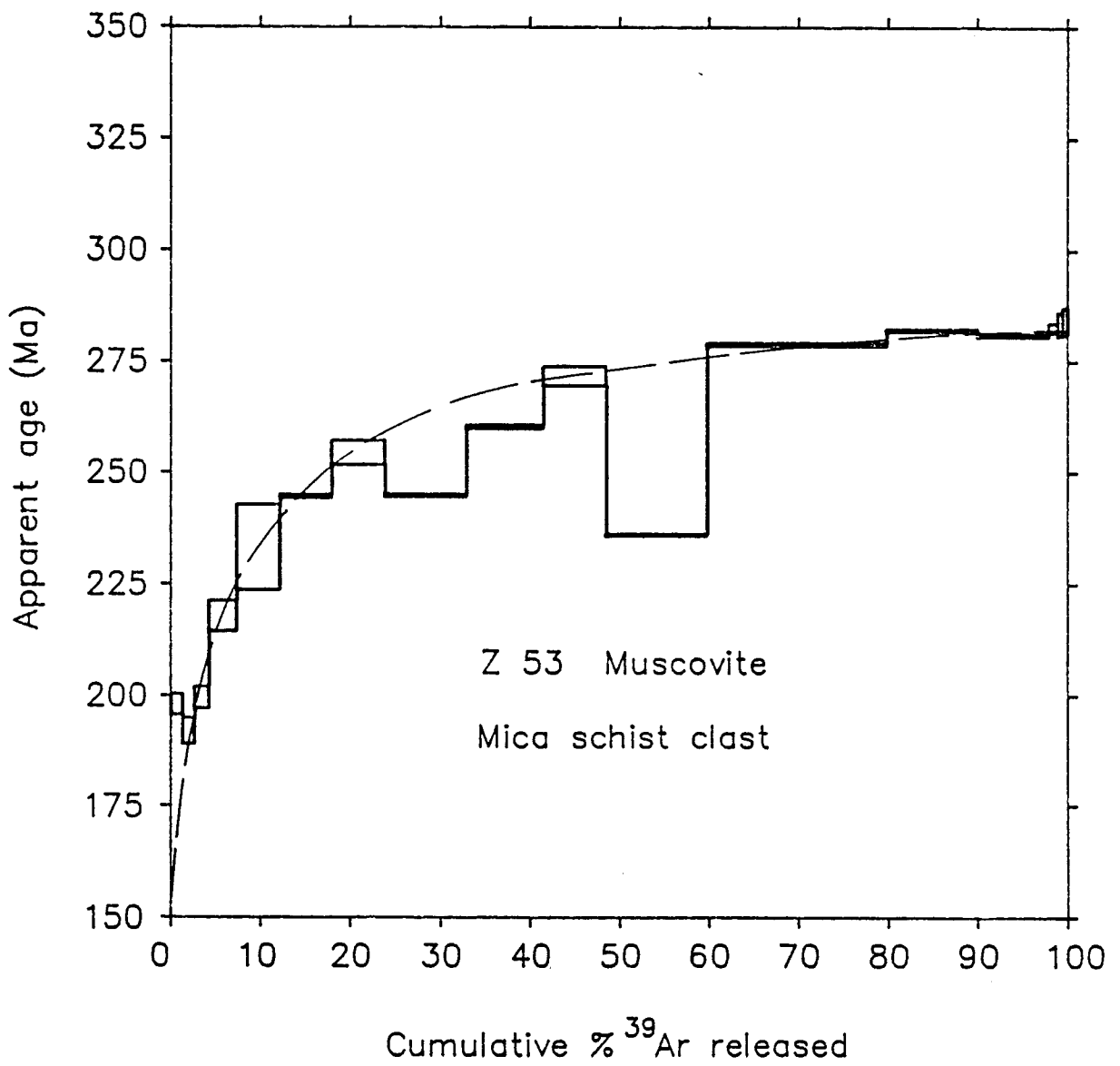


Figure 5.14

two steps showing ages that are obviously too young to fit the loss profile. Moreover, the analytical uncertainty for the first seven steps or so appears to be uncharacteristically large, suggesting a possible problem during the gettering process. Interpolating through the irregularities mentioned above, the apparent ages of steps comprising the first 50% of total ^{39}Ar released rise along a convex upward curve from 190 Ma to 275 Ma. The remaining steps define a small, but well constrained plateau that reveals an plateau age of 280 ± 0.5 Ma. The proportional loss of ^{40}Ar is about 20% of the total ^{40}Ar present and can be obtained by integration of the area above the interpolated loss curve. The lower y-intercept of the loss curve is not sufficiently resolved, but appears to project to an age of about 150 to 160 Ma.

5.4 Discussion

All analyzed hornblendes from gabbros in the LRO yield consistent ages of about 190 Ma, even though with quite large associated errors. Although most hornblende release spectra have indications of Ar-loss, the plateau ages are interpreted to approximate crystallization ages. Two lines of evidence support this interpretation:

(1) Nevadan metamorphism did not exceed prehnite-pumpellyite to lower greenschist grades, and therefore would not have affected the argon distribution in hornblendes. Closure with respect to argon diffusion in hornblende occurs at significantly higher temperatures than those reached during Nevadan regional metamorphism.

The observed argon loss in LR 10, and to a smaller extent in LR 171, LR 871, and LR 1573, however, is probably due to diffusion of ^{40}Ar from less retentive sites already at low temperatures. These sites are invariably associated with high K/Ca ratios, suggesting the presence of two phases with different argon retentivity. As pointed out in chapter 3.2, the amphiboles exhibit a pronounced zonation (see Fig. 3.17a) indicating such a heterogeneity. Alternatively, exsolution in metamorphic amphiboles is known to result in sites of contrasting argon retentivity (Harrison and Fitzgerald, 1986).

In particular the spectrum of LR 10 suggests the presence of two argon retention sites. Argon contained in a phase with high K/Ca ratios has obviously diffused more readily than argon sequestered in more retentive low-K phases. If these phases of high K/Ca were produced by exsolution processes, then the exsolution boundaries might have acted as paths for more rapid Ar diffusion at relatively low temperatures (Harrison and McDougall, 1981; Harrison and Fitzgerald, 1986). The isochron age of $149 \pm$

6 Ma for these early steps suggests that the thermal event causing the indicated argon-loss coincides with the Nevadan metamorphism. The timing of the Nevadan orogeny in the Klamath Mountains is tightly constrained by geochronologic and supporting field data as 146-150 Ma (Saleeby and others, 1982; Harper and Wright, 1984, Harper and others, 1986).

An alternative explanation of initial low ages associated with high K/Ca ratios considers the presence of a fine grained phyllosilicate phase. As seen, the hornblende grains display complex zonation and alteration, possibly to aggregates of minute, high-K phyllosilicates. Since the Ar-retentivity of phyllosilicates is known to be less than that of amphiboles, it would be likely that these phases experienced episodic argon loss during the Nevadan event.

Argon loss has also occurred in the other gabbro samples, but the presence of excess ^{40}Ar interferes with the indicated loss profiles. Excess ^{40}Ar is evidenced by consistently older apparent ages for steps comprising the first 10-20% of total ^{39}Ar released. Compositions of the trapped $^{40}\text{Ar}/^{36}\text{Ar}$ component obtained from γ -intercepts in isotope correlation diagrams, however, are usually atmospheric (within error).

(2) U/Pb age data on zircon from a plagiogranite dike within LR 10 are in apparent agreement with the 190 ± 9

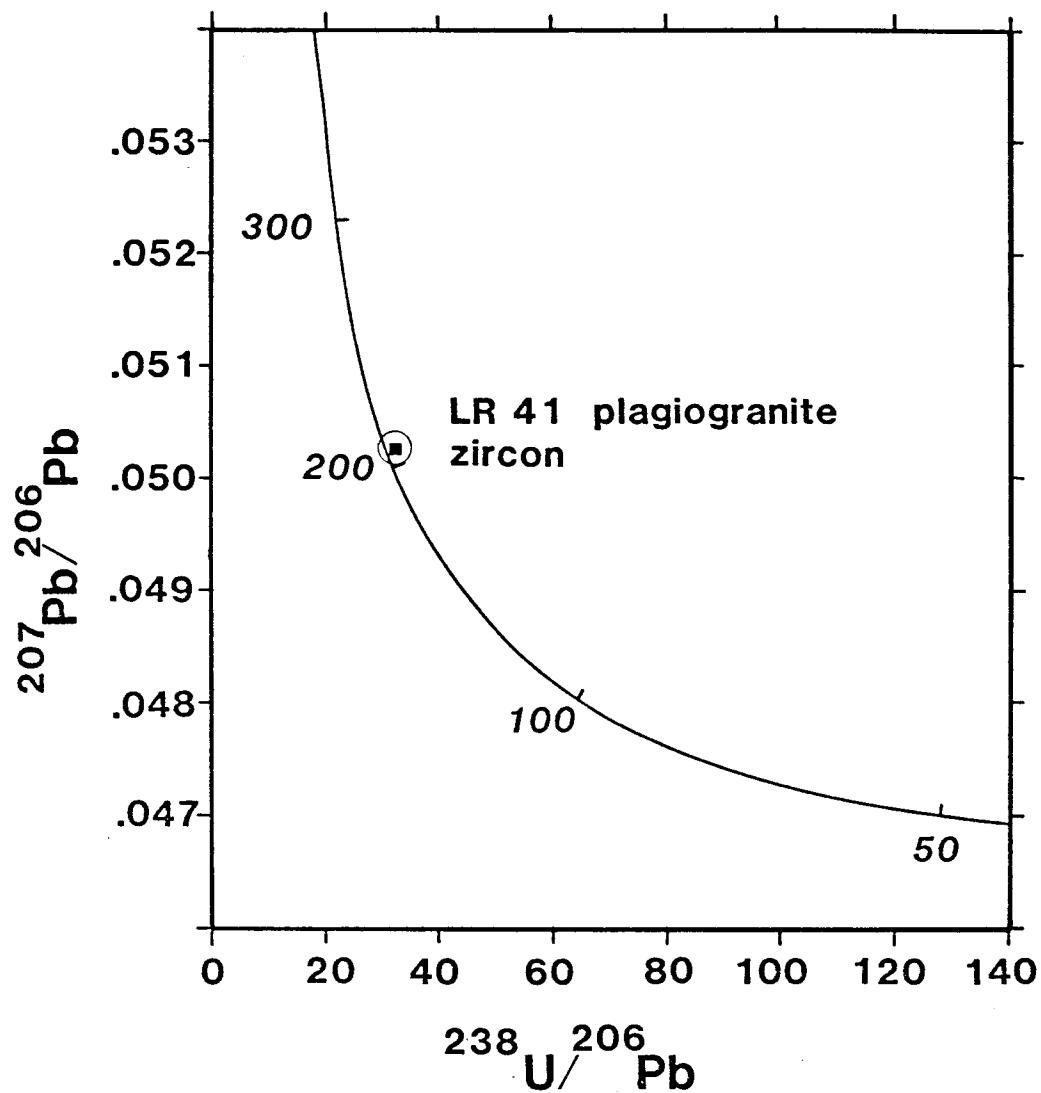


Figure 5.15 $^{207}\text{Pb}/^{206}\text{Pb}$ vs. $^{238}\text{U}/^{206}\text{Pb}$ ratios for zircon from plagiogranite LR 41.

Ma plateau age for hornblende from LR 10 (Wright, pers.comm., 1985; Ohr and others, 1986). The $^{206}\text{Pb}/^{238}\text{U}$ and $^{207}\text{Pb}/^{235}\text{U}$ ages are both 198 Ma, whereas the $^{207}\text{Pb}/^{206}\text{Pb}$ age is 205 Ma. U/Pb zircon ages are usually excellent indicators for crystallization ages of igneous rocks; however, for very young ages the small signal of radiogenic lead makes the U/Pb system less precise. For this age determination, approximately 25 kilogram of rock were collected; sample preparation and analysis was performed at J.Wright's laboratory at Stanford University. The zircon yield was poor, allowing only one size fraction to be analyzed. The U/Pb data are listed in Appendix IV; the $^{207}\text{Pb}/^{206}\text{Pb}$ vs. $^{206}\text{Pb}/^{238}\text{U}$ ratios are plotted in Fig. 5.15.

Harper and others (1983), Norman (1984), and Harper and others (1985) interpret the occurrence of gabbro within the LRO as either basement horsts or, in the case of readily recognizable clasts, as locally derived talus from the Josephine ophiolite. This study shows that all of the gabbro blocks found within the LRO are between 190 and 200 Ma old, clearly older than the Late Jurassic Josephine ophiolite. Dated plutons within the southern portion of the Rattlesnake Creek terrane (RCT) define an age range of 208-193 Ma based on U/Pb data on zircons (Wright, 1982; Wright and Wyld, 1985). Gray (1985) reports plutons within

the same age bracket from the Orleans area further to the north, thought to be correlative with the type RCT to the south (Irwin, 1972; Gray and Wright, 1984). Intrusive rocks of this age have not been found in other Klamath terranes, but are typical for an extensive Late Triassic to Early Jurassic magmatic belt that extends along much of the margin of North America (Gray, 1985).

The most abundant of these intrusive rocks in the RCT are hornblende gabbros and diorites (Gorman, 1985; Gray, 1985), equivalent to those found in the LRO. The presence of abundant gabbro blocks in the LRO that yield $^{40}\text{Ar}/^{39}\text{Ar}$ ages comparable to the Late Triassic-Early Jurassic U/Pb ages of Wright (1982) and Wright and Wyld (1985), is evidence that these blocks are derived from the Rattlesnake Creek terrane.

In chapter 3.3 it was speculated that LR 1273 could represent the basement of the LRO. If this is correct, then the 185 +/- 9 Ma age would have profound implications on the tectonic setting of deposition of the LRO. Norman (1984) mapped the thrust fault between the western Jurassic belt (WJB) and the RCT just east of the LRO. Thus the olistostrome is part of the younger WJB; this is also constrained by the presence of graywackes and shales of the Galice Formation which apparently conformably overlie the LRO (see chapter 3). If older Triassic and Early Jurassic rocks of the RCT form the basement to the LRO, then it

appears likely that they comprise at least parts of the structural basement of the WJB and thus of the Josephine ophiolite as well. Possible tectonic scenarios that explain the deposition of the LRO on top of a distinctly older structural basement will be presented in chapter 6.

Calc-alkaline dikes intruding the Josephine ophiolite and overlying Galice Formation are known to range in age from 146-151 Ma (Dick, 1976; Saleeby and others, 1982; Harper and others, 1986). These dikes are regionally metamorphosed, locally strongly deformed, and are inferred to be of pre-Nevadan or syn-Nevadan age (Harper and Wright, 1984). They therefore provide an older age bracket for the Nevadan orogeny. Dikes LR 82 and D-LRO belong to a suite of abundant north-south trending calc-alkaline dikes and sills that are related to the intrusion of the Summit Valley pluton. This pluton cuts the Preston Peak thrust and is therefore of syn- to post-Nevadan age. The obtained ages of 148 +/- 2 Ma and 149 +/- 4 Ma therefore further substantiate the tight timing for the Nevadan orogeny (Harper and others, 1986).

The age of the two dikes within the LRO also places a lower age bracket on the deposition of the olistostrome, since they cut across block-matrix boundaries. If the LRO were simply a thrust-related melange recording the emplacement of the RCT over the western Jurassic belt, then

these dikes should also record the deformation that would have caused the generation of such a melange.

The obtained total gas age of 173 +/- 8 Ma for the andesite clast LR 15 is identical to K/Ar ages of 168-177 Ma on volcanoclastic rocks of the western Hayfork terrane (Wright and Fahan, 1987). These rocks are interpreted to represent the extrusive section of a Middle Jurassic arc to the east. The K/Ar ages of Wright and Fahan are in agreement with Middle Jurassic U/Pb zircon ages on plutons that built the plutonic root for this arc (see also chapter I). Based on only one total $^{40}\text{Ar}/^{39}\text{Ar}$ gas age it is not possible to safely correlate the volcanoclastic components in the LRO to the Middle Jurassic arc of the western Hayfork terrane. More data are needed to further test this tempting suggestion.

Unfortunately it was not possible to separate the few isolated hornblende grains from rare crystal tuffs within the LRO. At the beginning of this study it was hoped to utilize a new state-of-the-art mass spectrometer to obtain single crystal ages. This facility, however was not available. The idea to date detrital hornblende as well as amphibole from volcanic fragments contained in the tuffaceous deposits, did not succeed for this reason. It is therefore not possible to constrain the age of the volcanoclastic matrix of the LRO.

A comparable metamorphic age to the plateau age of 280 +/- 0.5 Ma for the mica schist clast is not known from the Klamath Mountain terranes. Lanphere and others (1968) report distinctly older Devonian K/Ar ages from the central metamorphic belt of about 380 Ma. The Stuart Fork terrane has yielded K/Ar metamorphic ages as old as 220 Ma (Hotz and others, 1977). Again, one date is not sufficient to assess the character of a possible metamorphic source terrane: metamorphic ages of clasts in the LRO might well span a wider range. Since there is no shortage of metamorphic clasts in the pebbly mudstone section, a more rigorous sampling and dating project should clarify the relationships of these clasts to the older Klamath terranes to the east. Episodic loss of ^{40}Ar is clearly indicated in the obtained age spectrum (Fig. 5.14): the first infinitesimally small step of an ideal loss-profile (the y-intercept in a real age spectrum) determines an upper limit to the time at which argon diffusion occurred (Turner, 1968). Although the loss curve is insufficiently defined, its approximate intercept at about 150 Ma is consistent with the timing of the Nevadan thermal event.

Mica schist clasts within the pebbly mudstone often occur associated with fossiliferous limestone cobbles of eastern Klamath affinity (see chapter 3). Despite the lack of a clearly constrained source area for the mica schist clasts, they nevertheless require the proximity of a

continental-type source area, probably one of the adjacent Paleozoic terranes further to the east in the Klamath Mountains.

Summary

The ages of the clasts contained in either the tuffaceous or the argillaceous matrix can only indicate maximum ages for the deposition of the LRO:

- A mica schist clast yields a muscovite age of 280 Ma. This is a metamorphic age not yet reported from the Klamath Mountains, and is older than ages for common mica schists of the central metamorphic belt.
- Gabbro blocks yield consistent ages between 190 and 200 Ma, and are probably derived from the Rattlesnake Creek terrane.
- Gabbro from the possible basement of the LRO yields an age of 185 +/- 9 Ma, indistinguishable from gabbro blocks in the LRO.
- An andesite clast gives only ambiguous age information, but the total gas age of 173 Ma would correlate this clast to Middle Jurassic volcanoclastic rocks of the western Hayfork terrane.
- Calc-alkaline dikes yield ages of 148 and 149 Ma, respectively. This represents a lower age bracket for the deposition of the LRO and regional metamorphism.

Chapter VI

Discussion and Concluding Remarks

The preceding chapters were devoted to the petrography and stratigraphy of the LRO, to the geochemistry of its ophiolitic clasts and basement rocks, and to the geochronology of blocks and dikes in the LRO. This chapter attempts to briefly integrate these findings into a reconstruction of a possible ancient tectonic environment in which the LRO formed.

Norman and others (1983) coined the name "Lems Ridge olistostrome" to indicate its sedimentary origin. However, it appears obvious from the discussion in chapters II and III that this name is somewhat unfortunate: the occurrence of rocks which were definitely not derived from slumps or debris flows (e.g. bedded chert, graded sandstones) indicates that the LRO is a mappable unit that contains olistostromal material (e.g. pebbly mudstone), however is not an olistostrome per se. In addition, the limited structural data from the South Fork of the Smith River, as well as the observed gross outcrop pattern seem to suggest that the LRO contains local unconformities, implying a sequence of events that probably spanned an extended period of time and were caused by several mechanisms.

The LRO fits the descriptions of both type II and type III melange (Cowan 1985a, b). This accentuates the stark contrast between typical block-in-matrix textures (pebbly mudstone; gabbro blocks in tuffaceous and argillaceous matrices) on the one hand, and preserved stratiform layering on the other hand (mudstone interfingering with pillow lavas; interlayering of green tuff and pebbly mudstone; the presence of beds of graded sandstone, chert, and siliceous argillite). Unstratified, massive chaotic units represent slope instabilities and the resulting collapse of sediment accumulations in the respective volcanic and terrigenous source areas (slumps, debris flows, pyroclastic flows). This contrasts with more stable periods during which depositional conditions allowed the formation of stratigraphically more coherent sequences.

The LRO is, *sensu strictu*, a melange that contains abundant, but not exclusively olistostromal material. There is no evidence for predominant tectonic disruption of formerly continuous beds, nor are there hints for a tectonic emplacement of exotic blocks within the LRO. The LRO is most similar to type II and type III melanges, suggesting sediment accumulation in a structurally controlled basin adjacent to both volcanic and continental sources (Cowan, 1985b). The most convincing argument that the LRO is indeed a stratigraphic unit is derived from conformable relationships with the overlying and underlying

units. However, the contacts are gradational and therefore difficult to locate: the upper contact to the Galice Formation stretches from the local occurrence of graywacke beds along Buck Creek to the apparent paucity of pebbly mudstone and green tuff further eastward from Buck Creek. The lower contact displays interdigitating pebbly mudstone and pillow lavas along the Smith River, suggesting the contemporaneous accumulation of olistostromal material with the extrusion of the pillow basalts.

This situation is illustrated in the idealized cross-section through the LRO of Fig. 6.1. In this reconstruction the Buck Mountain fault is interpreted as a shallow thrust, truncating the igneous basement of the LRO at a rather shallow level. This notion is supported by gravity data for the western Klamath Mountains, shown in Fig. 6.2. The LRO is downfaulted along the northward continuation of the Buck Mountain fault -- if there were an ophiolitic basement of substantial thickness underlying the LRO, then this high-density basement should deflect the gravity contour lines in Fig. 6.2. However, the distribution of contour lines does not indicate any high-density subsurface unit north of the LRO, but rather follows closely the Preston Peak thrust.

Harper and others (1985) in a cross-section extended the JO below the LRO, implying that the LRO overlies pillow

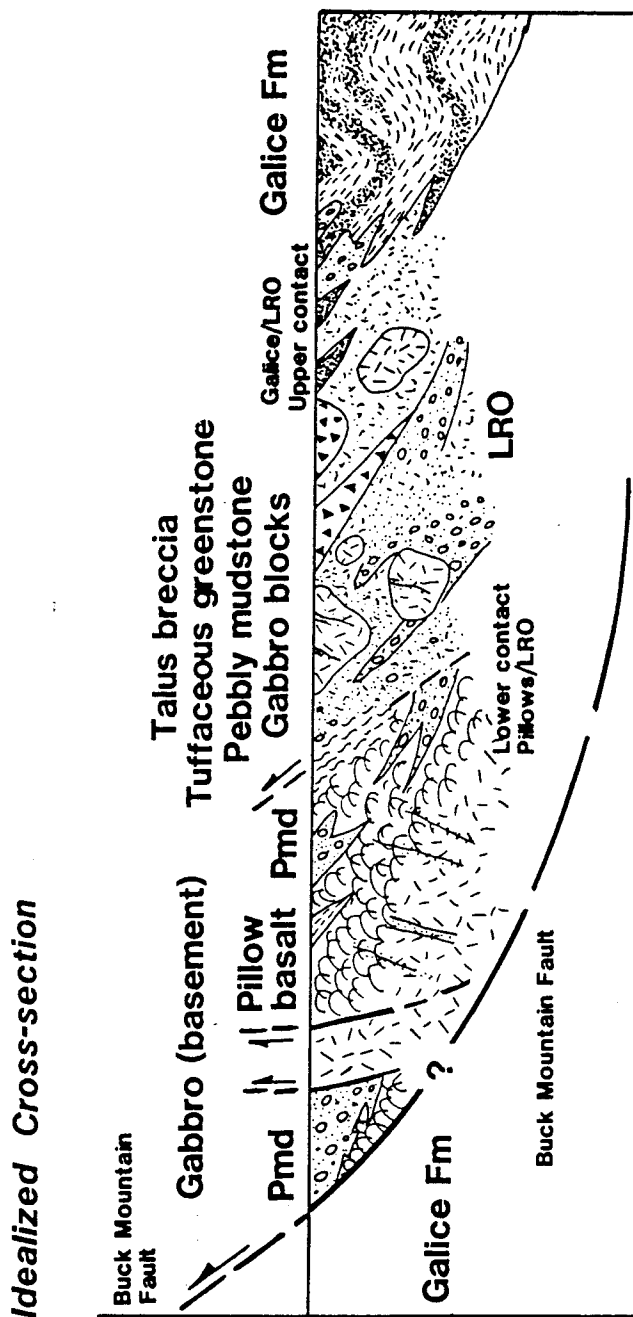


Figure 6.1

Idealized cross-section through the northern part of the Lems Ridge olistostrome, following the stratigraphic column of fig. 3.16.

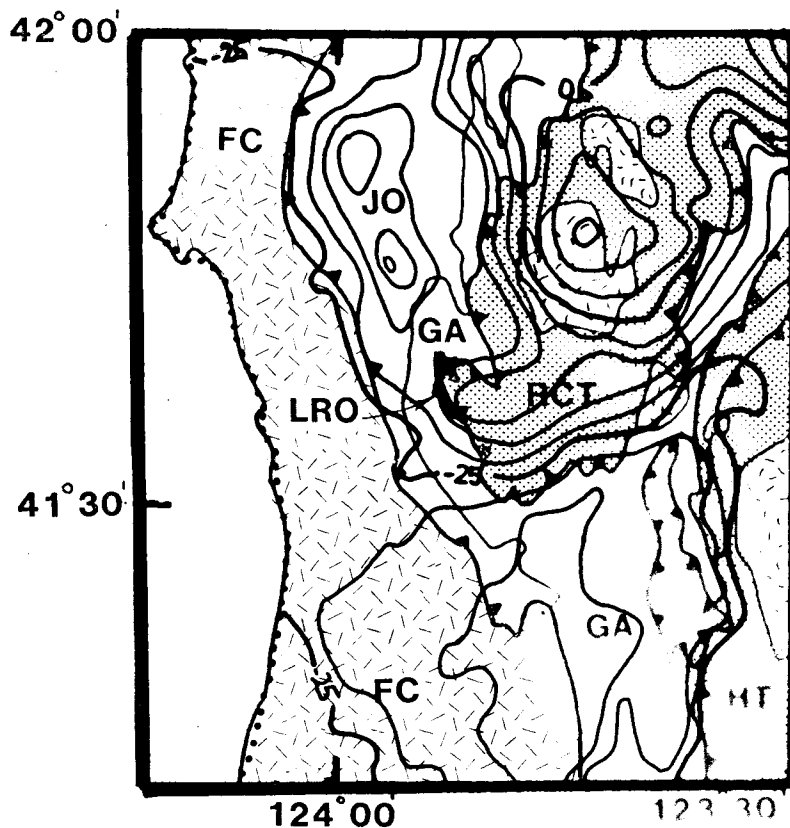


Figure 6.2

Generalized geology of the western Klamath Mountains with superimposed isostatic residual gravity map of the area. HT = Hayfork terrane, RCT = Rattlesnake Creek terrane, GA = Galice Formation, LRO = Lems Ridge olistostrome, JO = Josephine ophiolite, FC = Franciscan Complex (modified from Jachens and others, 1986).

lavas and gabbros of the Josephine ophiolite (JO). This is consistent with their interpretation of the LRO as a fracture zone deposit within the Josephine ophiolite.

Norman and others (1983), Norman (1984), and Harper and others (1985) summarize evidence pertaining to this interpretation. One line of argumentation emphasizes the direct genetic link between the JO and the LRO, including:

- The limited extent and the geometry of the LRO which is consistent with the inferred spreading geometry of the JO (spreading parallel to the outcrop pattern of the LRO).
- The thin crustal section of the JO, consistent with generation near a fracture zone, as oceanic crust is observed to be very thin in the vicinity of modern fracture zones (see chapter II).
- The conformable relationship of the LRO and an igneous basement, interpreted as equivalent to the JO.
- The Galice Formation conformably overlies both the JO and the LRO, implying that both are of about the same age and occur in a similar structural position.
- The occurrence of apparently Late Jurassic chert pebbles and boulders in the LRO.
- The occurrence of ophiolitic clasts that were apparently derived from the JO.
- The common appearance of Fe-Ti basalts in the upper part of the JO, as basalts are distinctly higher in

Fe, Ti, and incompatible elements adjacent to modern fracture zones (see chapter II).

Another group of arguments suggests a fracture zone related origin of the LRO, regardless of its connection to the Josephine ophiolite:

- The abundance of clasts of serpentinite, ultramafic rocks, and plutonic rocks. Similar assemblages are commonly dredged from modern fracture zones (e.g. Fisher and others, 1986).
- The cataclastic fabric of gabbro blocks is consistent with exposure of lower crustal rocks to the sea floor in an active fault environment.
- The occurrence of a matrix poor, igneous and ultramafic breccia is consistent with commonly observed mass wasting from oversteep fault scarps and flanking walls in recent fracture zones.
- Topographical depressions are associated with fracture zones, thus providing the depositional basin needed for the accumulation of the LRO over an extended period of time.

This study, in general, re-evaluated the former group of evidence while essentially verifying the latter group. It also added some of the much needed geochronological information pertaining on the character and source of the gabbro basement and blocks.

Certainly the most unexpected result is the surprisingly old age of both types of gabbro in the LRO. Ages clustering between 185 and 200 Ma strongly suggest a correlation with plutonic rocks from within the Rattlesnake Creek terrane. The conclusion appears unescapable that the LRO overlies a part of the Rattlesnake Creek terrane. However, the taxing question remains whether the basal pillow lavas are also of RCT origin, or if they are correlated in any way with the Josephine ophiolite.

The basal pillow basalts of the LRO range from within-plate lavas to enriched MORB and lack the characteristic supra-subduction zone signature of the vast majority of the JO pillows and dikes. Gorman (1985) reports basaltic rocks with E-type MORB chemistry from an area of the RCT adjacent to the LRO. These E-MORBs occur as blocks in the basal melange and as pillows and massive flows in the overlying volcanic unit. The age for these basalts is poorly constrained, but is tentatively estimated to be Late Triassic to pre-Late Jurassic (Gorman, 1985). Elsewhere in the RCT 193-208 Ma plutons intrude the basal melange unit, suggesting a Late Triassic minimum age. The comparable pillow lavas from the LRO overlie Early Jurassic cherts and are in structural contact with basement gabbro. Relative age, structural position and the enriched chemistry of these lavas could be consistent with an rifting event in the RCT, preceding the main spreading

that generated the Josephine ophiolite.

On the other hand, the only occurrence of E-type MORB in the JO is located just west of the LRO, leaving some room for speculation such as interpreting the basal pillow lavas as spillover basalts (Suppe and others, 1981). This term is used to describe basalts that flow from a spreading axis across a fracture zone trough, as reported from ridge-transform intersections (Karson and Dick, 1983). Not only would this model explain the deposition of the pillow lavas on an older and foreign basement, it also accounts for the observed interlayering of pillow basalt with sediment. In addition, sparse mafic dikes with the same enriched geochemistry as the pillows could be interpreted as occasional feeder dikes to those spillover lavas.

The geochemistry of the Buck Mountain block breccia is less controversial; the occurrence of both transitional and primitive island-arc tholeiitic basalts reflects the same geochemical trend as in the Josephine ophiolite. Mafic dikes and diabase breccias with a similar geochemical signature also occur in the Preston Peak area (Snoke, 1977) and in the RCT adjacent to the LRO. However, unlike the Buck Mountain breccia, those breccias are not associated with blocks of ultramafic cumulates and serpentinized refractory mantle rocks. In lieu of other promising interpretations, the Buck Mountain breccia is therefore thought as being derived from the JO: ultramafic rocks,

serpentinites, and diabase blocks containing sheeted dikes are probably a talus deposit that formed along a submarine fault scarp. The lack of extrusives in this talus breccia is consistent with the predominant exposure of lower crustal rocks and mantle lithologies in modern oceanic transform environments.

Pebbly mudstone and the tuffaceous rocks of the LRO suggest a bilateral filling from a continental margin and active island arc, respectively.

The most peculiar clasts within pebbly mudstone are scorias with a distinct alkaline within-plate chemistry. Their sheer presence suggests that the deposition of pebbly mudstone is perhaps contemporaneous with the early stages of intra-arc rifting within the existing island-arc system; however, silicic members of the usually bimodal rift-volcanism were not found. Other clasts include sedimentary and metamorphic lithologies, all of which are readily available from the older Klamath terranes to the east that constitute a long-lived continental margin during Middle to Late Jurassic times.

The chemistry of the abundant tuffaceous greenstones and breccias is transitional between island-arc tholeiitic and calc-alkaline; a tentative total gas age of an andesitic block is equivalent to reported K-Ar ages from the Middle Jurassic western Hayfork terrane. Unfortunately

no age information for the tuffaceous matrix is available. The implication that an active island-arc was present during the deposition of the LRO is unquestionable. However, the tuffaceous rocks could be either derived from the Middle Jurassic arc east of the LRO, or alternatively could be shed off the Late Jurassic arc system, whose rifting off the existing older arc initiated the generation of the Josephine ophiolite.

Geochronological information on the tuffaceous greenstones would help more than any other age information to constrain the real depositional age of the LRO. Thus far it is known that the LRO must be younger than approximately 190 Ma (gabbro blocks, basement), must be younger than Early Jurassic (radiolarians in bedded chert and chert pebble), and possibly younger than 173 Ma (questionable age on an andesite boulder). It is inferred that blocks of diabase, serpentized ultramafic rocks, and sparse plutonic rocks of a talus deposit are derived from the Josephine ophiolite: thus the age of the LRO may be as young as 160 Ma, the age of the Josephine ophiolite itself. Cross-cutting dikes have typical Nevadan ages around 150 Ma and indicate a minimum age for the LRO.

Figure 6.3 schematically illustrates the main conclusions pertaining on the tectonic setting and depositional environment of the LRO: the model suggested

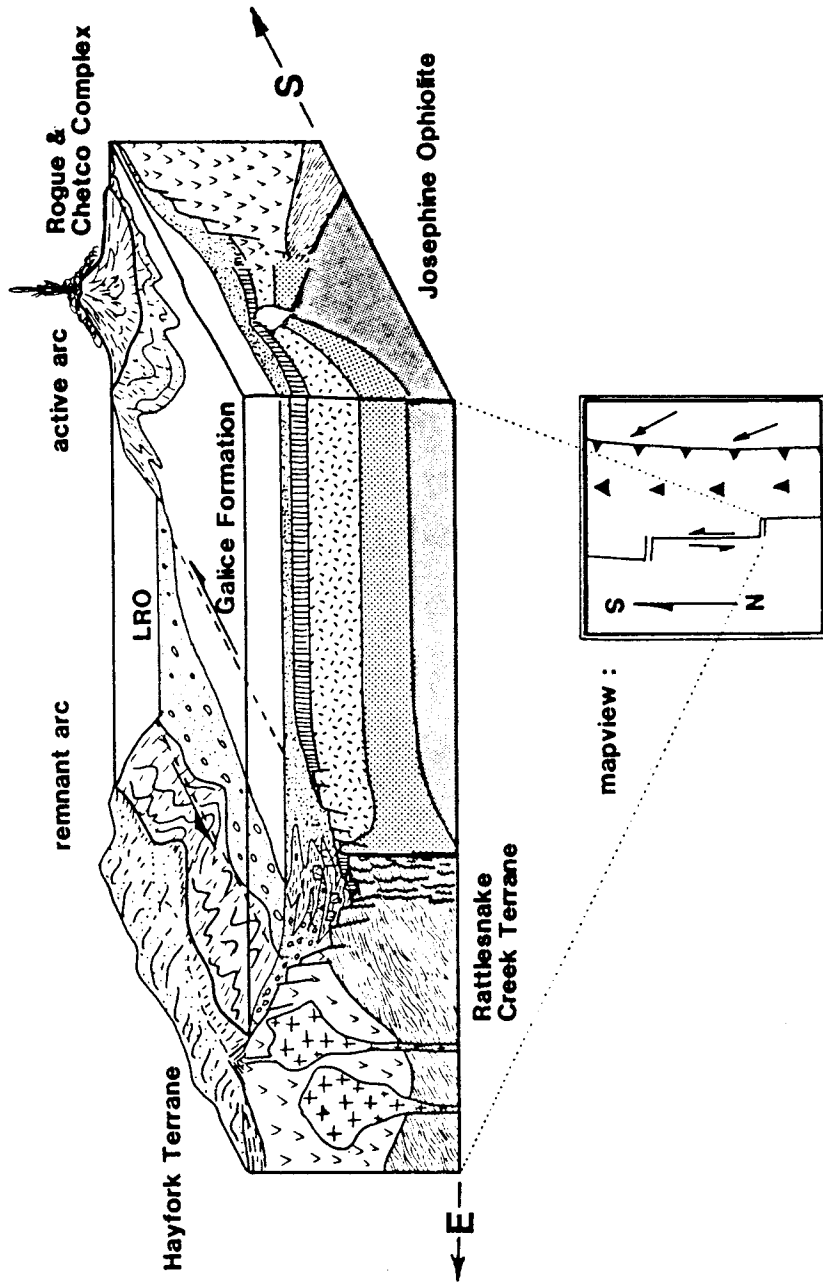


Figure 6.3

Schematic reconstruction of the paleo-tectonic setting of the Lems Ridge olistostrome; see text for explanation.

suggested has to integrate the following evidence:

- The LRO overlies a Late Triassic to Early Jurassic igneous basement which is probably part of the Rattlesnake Creek terrane.
- The range of detrital components in the LRO encompasses material of both continental and volcanic provenance.
- The geochemistry and geochronology on lithologies of the LRO suggest no singular source, but rather simultaneous derivation from the Rattlesnake Creek terrane, from a active convergent margin, and from the Josephine ophiolite.
- The Galice Formation overlies both the LRO and the Josephine ophiolite.

If the Josephine ophiolite formed in a transform dominated marginal basin (Harper and others, 1985) where spreading direction and transform motion parallel the continental margin, then the spreading geometry requires the presence of boundary transforms along the passive rifted margins. Therefore it is suggested that the western edge of the Hayfork-Rattlesnake Creek remnant arc was a transform boundary. The associated topographic depression served as a depositional trough for the LRO. The basin was floored by lithologies of the RCT; its flanking walls exposed rocks of the continental margin, the active and the

remnant arc, and of the Josephine ophiolite, respectively (Fig. 6.3). Giant igneous blocks, talus deposits, and ophiolitic breccias accumulated along submarine fault scarps, or were incorporated in sediment gravity flows. These flows occurred as a result of instabilities within the steep and rugged topography of the basin. The Late Jurassic collapse of the Josephine back-arc basin caused the imbrication of the back-arc triad. The Josephine ophiolite and its flysch cover were thrust beneath the continental margin; the thrust may have initiated along the existing transform system and thereby dismembered the LRO and its older structural basement from the rest of the RCT. This caused the preservation of the lateral continuity of Josephine ophiolite and its own rift-edge sequence.

The general tectonic situation depicted in Fig. 6.3 is not unlike the present day Gulf of California, where, in a transform dominated, extensional basin, the projection of oceanic fracture zones into the continent brings ophiolitic and margin sequences in close vicinity. Strike-slip dominated extension in the Josephine basin was probably caused by oblique southeast-ward subduction, or alternatively, by a major reorganization of the existing regional plate geometry just prior to Late Jurassic times.

Comparable olistostromal rift-edge deposits are known from the ancient Apulian margin of the western Alps (e.g.

Tricart and Lemoine, 1986); there crustal blocks of the rifted passive margin rotated along listric faults, forming grabens that collected syn-rifting sediments, to include ophiolitic breccias derived from the youthful Apulian ocean. Other chaotic rift-edge deposits are reported from DSDP site 651 in the Tyrrhenian Sea (ODP Leg 107, Scientific Party, 1986), located at the transition from thinned continental crust to incipient back-arc basin crust: basalt flows, basaltic breccias and alternating metasedimentary rocks overlie a basement of serpentinites and rare plutonic rocks.

The Lems Ridge olistostrome seems exceptional in a way that it represents a melange unit that is probably related to the formation of an ophiolite, rather than to its emplacement. Ophibreccias and ophicalcites from the Alps are also recently interpreted as equivalent to fracture zone deposits (e.g. Weissert and Bernoulli, 1985) that formed during the initial opening stage of an ocean basin.

In a region such as the western Klamath Mountains, with a well established regional geologic framework, and a well defined time scale of the geologic events, it should be worthwhile to attempt more geochronologic work, both radiogenic and faunal ages, to unravel the complete history of the Lems Ridge olistostrome.

REFERENCES

- Aalto, K.R., 1981, Multistage melange formation in the Franciscan Complex, northernmost California: *Geology*, v. 9, p. 602-607.
- Abbate, E., Bortolotti, V., and Passerini, P., 1970, Development of the Northern Apennines Geosyncline - olistostromes and olistoliths: *Sedimentary Geology*, v. 4, p. 521-557.
- Allan, J.E., 1986, Geology of the northern Colima and Zacoalco grabens, southwest Mexico: Late Cenozoic rifting in the Mexican volcanic belt: *Geological Society of America Bulletin*, v. 97, p. 473-485.
- Amalixsen, K.G., and Sturt, B.M., 1986, The Sore Lyklingsholmen Formation: Coarse sedimentary breccias related to submarine faulting in the Iapetus ocean: *Journal of Geology*, v. 84, p. 109-120.
- Anderson, R.N., DeLong, S.E., and Schwarz, W.H., 1978, Thermal modelling for subduction with dehydration in the downgoing slab: *Journal of Geology*, v. 86, p. 731-739.
- Ando, C.J., Irwin, W.P., Jones, D.L., and Saleeby, J.B., 1983, The ophiolitic North Fork terrane in the Salmon River region, central Klamath Mountains, California: *Geological Society of America Bulletin*, v. 94, p. 236-252.
- Bailey, D.K., 1982, Mantle metasomatism - continuing chemical change within the earth: *Nature*, v. 296, p. 525-530.
- Baker, B.H., Goles, G.G., Leeman, W.P., and Lindstrom, M.M., 1977, Geochemistry and petrogenesis of a basalt-benmoreite trachyte suite from the southern part of the Gregory Rift, Kenya: *Contributions Mineralogy and Petrology*, v. 64, p. 303-322.
- Baker, P.E., 1982, Evolution and classification of orogenic volcanic rocks: in, Thorpe, R.S., ed., *Andesites*, John Wiley and Sons, p. 11-23.
- Barnes, S.J., 1985, Solubility of chromium in a synthetic Bushveld/Stillwater parent liquid at 1 atm as a function of temperature and oxygen pressure: *Lunar and Planetary Science Conference XVII (abstract)*, p. 27-28.

- Beccaluva, L., Ohnenstetter, D., and Ohnenstetter M., 1979, Geochemical discrimination between ocean floor and island-arc tholeiites - applications to some ophiolites: Canadian Journal of Earth Science, v. 16, p. 1874-1882.
- Bender, J.F., Langmuir, C.H., and Hanson, G.N., 1983, Petrogenesis of basalt glasses from the Tamayo region, East Pacific Rise: Journal of Petrology, v. 25, p. 213-254.
- Berkland, J.O., Raymond, L.A., Kramer, J.C., Moores, E.M., and O'Day, M., 1972, What is Franciscan: American Association of Petroleum Geologists Bulletin, v. 56, p. 2295-2302.
- Best, M.G., 1975, Migration of hydrous fluids in the upper mantle and potassium variations in calc-alkalic rocks: Geology, v. 3, p. 429-432.
- Bonatti, E., and Honnorez, J., 1976, Sections of the Earth's crust in the equatorial Atlantic: Journal of Geophysical Research, v. 81, p. 4104-4116.
- Bosworth, W., 1984, The relative role of boudinage and structural slicing in the disruption of layered rock sequences: Journal of Geology, v. 92, p. 447-456.
- Cameron, W.E., Nisbett, E.G., and Dietrich, V.J., 1979, Boninites, komatiites, and ophiolitic basalts: Nature, v. 280, p. 550-553.
- Choukroune, P., Franchteau, J., and LePichon, X., 1976, In situ structural observations along transform fault A in the Famous area, mid-Atlantic ridge, Geological Society of America Bulletin, v. 89, p. 1013-1029.
- Cloos, M., 1982, Flow melanges: Numerical modelling and geologic constraints on their origin in the Franciscan subduction complex, California: Geological Society of America Bulletin, v. 93, p. 330-345.
- Coleman, R.G., 1977, Ophiolites: Springer Verlag, Berlin, 229 pp.
- Coleman, R.G., 1984, The diversity of ophiolites: Geologie en Mijnbouw, v. 63, p. 141-150.
- Coleman, R.G., and Irwin, W.P., 1974, Ophiolites and ancient continental margins: in, Burk, C.A., and Drake, C.L., eds., The Geology of Continental Margins,

- Springer Verlag, Berlin, p. 921-931.
- Connelly, W., 1978, Uyak Complex, Kodiak Islands, Alaska: A Cretaceous subduction complex: Geological Society of America Bulletin, v. 89, p. 755-769.
- Cormier, M.H., and Detrick, R.S., 1984, Anomalously thin crust in oceanic fracture zones: New seismic constraints from the Kane fracture zone: Journal of Geophysical Research, v. 89, p. 10249-10266.
- Cornelius, H.P., 1935, Geologie der Err-Julier Gruppe. Teil I. Das Baumaterial: Geologische Karte Schweiz, Beitrage, Neue Serie, v. 70, 321 pp.
- Cowan, D.S., 1974, Deformation and metamorphism of the Franciscan subduction zone complex northwest of Pacheco Pass, California: Geological Society of America Bulletin, v. 85, p. 1623-1634.
- Cowan, D.S., 1978, Origin of blueschist bearing chaotic rocks in the Franciscan Complex, San Simeon, California: Geological Society of America Bulletin, v. 89, p. 1415-1423.
- Cowan D.S., 1985a, Structural styles in Mesozoic and Cenozoic melanges in the western Cordillera of North America: Geological Society of America Bulletin, v. 96, p. 451-462.
- Cowan, D.S., 1985b, The origin of some common types of melange in the western Cordillera of North America: in, Nasu, N., Kobayashi, K., Uyeda, S., Kushiro, I., and Kagami, H., eds., Formation Of Active Oceanic Margins: Terra Publishing, Tokyo, p. 257-273.
- Cox, K.G., Bell, J.D., and Pankhurst, R.J., 1979, The Interpretation of Igneous Rocks. Allan and Unwin, London, 450 pp.
- Crawford, A.J., Beccaluva, L., and Serri, G., 1981, Tectonomagmatic evolution of the west Philippine-Mariana region and the origin of boninites: Earth and Planetary Science Letters, v. 54, p. 346-356.
- Crawford, A.J., Beccaluva, L., Serri, G., and Dostal J., 1986, Petrology, geochemistry, and tectonic implications of volcanics dredged from the intersection of the Yap and Marianas trenches: Earth and Planetary Science Letters, v. 80, p. 265-281.

- Dalrymple, G.B., and Lanphere, M.A., 1971, $^{40}\text{Ar}/^{39}\text{Ar}$ technique of K/Ar dating. A comparison with the conventional technique: *Earth and Planetary Science Letters*, v. 12, p. 300-308.
- Dalrymple, G.B., Alexander, E.C., Lanphere, M.A., and Kraker, G.P., 1981, Irradiation of samples for $^{40}\text{Ar}/^{39}\text{Ar}$ dating using the Geological Survey TRIGA reactor: US Geological Survey Professional Paper 1173.
- Dalziel, I.W.D., DeWit, M.J., and Palmer, K.F., 1974, Fossil marginal basin in the southern Andes: *Nature*, v. 250, p. 291-294.
- Davis, G.A., and Lipmann, P.W., 1962, Revised structural sequence of pre-Cretaceous metamorphic rocks in the southern Klamath Mountains, California: *Geological Society of America Bulletin*, v. 73, p. 1547-1552.
- Day, H.W., Moores, E.M., and Tuminas, A.C., 1985, Structure and tectonics of the northern Sierra Nevada: *Geological Society of America Bulletin*, v. 96, p. 436-450.
- DeLong, S.E., Dewey, J.F., and Fox, P.J., 1979, Topographic and geologic evolution of fracture zones: *Journal Geological Society London*, v. 136, p. 303-310.
- Detrick, R.S., and White, R.S., 1986, Crustal structure of oceanic fracture zones from seismic reflection and refraction studies: *Journal Geological Society London*, v. 143, p. 739-742.
- Dick, H.J.B., 1976, The origin and emplacement of the Josephine peridotite of southwestern Oregon: unpublished Ph.D. thesis, Yale University, New Haven, 409 pp.
- Fahan, M.R., and Wright, J.E., 1983, Plutonism, volcanism, folding, regional metamorphism, and thrust faulting: Contemporaneous aspects of a major orogenic event in the Klamath Mountains, California: *Geological Society of America Abstracts with Programs*, v. 15, p. 272.
- Faure, G., 1977, *Principles of Isotope Geology*. John Wiley & Sons, New York, 464 pp.
- Fisher, R.L., Dick, H.J.B., Natland, J.H., and Meyer, P.S., 1986, Mafic/ultramafic suites of the slowly spreading southwest Indian Ridge: Protea exploration of the Antarctic plate boundary, 24°E to 47°E , 1984: *Ophioliti*, v. 11, p. 147-178.

- Fisk, M.R., 1986, Basalt interaction with harzburgite and the formation of high-Mg-andesites: *Geophysical Research Letters*, v. 13, p. 467-470.
- Flanagan, F.J., 1973, 1972 values for international geochemical reference samples: *Geochimica and Cosmochimica Acta*, v. 37, p. 1189-1200.
- Flint, R.F., Sanders, J.E., and Rodgers, J., 1960, Diamictite, a substitute term for synmictite: *Geological Society of America Bulletin*, v. 71, p. 1809.
- Flores, G., 1955, Discussion, in Benno, E., *Les resultats des etudes pour la recherche petrolifere en Sicilie (Italie): 4th World Petroleum Congress, Rome, Proceedings section 1*, p. 121-122.
- Fox, P.J., Detrick, R.S., and Purdy, G.M., 1980, Evidence for crustal thinning near fracture zones: Implications for ophiolites: in Panayiotou, A., ed., *Proceedings of the International Ophiolite Symposium, Nicosia, Cyprus Geological Survey Department*, p. 161-168.
- Fox, P.J., and Gallo, D.G., 1984, A tectonic model for ridge-transform boundaries: Implications for the structure of the oceanic lithosphere: *Tectonophysics*, v. 104, p. 205-242.
- Francis, T.J.G., 1981, Serpentinization faults and their role in the tectonics of slow spreading ridges: *Journal of Geophysical Research*, v. 86, p. 616-622.
- Francis, T.J.G., Porter, I.T., and McGrath, J.R., 1977, Ocean bottom seismograph observations on the mid-Atlantic ridge near 37° N: *Geological Society of America Bulletin*, v. 88, p. 664-677.
- Gansser, A., 1974, The ophiolite melange: A worldwide problem on Tethyan examples: *Eclogae Geologicae Helvetiae*, v. 67, p. 479-507.
- Garcia, M.O., 1978, Criteria for the identification of ancient volcanic arcs: *Earth Science Reviews*, v. 14, p. 147-165.
- Garcia, M.O., 1979, Petrology of the Rogue and Galice Formations, Klamath Mountains, Oregon: identification of a Jurassic island-arc sequence: *Journal of Geology*, v. 86, p. 29-41.

- Garcia, M.O., 1982, Petrology of the Rogue River island-arc complex, southwest Oregon: *American Journal of Science*, v. 282, p. 783-807.
- Garner, E.L., Murphy, T.J., Gramlich, J.W., Paulsen, P.J., and Barnes, I.L., 1975, Absolute isotopic abundance ratios and the atomic weight of a reference sample of potassium: *Journal National Bureau of Standards*, v. 79a, p. 713-725.
- Gast, P.W., 1968, Trace element fractionation and the origin of tholeiitic and alkaline magma types: *Geochimica et Cosmochimica Acta*, v. 32, p. 1057-1086.
- Gill, J.B., 1976, Composition and age of the Lau Basin and Ridge volcanic rocks: Implications for evolution of an intra-arc basin and remnant arc: *Geological Society of America Bulletin*, v. 87, p. 1384-1395.
- Gill, J.B., 1981, *Orogenic Andesites and Plate Tectonics*, Springer Verlag, Berlin, 390 pp.
- Gorman, C., 1985, Geology, geochronology, and geochemistry of the Rattlesnake Creek terrane, west-central Klamath Mountains, California (M.S. thesis): Salt Lake City, University of Utah, 112 pp.
- Gray, G.G., 1985, Structural, geochronologic, and depositional history of the western Klamath Mountains, California and Oregon: Implications for the early to middle Mesozoic evolution of the western North American Cordillera (Ph.D. thesis): Austin, University of Texas, 162 pp.
- Gray, G.G., 1986, Native terranes of the central Klamath Mountains, California: *Tectonics*, v. 5, p. 1043-1054.
- Gray, G.G., and Peterson, S.W., 1982, Northward continuation of the Rattlesnake Creek terrane, central Klamath Mountains, California: *Geological Society of America Abstracts with Programs*, v. 14, p. 167.
- Gray, G.G., and Wright, J.E., 1984, Nature and tectonic setting of the Rattlesnake Creek terrane, central Klamath Mountains, California: *Geological Society of America Abstracts with Programs*, v. 16, p. 524.
- Green, D.H., 1973, Experimental melting studies on a model upper mantle composition at high pressures under water-saturated and water-undersaturated conditions:

- Earth and Planetary Science Letters, v. 19, p. 37-53.
- Greenly, E., 1919, The Geology of Angelsey: Great Britain Geological Survey Memoirs 1, 980 pp.
- Griesbach, C.L., 1891, Geology of the Central Himalayas: Memoirs Geological Survey India, v. 23.
- Hamilton W., 1969, Mesozoic California and the underflow of Pacific mantle: Geological Society of America Bulletin, v. 80, p. 2409-2430.
- Harding, D.J., 1987, The Structure of the Josephine Peridotite (Ph.D. thesis): Cornell University, Ithaca, New York.
- Harper, G.D., 1980, Structure and petrology of the Josephine ophiolite and overlying metasedimentary rocks, northwestern California (Ph.D.thesis): University of California, Berkeley, California, 260 pp.
- Harper, G.D., 1983, A depositional contact between the Galice Formation and a Late Jurassic ophiolite in northwestern California and southwestern Oregon: Oregon Geology, v. 45, p. 3-9.
- Harper, G.D., 1984, The Josephine ophiolite, northwestern California: Geological Society of America Bulletin, v. 95, p. 1009-1024.
- Harper, G.D., Norman, E.A., and Jones, D.L., 1983, The Lems Ridge olistostrome - sediment fill of an ancient fracture zone: Geological Society of America Abstracts with Program, v. 15, p. 427.
- Harper, G.D., and Wright, J.E., 1984, Middle to Late Jurassic tectonic evolution of the Klamath Mountains, California-Oregon: Tectonics, v. 3, p. 759-772.
- Harper, G.D., Saleeby, J.B., and Norman, E.A., 1985, Geometry and tectonic setting of sea-floor spreading for the Josephine ophiolite, and implications for Jurassic accretionary events along the Californian margin: in, Howell, D.G., ed., Tectonostratigraphic Terranes of the Circum-Pacific Region: Circum-Pacific Council for Energy and Mineral Resources, Earth Science Series No.1, Houston, p. 239-257.
- Harper, G.D., Saleeby, J.B., Cashman, S., and Norman, E.A., 1986, Isotopic age of the Nevadan orogeny in the

- western Klamath Mountains, California-Oregon:
Geological Society of America Abstracts with Programs,
v. 18, p. 114.
- Harrison T.M., 1981, Diffusion of ^{40}Ar in Hornblende:
Contributions to Mineralogy and Petrology, v. 78, p.
324-331.
- Harrison, T.M., 1983, Some observations on the
interpretation of $^{40}\text{Ar}/^{39}\text{Ar}$ age spectra: Isotope
Geoscience, v. 1, p. 319-338.
- Harrison, T.M., and McDougall, I., 1981, Excess ^{40}Ar in
metamorphic rocks from Broken Hill, New South Wales:
Implications for $^{40}\text{Ar}/^{39}\text{Ar}$ age spectra and the thermal
history of the region: Earth and Planetary Science
Letters, v. 55, p.123-149.
- Harrison, T.M., and FitzGerald, J.D., 1986, Exsolution in
hornblende and its consequences for $^{40}\text{Ar}/^{39}\text{Ar}$ age
spectra and closure temperature: Geochimica and
Cosmochimica Acta, v. 50, p. 247-253.
- Harrison, T.M., and Heizler, M., 1987, Multiple trapped
argon isotopic components revealed by $^{40}\text{Ar}/^{39}\text{Ar}$
isochron analysis: American Geophysical Union
Abstracts with Programs, v. 68, p. 431.
- Hart, S.R., Erlank, A.J., and Kable, E.J.D., 1974, Sea
floor alteration: some chemical and strontium isotopic
effects: Contributions Mineralogy and Petrology, v.
44, p. 219-230.
- Hawkesworth, C.J., O'Nions, R.K., Pankhurst, R.J.,
Hamilton, P.J., and Evensen, N.M., 1977, A geochemical
study of island-arcs and back-arc tholeiites from the
Scotia Sea: Earth and Planetary Science Letters, v.
36, p. 253-262.
- Hawkins, J.W., 1979, Petrology of back-arc basins and
island-arcs: their possible role in the origin of
ophiolites: in, Panayiotou, A., ed., Proceedings of
the International Ophiolite Symposium, Nicosia, Cyprus
Geological Survey Department, p. 244-254.
- Hekianen, R., and Thompson, G., 1976, Comparative
geochemistry of volcanics from rift valleys, transform
faults, and aseismic ridges: Contributions Mineralogy
and Petrology, v. 57, p. 145-162.
- Hellman, P.L., and Henderson, P., 1977, Are the rare earth
elements mobile during spilitization?: Nature, v.

267, p. 38-40.

- Hickey, R.L., and Frey, F.A., 1982, Geochemical characteristics of boninite series volcanism: implications for their source: *Geochimica and Cosmochimica Acta*, v. 46, p. 2099-2115.
- Honnorez J., Mivel, C., and Montigny, R., 1984, Geotectonic significance of gneissic amphibolites from the Vema fracture zone, equatorial mid-Atlantic ridge: in, Gass, I.G, Lippard, S.J., and Shelton, A.W., eds., *Ophiolites and Oceanic Lithosphere*, The Geological Society Special Publication, v. 13, p. 121-130.
- Hopson, C.A., and Mattinson, J.M., 1973, Ordovician and Late Jurassic ophiolite assemblages in the Pacific Northwest: *Geological Society of America Abstracts with Programs*, v. 5, p. 57.
- Hotz, P.E., 1971, Plutonic rocks of the Klamath Mountains, California and Oregon: U.S. Geological Survey Professional Paper 684-B, 19 pp.
- Hsu, K.J., 1968, Franciscan melanges and their bearing on the Franciscan-Knoxville paradox: *Geological Society of America Bulletin*, v. 79, p. 1063-1074.
- Hsu, K.J., 1974, Melanges and their distinction from olistostromes: in, Dott, R.H., and Shaver, R.H., eds., *Modern and Ancient Geosynclinal Sedimentation*, Society of Economic Paleontologists and Mineralogists Special Publication 19, p. 321-333.
- Hussong, D.M., and Fryer, P., 1983, Back-arc seamounts and the SeaMARC-II seafloor mapping system: *EOS Transactions American Geophysical Union*, v. 64, p. 627-632.
- Ingersoll, R.V., and Schweickert, R.A., 1986, A plate-tectonic model for Late Jurassic ophiolite genesis, Nevadan orogeny and forearc initiation, northern California: *Tectonics*, v. 5, p. 901-912.
- Irwin, W.P., 1960, Geologic reconnaissance of the northern Coast Ranges and Klamath Mountains, California, with a summary of the mineral resources: *California Division of Mines and Geology Bulletin* 179, p. 19-38.
- Irwin, W.P., 1972, Terranes of the western Paleozoic and Triassic belt in the southern Klamath Mountains, California: U.S. Geological Survey Professional Paper 800-C, p. 103-111.

- Irwin, W.P., 1973, Sequential minimum ages of oceanic crust in accreted tectonic plates of northern California and southern Oregon: Geological Society of America Abstracts with Programs, v. 5, p. 62-63.
- Irwin, W.P., 1981, Tectonic accretion of the Klamath Mountains: in, Ernst, W.G., ed., The Geotectonic Development of California (Rubey Volume 1): Englewood Cliffs, New Jersey, Prentice Hall, p. 29-49.
- Irwin, W.P., 1985, Age and tectonics of plutonic belts in accreted terranes of the Klamath Mountains, California and Oregon: in, Howell, D.G., ed., Tectonostratigraphic Terranes of the Circum-Pacific Region, Earth Science Series, v. 1, Circum Pacific Council for Energy and Mineral Resources, Houston, Texas, p. 187-199.
- Irwin, W.P., Jones D.L., and Pessagno, E.A., Jr., 1977, Significance of Mesozoic radiolaria from the pre-Nevadan rocks of the southern Klamath Mountains, California: Geology, v. 5, p. 557-562.
- Irwin, W.P., Jones, D.L., and Kaplan, T.A., 1978, Radiolarians from pre-Nevadan rocks of the Klamath Mountains, California and Oregon: in, Howell, D.G., and McDougall, K.A., eds., Mesozoic Stratigraphy Of The Western United States: Society of Economic Paleontologists and Mineralogists, Pacific Coast Paleogeography Symposium 2, p. 303-310.
- Irwin, W.P., Wardlaw, B.R., and Kaplan, T.A., 1983, Conodonts of the western Paleozoic and Triassic belt, Klamath Mountains, California and Oregon: Journal of Paleontology, v. 57, p. 1030-1039.
- Jachens, R.C., Barnes, C.G., and Donato, M.M., 1986, Subsurface configuration of the Orleans fault: Implications for deformation in the western Klamath Mountains, California: Geological Society of America Bulletin, v. 97, p. 388-395.
- Jakes, P., and Gill, J., 1970, Rare earth elements and the island-arc tholeiite series: Earth and Planetary Science Letters, v. 9, p. 17-28.
- Jakes, P., and White, A.J.R., 1971, Composition of island-arcs and continental growth: Earth and Planetary Science Letters, v. 12, p. 224-230.
- Joron, J.L., and Treuil, M., 1977, Utilisation des

proprietes des elements fortement hygromagmatophiles pour l'etude de la composition chimique et de l'heterogenetie du manteau: Bulletin Societe Geologie du France, v. 19, p. 1197-1205.

- Karson, J.A., and Dewey, J.F., 1978, Coastal complex, western Newfoundland: an early Ordovician fracture zone: Geological Society of America Bulletin, v. 89, p. 1037-1049.
- Karson, J.A., and Dick, H.J.B., 1983, Tectonics of ridge-transform intersections at the Kane fracture zone: Marine Geophysical Research, v. 6, p. 51-98.
- Karson, J.A., and Elthon, D., 1987, Evidence for variations in magma production along oceanic spreading centers: A critical appraisal: Geology, v. 15, p. 127-131.
- Kauffman, F.J., 1886, Emmen- und Schlierengegend nebst Kantone Schwyz und Zug und Buerckenstocks bei Stanz: Geologische Karte Schweiz, Beitraege, Neue Serie, v. 24.
- Kay, R.W., 1980, Volcanic arc magmas: implications of a melting-mixing model for element recycling in the crust - upper mantle system: Journal of Geology, v. 88, p. 497-522.
- Kay, R.W., 1984, Elemental abundances relevant to identification of magma sources: Philosophical Transactions Royal Society London, v. A 310, p. 535-547.
- Langmuir, C.H., and Bender, J.F., 1984, The geochemistry of oceanic basalts in the vicinity of transform faults: observations and implications: Earth and Planetary Science Letters, v. 69, p. 107-127.
- Lanphere, M.A., Irwin, W.P., and Hotz, P.E., 1968, Isotopic age of the Nevadan orogeny and older plutonic and metamorphic events in the Klamath Mountains, California: Geological Society of America Bulletin, v. 79, p. 1027-1052.
- Lanphere, M.A., and Dalrymple, G.B., 1976, Identification of excess ^{40}Ar by the $^{40}\text{Ar}/^{39}\text{Ar}$ age spectrum technique: Earth and Planetary Science Letters, v. 32, p. 141-148.
- LeRoex, A.P., and others, 1983, Geochemistry, mineralogy, and petrogenesis of lavas erupted along the SW-Indian ridge between the Bouvet triple junction and 11°W :

- Journal of Petrology, v. 24, p. 267-318.
- Lister, G.S., Etheridge, M.A., and Symonds, P.A., 1986, Detachment faulting and the evolution of passive continental margins: *Geology*, v. 14, p. 246-250.
- Lowe, D.R., 1979, Sediment gravity flows; their classification and some problems of application to natural flows and deposits: in, Doyle, L.J., and Pilkey, O.H., eds., *Geology Of Continental Slopes: Society of Economic Paleontologists and Mineralogists Special Publication 27*, p. 75-82.
- Ludden, J.N., and Thompson, G., 1979, An evaluation of the behaviour of the rare earth elements during the weathering of sea floor basalt: *Earth and Planetary Science Letters*, v. 43, p. 85-92.
- McCall, G.J.H., 1983, Introduction: in, McCall, G.J.H, ed., *Ophiolitic and Related Melanges, Hutchinson Ross, Stroudsburg*, p. 1-11.
- Merrihue, C., and Turner, G., 1966, Potassium-argon dating by activation with fast neutrons: *Journal of Geophysical Research*, v. 71, p. 2852-2857.
- Middleton, G.V., and Hampton, M.A., 1976, Subaqueous sediment transport and deposition by sediment gravity flows: in, Stanley, D.J., and Swift, D.J.P., eds., *Marine Sediment Transport And Environmental Management, John Wiley & Sons, New York*, p. 197-218.
- Mitra, G., 1984, Brittle to ductile transition due to large strain along the White Rock thrust, Wind River Mountains, Wyoming: *Journal of Structural Geology*, v. 6, p. 51-61.
- Moores, E.M., 1982, Origin and emplacement of ophiolites: *Reviews of Geophysics and Space Physics*, v. 20, p. 735-760.
- Moores, E.M., and Day, H.W., 1984, Overthrust model for the Sierra Nevada: *Geology*, v. 12, p. 416-419.
- Nardin, T.R., Hein, F.J., Gorsline, D.S., and Edwards, B.D., 1979, A review of mass movement processes, sediment and acoustic characteristics, and contrasts in slope and base-of-slope systems versus canyon-fan-basin floor system: in, Doyle, L.J., and Pilkey, O.R., eds., *Geology Of Continental Slopes: Society of Economic Paleontologists and Mineralogists Special Publication 27*, p. 61-73.

- Naylor, M.A., 1981, Debris flow (olistostromes) and slumping on a distal passive continental margin: the Palombini limestone-shale sequence of the northern Apennines: *Sedimentology*, v. 28, p. 837-852.
- Nier, A.O., 1950, A redetermination of the relative abundances of the isotopes of carbon, nitrogen, oxygen, argon, and potassium: *Physical Reviews*, v. 77, p. 789-793.
- Noble, L.F., 1941, Structural features of the Virgin Springs area, California: *Geological Society of America Bulletin*, v. 52, p. 941-1000.
- Norman, E.A., 1984, The structure and petrology of the Summit Valley area, Klamath Mountains, California (M.S.thesis): University of Utah, Salt Lake City, 148 pp.
- Norrell, G.T., Harper, G.D., and Smith, B., 1987, Oceanic faults and serpentinite mylonites in the Josephine ophiolite: *EOS Transactions American Geophysical Union*, v. 68, p. 425
- Oceanographer Transform Tectonic Research Team (OTTER), 1985, The geology of the Oceanographer transform: the transform domain: *Marine Geophysical Research*, v. 7, p. 329-358.
- Ocean Drilling Program, Leg 107, Scientific Party, 1986, Young Tyrrhenian Sea evolved very quickly: *Geotimes*, v. 31, p. 11-14.
- Ohr, M., Harper, G.D., and Wright, J.E., 1986, Fracture zone origin of the Lems Ridge olistostrome, northwestern California, Klamath Mountains: *EOS Transactions American Geophysical Union*, v. 67, p. 1210.
- O'Nions, R.K., Hamilton, P.J., and Eynsen, N.M., 1977, Variations in $^{143}\text{Nd}/^{144}\text{Nd}$ and $^{87}\text{Sr}/^{86}\text{Sr}$ ratios in oceanic basalts: *Earth and Planetary Science Letters*, v. 34, p. 13-22.
- Page, B.M., 1978, Franciscan melanges compared with olistostromes of Taiwan and Italy: *Tectonophysics*, v. 47, p. 223-246.
- Page, B.M., and Suppe, J., 1981, The Pliocene Lichi melange of Taiwan: its plate-tectonic and olistostromal origin: *American Journal of Science*, v. 281, p.

193-227.

- Pearce, J.A., 1975, Basalt geochemistry used to investigate past tectonic environment on Cyprus: *Tectonophysics*, v. 25, p. 41-67.
- Pearce, J.A., 1980, Geochemical evidence for the genesis and eruptive setting of lavas from Tethyan ophiolites: in, Panayiotou, A., ed., *Proceedings of the International Ophiolite Symposium, Nicosia, Cyprus* Geological Survey Department, p. 261-272.
- Pearce, J.A., 1982, Trace element characteristics of lavas from destructive plate boundaries: in, Thorpe, R.S., ed., *Andesites*, John Wiley and Sons, p. 525-548.
- Pearce, J.A., 1983, The role of subcontinental lithosphere in magma genesis at active continental margins: in, Hawkesworth, C.J., and Nurry, M.J., eds., *Continental Basalts and Mantle Xenoliths*, Shive Publishing, Nantwich, p. 230-249.
- Pearce, J.A., and Cann, J.R., 1973, Tectonic setting of basic volcanic rocks determined using trace element analyses: *Earth and Planetary Science Letters*, v. 19, p. 290-300.
- Pearce, J.A., and Norry, M.J., 1979, Petrogenetic implications of Ti, Zr, Y, and Nb variations in volcanic rocks: *Contributions Mineralogy and Petrology*, v. 69, p. 33-47.
- Pearce, J.A., Alabaster, T., Shelton, A.W., and Searle, M.P., 1981, The Oman ophiolite as a Cretaceous arc-basin complex: evidence and implications: *Philosophical Transactions Royal Society London*, v. A 300, p. 299-317.
- Pearce, J.A., Lippard, S.J., and Roberts, S., 1984, Characteristics and tectonic significance of supra-subduction zone ophiolites: in, Kokelaar, B.P., and Howells, M.F., eds., *Marginal Basin Geology*, The Geological Society, Special Publication # 16, p. 77-94.
- Pinto-Ausso, M., and Harper, G.D., 1985, Sedimentation, metallogenesis, and tectonic origin of the basal Galice Formation overlying the Josephine ophiolite, northwestern California: *Journal of Geology*, v. 93, p. 713-725.
- Prinz, M., Keil, K., Green, J.A., Reid, A.M., Bonatti, E.,

- and Honnorez, J., 1976, Ultramafic and mafic dredge samples from the equatorial mid-Atlantic ridge and fracture zones: *Journal of Geophysical Research*, v. 81, p. 4087-4103.
- Ramp, L., 1975, Geology and mineral resources of the upper Chetco River drainage area, Oregon, including the Kalmiopsis wilderness and Big Craggies botanical areas: *Oregon Department of Geology and Mineral Industries Bulletin*, v. 88, 49 pp.
- Saleeby, J.B., 1979, The Kings Kaweeh ophiolite, SW Sierra Nevada Foothills, California: *Geological Society of America Bulletin*, v. 89, p. 617-636.
- Saleeby, J.B., 1984, Pb/U zircon ages from the Rogue River area, western Jurassic belt, Klamath Mountains, Oregon: *Geological Society of America Abstracts with Program*, v. 16, p. 331.
- Saleeby, J.B., Harper, G.D., Snoke, A.W., and Sharp, W., 1982, Time relations and structural-stratigraphic patterns in ophiolite accretion, west-central Klamath Mountains, California: *Journal of Geophysical Research*, v. 87, p. 3831-3848.
- Saunders, A.D., Tarney, J., Marsh, N.G., and Wood, D.A., 1979, Ophiolites as ocean crust or marginal basin crust: a geochemical approach: in, Panayiotou, A., ed., *Proceedings of the International Ophiolite Symposium*, Nicosia, Cyprus Geological Survey Department, p. 193-204.
- Saunders, A.D., Skinner, A.C., and Tarney, J., 1980, Transverse geochemical variations across the Antarctic Peninsula: Implications for the genesis of calc-alkaline magmas: *Earth and Planetary Science Letters*, v. 46, p. 344-360.
- Saunders, A.D., and Tarney, J., 1984, Geochemical characteristics of basaltic volcanism within back-arc basins: in, Kokelaar, B.P., and Howells, M.F., eds., *Marginal Basin Geology*, The Geological Society, Special Publication # 16, p. 59-76.
- Schilling, J.G., 1973, Iceland mantle plume: Geochemical study of Reykjanes Ridge: *Nature*, v. 242, p. 565-572.
- Schilling, J.G., and others, 1983, Petrological and geochemical variations along the mid-Atlantic ridge from 29° N to 73° N: *American Journal of Science*, v.

- 283, p. 510-588.
- Schweickert, R.A., Bogen, N.L., Girty, G.H., Hanson, R.E., and Merguerian, C., 1983, Timing and structural expression of the Nevadan orogeny, Sierra Nevada, California: Geological Society of America Bulletin, v. 95, p. 967-979.
- Searle, R.L., 1983, Multiple, closely spaced transform faults in fast slipping fracture zones: Geology, v. 11, p. 607-610.
- Searle, R.L., 1986, GLORIA investigations of oceanic fracture zones: a comparative study of the transform fault zone: Journal Geological Society of London, v. 143, p. 743-756.
- Shaw, D.M., 1970, Trace element fractionation during anatexis: Geochimica et Cosmochimica Acta, v. 34, p. 237-243.
- Shervais, J.W., 1982, Ti-V plots and the petrogenesis of modern and ophiolitic lavas: Earth and Planetary Science Letters, v. 59, p. 101-118.
- Shibata, T., Thompson, G., and Frey, F.A., 1979, Tholeiitic and alkali basalts from the mid-Atlantic ridge at 43° N: Contributions Mineralogy and Petrology, v. 70, p. 127-141.
- Sibson, R.H., 1977, Fault rocks and fault mechanism: Journal Geological Society London, v. 133, p. 191-213.
- Silver, E.A., and Beutner, E.C., 1980, Melanges: Geology, v. 8, p. 32-34.
- Simonian, K.O., and Gass, I.G., 1978, The Arakapas fault belt, Cyprus: a fossil transform fault: Geological Society of America Bulletin, v. 89, p. 1220-1230.
- Sinha, M.C., and Loudon, K.E., 1983, The Oceanographer fracture zone. Crustal structure from seismic refraction studies: Geophysical Journal Royal Astronomical Society, v. 75, p. 713-736.
- Sinton, J.M., Wilson, D.S., Christie, D.M., Hey, R.N., and Delaney, J.R., 1983, Petrologic consequences of rift propagation on oceanic spreading ridges: Earth and Planetary Science Letters, v. 62, p. 193-207.
- Smewing, J.D., 1980, An upper Cretaceous ridge-transform

- intersection in the Oman ophiolite: in, Panatyioutou, A., ed., Proceedings International Ophiolite Symposium, Nicosia, Cyprus Geological Survey Department, p. 407-413.
- Snoke, A.W., 1977, A thrust plate of ophiolitic rocks in the Preston Peak area, Klamath Mountains, California: Geological Society of America Bulletin, v. 88, p. 1641-1659.
- Solano, A., and Bibee, D., 1985, Seismicity of the Gorda Ridge: EOS Transactions American Geophysical Union, v. 66, p. 24.
- Steiger, R. H., and Jaeger, E., 1977, Subcommittee on geochronology: Convention on the use of decay constants in geo- and cosmochronology: Earth and Planetary Science Letters, v. 36, p. 359-362.
- Stroup, J.B., and Fox, P.J., 1981, Geological investigations in the Cayman trough: evidence for thin oceanic crust along the mid-Cayman rise: Journal of Geology, v. 89, p. 395-420.
- Sun, S.S., and Nisbett, R.W., 1978, Geochemical regularities and genetic significance of ophiolitic basalts: Geology, v. 6, p. 689-693.
- Sun, S.S., Nisbett, R.W., and Sharaskin, A.Y., 1979, Geochemical characteristics of mid-ocean ridge basalt: Earth and Planetary Science Letters, v. 44, p. 119-138.
- Sundell, K.A., and Fisher, R.V., 1985, Very coarse grained fragmental rocks: A proposed size classification: Geology, v. 13, p. 692-695.
- Suppe, J., Liou J.G., and Ernst, W.G., 1981, Paleogeographic origin of the East Taiwan ophiolite: American Journal of Science, v. 281, p. 228-246.
- Tarney, J., Saunders, A.D., and Weaver, S.D., 1977, Geochemistry of volcanic rocks from island-arcs and marginal basins of the Scotia arc region: in, Talwani, M., and Pitman, W.C., eds., Island-Arcs, Deep Sea Trenches, and Back-Arc Basins, Maurice Ewing Series, v. 1, American Geophysical Union, Washington, p. 367-378.
- Thompson, G., and Melson, W.G., 1972, The petrology of oceanic crust across fracture zones in the Atlantic Ocean: evidence of a new kind of seafloor spreading:

- Journal of Geology, v. 80, p. 526-538.
- Thompson, G., Bryan, W.B., and Melson, W.G., 1980, Geological and geophysical investigation of the mid-Cayman rise spreading center: geochemical variations and petrogenesis of basalt glasses: Journal of Geology, v. 88, p. 41-55.
- Thompson, R.N., Morrison, M.A., Hendry, G.L., and Parry, S.J., 1984, An assessment of the relative roles of crust and mantle in magma genesis: an elemental approach: Philosophical Transactions Royal Society London, v. A 310, p. 549-590.
- Toomey D.R., Solomon, S.C., and Purdy, G.M., and Murray, M.H., 1985, Microearthquakes beneath the median valley of the mid-Atlantic ridge near 23°N: Hypocenters and focal mechanisms: Journal Geophysical Research, v. 90.
- Tricart, P., and Lemoine, M., 1986, From faulted blocks to megamoulines and megaboudins: Tethyan heritage in the structure of the western Alps: Tectonics, v. 5, p. 95-118.
- Turner, G., 1968, The distribution of potassium and argon in chondrites: in, Ahrens, L.H., ed., Origin and Distribution of the Elements, Pergamon Press, London, p. 387-389.
- Upadhyay, H.D., and Neale, E.R.W., 1979, On the tectonic regime of ophiolite genesis: Earth and Planetary Science Letters, v. 43, p. 93-102.
- Vacquier, V., 1959, Mechanism of horizontal displacement along faults in the ocean floor: Nature, v. 183, p. 452-453.
- Watson, E.B., 1980, Apatite and phosphorus in mantle source regions: An experimental study of apatite/melt equilibria at pressures to 25 kilobar: Earth and Planetary Science Letters, v. 51, p. 322-335.
- Weaver, S.D., Saunders A.D., Pankhurst, R.J., and Tarney, J., 1979, A geochemical study of magmatism associated with the initial stages of back-arc spreading: Contributions Mineralogy and Petrology, v. 68, p. 151-169.
- Wells, F.G., and Walker, G.W., 1953, Geology of the Galice quadrangle, Oregon: U.S. Geological Survey Geological Quadrangle Map GQ-25, scale 1:62,500.

- Weissert, H.J., and Bernoulli, D., 1985, A transform margin in the Mesozoic Tethys: evidence from the Swiss Alps: *Geologische Rundschau*, v. 74, p. 665-679.
- Whitehead, J.A., Dick, H.J.B., and Schouten, H., 1984, A mechanism for magmatic accretion under spreading centers: *Nature*, v. 312, p. 146-148.
- Williams, P.R., Pigram, C.J., and Dow, D.B., 1984, Melange production and the importance of shale diapirism in accretionary terrains: *Nature*, v. 309, p. 145-146.
- Wilson, J.T., 1965, A new class of faults and their bearing on continental drift: *Nature*, v. 207, p. 452-453.
- Wood, D.A., 1979, A variably veined suboceanic upper mantle - genetic significance for mid ocean ridge basalts from geochemical evidence: *Geology*, v. 7, p. 499-503.
- Wood, D.A., Gibson, I.L., and Thompson, R.N., 1976, Elemental mobility during Zeolite facies metamorphism of the tertiary basalts of eastern Iceland: *Contributions Mineralogy and Petrology*, v. 55, p. 241-254.
- Wood, D.A., Joron, J.L., and Treuil, M., 1979, A reappraisal of the use of trace elements to classify and discriminate between magma series erupted in different tectonic settings: *Earth and Planetary Science Letters*, v. 45, p. 326-336.
- Wright, J.E., 1981, *Geology and U-Pb geochronology of the western Paleozoic and Triassic subprovince, Klamath Mountains, northern California* (Ph.D. thesis): Santa Barbara, California, University of California, 300 pp.
- Wright, J.E., 1982, Permo-Triassic accretionary subduction complex, southwestern Klamath Mountains, northern California: *Journal of Geophysical Research*, v. 87, p. 3805-3818.
- Wright, J.E., and Fahan, M.R., 1987, An expanded view of Jurassic orogenesis for the western U.S. Cordillera, part 1: Middle Jurassic (pre-Nevadan) regional deformation/metamorphism and thrust faulting within an ancient arc environment, Klamath Mountains, Northern California:
- Wyld, S.J., 1985, *Geology of the western Jurassic belt,*

South Fork Trinity area, Klamath Mountains, California
(M.S. thesis): Berkeley, University of California, 168
pp.

York, D., 1969, Least square fitting of a straight line
with correlated errors: Earth and Planetary Science
Letters, v. 5, p. 320-324.

APPENDIX I

Major And Trace Element Analyses
Of Samples From The
Lems Ridge Olistostrome

Table I.1:

MAJOR AND TRACE ELEMENT ANALYSES OF LR-SAMPLES

Sample	LR 3a	LR 3b	LR 5	LR 6	LR 10	LR 11a
	db	db	db	db	gb	db

SiO ₂	52.23	47.65	49.42	48.78	53.29	50.36
TiO ₂	1.06	0.92	1.51	0.46	0.47	1.19
Al ₂ O ₃	15.92	16.96	15.41	18.20	10.63	13.97
Fe ₂ O ₃	9.41	9.36	11.48	8.09	8.29	11.41
MnO	0.15	0.14	0.19	0.14	0.16	0.16
MgO	6.65	7.51	7.24	8.05	13.15	7.81
CaO	8.43	12.05	6.73	9.51	9.03	9.65
Na ₂ O	4.71	3.34	5.20	2.84	2.25	3.53
K ₂ O	0.21	0.07	0.09	0.60	1.18	0.15
P ₂ O ₅	0.10	0.10	0.14	0.24	0.08	0.12
L.O.I	1.87	2.66	3.26	3.83	1.74	1.89

Total	100.74	100.16	100.67	100.74	100.27	100.64
Ti	6335	5515	9052	2758	2818	7134
Zr	77	57	92	31	59	71
Y	22	19	32	8	12	23
Sr	411	208	212	278	122	220
Rb	15	12	13	25	25	13
Ba	151	31	10	195	60	26
Cr	130	261	130	372	668	177
Ni	61	79	72	128	178	79
V	264	214	319	261	231	277
Hf	1.992		2.736		1.968	1.728
Th	0.386		0.326		0.406	0.368
Ta	0.184		0.247		*	0.344
Ti/V	24.0	25.8	28.4	10.6	12.2	25.8
Ti/Cr	48.7	21.1	69.6	7.4	4.2	40.3
Zr/Y	3.5	3.0	2.9	3.9	4.9	3.1

* = below detection limit

Table I.2:

MAJOR AND TRACE ELEMENT ANALYSES FOR LR-SAMPLES

Sample	LR 13	LR 15	LR 16	LR 17	LR 18	LR 21
	gs/pb	and	pb/SR	pb/SR	pb/SR	pb/SR

SiO ₂	45.51	60.24	41.72	47.12	48.25	46.68
TiO ₂	1.36	0.53	0.98	1.42	1.24	1.02
Al ₂ O ₃	15.06	15.92	15.37	15.46	15.40	15.68
Fe ₂ O ₃	10.43	6.60	9.86	12.55	10.55	10.18
MnO	0.15	0.11	0.13	0.19	0.17	0.13
MgO	8.04	5.03	3.89	7.47	5.61	4.32
CaO	12.50	2.79	16.94	8.54	12.25	14.17
Na ₂ O	2.16	5.01	3.56	2.38	3.51	3.72
K ₂ O	0.52	1.70	0.05	1.95	0.21	0.34
P ₂ O ₅	0.15	0.14	0.08	0.12	0.10	0.09
L.O.I	4.79	2.20	8.35	3.49	3.59	4.62

Total	100.67	100.27	100.93	100.69	100.83	100.95
Ti	8153	3177	5875	8513	7434	6115
Zr	84	91	68	82	75	69
Y	24	13	23	23	23	24
Sr	353	151	146	116	151	196
Rb	20	38	12	50	15	16
Ba	46	268	10	267	18	10
Cr	319	37	207	137	154	328
Ni	169	21	97	90	121	120
V	250	172	250	294	245	241
Hf				2.136		
Th				0.370		
Ta				0.364		
Ti/V	32.6	18.5	23.5	29.0	30.3	25.4
Ti/Cr	25.6	85.9	28.4	62.1	48.3	18.6
Zr/Y	3.5	7.0	3.0	3.6	3.3	2.9

* = below detection limit

Table I.3:

MAJOR AND TRACE ELEMENT ANALYSES OF LR-SAMPLES

Sample	LR 23	LR 24	LR 27	LR 28	LR 30	LR 31
	gs/tf	tf	pb/cl	sc	sc	sc

SiO ₂	58.16	54.82	49.16	48.53	44.12	47.53
TiO ₂	0.52	0.71	1.44	2.61	2.98	2.08
Al ₂ O ₃	15.07	16.05	14.61	13.39	17.07	17.02
Fe ₂ O ₃	6.78	8.48	9.46	11.57	13.75	7.63
MnO	0.11	0.14	0.16	0.12	0.33	0.36
MgO	5.94	5.44	4.58	4.49	8.49	4.25
CaO	5.56	6.05	8.59	7.93	2.39	6.89
Na ₂ O	3.10	5.07	2.57	2.05	3.16	2.80
K ₂ O	1.58	0.61	2.14	3.07	1.05	4.00
P ₂ O ₅	0.12	0.13	0.19	0.37	1.44	1.82
L.O.I	3.36	3.15	7.66	5.49	5.90	5.96

Total	100.30	100.65	100.56	99.62	100.68	100.34
Ti	3117	4256	8633	15647	17865	13489
Zr	77	92	87	252	291	263
Y	13	19	26	26	56	65
Sr	149	197	249	345	192	287
Rb	31	20	52	50	35	104
Ba	133	123	581	821	444	1341
Cr	142	121	242	236	490	169
Ni	48	59	158	165	369	113
V	199	236	261	199	322	151
Hf				6.960	7.584	6.048
Th				5.976	5.060	4.920
Ta				2.628	3.168	3.510
Ti/V	15.7	18.0	33.1	78.6	55.5	89.3
Ti/Cr	21.9	35.2	35.7	66.3	36.5	79.8
Zr/Y	5.9	4.8	3.4	9.7	5.2	4.1

* = below detection limit

Table I.4:

MAJOR AND TRACE ELEMENT ANALYSES OF LR-SAMPLES

Sample	LR 36	LR 50	LR 51	LR 62	LR 67	LR 70
	gb	gs	gb	pb/SR	pb/cl	gs/tf

SiO ₂	50.88	42.50	53.61	43.42	49.53	55.49
TiO ₂	0.70	0.84	0.44	0.96	1.40	0.53
Al ₂ O ₃	17.16	14.33	16.66	16.43	14.23	14.03
Fe ₂ O ₃	9.48	9.30	8.52	10.03	9.70	6.49
MnO	0.16	0.14	0.15	1.19	0.15	0.14
MgO	7.67	7.64	6.54	6.76	4.85	5.59
CaO	6.62	15.52	5.89	15.97	7.91	8.33
Na ₂ O	3.76	2.32	0.20	1.86	2.40	4.45
K ₂ O	0.61	0.14	5.82	0.16	1.88	0.88
P ₂ O ₅	0.16	0.09	0.10	0.06	0.19	0.18
L.O.I	3.23	8.02	2.98	4.97	7.87	4.32

Total	100.43	100.84	100.91	100.81	100.11	100.43
Ti	4197	5036	2638	5755	8393	3177
Zr	57	64	20	61	84	80
Y	14	18	7	26	25	14
Sr	468	183	149	83	221	234
Rb	21	14	15	14	46	20
Ba	215	24	49	10	308	121
Cr	61	340	127	445	246	186
Ni	68	187	38	203	135	56
V	250	208	222	261	244	186
Hf	1.440				2.400	2.232
Th	0.248				0.698	1.140
Ta	0.083				0.691	0.030
Ti/V	16.8	24.2	11.9	22.1	34.4	17.1
Ti/Cr	68.8	61.4	20.8	12.9	34.1	17.1
Zr/Y	4.1	3.6	2.9	2.3	3.4	5.7

* = below detection limit

Table I.5:

MAJOR AND TRACE ELEMENT ANALYSES OF LR-SAMPLES

Sample	LR 76	LR 83	LR 113	LR 174	LR 575	LR 774
	pb/cl	and	tf	tf	db	tf

SiO ₂	40.64	51.69		51.52	50.18	55.82
TiO ₂	2.53	0.70		1.08	0.48	0.53
Al ₂ O ₃	14.19	18.70		14.60	16.40	15.20
Fe ₂ O ₃	10.07	10.27		11.51	7.89	6.77
MnO	0.17	0.14		0.18	0.14	0.11
MgO	6.14	4.54		6.68	9.65	6.49
CaO	12.43	3.22		8.85	10.30	5.33
Na ₂ O	3.85	6.16		3.50	2.96	4.39
K ₂ O	0.29	0.75		0.56	0.21	0.65
P ₂ O ₅	0.44	0.04		0.14	0.03	0.12
L.O.I	9.50	4.13		1.96	2.44	4.33

Total	100.25	100.34		100.58	100.68	99.74
Ti	15167	4197	2640	6475	2858	3177
Zr	216	95	103	76	22	75
Y	29	28	20	26	11	26
Sr	381	485	469	524	236	519
Rb	19	29	14	7	7	7
Ba	146	759	766	85	38	28
Cr	237	68	80	127	426	303
Ni	150	37	27	74	101	128
V	221	238	151	212	199	172
Hf			2.280		0.480	
Th			0.762		*	
Ta			*		0.108	
Ti/V	68.6	17.6	17.5	30.5	14.4	18.5
Ti/Cr	64.0	61.7	33.0	51.0	6.7	10.5
Zr/Y	7.5	3.4	5.2	2.9	2.0	2.9

* = below detection limit

Table I.6:

MAJOR AND TRACE ELEMENT ANALYSES OF LR-SAMPLES

Sample	Z 43	Z 45	Z 45b	Z 45e	Z 46	Z 47b
	pb/SR	pb/GO	pb/GO	pb/GO	pb/GO	pb/GO

SiO ₂	55.90	44.60	48.60	44.53	45.90	46.60
TiO ₂	1.33	3.35	2.11	1.19	1.78	1.95
Al ₂ O ₃	15.70	16.40	14.20	14.27	16.60	17.10
Fe ₂ O ₃	9.69	13.34	12.23	10.28	10.53	11.04
MnO	0.15	0.14	0.14	0.15	0.16	0.17
MgO	4.50	2.30	4.80	5.78	4.90	5.30
CaO	7.67	8.46	10.89	13.11	10.79	10.41
Na ₂ O	4.00	4.67	5.54	3.46	4.80	3.20
K ₂ O	0.49	2.85	0.33	0.71	0.31	0.28
P ₂ O ₅	0.20	1.48	0.28	0.11	0.20	0.23
L.O.I	1.84	3.37	1.98	6.91	4.86	5.01

Total	101.47	100.96	101.10	100.50	100.83	102.29
Ti	7973	20083	12649	7134	10671	11690
Zr	74	228	120	69	128	135
Y	28	62	25	25	24	33
Sr	241	308	229	211	209	213
Rb	10	58	12	18	7	9
Ba						44
Cr	338	77	254	174	106	94
Ni	171	50	197	164	39	46
V	314	297	235	255	270	291
Hf						3.027
Th						0.758
Ta						0.732
Ti/V	25.4	67.6	53.8	28.0	39.5	40.2
Ti/Cr	23.6	261.0	49.8	41.0	101.0	124.4
Zr/Y	2.6	3.7	4.8	2.8	5.3	4.4

* = below detection limit

Table I.7:

MAJOR AND TRACE ELEMENT ANALYSES OF LR-SAMPLES

Sample	Z 48	Z 49	Z 50	Z 51	BM 1
	pb/GO	pb/GO	pb/cl	pb/cl	pb/GO

SiO ₂	47.70	48.20			55.80
TiO ₂	1.44	2.13			1.74
Al ₂ O ₃	19.00	15.40			15.40
Fe ₂ O ₃	8.46	10.81			8.31
MnO	0.12	0.15			0.12
MgO	4.10	6.40			5.60
CaO	7.36	8.70			7.89
Na ₂ O	3.05	3.55			4.04
K ₂ O	2.60	0.38			0.89
P ₂ O ₅	0.18	0.25			0.23
L.O.I	7.22	4.50			2.32

Total	101.23	100.47			100.34
Ti	8633	12769	7374	7314	10431
Zr	105	156	68	72	116
Y	24	37	41	25	30
Sr	256	215	155	187	192
Rb	47	6	37	16	12
Ba					
Cr	108	75	371	350	83
Ni	43	43	127	85	56
V	214	303	223	303	256
Hf		3.600		1.630	
Th		1.100		*	
Ta		1.800		0.26	
Ti/V	40.3	42.1	33.1	24.1	40.7
Ti/Cr	79.9	170.0	19.9	20.9	126.0
Zr/Y	4.4	4.2	1.7	2.9	3.9

* = below detection limit

Table I.8

X-RAY FLUORESCENCE SPECTROMETRY				
	SCo-1		SGR-1	
	USGS-Std	McGill	McGill	USGS-Std

SiO ₂	63.39	63.03	28.61	28.30
TiO ₂	0.62	0.58	0.24	0.24
Al ₂ O ₃	13.70	14.09	6.69	6.49
Fe ₂ O ₃	5.22	5.31	2.98	2.98
MnO	0.05	0.05	0.03	0.03
MgO	2.76	2.76	4.54	4.57
CaO	2.61	2.64	8.32	8.39
Na ₂ O	0.95	0.96	3.06	3.02
K ₂ O	2.82	2.79	1.64	1.63
P ₂ O ₅	0.22	0.18	0.24	0.29
Cr	71	65	23	33
Ni	30	19	25	34
Ba	590	515	22	290
V	135	119	141	125
Zr	135	173	82	55
Y	24	25	11	13
Sr	170	169	455	430
Rb	115	104	85	81
Nb	10	23	21	5

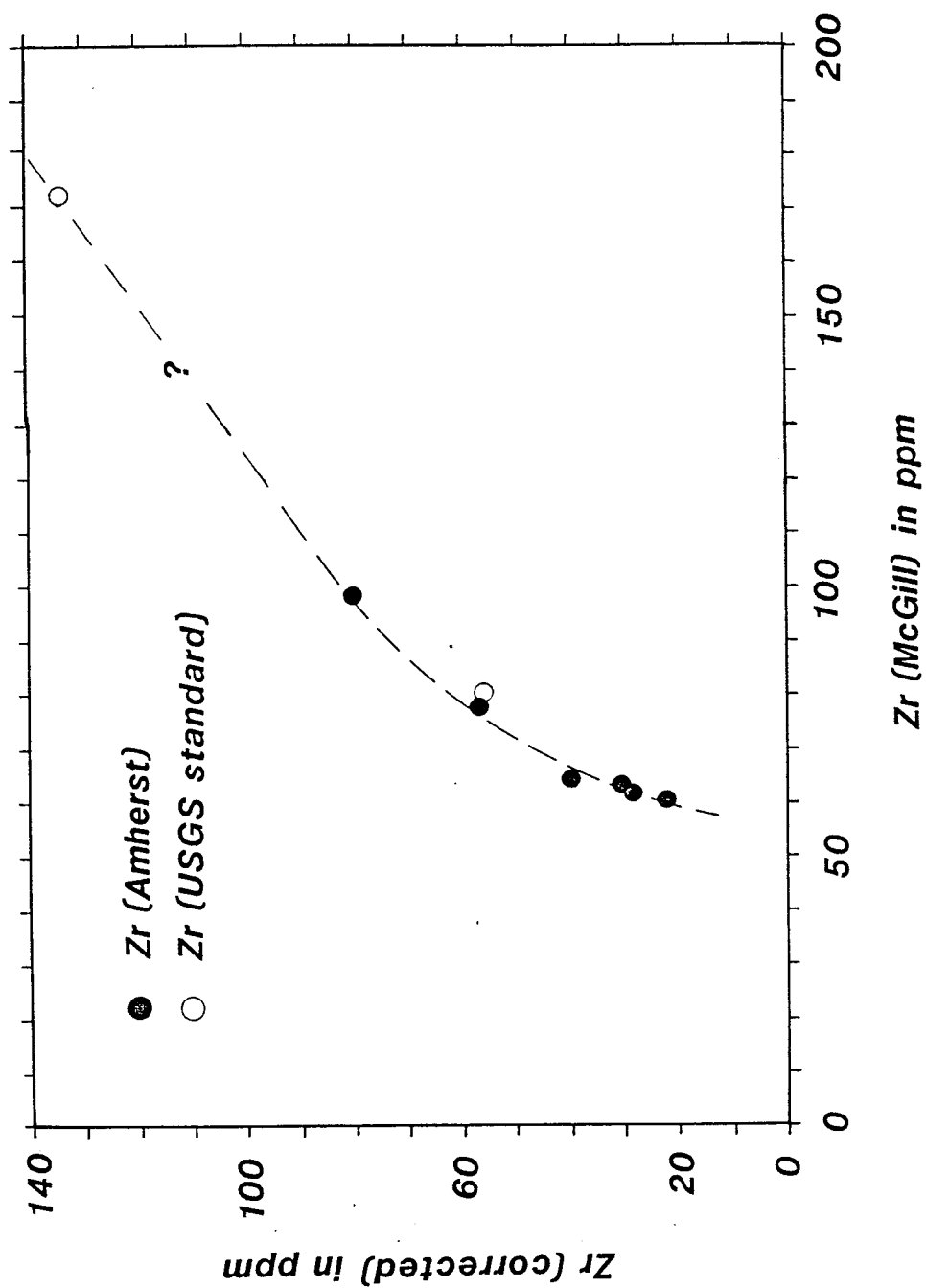


Figure I.1

Empirical diagram for graphical correction of Zr data from McGill University (XRF), using data from University of Mass. (Amherst), and USGS standards)

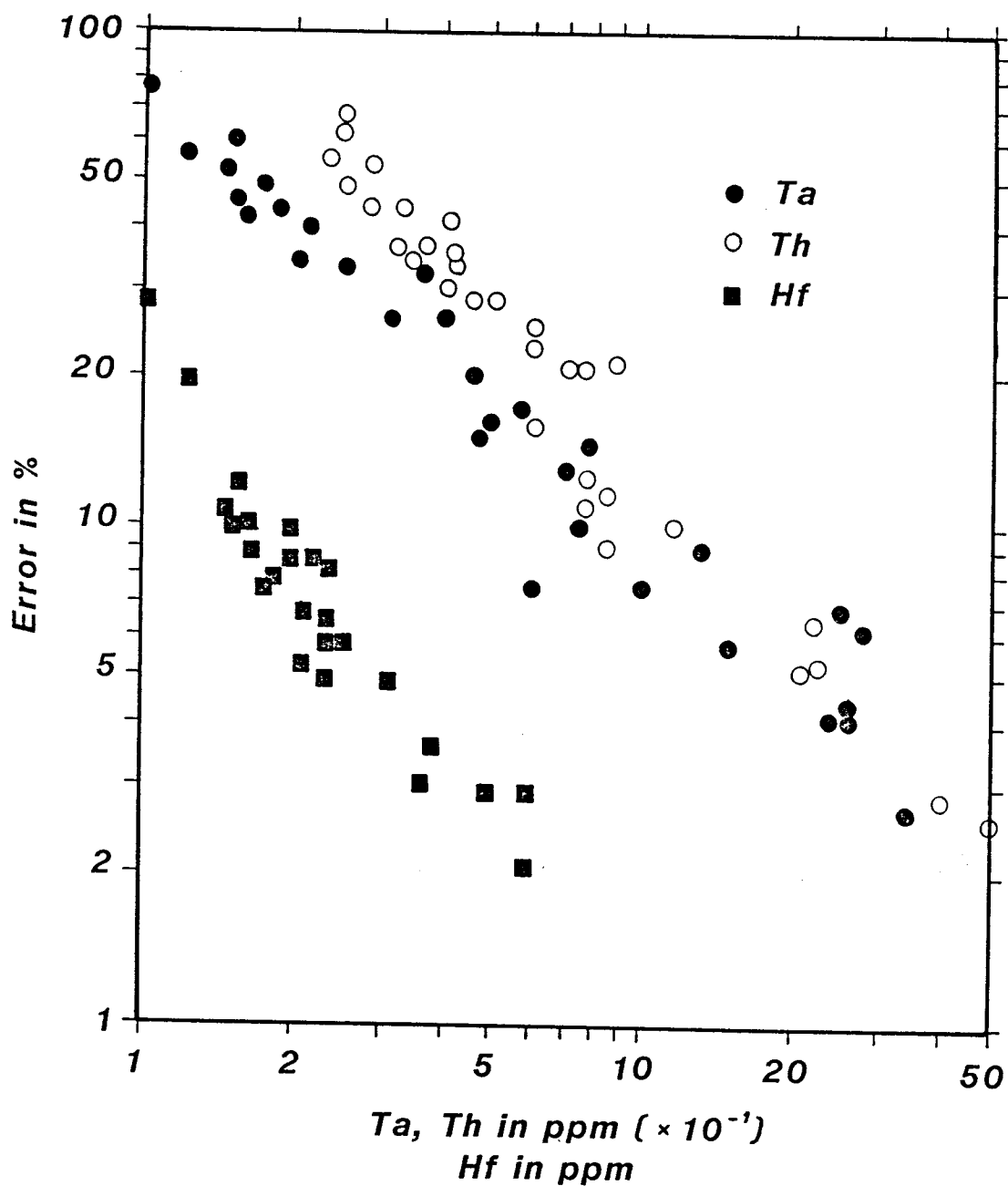


Figure I.2

Empirical diagram to estimate the correlation of the analytical errors in % with the concentration of Ta, Th, and Hf.

APPENDIX II

Rare Earth Element Analyses
Of Samples From The
Lems Ridge Olistostrome

And From The
Josephine Ophiolite

Table II.1

Sample #	La	Ce	Sm	Eu	Tb	Yb	Lu

LR 3a	3.769 ₃ 10.0	11.20 ₇ 11.4	2.684 ₂ 11.7	0.915 ₃ 10.6	0.713 ₁₀ 12.1	2.565 ₁₃ 10.4	0.356 ₈ 9.2
LR 5	5.156 ₃ 13.6	15.11 ₇ 15.5	3.833 ₁ 16.7	1.241 ₂ 14.3	0.965 ₈ 16.4	3.511 ₉ 14.1	0.503 ₆ 13.0
LR 10	4.677 ₃ 12.4	14.60 ₇ 15.0	2.542 ₁ 11.1	0.702 ₃ 8.1	0.443 ₁₄ 7.5	1.412 ₁₄ 5.7	0.203 ₁₀ 5.3
LR 11a	4.278 ₃ 11.3	10.95 ₈ 11.3	2.547 ₁ 11.2	0.854 ₃ 9.9	0.640 ₁₁ 10.9	2.549 ₁₄ 10.3	0.348 ₈ 9.0
LR 17	4.092 ₃ 10.8	12.10 ₈ 12.4	3.091 ₁ 13.4	0.901 ₃ 10.0	0.741 ₁₁ 12.6	2.665 ₁₃ 10.6	0.354 ₈ 9.1
LR 28	39.60 ₁ 104.8	78.06 ₂ 80.0	8.649 ₁ 37.6	2.892 ₂ 33.4	1.261 ₆ 21.4	2.437 ₁₄ 9.7	0.306 ₈ 7.8
LR 30	67.47 ₂ 178.5	99.26 ₃ 101.7	16.35 ₁ 71.1	4.161 ₂ 48.0	2.291 ₅ 38.9	4.107 ₁₀ 16.5	0.596 ₇ 15.4
LR 31	111.6 ₂ 295.4	169.4 ₁ 173.5	17.97 ₁ 78.1	3.720 ₂ 42.9	2.448 ₅ 41.6	5.849 ₁₂ 23.4	0.809 ₇ 20.3
LR 36	3.728 ₃ 9.9	10.29 ₈ 10.5	2.373 ₁ 10.3	0.759 ₃ 8.8	0.415 ₁₃ 7.1	1.377 ₁₅ 5.5	0.202 ₁₀ 5.2
LR 67	16.15 ₂ 42.7	27.52 ₄ 28.2	3.719 ₂ 16.2	1.480 ₂ 17.1	0.798 ₉ 13.6	2.661 ₁₂ 10.7	0.391 ₈ 10.1
LR 70	10.45 ₂ 27.7	22.27 ₄ 22.9	3.550 ₂ 15.5	0.972 ₂ 11.4	0.555 ₁₀ 9.5	1.602 ₁₅ 6.4	0.203 ₈ 6.2
LR 113	8.963 ₂ 23.7	18.99 ₃ 19.5	3.068 ₂ 13.3	0.909 ₂ 10.5	0.407 ₁₀ 8.0	1.469 ₁₆ 5.9	0.228 ₉ 5.9
LR 575	0.668 ₉ 1.8	4.007 ₃₂ 4.1	0.989 ₂ 4.3	0.343 ₈ 3.9	0.251 ₃₆ 4.3	0.798 ₁₃ 4.6	0.199 ₈ 5.1

Table II.2

Sample	La	Ce	Sm	Eu	Tb	Yb	Lu

G 54	7.711 ² 20.4	21.44 ³ 22.0	5.189 ¹ 22.6	1.508 ¹ 17.4	1.253 ⁵ 21.3	4.888 ⁶ 19.6	0.650 ³ 16.8
D 74a	3.880 ³ 10.3	11.35 ⁷ 11.6	2.884 ¹ 12.5	0.976 ² 11.3	0.739 ⁸ 12.6	2.664 ⁸ 10.7	0.347 ⁴ 9.0
Z 30	2.880 ³ 7.6	7.723 ¹⁰ 7.9	2.214 ¹ 9.6	0.728 ³ 8.4	0.493 ¹² 8.4	2.027 ¹⁴ 8.1	0.287 ⁶ 7.4
CC 5	3.324 ⁴ 8.8	10.24 ¹⁰ 10.5	2.473 ² 10.8	0.745 ³ 8.6	0.591 ¹¹ 10.0	2.113 ¹³ 8.5	0.306 ⁹ 7.9
D 71	5.877 ³ 15.5	15.79 ⁷ 16.2	3.656 ¹ 15.9	1.209 ² 14.0	0.914 ⁸ 15.5	3.322 ⁹ 13.3	0.458 ⁶ 11.8
Z 58	4.313 ³ 11.4	12.72 ⁷ 13.0	2.873 ¹ 12.5	1.023 ² 11.9	0.710 ⁹ 12.1	2.606 ¹⁰ 10.5	0.345 ⁷ 8.9

Z 47b	9.379 ² 24.8	22.24 ⁴ 22.8	4.231 ¹ 18.4	1.387 ² 16.0	0.896 ⁶ 15.2	2.790 ⁸ 11.2	0.362 ⁵ 9.4
Z 49 ¹	11.50 30.4	30.00 30.7	5.30 23.0	1.65 19.0	0.66 11.2	3.60 14.5	0.53 13.7
Z 51	2.706 ⁴ 7.2	7.601 ¹¹ 7.8	2.460 ¹ 10.7	0.963 ² 11.1	0.728 ⁶ 12.4	3.012 ⁸ 12.1	0.390 ⁵ 10.1

A 20	1.155 ⁵ 3.1	5.130 ¹⁴ 5.3	0.876 ¹ 3.8	0.330 ⁵ 3.8	0.292 ¹⁶ 5.0	1.154 ¹³ 4.6	0.172 ⁷ 4.5
R 20	2.643 ³ 7.0	8.176 ¹² 8.4	1.297 ¹ 5.6	0.410 ⁵ 4.7	0.186 ³⁰ 3.2	0.935 ¹⁶ 3.2	0.174 ⁸ 4.5
Y 5	2.333 ⁴ 6.2	7.138 ²² 7.3	0.884 ² 3.8	0.217 ¹⁴ 2.5	0.138 ⁶² 2.3	0.890 ¹⁵ 3.8	0.166 ¹⁰ 4.6

¹: analyzed at Portland State University

Table II.3

Instrumental Neutron Activation Analysis

W-1 USGS-Standard

		(Flanegan, 1973)	(Cornell University)

La	11	10.86	+/- 0.12
Ce	23	23.04	+/- 0.73
Sm	3.5	3.29	+/- 0.02
Eu	1.11	1.04	+/- 0.02
Tb	0.65	0.68	+/- 0.04
Yb	2.1	2.09	+/- 0.06
Lu	0.34	0.29	+/- 0.01
Hf	2.6	2.32	+/- 0.13
Ta	0.50	0.47	+/- 0.07
Th	2.42	2.07	+/- 0.11
Sc	35	36	+/- 0.2
Cr	120	128	+/- 2
Ni	84	84	+/- 12
Co	46	46	+/- 0.3
Na ₂ O	2.14	2.16	+/-0.02

Principles of Neutron Activation Analysis

Since most of the critical data for this study were obtained by INAA (the rare earth elements and the elements Ta, Th, and Hf), an outline of the analytical techniques is in order.

The underlying principle of INAA is the transmutation of naturally occurring stable isotopes into synthetic radioactive isotopes. Their abundances can be quantitatively determined by detection of γ -rays produced by their decay. This transmutation takes place by exposure of the sample to a high flux of neutrons in a nuclear reactor, resulting in neutron capture by certain stable isotopes. The abundance of the product nuclei is proportional to the original concentration of the particular element and can be determined by monitoring the γ -rays associated with their decay to a stable daughter. Since these γ -rays emitted have distinct energies for each specific nuclide, and since appropriate detection devices can effectively discriminate these energies, the complex decay of many nuclides can be detected in a single sample. Ideally the chemical abundances could be calculated using the proportionalities listed in the qualitative relation below:

$$c^* \propto c_0 \cdot \phi e^{-\lambda t}$$

C^*	= abundance of product nuclide after irradiation
C_0	= abundance of stable parent nuclide
ϕ	= neutron flux in neutrons per cm^2 per time
λ	= decay constant of the radioactive product
t	= complex time term including the duration of radiation, and the time elapsed since removal from the neutron flux.

This is impractical, however, due to variations of the irradiation parameters. Instead, standards with known element concentration are irradiated and counted together with the unknown. Unknown concentrations can then be calculated from the corrected counting ratios of sample/standard, where the concentration of a particular element is directly proportional to the peak area in a γ -spectrum associated with the specific isotope.

Corrections are necessary to account for the following variations:

- (1) different counting time = decay correction
- (2) position within the reactor = flux correction
- (3) position relative to the detector during counting = geometry correction.

Other corrections account for "tailing" and interference effects of closely spaced γ -peaks in the spectrum. Yet another type of correction removes contamination of W, Ta, and Co which is introduced by

powdering samples in a Tungsten-carbide shatterbox. Since all shatterboxes have different W/Ta ratios, the data reduction program usually corrects only for a specific shatterbox (in this case, the one at Cornell). Therefore it is necessary to determine the W/Ta ratio of the specific shatterbox used for sample preparation by running a blank sample that was ground in this box. Another possibility is to avoid contamination all together and to use a Al_2O_3 or porcellain powdering device, as done for this study.

The half-lives of the rare earth radionuclides range from a few hours up to hundreds of days. In order to obtain a sufficient resolution for the short-lived as well as for the long-lived isotopes, a minimum of two counting sessions is required. A first count is scheduled about one week after irradiation. This allows for the "hot" radioactivity to die away, while assuring reasonably timed counting (between 1 and 2 hours, depending upon the activity of the sample). A second count includes the longer lived isotopes and therefore can be scheduled more flexibly: however, a time lag of approximately 40 days between irradiation and second count appears to be the best choice. A third count about six months after irradiation to improve the Tb and Gd data is optional, but usually not performed.

The detection assembly is comprised of a high purity Germanium detector together with a multi-channel analyzer

(MCA) and analog-to-digital converter. Each channel of the MCA represents an energy increment. Pulses from the detector are digitized to pulse counts and assigned to the channel with the particular energy. In order to record a γ -spectrum with sufficient resolution, it is necessary to assign a minimum of 4000 channels or so to the energy range, resulting in a resolution of about 0.40 keV per channel. The detection assembly is interfaced with both a mainframe computer and PC's for data storage and reduction.

Effective counts in a γ -peak area are determined by a 1/2-width - full-height method: that is, by subtracting the background counts b_i from the total peak counts p_i , where i is the number of channels in the region of the peak. In selecting channels for background determination, one tries to find channels free of interferences on each side of the peak, and channels as close to the peak as possible without overlapping into the tail of the peak. The background usually has a slope and subtracting from both sides of the peak allows a more realistic estimate of the actual background noise. While the choice of peak- and background areas has to be performed manually, the data reduction is completely automated.

APPENDIX III

MORB Normalized Element Abundances

For Samples From The
Lems Ridge Olistostrome

And From The
Josephine Ophiolite

Table III.1

N-MORB normalized element abundances for LR samples
 Normalization factors are from PEARCE (1983)

Sample #	Ba	Th	Ta	Ce	Zr	Hf	Sm	Ti	Y	Yb	Ni	Cr
in ppm	20	0.20	0.18	10	90	2.40	3.30	8993	30	3.40	138	290
*****	*****	*****	*****	*****	*****	*****	*****	*****	*****	*****	*****	*****
LR 3a	7.55	1.93	1.02	1.12	0.86	0.83	0.81	0.70	0.73	0.75	0.44	0.45
LR 5	0.50	1.63	1.37	1.51	1.02	1.14	1.16	1.01	1.07	1.03	0.52	0.45
LR 10	3.00	2.03	*	1.46	0.66	0.82	0.77	0.31	0.40	0.42	1.29	2.30
LR 11a	1.30	1.84	1.91	1.09	0.79	0.72	0.77	0.79	0.77	0.75	0.88	0.61
LR 17	13.40	1.85	2.02	1.21	0.91	0.89	0.94	0.95	0.77	0.78	0.65	0.47
LR 28	41.10	19.20	14.60	7.81	2.80	2.90	2.62	1.74	0.87	0.72	1.20	0.81
LR 30	22.20	25.30	17.60	9.93	3.23	3.16	4.95	1.99	1.87	1.21	2.67	1.69
LR 31	67.10	24.60	19.50	16.90	2.92	2.52	5.45	1.50	2.17	1.72	0.82	0.58
LR 36	10.80	1.24	0.46	1.03	0.63	0.60	0.72	0.47	0.46	0.40	0.49	0.21
LR 67	15.40	3.49	3.84	2.75	0.93	1.00	1.13	0.93	0.83	0.78	0.98	0.85
LR 70	6.05	5.70	0.19	2.23	0.89	0.93	1.08	0.35	0.47	0.47	0.41	0.64
LR 113	38.30	3.81	*	1.90	0.93	0.95	0.93	0.29	0.67	0.43	0.20	0.28
LR 575	1.91	*	0.60	0.40	0.24	0.20	0.30	0.31	0.36	0.23	0.73	1.47
Z 47b	2.20	3.80	4.06	2.22	1.50	1.26	1.28	1.25	1.10	0.82	0.33	0.32
Z 49	-	9.00	6.00	3.00	1.73	1.50	1.60	1.41	1.23	1.05	0.31	0.25
Z 51	-	*	1.44	0.76	0.80	0.68	0.74	0.81	0.83	0.88	0.61	1.20

* = below detection limit

Table III.2

N-MORB normalized element abundances for Josephine samples

Sample #	Ba	Th	Ta	Ce	Zr	Hf	Sm	Ti	Y	Yb	Ni	Cr
in ppm	20.00	0.20	0.18	10.00	90.00	2.40	3.30	8993.00	30.00	3.40	138.00	290.00
	-	2.62	0.93	1.57	1.04	0.98	1.11	0.83	1.03	0.98	0.20	0.10
Z 58	4.55	1.77	0.95	1.27	1.09	0.96	0.87	0.81	0.83	0.77	0.30	0.21
D 74	15.00	1.69	0.93	1.14	0.79	0.77	0.87	0.79	0.93	0.78	0.25	0.33
CC 5	-	1.37	0.79	1.02	0.83	0.82	0.75	0.69	0.73	0.66	0.62	0.59
Z 30	-	1.06	0.67	0.77	0.68	0.68	0.67	0.51	0.73	0.60	0.58	0.33
A 20	1.00	*	0.28	0.51	0.26	0.29	0.27	0.24	0.37	0.34	1.95	3.26
R 20	1.46	2.05	*	0.82	0.41	0.34	0.39	0.24	0.37	0.28	2.72	3.28
Y 5	5.05	1.82	0.36	0.71	0.31	0.33	0.26	0.15	0.30	0.26	2.60	3.06

* = below detection limit

APPENDIX IV

$^{40}\text{Ar}/^{39}\text{Ar}$ Data Tables

Table IV.1

Isotopic abundances of potassium¹ and
atmospheric argon²

Isotope	Atomic abundance (%)
³⁹ K	93.2581 +/- 0.0029
⁴⁰ K	0.01167 +/- 0.00004
⁴¹ K	6.7302 +/- 0.0029
⁴⁰ Ar	99.600
³⁸ Ar	0.063
³⁶ Ar	0.337

- ¹ : after Garner and others (1975)
² : after Nier (1950)

Table IV.2

Decay constants for ^{40}K ¹

Quantity	Value
λ_{β^-}	$4.962 \times 10^{-10} \text{ yr}^{-1}$
λ_e	$0.581 \times 10^{-10} \text{ yr}^{-1}$
$\lambda = \lambda_e + \lambda_{\beta^-}$	$5.543 \times 10^{-10} \text{ yr}^{-1}$
λ/λ_e	9.540
half-life	$1.250 \times 10^9 \text{ yrs}$

¹ : after Steiger and Jäger (1977)

Table IV.3

Temp (°C)	40Ar/39Ar	37Ar/39Ar	36Ar/39Ar (E-3)	39Ar (E-13mol)	339Ar rel.	340Ar*	40Ar*/39Ar	Age (Ma)
LR 10 Hornblende								
750	55.31	2.373	129.7	1.270	10.1	30.9	17.16	185.2 +/- 5.0
850	17.31	0.830	9.706	2.110	26.9	83.4	14.48	157.5 +/- 2.8
900	15.76	2.090	3.924	0.826	33.4	92.8	14.74	160.2 +/- 5.8
940	15.61	7.096	7.193	1.030	41.6	88.8	14.00	152.5 +/- 6.9
980	17.56	21.49	21.42	0.786	47.9	71.4	12.81	140.0 +/- 4.1
1000	21.88	41.50	30.86	0.588	52.5	70.2	15.95	172.7 +/- 12
1015	23.26	47.35	31.99	0.565	57.0	72.1	17.50	188.7 +/- 9.4
1030	23.12	46.39	31.03	0.534	61.3	72.9	17.58	189.5 +/- 5.7
1045	22.66	45.26	26.90	0.537	65.5	77.3	18.27	196.6 +/- 10
1060	22.54	43.70	22.65	0.364	68.4	82.1	19.32	207.2 +/- 7.4
1080	22.61	42.98	22.55	0.363	71.3	82.0	19.36	207.6 +/- 12
1100	22.84	43.20	36.04	0.209	73.0	64.5	15.50	168.1 +/- 21
1120	23.53	44.17	27.91	0.219	74.7	75.9	19.77	201.7 +/- 20
1140	21.96	42.70	37.72	0.243	76.6	60.9	14.03	152.8 +/- 13
1160	20.76	34.53	20.55	0.257	78.7	60.3	17.37	187.4 +/- 18
1190	20.78	41.58	21.94	0.802	85.1	81.5	17.53	189.5 +/- 0.7
1250	21.10	41.28	22.82	0.353	91.8	80.3	17.58	189.5 +/- 5.2
1400	26.57	36.35	39.15	1.030	100	65.3	17.89	192.7 +/- 5.5

Table IV.4

Temp (°C)	40Ar/39Ar	37Ar/39Ar	36Ar/39Ar (E-3)	39Ar (E-13mol)	339Ar rel.	340Ar*	40Ar*/39Ar	Age (Ma)
LR 171 Hornblende								
750	54.70	4.295	120.1	0.479	2.89	34.9	19.53	210.0 +/- 4.0
850	20.95	5.940	14.05	0.529	6.09	78.3	17.23	186.5 +/- 4.0
900	17.42	5.008	2.923	0.495	9.08	91.4	16.92	183.3 +/- 2.7
950	16.13	8.568	2.643	0.551	12.4	93.2	15.98	173.6 +/- 3.2
1000	16.25	15.34	7.081	0.782	17.1	89.6	15.30	166.6 +/- 1.7
1030	18.17	20.08	9.019	0.453	19.9	87.1	17.04	184.6 +/- 5.3
1060	19.63	20.53	11.60	0.805	24.7	86.5	17.78	192.2 +/- 4.0
1090	19.17	19.61	8.893	3.160	43.8	92.0	18.05	195.0 +/- 1.6
1120	19.09	18.72	10.24	1.210	51.1	88.5	17.50	189.3 +/- 2.1
1140	19.28	18.65	4.693	0.761	55.7	95.7	19.35	208.3 +/- 1.5
1160	19.34	19.15	8.561	0.564	59.1	89.1	18.29	197.5 +/- 2.8
1180	19.47	19.96	13.49	0.370	61.3	80.5	17.01	184.3 +/- 4.8
1220	20.46	18.92	14.02	1.020	67.5	83.6	17.78	192.2 +/- 3.4
1260	20.39	17.15	16.06	1.200	74.8	80.4	16.95	183.7 +/- 2.4
1400	18.87	18.55	9.774	4.180	100	90.4	17.40	188.3 +/- 0.9

Table IV.5

Temp (°C)	40Ar/39Ar	37Ar/39Ar	36Ar/39Ar (E-3)	39Ar (E-13mol)	39Ar rel.	40Ar*	40Ar*/39Ar	Age (Ma)
LR 871 Hornblende								
750	104.7	9.505	278.2	0.353	5.81	21.7	23.24	248.0 +/- 10
850	25.46	2.149	15.55	0.142	8.16	72.4	21.00	225.6 +/- 15
920	29.36	2.255	36.40	0.290	12.9	60.2	18.75	202.7 +/- 16
980	18.82	9.860	18.10	0.420	19.9	70.4	14.19	155.4 +/- 5.4
1030	17.39	29.29	18.29	0.418	26.8	74.6	14.18	155.3 +/- 8.6
1070	19.07	28.81	3.502	0.375	32.9	97.4	20.33	218.7 +/- 3.7
1100	19.20	24.47	11.24	1.110	51.3	88.8	17.77	192.6 +/- 3.9
1140	18.87	25.05	11.61	0.717	63.1	87.1	17.37	188.5 +/- 3.6
1160	17.37	28.11	6.955	0.169	65.9	84.2	17.49	189.7 +/- 7.3
1190	18.29	30.95	14.76	0.245	69.9	78.3	16.30	177.5 +/- 13
1250	19.25	28.55	12.49	0.539	78.8	86.2	17.77	192.6 +/- 5.9
1400	19.72	25.33	12.52	1.290	100	87.7	17.99	194.9 +/- 2.0

Table IV.6

Temp (°C)	40Ar/39Ar	37Ar/39Ar	36Ar/39Ar (E-3)	39Ar (E-13mol)	39Ar rel.	40Ar*	40Ar*/39Ar	Age (Ma)
LR 1273 Hornblende								
750	89.79	17.17	229.6	0.296	3.73	25.2	23.35	248.5 +/- 15
850	32.22	19.76	46.61	0.101	5.01	53.0	20.01	215.0 +/- 19
920	30.30	16.24	40.95	0.108	6.36	55.0	19.47	209.5 +/- 24
990	19.95	20.14	13.42	0.213	9.05	77.4	17.53	189.3 +/- 8.7
1050	19.23	50.30	21.08	0.484	15.2	80.2	16.90	183.2 +/- 5.5
1075	20.16	36.27	15.54	0.877	26.2	86.4	18.41	188.7 +/- 4.5
1100	19.41	32.61	13.38	0.561	33.3	86.5	18.00	194.5 +/- 4.4
1130	19.23	33.13	10.73	0.465	39.2	89.6	18.66	201.3 +/- 7.3
1170	19.60	30.78	13.92	0.716	48.2	86.0	17.88	193.3 +/- 4.5
1210	19.61	34.35	15.43	0.480	54.3	83.6	17.72	191.7 +/- 5.2
1250	20.32	32.94	15.53	1.470	72.8	86.4	18.31	197.7 +/- 3.5
1400	20.83	31.90	17.70	2.150	100	83.8	18.08	195.4 +/- 1.1

Table IV.7

Temp (°C)	40Ar/39Ar	37Ar/39Ar	36Ar/39Ar (E-3)	39Ar (E-13mol)	%39Ar rel.	%40Ar*	40Ar*/39Ar	Age (Ma)
LR 1573 Hornblende.								
800	94.84	32.25	262.8	0.322	4.08	20.1	19.74	213.3 +/- 13
900	30.77	7.284	45.53	0.107	5.44	52.9	17.85	194.0 +/- 24
970	18.62	28.25	16.72	0.395	10.4	79.9	15.83	173.1 +/- 7.4
1030	20.55	39.44	19.43	0.820	20.9	83.0	17.88	194.3 +/- 5.2
1050	20.92	33.52	14.13	0.548	27.8	88.0	19.40	209.8 +/- 6.8
1070	20.43	31.37	11.90	0.512	34.3	90.1	19.38	209.7 +/- 5.5
1100	30.41	29.41	12.16	0.700	43.2	89.8	19.13	207.1 +/- 2.7
1130	19.75	28.19	12.14	1.150	57.8	89.8	18.37	199.3 +/- 3.9
1150	19.89	28.08	12.92	0.699	66.7	88.0	18.27	198.3 +/- 3.2
1170	21.21	29.06	7.999	0.305	70.5	93.4	21.20	228.2 +/- 10
1200	21.94	31.54	13.25	0.348	74.9	87.9	20.55	221.5 +/- 8.4
1240	23.00	29.87	26.93	0.672	83.5	72.3	17.35	182.8 +/- 5.4
1280	23.13	26.35	29.60	0.248	86.6	66.0	16.40	178.9 +/- 13
1400	21.07	27.91	16.75	1.060	100	83.2	18.30	198.6 +/- 3.4

Table IV.8

Temp (°C)	40Ar/39Ar	37Ar/39Ar	36Ar/39Ar (E-3)	39Ar (E-13mol)	%39Ar rel.	%40Ar*	40Ar*/39Ar	Age (Ma)
LR 82 Hornblende								
850	17.32	0.6388	5.141	2.100	9.52	91.1	15.83	171.5 +/- 1.5
900	15.07	0.8352	3.099	1.570	16.6	93.8	14.20	154.5 +/- 3.5
940	15.15	2.140	1.829	0.970	21.0	96.7	14.75	160.3 +/- 5.5
970	14.43	5.929	6.164	0.664	24.0	89.1	13.02	142.3 +/- 7.0
1000	14.48	17.20	20.06	0.319	25.5	65.5	9.780	107.9 +/- 18
1030	14.50	25.50	9.377	0.260	26.7	90.3	13.64	148.7 +/- 23
1050	14.77	17.57	12.07	0.342	28.2	82.1	12.49	136.6 +/- 18
1075	14.34	13.68	9.872	1.030	32.9	85.3	12.42	136.0 +/- 4.1
1095	14.43	13.22	4.316	1.600	40.1	96.6	14.14	153.9 +/- 2.2
1100	14.48	12.56	8.585	1.240	45.8	87.7	12.86	140.6 +/- 3.1
1125	14.52	12.03	5.847	0.988	50.3	92.8	13.67	149.1 +/- 5.2
1135	14.51	11.74	9.831	1.020	54.9	84.6	12.45	136.3 +/- 7.0
1150	15.30	11.66	10.25	0.936	59.1	84.5	13.12	143.3 +/- 4.4
1170	14.35	11.48	5.717	1.610	66.4	93.0	13.50	147.3 +/- 3.7
1190	14.30	11.07	3.268	2.520	77.8	97.9	14.15	154.0 +/- 1.5
1210	14.24	11.12	6.112	3.250	92.5	92.1	13.25	144.7 +/- 1.1
1260	17.76	12.28	8.118	0.700	95.7	90.3	16.29	176.3 +/- 9.5
1400	66.52	14.18	178.9	0.945	100	21.9	14.71	159.0 +/- 6.8

Table IV.9

Temp (°C)	40Ar/39Ar	37Ar/39Ar	36Ar/39Ar (E-3)	39Ar (E-13mol)	%39Ar rel.	%40Ar*	40Ar*/39Ar	Age (Ma)
D-LRO Hornblende								
850	24.39	2.041	27.30	3.160	11.3	66.9	16.45	179.8 +/- 1.5
920	14.44	0.951	1.093	2.920	21.7	96.8	14.16	155.8 +/- 0.5
950	13.85	2.826	1.152	2.430	30.4	97.2	13.69	150.9 +/- 0.9
980	13.67	9.076	5.567	2.820	40.4	90.9	12.67	140.0 +/- 1.1
1000	14.46	11.42	5.523	0.673	42.8	89.1	13.65	150.5 +/- 2.7
1030	14.33	14.58	9.791	1.070	46.6	83.5	12.49	138.2 +/- 3.2
1060	14.75	13.11	6.299	0.863	49.7	89.4	13.85	152.5 +/- 3.5
1080	15.01	12.36	11.45	0.525	51.6	77.7	12.51	138.4 +/- 2.3
1100	14.87	12.51	10.16	0.450	53.2	79.2	12.77	141.4 +/- 6.0
1120	14.58	12.19	3.646	0.852	56.2	94.1	14.40	158.4 +/- 1.4
1150	14.02	11.66	5.787	2.670	65.8	91.8	13.16	145.2 +/- 1.1
1170	14.30	12.45	7.071	2.290	73.9	89.5	13.12	144.8 +/- 1.1
1190	14.83	13.02	8.492	1.950	80.9	87.1	13.27	146.4 +/- 1.7
1210	16.06	13.31	10.57	1.000	84.5	83.2	13.91	153.2 +/- 1.4
1240	16-94	13.19	14.16	1.780	90.8	78.9	13.72	151.2 +/- 1.6
1400	14.44	12.98	6.015	2.580	100	92.1	13.61	150.0 +/- 1.0

Table IV.10

Temp (°C)	40Ar/39Ar	37Ar/39Ar	36Ar/39Ar (E-3)	39Ar (E-13mol)	%39Ar rel.	%40Ar*	40Ar*/39Ar	Age (Ma)
LR 15 Hornblende								
750	39.89	2.545	81.84	1.410	15.1	39.7	15.88	172.6 +/- 3.9
830	18.81	2.158	10.75	0.715	22.8	83.2	15.77	171.5 +/- 6.9
900	16.86	4.438	15.83	0.627	29.6	73.3	12.49	137.2 +/- 8.2
1000	17.16	43.56	18.84	0.538	35.4	83.3	14.91	162.6 +/- 12
1020	20.57	33.57	39.38	0.161	37.1	52.7	11.39	125.5 +/- 28
1040	21.51	30.14	58.16	0.175	39.0	28.5	6.416	71.8 +/- 33
1070	20.97	30.93	24.32	0.513	44.6	74.7	16.16	175.6 +/- 6.1
1090	20.04	30.96	26.30	0.671	51.8	70.8	14.60	159.4 +/- 10
1100	20.05	31.34	16.13	0.612	58.4	85.5	17.73	191.8 +/- 9.8
1110	23.12	30.11	20.32	0.330	61.9	81.6	19.50	209.8 +/- 12
1125	20.71	31.21	15.92	0.469	67.0	86.3	18.45	199.2 +/- 8.4
1140	20.32	31.47	15.66	0.479	72.1	86.5	18.16	196.2 +/- 7.7
1160	20.42	33.14	15.72	0.710	79.8	87.2	18.38	198.4 +/- 5.9
1185	21.63	33.17	29.03	0.766	88.0	69.9	15.59	169.6 +/- 14
1210	23.24	34.54	16.31	0.200	90.2	87.4	21.21	227.1 +/- 18
1240	22.77	31.35	45.45	0.220	92.5	49.1	11.64	128.1 +/- 8.5
1400	60.71	28.25	157.1	0.692	100	26.5	16.47	178.8 +/- 9.0

Table IV.11

Temp (°C)	40Ar/39Ar	37Ar/39Ar	36Ar/39Ar (E-3)	39Ar (E-13mol)	%39Ar rel.	%40Ar*	40Ar*/39Ar	Age (Ma)
Z 53 Muscovite								
600	26.06	0.2878	26.10	2.44	1.32	69.8	18.34	197.8 +/- 2.2
670	21.47	0.2169	12.53	2.45	2.64	81.9	17.75	191.8 +/- 3.0
730	25.14	0.1846	22.45	2.94	4.23	73.0	18.49	199.3 +/- 2.5
760	23.43	0.0947	10.51	5.77	7.34	86.3	20.29	217.7 +/- 3.4
810	21.99	0.0079	0.4667	8.94	12.2	99.0	21.82	233.0 +/- 9.6
850	23.85	0.0091	2.903	10.6	17.9	96.0	22.96	244.4 +/- 0.4
880	24.23	0.0140	0.8645	10.9	23.8	98.6	23.94	254.1 +/- 2.8
920	23.27	0.0112	0.8881	16.8	32.8	98.5	22.98	244.6 +/- 0.3
950	24.74	0.0205	0.5885	15.9	41.4	99.0	24.54	260.0 +/- 0.5
980	26.84	0.0510	3.763	13.0	48.4	95.5	25.70	271.5 +/- 2.2
1020	22.42	0.0530	0.9938	20.9	59.7	98.4	22.10	235.8 +/- 0.3
1060	26.62	0.0350	0.5452	37.1	79.7	99.1	26.43	278.6 +/- 0.4
1110	27.13	0.0407	1.148	18.9	89.9	98.4	26.76	281.8 +/- 0.4
1160	26.93	0.0754	0.8765	14.7	97.9	98.7	26.65	280.7 +/- 0.4
1200	27.54	0.2025	2.406	1.87	98.9	96.4	26.81	282.4 +/- 1.1
1250	27.86	0.3619	3.230	1.04	99.4	94.9	26.90	283.3 +/- 2.7
1400	35.68	8.040	31.70	1.05	100	74.1	26.97	283.9 +/- 3.1

Table IV.12

U/Pb data for LR 41:

Sample weight: 5.54 mg
 U (total) : 189.95 ppm $^{206}\text{Pb}^*$: 5.099 ppm

Measured ratios: $^{208}\text{Pb}/^{206}\text{Pb} = 0.13052$
 $^{207}\text{Pb}/^{206}\text{Pb} = 0.053298$
 $^{206}\text{Pb}/^{204}\text{Pb} = 4690$

Atomic ratios: $^{206}\text{Pb}^*/^{238}\text{U} = 0.031201$
 $^{207}\text{Pb}^*/^{235}\text{U} = 0.216070$
 $^{207}\text{Pb}^*/^{206}\text{Pb}^* = 0.050226$

Ages: $^{206}\text{Pb}/^{238}\text{U} = 198.1 \text{ Ma}$
 $^{207}\text{Pb}/^{235}\text{U} = 198.6 \text{ Ma}$
 $^{207}\text{Pb}/^{206}\text{Pb} = 205 \text{ Ma}$